Preparation and Characterization of thin films of organic semiconductors and their heterostructures

Dissertation

zur
Erlangung des Doktorgrades
der Naturwissenschaften
(Dr. rer. nat)

dem

Fachbereich Physik
der Philipps-Universität Marburg

vorgelegt von

Dipl.-Phys. Tobias Breuer

aus

Köln, Deutschland

Marburg/Lahn, 2013

Erstgutachter: Prof. Dr. Gregor Witte
Zweitgutachter: PD Dr. Sangam Chatterjee
Einreichungsdatum: 28.06.2013
Als Dissertation angenommen: 31.07.2013
Tag der mündlichen Prüfung: 09.08.2013
Hochschulkennziffer: 1180

Contents

CHAPTER 1

Introduction

Enabling novel applications and transformations of existing technology to further areas of operation, the so-called *Organic Electronics* have gained enormous interest within the last years. Providing efficient processibility at low energetic and monetary costs, especially a lot of industrial companies have made great efforts to realize devices like *organic solar cells (OSC)* [1, 2], *organic field effect transistors (OFET)* [3, 4] or *organic light emitting diodes (OLED)* [5–7]. It may be expected that within the near future a lot of those applications will conquer the markets, as the aforementioned properties as well as the nearly unlimited availability of organic compounds and the well manageable specific control over organic compounds to prepare new materials with desired properties render significant advantages over inorganic compounds [8–11].

Nevertheless, still many fundamental uncertainties exist, of which clearance the industrial research most probably cannot achieve due to its non basic-research, but more application-related focus. To give an example, many organic compounds and therefore also devices that consist of them undergo severe degradation effects, depending on the ambient conditions, typically with critical influence of heat, humidity, oxygen atmosphere and radiation [12–16] - which is obviously a significant issue for organic solar cells. Furthermore, the nucleation process into the solid state of most organic compounds is quite complex and strongly dependent on the preparation conditions. As the microscopic structure, as well as their homogeneity and purity and their structural conformation - due to the highly anisotropic characteristics of the compounds like the charge carrier mobility - strongly influence potential device performance [17–20], the fundamental processes must be enlightened. For that purpose, the analysis of *organic thin films* offers some advantages over the analysis of *organic single crystals*. First, the preparation of the latter is very difficult, resulting in very limited availability. Moreover, they typically exhibit rather strong absorption, which complicates the application of many spectroscopic techniques. Thin films on the other hand allow to circumvent these obstacles. Furthermore, by choice of ideal preparation conditions, these can also be produced such, that they feature high crystalline order and enable precise spectroscopic analyses with respect to the molecular geometry.

With higher complexity of targeted applications, typically the number of involved compounds rises. For example in organic field effect transistors the device characteristic

is not only determined by the properties of the organic material but also by those of the deployed gate dielectric, the contacts and especially by the interfaces between those [21–24]. In organic solar cells, the process of light absorption, charge-carrier generation and transmission to extractable electric current requires two different organic compounds, an *acceptor* material which offers high mobility for electrons and a *donor* material to extract the holes produced by the exciton-generation. In this case, the question whether or whether not a specific material combination works, is strongly determined by the way the two materials intermix or separate from each other [25–27].

Throughout this thesis it has been tried to approach a number of these topics. Of course it is neither possible to provide ultimate answers, nor to reproduce the exact configurations of all possible material combinations. Therefore it was the aim of this work to find model systems, which are simple enough to be understood but at the same time close enough to real applications or fundamental questions to be of interest. The detailed, multi-technique investigation of these model-systems allowed to find correlations for example between preparation and sample structure, spectroscopic characteristics to one another and to monitor the evolution of prepared systems under the variation of external parameters like the temperature or the surface quality. The observation of these issues from different points of view, as represented by different experimental set-ups and methods, allowed to render complex and extensive images of the nanoscopic reality and at the same time required the continuous alignment between the experimentalist's view on reality and the new, steadily increasing experimental results, which is probably the nature of fundamental research.

As initial point for the selection of appropriate model systems, the well-known organic semiconductor pentacene was chosen. As in many regards, extensive pre-studies are available, it appeared as ideal object of comparison to study the effect of slight chemical and structural variations on nano- and microscopic properties. Furthermore, pentacene exhibits a comparably high charge-carrier-mobility for p-type charge carriers of more than 1 $\mathrm{cm}^2/\mathrm{Vs}$ [28] and is therefore frequently used in organic field effect transistors, which means, that it is as prerequisited before, comparably close to commercial application.

The preparation and the characterization of these model systems often required the advancement and redevelopment of experimental techniques to be sensitive for the specific configuration. This is especially true for theoretical methods, that still struggle to describe molecular solids accurately due to their complexity in form and the comparably weak and long-ranging van-der-Waals that stabilize them. These methods of course require very precise experimental data to be benchmarked and readjusted with. The experimental acquisition of such data allowing to make progress in this issue was also an aim that accompanied the process of this thesis along the way.

This dissertation is written in cumulative form. Therefore, the research results are presented in short abstracts, whereas the detailed results have already been published in these publications:

1. Tobias Breuer and Gregor Witte, *Epitaxial growth of perfluoropentacene films with predefined molecular orientation: A route for single-crystal optical studies*, Physical Review B 83 (2011), No. 15, 155428.
   http://dx.doi.org/10.1103/PhysRevB.83.155428 [29]

2. Benedikt Haas, Andreas Beyer, Wiebke Witte, Tobias Breuer, Gregor Witte, and Kerstin Volz, *Application of transmission electron microscopy for microstructural characterization of perfluoropentacene thin films*, Journal of Applied Physics 110 (2011), No. 7, 073514.
   http://dx.doi.org/10.1063/1.3646549 [30]

3. Tobias Breuer, Ingo Salzmann, Jan Götzen, Martin Oehzelt, Antonia Morherr, Norbert Koch, and Gregor Witte, *Interrelation between Substrate Roughness and Thin-Film Structure of Functionalized Acenes on Graphite*, Crystal Growth & Design 11 (2011), No. 11, 4996-5001.
   http://dx.doi.org/10.1021/cg200894y [31]

4. Manuel Marks, Christian Schmidt, Christian H. Schwalb, Tobias Breuer, Gregor Witte, and Ulrich Höfer, *Temperature Dependent Structural Phase Transition at the Perfluoropentacene/Ag(111) Interface*, Journal of Physical Chemistry C 116 (2012), No. 2, 1904-1911.
   http://dx.doi.org/10.1021/jp2094577 [32]

5. Tobias Breuer, Mehmet A. Celik, Peter Jakob, Ralf Tonner, and Gregor Witte, *Vibrational Davydov-Splittings and Collective Mode Polarizations in Oriented Organic Semiconductor Crystals*, Journal of Physical Chemistry C 116 (2012), No. 27, 14491-14503.
   http://dx.doi.org/10.1021/jp304080g [33]

6. Christian Schmidt, Tobias Breuer, Stefan Wippermann, Wolf G. Schmidt, and Gregor Witte, *Substrate induced thermal decomposition of perfluoro-pentacene thin films on the coinage metals*, Journal of Physical Chemistry C 116 (2012), No. 45, 24098-24106.
   http://dx.doi.org/10.1021/jp307316r [34]

7. Ingo Salzmann, Armin Moser, Martin Oehzelt, Tobias Breuer, Xinliang Feng, Zhen-Yu Juang, Dmitrii Nabok, Raffaele G. Della Valle, Steffen Duhm, Georg Heimel, Aldo Brillante, Elisabetta Venuti, Ivano Bilotti, Christos Christodoulou, Johannes Frisch, Peter Puschnig, Claudia Draxl, Gregor Witte, Klaus Müllen, and Norbert Koch, *Epitaxial Growth of π-Stacked Perfluoropentacene on Graphene-Coated Quartz*, ACS Nano 6 (2012), No. 12, 10874-10883.
http://dx.doi.org/10.1021/nn3042607 [35]

8. Tobias Breuer and Gregor Witte, *Thermally activated intermixture in pentacene-perfluoropentacene heterostructures*, Journal of Chemical Physics 138 (2013), No. 11, 114901.
http://dx.doi.org/10.1063/1.4795004 [36]

9. Tobias Breuer and Gregor Witte, *Diffusion-controlled growth of molecular heterostructures: fabrication of 2D, 1D and 0-Dimensional C60-nanostructures on pentacene substrates*, Advanced Materials, *submitted*

The publication regarding polarization-resolved measurements of PFP thin films on NaF(100) substrates with the working title *"'Polarization resolved absorption in highly ordered organic semiconductors: One dimensional anisotropic response beyond the Davydov splitting"'* is still in preparation for publication.
Additionally, another work has been published within the process time of this thesis, which is not part of the cumulative framework:

1. Jonas Schwaben, Niels Münster, Tobias Breuer, Michael Klues, Klaus Harms, Gregor Witte, and Ulrich Koert, *Synthesis and solid-state structures of 6,13-Bis(trifluoromethyl)- and 6,13-Dialkoxypentacene*, European Journal of Organic Chemistry (2013), No. 9, 1639-1643.
http://dx.doi.org/10.1002/ejoc.201201714 [37]

CHAPTER 2

Materials and Experimental Methods

2.1 Materials

In this section, the major materials which have been investigated throughout this thesis, pentacene ($C_{22}H_{14}$) and perfluoropentacene ($C_{22}F_{14}$) are shortly introduced. Additional compounds that have been of concern, like pentacene-tetrone ($C_{22}H_{10}O_4$) and Buckminster fullerene (C_{60}) are discussed within the corresponding publications.

2.1.1 Pentacene (PEN, $C_{22}H_{14}$)

Pentacene (PEN) is a linear, planar *polycyclic aromatic hydrocarbon (PAH)* composed of five fused phenyl rings (cf. Fig. 2.1 b)). Its molecular mass amounts to 278 amu, its density to 1.33 $^{g}/_{cm^3}$. PEN has been studied very thoroughly within the last decades, which results from its comparably high charge carrier mobility for p-type charge carriers of above 1 $^{cm^2}/_{Vs}$ [28] - in one work even a value as high as 5.5 $^{cm^2}/_{Vs}$ has been reported [38] - and its simple structure, which renders it an ideal prototypical model system.

As often found for PAHs [39], PEN crystallizes in a herringbone structure with two molecules in the unit cell. Interestingly, different polymorphs with slight deviations from one another exist: The Siegrist-phase and the Campbell-phase. While both of these are found in bulk structures, there is furthermore a so-called thin film phase, which appears in the first layers of thin films deposited on weakly interacting substrates like oxidized silicon wafers, mostly at thicknesses below 100 nm and preferentially at substrate temperatures close to room temperature. Typically, the following structures are found upon PEN deposition on different substrates:

- **Influence of Substrate Temperature:** At cryogenic substrate temperatures, the formation of large crystalline regions is prohibited due to the lack of sufficient diffusion and processed thin films are amorphous, while with increasing substrate temperature higher crystallinity is found. At substrate temperatures above 360 K the sticking coefficient is significantly reduced, which limits the accessible temperature range during deposition.

- **Weakly interacting substrates:** PEN deposition onto weakly interacting substrates like oxidized silicon [40], glass [41] or alkali halides [42] yields crystalline uprightly (001)-oriented thin films. For higher film thicknesses, still the molecular (001)-orientation is obtained, however, the upper layers crystallize in the Campbell-phase [40]. In the case of isotropic substrates, the grains are isotropically distributed within the surface plane, but if adequate epitaxial relationships exist, like in the case of KBr(100) and KCl(100) [42, 43], only discrete structural conformations are found.

- **Graphite substrates:** Preparation on graphite (HOPG) surfaces yields very smooth films in recumbent (022)-orientation in the Siegrist-phase [44].

- **Metal substrates:** Upon PEN deposition onto single-crystalline metal surfaces like Au(111) and Ag(111) thin films with mostly recumbent orientation are found, which nucleate on top of a completely flat monolayer, that furthermore exhibits thermal stabilization compared to the multilayer [45, 46]. Moreover, the multilayers exhibit significant dewetting, causing comparably rough morphologies. The actual structure in these cases, as well as in the case of HOPG surfaces strongly depends on the surface quality, such that damaged HOPG and polycrystalline gold surfaces yield PEN films in upright orientation due to the absence of sufficient coherence within the substrate to enable efficient interaction between the substrate and the PEN molecules [44, 45].

- **Oxide substrates:** Deposition onto ZnO-surfaces yields thin films in upright (001)-orientation, regardless of the termination of the ZnO substrate [47]. On TiO_2(110) surfaces, the formation of flat-lying molecular films in the monolayer and thin multilayers has been reported [48], which constitutes an interesting system, as in contrast to metal surfaces, where the PEN monolayers are electronically modified by chemical interaction with the substrate, these films allow spectroscopic access to unmodified PEN thin films in lying orientation.

The experimental structural parameters of the different PEN polymorphs are presented in table 2.1.

Polymorph	a	b	c	α	β	γ	space group
Campbell [49]	6.06 Å	7.90 Å	14.88 Å	96.74°	100.54°	94.20°	P $\bar{1}$
Siegrist [50]	6.265 Å	7.786 Å	14.511 Å	76.65°	87.50°	84.61°	P $\bar{1}$
thin film [51]	5.958 Å	7.596 Å	15.610 Å	81.25°	86.56°	89.80°	P $\bar{1}$

Table 2.1: Structural parameters of different PEN polymorphs

Due to its mentioned interesting electronic properties and its model character, several efforts have been made to prepare devices based on PEN like OFETs and solar cells. However, the actual realization of commercial devices using PEN appears unrealistic, due to its susceptibility to oxidation upon exposure to oxygen and UV radiation as well as

its poor solubility [12, 13, 52, 53], which obviates the application of commercially utilized preparation methods like inkjet printing.

2.1.2 Perfluoropentacene (PFP, $C_{22}F_{14}$)

The perfluorinated sibling of PEN, *perfluoropentacene (PFP)*, has first been synthesized in 2004 by Sakamoto et al. [55]. Its molecular mass amounts to 530 amu, its density to 2.21 g/cm^3. As perfluorination of organic compounds is a well-established strategy to enhance their stability against degradation processes [56], PFP was expected to be more stable against catalytic processes in combination with reactive surfaces. However, throughout this work it has been shown that actually in combination with some surfaces, such processes do occur (cf. section 5.6).

The high electronegativity of the fluorine atoms compared to the carbon backbone leads to a reduced electron density within the molecular center and an agglomeration of negative charge in the rim of the molecule. As this charge carrier density is the qualitative opposite to the one of PEN, effective quadrupolar interaction between PEN and PFP is expected (cf. Fig. 2.1 b)). Moreover, this inverse charge carrier distribution also leads to an inversion of the charge carrier mobilities in PFP compared to PEN: Consequently, PFP has a comparably high n-type charge-carrier mobility of about 0.22 cm^2/Vs [57].

In its bulk structure, PFP also exhibits a herringbone motif, in this case with almost perpendicular relative orientation of both molecules in the unit cell. This exceptional molecular conformation allows interesting insights, as by polarization-resolved measurements, the different coupling mechanisms between parallel and tilted molecules can be ideally discriminated.

Like in the case of PEN, a slightly modified crystal structure is found in thin films deposited on weakly interacting substrates [58]. Furthermore, an additional polymorph has been identified and characterized within the framework of this thesis (cf. 5.7), where instead of a herringbone motif, the molecules crystallize in planar conformation. This polymorph is denoted as Salzmann polymorph. As this configuration enhances the overlap of the π-orbitals, more efficient charge transport may be expected in such structures. Indeed, as presented within this work, the charge carrier mobility has been shown to be

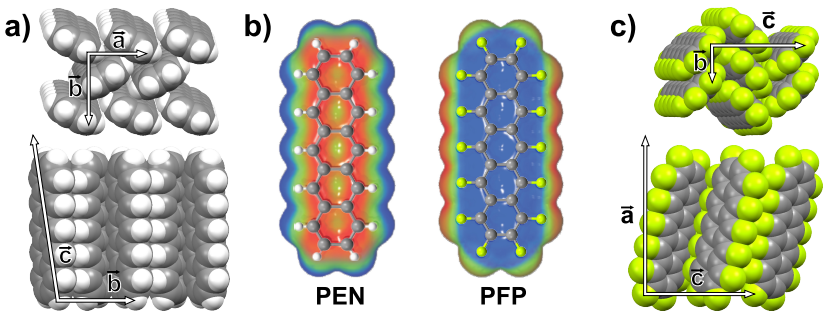

Figure 2.1: Crystal structure of a) PEN and c) PFP with axes denotation, both in their thin film phase, b) molecular structure and electron density maps (color coding: blue-green-red (increasing intensity), taken from [54])

significantly enhanced by a factor greater than 10 compared to the aforementioned value. The different polymorphs are summarized in table 2.2. Note that due to inconsistencies in lattice definition, in the PEN-lattice the $\vec{c}$-vector is mostly parallel to the long molecular axis, while in case of PFP the $\vec{a}$-vector is.

polymorph	a	b	c	α	β	γ	space group
bulk [55]	15.51 Å	4.49 Å	11.45 Å	90°	90.4°	90°	P 2_1/c
thin film [58]	15.76 Å	4.51 Å	11.48 Å	90°	91.57°	90°	P 2_1/c
Salzmann [35]	15.13 Å	8.94 Å	6.51 Å	78.56°	108.41°	92.44°	P 1

Table 2.2: Structural parameters of different PFP polymorphs

In many regards, the correlations between substrate choice, temperature and quality and the resulting structure that have been discussed for PEN thin films are also valid for PFP thin films. Each of those correlations - except from the growth on TiO_2 and ZnO surfaces - has been analyzed within this thesis and will be discussed in the upcoming chapters.

Due to the high sterical compatibility and the inverse quadrupole moments, heterostructures of PEN and PFP appear very interesting. As shown by structural analyses [58, 59] PEN and PFP actually mix at the molecular level and nucleate in a new, combined crystal structure. As both compounds are not only compatible regarding their shape, but also complementary with respect to their electronic properties, also electronic properties of the heterostructure have been analyzed and prototypical bipolar OFETs [55] have been prepared. The analyses of optical absorption spectra [60] and fluorescence spectra [61] have proven electronic interaction between the compounds, resulting in the reduction of the optical band gap by the appearance of a new discrete charge-transfer related absorption band.

Within this thesis, the morphology, the thermal stability as well as the electronic properties of differently prepared PEN:PFP heterostructures have been analyzed in detail (cf. section 5.8).

2.2 Experimental Methods

2.2.1 Organic Molecular Beam Deposition (OMBD)

The samples which are analyzed throughout this work have been prepared by means of *organic molecular beam deposition (OMBD)*. In this preparation technique, the processed compound is stored in a heatable crucible under ultra-high vacuum conditions. Upon elevation of the crucible temperature, material sublimation is activated. While the material flux can be measured by quartz-crystal microbalance, positioning of substrates in the molecular beam enables re-sublimation on these substrates and therefore the fabrication of molecular thin films.

Despite the principally simple fabrication process, the actual thin film structure strongly depends on a number of process parameters like the evaporation rate, the substrate quality and the substrate temperature during deposition, which have to be considered and tuned carefully in order to prepare thin films of satisfactory quality and reliability. In many cases, the substrate temperature is a crucial parameter, which often leads to amorphous films in the case of low substrate temperatures and enhanced crystallinity at higher substrate temperatures. Due to the dependence on the ratio of the flux and the substrate temperature of many nanoscopic processes during thin film formation, the reverse is true for variations of the flux: While high fluxes usually obviate the formation of highly ordered thin films, their quality rises with decreasing fluxes.

The thin films have been prepared in a UHV-chamber (cf. Fig. 2.2, typically $p < 10^{-9}$ mbar) with load lock system to enable quick sample transfers. The chamber has been built up and constantly advanced throughout the process time of this thesis. By combination of liquid nitrogen cooling and electron bombardment heating, a temperature range of 120 - 1000 K at three sample holders was accessible. The implementation of a PID-feedback control allowed precise control over the temperature and the employment of exact heating ramps. To process different compounds within reasonable time scales and to prepare heterostructures of different compounds, the chamber comprises four different evaporation cells. For means of sample preparation, an ion sputter gun is attached, while a quadrupole mass spectrometer enables thermal desorption spectroscopy measurements.

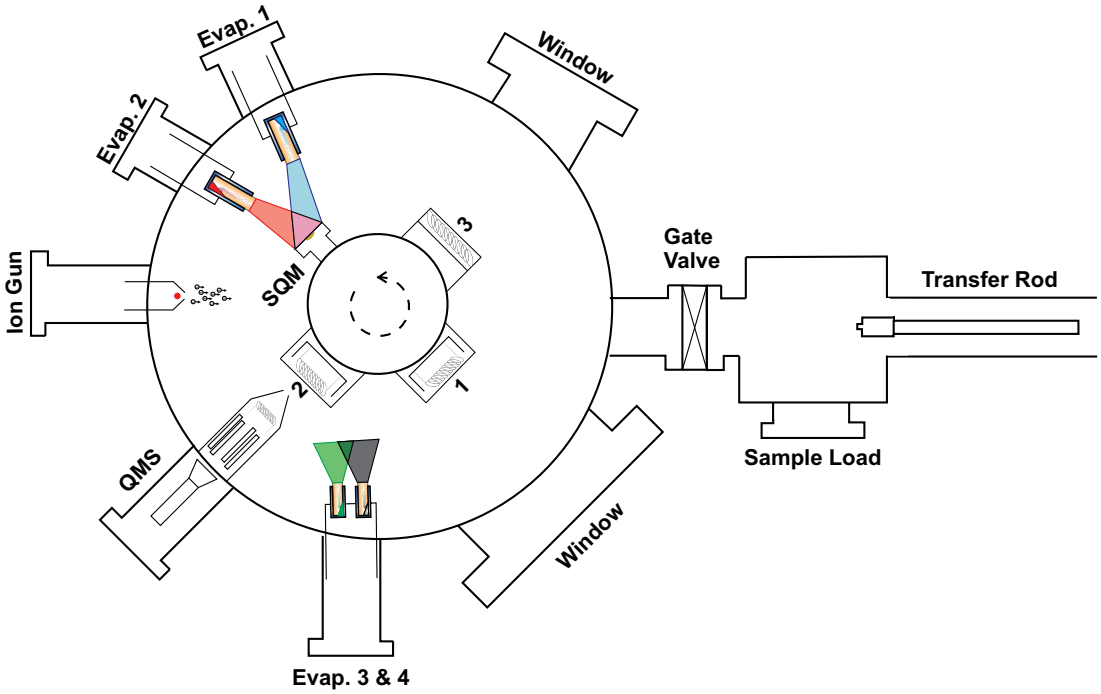

Figure 2.2: Sketch of OMBD-chamber, 1-3 denote the different sample holders

2.2.2 Atomic Force Microscopy (AFM)

Allowing to circumvent the optical diffraction limit, enabling measurements of insulators and providing high-resolution information on surface topography, *atomic force microscopy (AFM)* has become an essential technique in the analysis of nanostructures.

The fundamental principle is that the forces between a tip of few nanometers radius of curvature and the sample are measured and translated into topographical images. For that purpose, piezo scanners move the cantilever that comprises the tip along the sample and the forces are analyzed at each individual point.

Generally, two operation modes can be distinguished: Static operation (*Contact Mode*) and Dynamic operation (*Non-Contact Mode* and *Tapping Mode*). In the first mode, the AFM tip is dragged along the sample surface and the actual height[1] of the tip is used to image the sample topography. Though this operation mode works quite intuitively and allows quick image acquisition, it has one severe disadvantage: The movement of the tip introduces high lateral forces to the surface which may damage the sample, especially in the case of organic samples[2].

In the dynamic mode, the cantilever is excited to an oscillation close to its resonance frequency and the changes of amplitude and frequency of the driven oscillation are monitored. Using a feedback loop, the z-position of the cantilever is manipulated such that the amplitude stays virtually constant. The position of the corresponding piezo actuator is interpreted as the topography information, while the deviations from the initial amplitude and phase values are also analyzed. As the latter are strong, when changes in

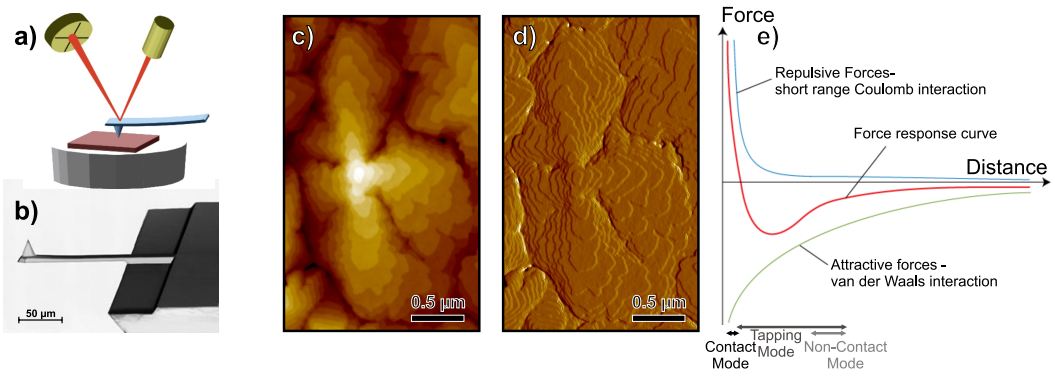

Figure 2.3: a) Visualization of AFM operation [62], b) SEM image of AFM tip [63], c) AFM topography image of 30 nm PEN deposited on SiO_2, d) resp. amplitude image, e) Force-distance curve for different acquisition modes [64]

1 This describes the case of the commonly used *Constant Force* mode, where a feedback loop controlling the relative height is used to keep the force between the tip and the sample constant, while in the *Constant Height* mode, the distance between tip and sample remains constant and the difference in the mutual forces is used to calculate the topography image. As throughout this work, all images have been acquired in the Constant Force mode, the Constant Height mode is not described in detail.

2 In some cases, this effect is utilized to produce damages in the sample, for example to brush the film aside at one part at the sample and by comparing the pristine level to the covered level determine the sample thickness.

the morphology occur, they can be interpreted as derivative of the topography and feature sharp illustrations of domain borders and steps (cf. Fig. 2.3 c),d)).

The two most common different dynamic modes, tapping mode and non-contact mode differ such that the oscillations take place in different distances from the sample surface. While in tapping mode the tip oscillates within the attractive (*van-der-Waals*) regime as well as in the repulsive (*Pauli repulsion*) regime, in non-contact mode the oscillation is limited to the attractive regime. As a consequence, in tapping mode the lateral forces are minimized and images can be obtained at reasonable times at ambient conditions. Non-contact mode on the other hand also minimizes the normal forces and therefore additionally reduces sample damages. Under ideal conditions, atomic resolution can be achieved with this operation mode (Fig. 2.4 a)). However, this results in slower scan speeds and in most cases in the necessity to conduct the experiments in UHV to circumvent acquisition problems due to adsorbed water on the samples, as well as extreme sensitivity to vibrations and acoustic noise in the laboratory.

Though being a simple technique in general, several problems may arise during AFM measurements: For example artifacts may be produced if the AFM tip is not sharp enough (cf. Fig. 2.4 b)-d)), it contains double tips or the control parameter of the feedback control are not correctly chosen.

The general concept of precise positioning at nanometer-scale also offers the opportunity to some advanced detection and manipulation applications. To name only a few, there are techniques that probe the magnetism (*Magnetic force microscopy*), chemical termination using functionalized tips (*Chemical force microscopy*) and the electrical properties (*Current sensing atomic force microscopy*) of the sample. Moreover, some efforts have been made to facilitate storage devices that use AFM tips to read and write the individual sectors at ultrahigh storage density (*Millipede-Project* [67]).

The presented data have been acquired with an Agilent 5500 AFM operated in tapping mode at ambient conditions. AFM tips with resonance frequencies of about 260 kHz, radii of 7 nm and force constants of 26.1 $^{N}/_{m}$ were used.

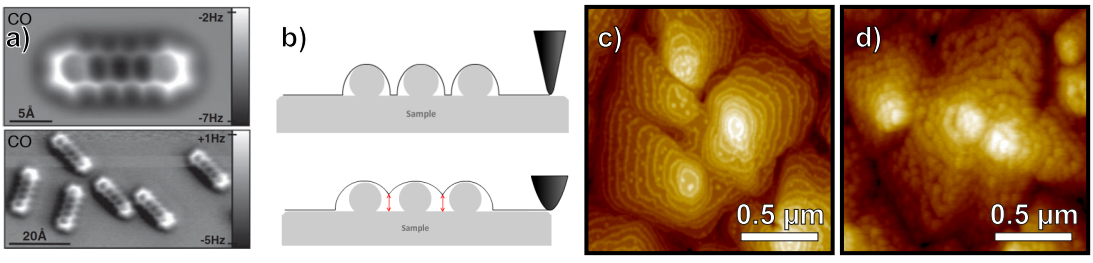

Figure 2.4: a) Non-Contact Mode AFM images of PEN [65], b) Schematic of different imaging quality with sharp (top) and blunt (bottom) tip, c) AFM image of 0.5 nm C_{60} deposited on top of 30 nm PEN on SiO_2 with sharp tip [66], d) with blunt tip

2.2.3 X-Ray Diffraction (XRD)

While AFM is used to characterize the morphology of the sample surface, *x-ray diffraction (XRD)* allows to determine the crystal structure of the sample by analyzing diffraction phenomena of the x-rays by the crystalline sample lattice. This is enabled by the wavelength range of x-ray radiation of 10^{-8} m to 10^{-12} m, which embraces typical atomic distances (e.g. a_{Au}=4.08 · 10^{-10} m). In practice, the intensity of the scattered x-ray signal is monitored as function of the angles ω between x-ray source and the sample and θ between the sample and the detector. In the case of periodically distributed atoms, like in crystals, discrete peaks in this *diffractogram* are observed, which arise from constructive interference of x-rays scattered by atoms in equivalent lattice planes. As constructive interference requires integer ratios between the wavelength and the path difference between two scattered beams, the Bragg law can be derived:

$$n\lambda = 2d\sin(\theta) \tag{2.1}$$

where n describes the diffraction order, λ the wavelength of the x-rays (cf. Fig. 2.5 a)) and d the lattice plane spacing.

Bragg-Brentano geometry

Consequently, continuous symmetric variation of ω and θ in the so-called *Bragg-Brentano geometry* allows to probe the periodicity of the sample in out-of-plane direction (which means parallel to the surface normal). The angle θ at which the constructive interference is observed can then be used to calculate the corresponding out-of-plane lattice spacing, denoted as $d_\perp$. In the case of known crystal structures, comparisons with the calculated diffractograms allow a direct correspondence to the actual sample structure. In Fig. 2.5 c), three different structures of PFP thin films as well as their corresponding diffractograms are

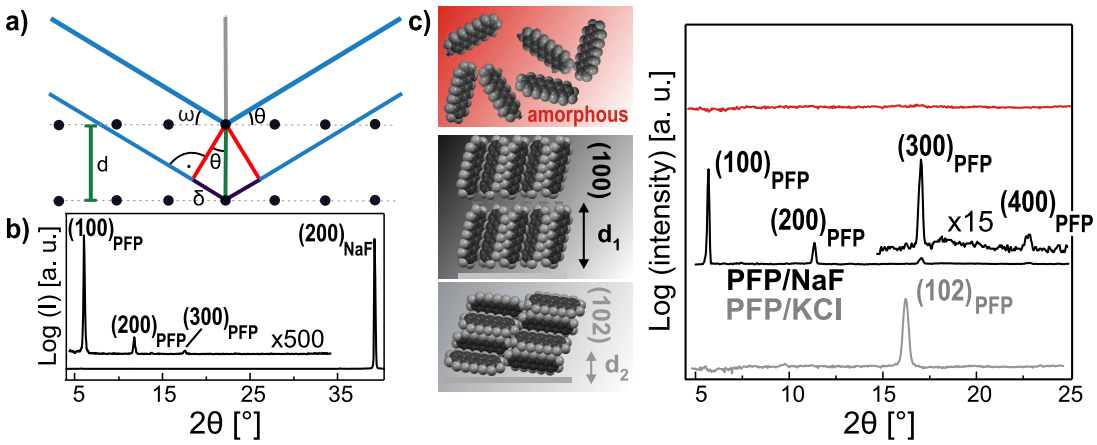

Figure 2.5: a) Geometric derivation of Bragg law [68], b) Bragg-Brentano-Scan of 150 nm PFP deposited on NaF(100), c) Bragg-Brentano-Scan of PFP in different orientations: amorphous (top), upright (100)-orientation (middle), recumbent (102)-orientation (bottom)

presented. While in the case of amorphous films with random distribution of the molecules and absence of any crystalline domains no diffraction peaks are observed (top panel), in the case of uprightly oriented PFP-molecules in (100)-orientation (middle) diffraction peaks are found at the (n00)-positions, e.g. in first order at θ=5.695°, corresponding to a lattice spacing of 15.51 Å. If the molecules exhibit the recumbent (102)-orientation, this gives rise to a peak at the higher Bragg angle of θ=16.646°, which corresponds to $d_{\perp}$=5.32 Å.

Note that the analyzed thin films of organic compounds exhibit quite low diffraction cross sections as they mainly consist of carbon atoms. As consequence, the highest intensity typically results from substrate contributions, while the thin film peaks are significantly weaker (cf. Fig. 2.5 b)). Therefore, the used diffractometer has to feature high beam intensities and very sensitive detectors.

Rocking Curves

If samples are analyzed in the Bragg-Brentano geometry, only those crystallites contribute to the signal, that exhibit lattice planes in exact parallelism to the sample surface. In some cases however, some crystallites can be slightly tilted with respect to the surface normal. Thus, a scan along the ω angle at fixed detector position and therefore fixed lattice plane spacing, allows to probe the tilt distribution of the crystallites. Specifically, the broadness of this so-called *rocking curve* is considered as benchmark of the sample quality. Typically samples, which were prepared under non-ideal conditions (e.g. high deposition rates, low substrate temperatures, poor substrate quality) exhibit broad peaks in rocking curves. Fig 2.6 a) presents an example for such a behavior: It compares the rocking curves of an epitaxial gold film grown on a muscovite surface (details on this procedure can be found in [69, 70]) before and after an annealing step of the sample, obtained at the gold

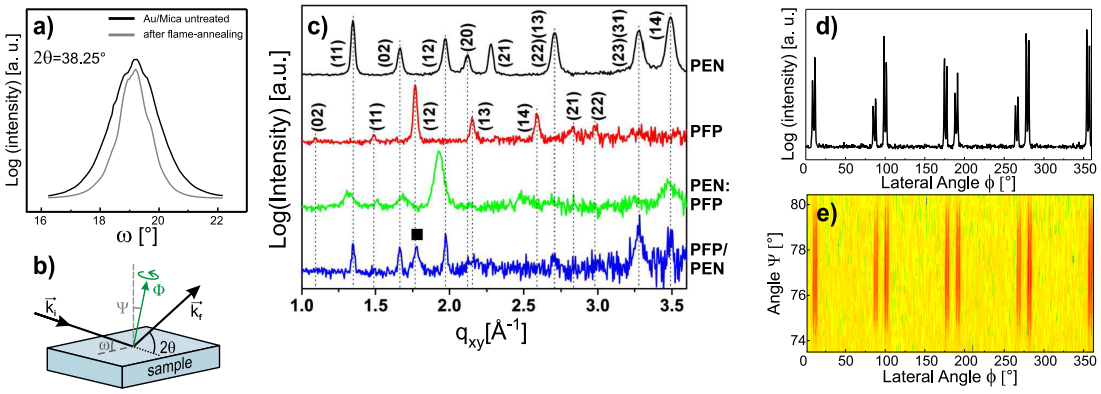

Figure 2.6: a) Rocking curve of Au(111) grown on muscovite surface before and after annealing step, b) denotation of relevant angles in the experimental set-up, c) GIXD measurements of PEN, PFP, co-evaporated PEN:PFP and layered PFP/PEN [58], d) ϕ-scan along the PFP (112) and (11$\bar{2}$) lattice plane of 150 nm PFP deposited on NaF (100), e) corresponding pole figure (color coding: green-yellow-red (increasing intensity))

(111) diffraction peak. It becomes obvious that the rocking width of the sample before the annealing process amounts to a significantly higher value (1.88°) than afterwards (1.22°).

In-plane Diffraction

While the standard Bragg-Brentano geometry allows to probe the vertical periodicity of the lattice, it may also be of interest in some cases to gain insight into the in-plane orientation of a sample. In this case, the sample is rotated along the angle Ψ (cf. Fig. 2.6 b)) to allow momentum transfer of the x-ray beam not only perpendicular ($\vec{k_\perp}$), but also parallel to the sample surface ($\vec{k_\parallel}$).

When this rotation considers the orientation of the in-plane lattice plane relative to the sample surface correctly, the corresponding in-plane diffraction peaks can be observed in Bragg-Brentano scans. In many cases, the lattice planes perpendicular to the sample surface are investigated by means of in-plane diffraction, which requires a sample tilt of exactly 90°. In this case, the angle between the x-ray source and the sample is very small (typically α=0.2°), which also enhances the surface sensitivity of this *grazing incidence x-ray diffraction (GIXD)* technique. Fig. 2.6 c) presents various GIXD scans of PEN and PFP films as well as several heterostructures which have been prepared and analyzed in [58].

In the common case of thin films with preferred out-of-plane orientation, but azimuthally isotropic distribution (so-called *2D-powder*), only a small fraction of all crystallites contributes to the intensity of these peaks, which introduces additional requirements on the sensitivity of the apparatus and the data acquisition time.

ϕ-Scans and Pole Figures

If thin films do not only exhibit preferred out-of-plane orientation, but also crystallize in discrete azimuthal orientations on the substrate, these films are denoted as epitaxial thin films. Those epitaxial films enable another acquisition method: *ϕ-scans*. Here, the angles θ and Ψ are set to the correct values for the lattice plane of interest and the sample is rotated along its surface normal (cf. Fig. 2.6 b)). As the crystallites are non-isotropically distributed, the corresponding lattice planes can fulfill the Bragg condition only at discrete orientations. Depending on the symmetry of the epitaxial film growth and the appearance of mirror domains, quite high numbers of such peaks may occur. Fig. 2.6 d) presents a ϕ-scan along the PFP (112) and (11$\overline{2}$) lattice plane at a sample of 150 nm PFP deposited on NaF(100). An analysis of such ϕ-scans allows to derive the actual structural conformation of the thin film (see section 5.1).

Combinations of the variation along ϕ and Ψ to simultaneously determine the rotational distribution and the rocking width are denoted as *Pole Figures* (cf. Fig. 2.6 e)).

More information on x-ray diffraction applied for thin film analysis can be found in [71].

Experimental-Setup

If not stated differently, the XRD measurements were conducted with a Bruker D8 Discover diffractometer using Cu K_α radiation (λ=1.54056 Å) and a LynxEye detector. In case of the publications [30],[31],[35],[36] and [37] different set-ups were used, which are described in detail in the experimental sections of the corresponding publications.

2.2.4 UV / Vis Absorption Spectroscopy

As the transitions between the *highest occupied molecular orbital (HOMO)* and the *lowest unoccupied molecular orbital (LUMO)* as well as the excitonic transitions of many PAHs and especially PEN and its substituted derivatives are in the energetic range of several eV, *UV / Vis absorption spectroscopy* is a powerful tool to investigate these characteristics.

When absorbing light, the corresponding molecule is excited into a level above the ground-state. Consequently, the charge distribution within the molecule changes. Comparing the optical spectra of isolated molecules, represented by solution spectra[1], and molecular solids, represented by thin films, some striking differences are observed (cf. Fig. 2.7 a)). Most prominently, absorption bands are found at energies below the fundamental optical band gap (HOMO-LUMO transition[2]). To understand this, one has to regard the different molecular vicinities. In case of isolated molecules, all excitations have to occur within one single molecule. Contrary, in solids interactions between several molecules take place. One such interaction is the formation of excitonic states. These states are stabilized by mutual Coulomb-interacting between the excited charge-carriers and their vicinity. As a consequence, the energy required to excite this state is lower than the energy of the

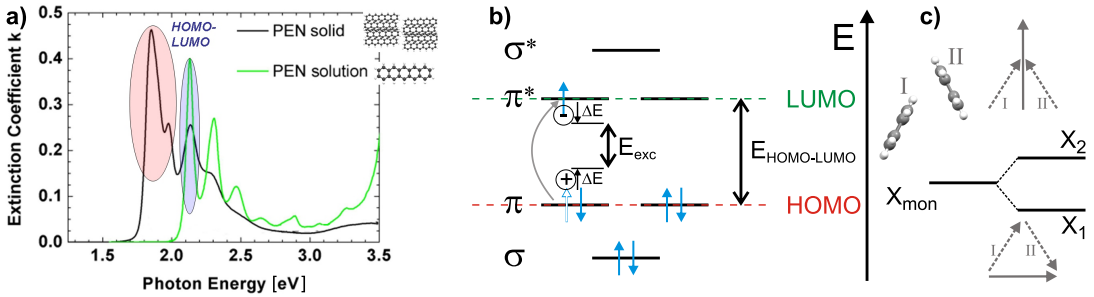

Figure 2.7: a) Comparison of solution and solid spectra of PEN (modified from [72]), b) energy scheme of relevant excitations, c) schematic of Davydov-Splitting

1 Unfortunately, in solution spectra additional parasitic effects like solvent-shifts due to the non-negligible polarizability of the solvent come into play. As frequently no gas-phase spectra were available (especially for larger PAHs) and the solvent-shifts are expected to be small compared to the peak broadness, they are used to represent isolated molecules anyway in this case.

2 Though denoted as HOMO-LUMO transition, note that the energy of this transition is not exactly determined by the energy difference between the HOMO and LUMO levels determined by PES and IPES. The reason for this is that also in isolated molecules excitation of an electron also influences the charge-carrier distribution of the residual molecule, which is denoted as hole. As these two attract each other by Coulomb interaction, the energy difference is decreased [73]

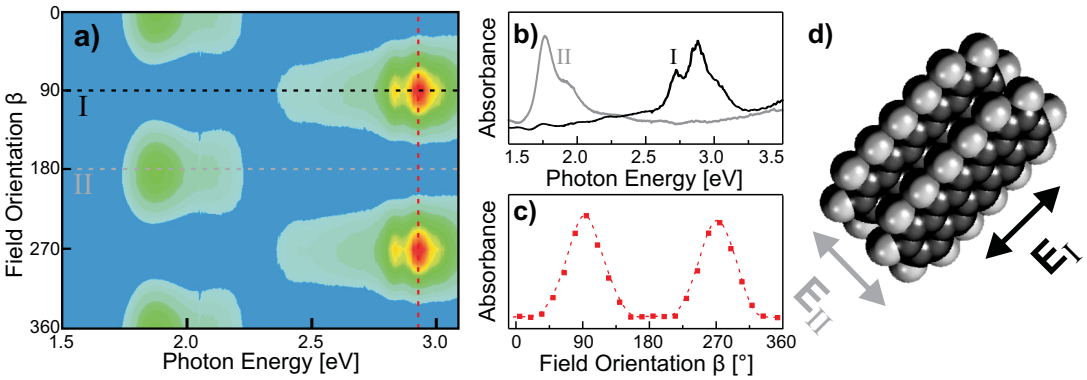

Figure 2.8: Polarization-Resolved optical spectra of PFP thin films deposited onto a KCl(100) surface. a) False-color contour plot of absorption measurements as function of linear light polarization (color coding: blue-green-yellow-red (increasing intensity)), b) cuts along the energy, c) along the polarization axis, d) scheme of orientation of light polarization to molecular confirmation

fundamental transition (Fig. 2.7 b)). The difference between both energies is defined as binding energy of the exciton.

Two different limiting scenarios are commonly discussed: The *Mott-Wannier-Exciton* and the *Frenkel-Exciton*[1]. The first is usually found in materials with high dielectric constant and features low binding energies and therefore high radii (defined as average distance between electron and hole). Mott-Wannier Excitons are typically found in covalent, inorganic semiconductors like gallium arsenide. Frenkel-Excitons on the other hand typically appear in materials with small dielectric constant. This characteristic results in comparably high binding energies (in the order of some 100 meV) and therefore tightly bound electrons and holes, separated by few or even only parts of single molecules. In organic materials, often excitons of Frenkel-type are found. Nevertheless, in most cases none of both limiting cases is purely present, but the actual character of the exciton is somewhere in-between.

If the molecular crystal features a unit cell with more than one translationally unequal molecule, these excitations are additionally splitted. To describe this effect, a crystal with two unequal molecules in the unit cell shall be considered. Due to the indistinguishability of both molecules, symmetrical and anti-symmetrical linear-combined states occur. As the exchange interaction is different in these two cases, the resulting excitation energies are different and the modes split in two (cf. 2.8 c)), which is called *Davydov-Splitting*. Both, the intensity and the splitting of the modes are functions of the relative angle between both molecules in the unit cell. These considerations also apply to crystals with more than two molecules in the unit cell and in that case result in splitting into Z different modes with Z as number of translationally unequal molecules in the unit cell. The Davydov-Splitting is discussed in detail in references [74] and [75]. Furthermore, depending on the actual packing motif, also the coupling between translationally equal

1 Sometimes also denoted as *Poole-Frenkel-Exciton*

molecules have to be considered. This effect has been found for PFP and is discussed in section 5.10.

To induce a specific excitation, not only the energy has to amount to the correct value, but furthermore also the light polarization must be compatible with the difference between the electronic charge distribution (orbital) of the initial and the excited state. This geometrical parameter is considered by the fact that the *Transition Dipole Moment (TDM)* is of vector type and its norm describes the corresponding oscillator strength. As a consequence, systematic variations of the relative orientation between the electrical field vector of the linearly polarized light and the TDM allow to determine the sample orientation if the TDM orientation is known and allow the assignment of the TDM orientation if the sample structure is precisely known. In the common case of thin films with uniform texture but equally distributed grains in the lateral dimension, all excitations with TDM in the sample plane are visible (in transmission geometry).
Figure 2.8 shows the application of this technique on epitaxially grown films of PFP on KCl(100) surfaces. By varying the light polarization relative to the sample, the intensity of the absorption bands at 1.75 eV and 2.75 eV is inverted, which represents the different TDM orientations of the corresponding transitions[1]. As the intensity is proportional to the square of the inner product between the E-field vector of the light and the TDM-vector, it scales with $cos^2(\alpha)$ (where α is the angle between both vectors).

In order to allow unambiguous and quantitatively reliable conclusions, the signal contributions from the apparatus and the substrate have also be taken into consideration. For that purpose, in each case reference spectra $I_0(\lambda)$ are acquired and considered in the evaluation.

As known from Beer's law of absorption, the intensity of transmitted light decays exponentially with the sample thickness:

$$I(\lambda,d) = I_0 e^{-\alpha(\lambda)d} \tag{2.2}$$

Therefore, the relative intensity of two different absorption modes (with individual attenuation coefficients α) is a function of the sample thickness.
To circumvent this undesired effect, the parameter absorbance (A=ln($\frac{I_0}{I(d)}$)) is used instead of the transmittance, which is T=$\frac{I(d)}{I_0}$, resulting in equal spectral shape (except for peak broadness) for different sample thicknesses.

Throughout this thesis, the optical spectra were acquired using an Agilent 8453 spectrometer, which enabled measurements in the energetic range of 1.1 to 6.5 eV with spectral resolution of 1 nm. Additional experiments (section 5.10) were conducted using a home-

1 Note that the strong contrast between the absorption spectra as function of the light polarization is only achieved, as the sample which usually exhibits four-fold symmetry is illuminated only in a region where one of the rotational domains is in strong majority compared to the other. For more details on the data, see 5.1.

built setup with tungsten-halogen and deuterium lamps as light sources. This setup enabled measurements with spot sizes below 30 µm in diameter and precise positioning of the spot by combination with an optical microscope. The sample was mounted inside a liquid He-flow cryostat, which allowed access to sample temperatures in the range of 4-500 K. The accessible energetic range in this setup was 0.8 eV to 5.5 eV with spectral resolution of 1 nm.

2.2.5 Fourier-Transform-Infrared-Spectroscopy (FTIR)

Embracing the energetic range between 1 meV and 1.7 eV (resp. 700 nm to 1 mm in wavelengths or 10 cm^{-1} to 13.500 cm^{-1} in wave-numbers), *infrared spectroscopy* is sensitive to vibrational transitions.

In the case of PAHs due to their structure and conjugation, the typically applied mode-assignment via finger-print-identification is not applicable, as the actual displacement patterns are distributed over the entire molecule (cf. Fig 2.9 a) and Ref. [29]). Consequently, in order to fully understand the spectra, detailed correspondence between experiment and theoretical calculations is necessary. The theoretical calculations on the other hand require sufficient consideration of the molecular structure and especially the molecular vicinity. As the analyzed molecular crystals are mostly van-der-Waals-bound, the van-der-Waals-interaction has to be considered in the calculations. In this work this was achieved by using the DFT package *Vienna Ab Initio Simulation Package* (VASP [76, 77]) with periodic boundary conditions (more details in section 5.5).

In the case of *Fourier-Transform-Infrared-Spectroscopy (FTIR)*, the spectra are not acquired by means of discrete measurements at different wave-numbers (*dispersive spectroscopy*) as implemented by using monochromators (like for example in the before discussed UV/Vis spectroscopy) but instead by acquiring the intensity as function of the optical retardation using a Michelson-Interferometer. This allows to measure all frequencies at the same time, resulting in very quick data acquisition times and very good signal-to-noise-ratios. By applying the *Fourier-Transformation* to transform the data from the time

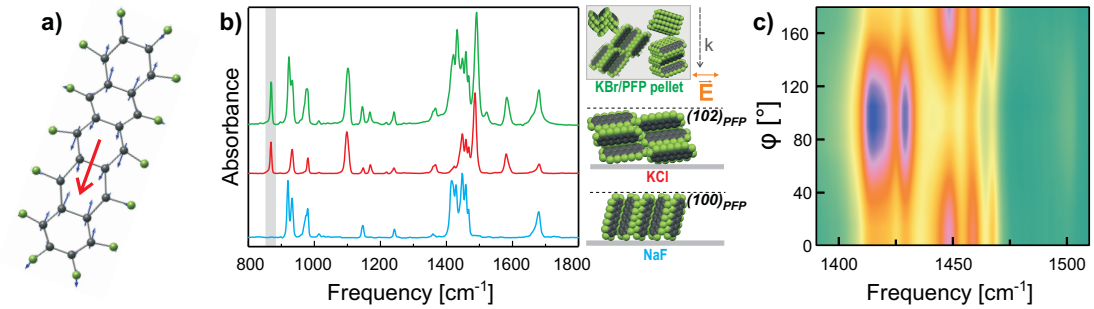

Figure 2.9: a) Displacement pattern of PFP-vibration at ν=867.3 cm^{-1} (shaded in grey in b)), b) Transmission IR spectra for differently oriented PFP crystallites, c) False color 3D plots of polarization-resolved IR absorption spectra of epitaxial PFP film on NaF(100) (color coding: green-yellow-red-blue (increasing intensity)). All figures have been adapted from [33]

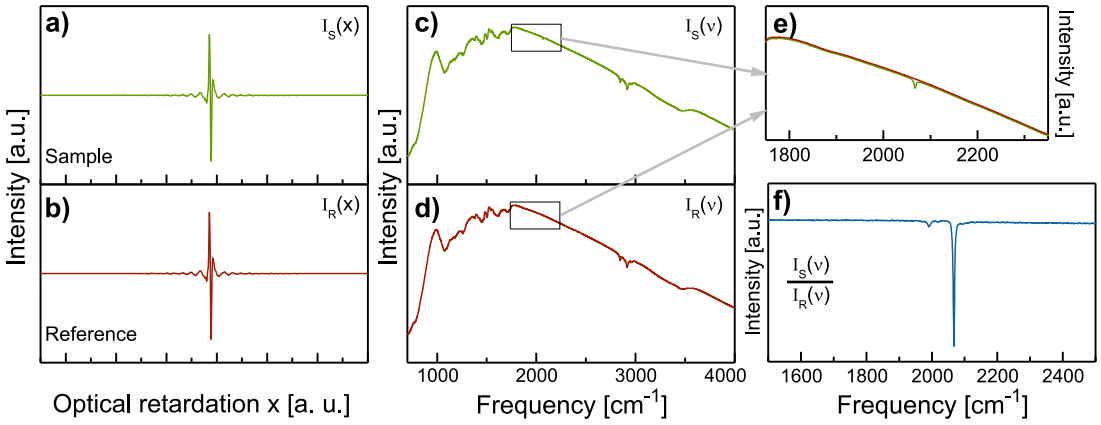

Figure 2.10: Spectra illustrating the typical workflow in FTIR spectra acquisition: a),b) Interferograms of sample / reference, c),d) energetic spectra of sample / reference, e) magnification with comparison of both signals, f) final spectrum $\frac{I_{Sample}(\nu)}{I_{Reference}(\nu)}$ (Data: Interferograms of clean Cu/Ru(0001) sample after and before CO adsorption. Figure from [78])

domain to the frequency domain, the energy spectrum is obtained. To exclude parasitic effects from the substrate and the optics, the final absorbance spectra are generated by referencing with non-covered substrates. Though the actual signals from the covered and the non-covered sample appear very similar, at close inspection distinct absorption modes become visible (cf. Fig 2.10) and this technique is easily able to resolve signals from sub-monolayer coverages (see for example [79]).

The remarks noted in the UV/Vis spectroscopy section regarding absorbance, Davydov-Splitting and polarization dependence are also valid for the infrared spectroscopy. Additionally, a further selection rule for infrared modes exists: Only vibrations that reveal a change of the dipole moment of the molecule, i.e. asymmetric vibrations, are visible in infrared spectroscopy. Contrary, the opposite is true for Raman-Spectroscopy. Here, modes with asymmetric displacement patterns remain invisible, while symmetric vibrations can be observed. Consequently, Raman and Infrared spectra exhibit no overlap (*rule of mutual exclusion*).

The fundamental difference between IR-spectroscopy and Raman spectroscopy, where the information about the energetics of the vibrations is obtained by analysis of inelastic scattering of light, was summarized very nicely by Albert Einstein [80]:

> *"Insert 10 cents into a Coke machine and receive a Coke: INFRARED; insert 1 Dollar and receive a Coke and 90 cents change: RAMAN."*

Typically, reference data for uncharacterized material or material of unknown composition is acquired by preparation of potassium bromide (KBr) pellets, utilizing the IR transparency of KBr. Because the analyzed material is oriented statistically within this pellet, this approach allows to determine the relative oscillator strength of the individual absorption modes and to obtain high quality data very simply and with low material consumption. Furthermore, detailed composition analyses are enabled and applied for example in the pharmaceutical sector [81, 82].

In spectra of thin films with preferred orientation on the other hand, only those modes are visible, where the light polarization is compatible with the dynamic dipole moment vector, like in the case of UV / Vis spectroscopy (cf. Fig 2.9 b) and c)). This polarization dependence of the absorption modes can be used to determine the orientation of the compound - supposed the exact relation between the TDM and the structure is known - and to monitor structural changes.

The spectra have been acquired using a Bruker IFS66v spectrometer with water-cooled globar as light source and liquid-nitrogen cooled mercury-cadmium-tellurid as detector. To circumvent the appearance of water absorption bands, all measurements have been conducted in vacuum (p < 1 mbar).

For further details on infrared and Raman spectroscopy, refer to expert textbooks like [83] and [80].

2.2.6 Thermal Desorption Spectroscopy (TDS)

In order to characterize the thermal stability of compounds under high- and ultra-high-vacuum conditions, *thermal desorption spectroscopy (TDS)* is the method of choice. In TDS, a mass spectrometer with variable detection values m/z (mass-to-charge-ratio) is utilized to monitor the desorption process as function of temperature and mass-to-charge-ratio, allowing chemical sensitivity.

Within the equipped mass spectrometer, a filament is used to ionize gas-phase molecules, which therefore carry charge. Consequently, the ions, which are afterwards accelerated, interact differently with electrical fields, depending on their actual m/z value. In quadrupole mass spectrometers, AC voltages are applied between two rod pairs, where respectively two opposing rods constitute one pair and are therefore interconnected. Thus, ions passing through this quadrupolar electrical field exhibit sinusoidal trajectories, where - depending on the actual choice of the AC voltage - only ions with a certain m/z-value have a stable trajectory and can reach the detector (cf. Fig. 2.11 a)) (Faraday-Cup or Secondary Electron Multiplier).

Generally, the desorption rate of the adsorbate from the surface is described by the Polanyi-Wigner equation:

$$\frac{d\Theta}{dt} = \Theta^m \nu(m) e^{-\frac{E_{des}}{RT(t)}} \tag{2.3}$$

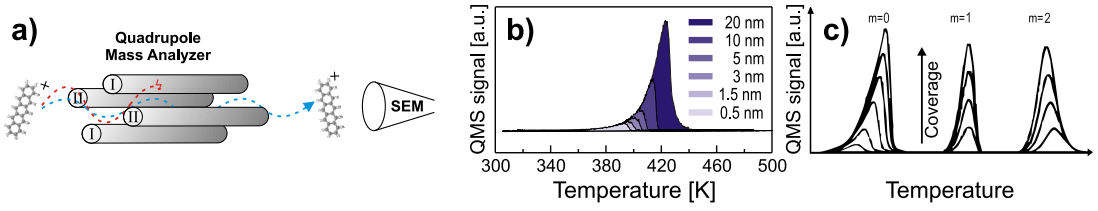

Figure 2.11: a) Working principle of quadrupole mass analyzer, b) TD-spectra of PEN thin films of different thickness, c) Peak shape of different desorption kinetics for different initial coverages [84]

where Θ is the coverage, ν the pre-exponential factor and m the desorption order.

The actual signal form of the desorption process depends critically on the nature of the microscopic desorption process. Zero-order desorption (m = 0) describes the desorption of physisorbed molecules. The corresponding QMS signals exhibit an exponential increase with temperature until the complete layer has desorbed. At that point, the signal instantly drops (tearing edge). While the ascending flank is independent of the initial coverage and its slope can be used to calculate the sublimation enthalpy [85], the tearing edge depends strongly on the coverage such that it shifts to higher temperatures with increasing coverages (Fig. 2.11 b)).

The cases of (m = 1) and (m = 2) are also of importance for the analysis of TD-spectra. The first describes chemisorbed monolayers and is characterized by a symmetric peak shape, of which center position does not change with the coverage. The case of (m = 2) is assigned to recombinative desorption; in this case the peak is symmetric but its broadness as well as its center shift with coverage such that it becomes sharper and shifts to lower temperatures with increasing coverage (cf. Fig. 2.11 c)).

In the present work, all TD-spectra were acquired using a Pfeiffer QMG 220 M3 with detection range of $^{m}/_{z}$=1-300 amu. To provide reliable temperature measurements, K-type thermocouples were attached directly to the sample surfaces. The spectra were acquired during a linear increase of the substrate temperature with a heating rate of $\beta = 0.5\ ^{\mathrm{K}}/_{\mathrm{min}}$ using a self-implemented computer-controlled PID-feedback control. To avoid parasitic contributions from the sample holder and the manipulator, a movable Feulner cup was positioned close to the sample surface [86].

More detailed introductions on Thermal Desorption Spectroscopy can be found for example in [85, 87, 88].

2.2.7 Near-Edge X-Ray Absorption Fine Structure Spectroscopy (NEXAFS)

Despite from diffraction effects (XRD) and photoionization of core electrons (XPS), the interaction between x-rays and solids / gases can also lead to resonant excitation of core-electrons into unoccupied molecular states (cf. Fig. 2.12 a)). Therefore, if the energy of the x-ray beam is correct, the sample will absorb the beam with increased efficiency. As the absorption due to the resonant excitation does not occur at higher energies than the resonant energy, a discrete peak is found. This is in contrast to photoionization processes (XPS), where any energy equal or higher than the difference between the vacuum level and the core level is suitable, as the excess energy is converted into kinetic energy of the photoelectron. This leads to an absorption edge in the acquired spectra, that superimposes with the resonant absorption peaks.

As energy-dispersive technique, the acquisition of *near-edge x-ray absorption fine structure (NEXAFS)* spectra requires an adjustable x-ray beam. As this is not easily feasible within home-laboratories, typically synchrotron facilities are visited to perform NEXAFS measurements.

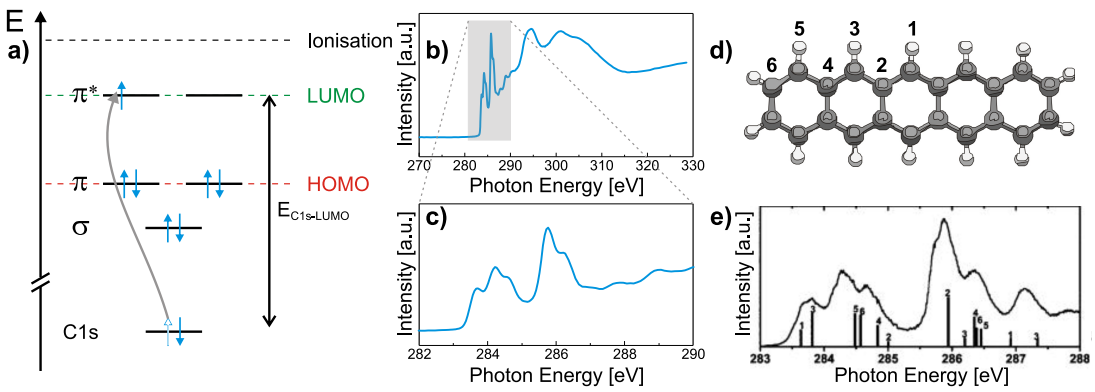

Figure 2.12: a) Energy scheme illustrating typical excitation monitored by NEXAFS, b) NEXAFS spectrum of PEN thin film deposited on SiO_2 acquired at sample orientation 55° (details on angles: see text), c) zoom into π^* region, d) illustration of non-symmetrical carbon atoms in PEN, e) peak assignment of PEN NEXAFS spectrum by DFT calculations [89]

The actual detection of the absorption spectrum works such that the re-filling processes of the core-holes are monitored. The core-hole which arises from the excitation of the core electron is refilled by an electron from a higher energetic level. Due to the conservation of energy the corresponding energy difference has to be compensated. This happens either by fluorescence or the emission of Auger electrons, whereat the relative intensity of both effects depends on the atomic number of the involved elements, with high Auger electron yield for light elements and high fluorescence yield for heavy elements. In either case, the re-fill process can be monitored by appropriate detectors. As in organic compounds mainly Auger electrons are emitted, a channel-plate detector is used to detect this flux and therefore indirectly the absorption in the sample. The sensitivity for Auger electrons introduces an additional advantage: As the mean free path of electrons at an energy of 280 eV is about 8 Å, this detection method brings along high surface sensitivity. To further enhance the surface sensitivity, typically a retarding field is applied in front of the detector to block secondary electrons.

Fig. 2.12 b),c) provides a NEXAFS-spectrum of PEN. It becomes obvious, that a lot of resonances appear. This high number of resonances is due to the non-exact equivalence of the individual carbon atoms within the PEN molecule. Thus, each ground state level and also the final state - due to the different positions of the core holes - after the excitation are different for the individual core atoms. Therefore the corresponding peaks are found at different excitation energies - in the case of PEN the six non-symmetrically equivalent carbon atoms yield six individual resonances for each fundamental transition (e.g. C1s -> LUMO, cf. Fig 2.12 d,e)).

Similar to transitions in the optical and infrared regime, not only the energy of the incident photon beam has to amount to the exact value (difference between final state and initial state energies), but also the relative orientation between the electrical field vector and the corresponding transition dipole moment (TDM) must be correct. In preferentially oriented samples this leads to a strong dependence of the signal intensity

on the angle between the sample and the incident beam - the so-called *dichroism* - , as the synchrotron beam is linearly polarized. Consequently, knowledge about the TDM orientation of the individual excitations allows very precise determinations of the sample orientation. In contrast to x-ray diffraction, no crystalline condensation of the samples is necessary to detect the molecular orientation. As an example, in self-assembled monolayers on polycrystalline substrates often preferred orientations are found, though the films are non-crystalline and therefore exhibit no diffraction peaks in conventional x-ray diffraction techniques [90]. Furthermore, its surface sensitivity allows to exclusively probe the surface structure, independent of contributions from bottom layers (cf. Fig. 2.13 f)).

Fig. 2.13 a) defines the angles, which are used in this work in the framework of NEXAFS spectroscopy. The incident angle θ describes the orientation of the sample normal relative to the orientation of the E-vector of the x-ray beam[1], while the angle α describes the average orientation of the TDM-vector relative to the sample normal. In the case of PEN and PFP, the π^* transitions have TDM-vectors oriented perpendicular to the aromatic ring plane. Therefore an upright orientation of the molecules corresponds to an angle α of 90°. Of course, exact orientation analyses require adequate consideration of the molecular packing motif. In herringbone motifs for example, it is not possible to arrange both molecules in such way, that both lie with their carbon backbone parallel to the surface and therefore the case α equals 0° cannot occur, though nevertheless both molecules might be in a recumbent orientation with individual long axes parallel to the surface.

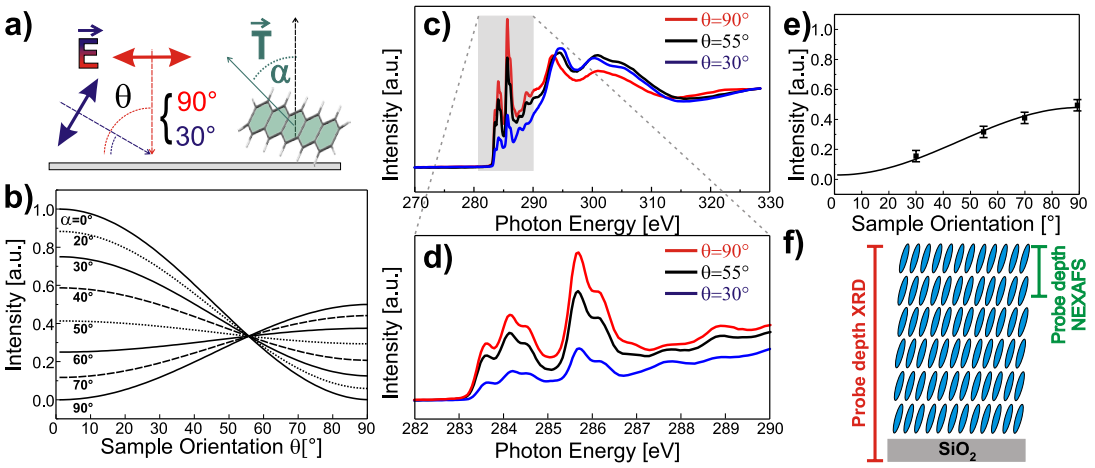

Figure 2.13: a) Definition of angles describing the sample orientation and the average molecular orientation, b) plot of resonance intensities as function of sample orientation θ for different average TDM orientations α, c),d) normalized NEXAFS spectra of PEN acquired at different sample orientations, e) fit of 2.8 to experimental data, f) illustration of probe depth of NEXAFS compared to XRD

1 This is equivalent to the orientation between the sample plane and the propagation direction of the x-ray beam

The exact intensity dependence for vector-type orbitals, like π^*-transitions in planar PAHs, is given by [91]:

$$I_{\pi*} \propto P\left(\cos^2\theta\cos^2\alpha + \sin^2\theta\sin^2\alpha\cos^2\phi + \sin\alpha\cos\alpha\sin\theta\cos\theta\cos\phi\right) + \sin^2\alpha\sin^2\phi \tag{2.4}$$

where P describes the degree of polarization of the synchrotron light and the angle ϕ represents the azimuthal orientation of the TDM vector projection on the surface.

In the case of substrates of at least twofold-symmetry, $\cos\phi$ averages to zero, yielding:

$$I_{\pi*} \propto P\left(\cos^2\theta\cos^2\alpha + \sin^2\theta\sin^2\alpha\cos^2\phi\right) + \sin^2\alpha\sin^2\phi \tag{2.5}$$

and in the case of the substrates of threefold or higher symmetry, $\cos^2\phi$ and $\sin^2\phi$ average to 1/2, which leads to:

$$I_{\pi*} \propto P\left(\cos^2\theta\cos^2\alpha + \frac{1}{2}\sin^2\theta\sin^2\alpha\right) + \frac{1}{2}\sin^2\alpha \tag{2.6}$$

$$= P\cos^2\theta\left(\frac{3\cos^2\alpha}{2} - \frac{1}{2}\right) + \frac{\sin^2\alpha}{2} \tag{2.7}$$

$$= P\cos^2\theta\left(cos^2\alpha + \frac{1}{2P}\tan^2\theta\sin^2\alpha\right) \tag{2.8}$$

From 2.8 it can be derived that for $\theta = \tan^{-1}(\sqrt{2P})$ the intensity of the absorption signal is independent of the average molecular TDM orientation α. Consequently, at this *magic angle* the corresponding plots presented in Fig. 2.13 b) cross. In order to determine the relative oscillator strength[1], spectra should be acquired at this angle, as thereby orientational influences are omitted. It amounts to about 54.7° in the case of ideally linear-polarized radiation (P=1). For samples featuring lower than threefold symmetry, there is no such magic angle independent of the azimuthal orientation. Instead, for substrates of twofold symmetry, the value of the magic angle depends on the azimuthal angle ϕ by $\theta_{magic} = \tan^{-1}(1/\cos\phi)$ (for P=1) and in cases of substrates with even lower symmetry, the dichroism plots for individual values of α do not cross at all (examples presented in appendix I).

Throughout this work, only samples of threefold or higher symmetry have been analyzed by means of NEXAFS spectroscopy. Therefore, in all cases equation 2.8 has been used for quantitative analyses. To reliably determine the exact molecular orientation from NEXAFS data, apparative contributions as well as the influence of the ionization edge have to be considered correctly. First, the energy axis has to be calibrated accurately,

1 The actual oscillator strength as determined by NEXAFS further depends on the exact overlap between the initial state and the final state, which leads to different peak heights for the transitions into equal orbitals from individual atoms (cf. Fig 2.12 c),e)). In the limiting case of a nodal plane (wave function amounts to zero) along a certain atom, the corresponding excitation is not possible at all. As an example, the transition from the nitrogen 1s level to the LUMO+1 cannot be excited in pyrazine molecules, as the LUMO+1 orbital has a nodal plane at the nitrogen atoms [54].

which is achieved by simultaneous recording of the current within a carbon-coated grid in front of the analysis chamber. The spectrum of the carbon coating exhibits a characteristic absorption peak at known energy (284.9 eV), which is used as intrinsic energy reference. Afterwards, the apparative background noise is subtracted, which is aforehand determined by recording a spectrum with closed beamshutter. Furthermore, the detector sensitivity as well as the actual ring current are accounted for by normalizing the spectrum at 270 eV to zero and at 330 eV to one. Additionally, the transmission characteristic of the monochromator grating has to be taken into account. This procedure is described in more detail in [54] and [92].

Finally, the resonance intensities of the normalized spectra (Fig. 2.13 c,d)) are determined as function of the incident angle θ and equation (2.8) is fitted to the experimental values by variation of the average molecular TDM orientation angle α (cf. Fig. 2.13 e)).[1]

All NEXAFS experiments have been conducted at the HE-SGM dipole beamline at the synchrotron storage ring BESSY II (Berlin) facilitated by the Helmholtz-Gesellschaft Deutschland. If not stated differently, a retarding field of -150 V was applied. The polarization factor of the synchrotron beam was 0.91. All spectra were recorded with a spectral width of the monochromatized light of 300 meV.

More details on the experimental set-up can be found in [93], while [91] provides a detailed introduction to NEXAFS spectroscopy.

1 In the case of substrates of lower symmetry, also ϕ is used as fit parameter.

CHAPTER 3

Results

The major projects of this thesis can be divided into three sections:

1. Substrate-mediated orientational control over the growth of organic semiconductor thin films
2. Spectroscopic characterization and phase-transitions of highly ordered organic semiconductor thin films
3. Preparation and spectroscopic and thermal characterization of organic heterostructures

As will become clear from the text, these sections are strongly interconnected and consequent developments of one another. However, a separation appears suitable for a stringent description.

3.1 Substrate-mediated orientational control over the growth of organic semiconductor thin films

Due to their high structural anisotropy, both in their molecular geometry and their crystalline lattice, the properties of molecular solids strongly depend on their nanoscopic structure. The actual formation of their structure is influenced by various parameters that are chosen during the preparation process like the deposition rate, the substrate temperature during deposition, the choice of the substrate as well as its surface quality and the atmospheric conditions. Furthermore, post-preparation processes like post-annealing can influence the final film structure.

Within this work, especially the influence of the substrate temperature during deposition, the substrate choice and substrate quality have been addressed.

3.1.1 Epitaxial perfluoropentacene thin films grown on alkali halide surfaces

Alkali halide surfaces are known to be suitable substrates to influence the structural ordering of organic compounds [42, 94–100], as their anisotropic surface exhibits high polarity,

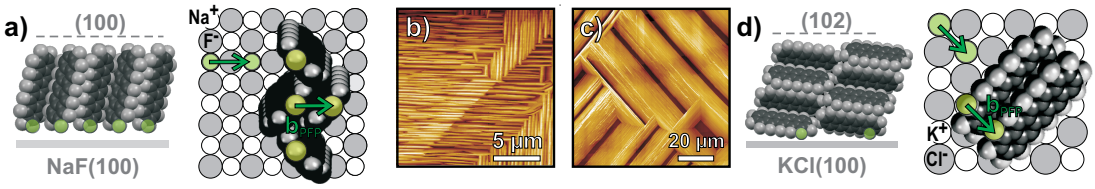

Figure 3.1: Scheme of molecular orientation of PFP on a) NaF(100) and d) KCl(100), AFM micrographs of PFP thin films on b) NaF(100) and c) KCl(100)

which allows efficient interaction with the organic compounds. However, the interaction is chemically rather weak (no chemisorption), so that the spectroscopic properties of deposited thin films are not modified by the substrate, as it is often the case for organic-metal-interfaces [101–104].

The aim of the study *"Epitaxial growth of perfluoropentacene films with predefined molecular orientation: A route for single-crystal optical studies"* (section 5.1) was to find alkali halide surfaces that serve as templates for epitaxial growth of PFP thin films. For that purpose, sodium fluoride and potassium chloride (100) surfaces have been chosen due to highly compatible lattice geometries between their surfaces and the PFP molecules: The $\vec{b}$-vector of the PFP crystal exhibits a norm of 4.49 Å which is very close to the norm of the NaF $\langle 010 \rangle$ vector, that amounts to 4.62 Å. An even closer agreement is found between the PFP $\vec{b}$-vector and the KCl $\langle 011 \rangle$ vector (4.45 Å). Indeed, on both substrates epitaxial films are found upon deposition of PFP. Furthermore, the orientation of the $\vec{b}$-vector in both cases coincides with the aforementioned surface directions that exhibit good congruence with the PFP $\vec{b}$-vector norm. However, the formation of epitaxial films further requires the correct substrate temperature during deposition, as in the case of temperatures lower than 330 K mostly polycrystalline films are found. Interestingly, not only the lateral ordering of the films is influenced by the substrate choice, but also the molecular conformation relative to the surface normal (cf. sketch in Fig. 3.1): While on NaF (100) surfaces, the PFP molecules adopt an upright (100) orientation, on KCl (100) they nucleate in the recumbent (102) orientation, which is ascribed to a higher order epitaxy between PFP and the KCl surface favoring the recumbent orientation. Summing up, the KCl(100) and NaF(100) surfaces serve as templates to control the structural conformation of PFP in different ways and therefore allow the preparation of epitaxial films of this compound in different orientation, which allows detailed polarization-resolved spectroscopic measurements. Such measurements have also been applied in this study in the framework of UV/Vis spectroscopy and have been expanded to more detailed, temperature dependent optical measurements (section 5.10) and vibrational spectroscopy (section 5.5).

3.1.2 Application of TEM Measurements for the characterization of PFP thin films

The application of *Transmission Electron Microscopy (TEM)* provides one specific advantage compared to other imaging or diffraction techniques: By variation of the lense

systems, TEM can be used to image real space as well as reciprocal space and therefore allows to characterize the crystalline structure as well as the morphology of a sample at the exact same position at the same time.

However, the application of TEM for organic thin films is quite challenging, as many organic compounds exhibit severe radiation damages. As a consequence, the acquisition of TEM images and diffraction data requires very cautious handling of the samples and the instrument. Within the work *"Application of transmission electron microscopy for microstructural characterization of PFP thin films"* (section 5.2), the acquisition process of TEM data was improved and adapted to reduce the radiation damage. By systematic variation of the exposition conditions we found that low dosages, low sample temperatures and high acceleration voltages (300 kV) provided the best conditions and allowed image acquisition times of about 50 seconds for PFP thin films deposited on SiO_2 substrates. The application of this method allowed to correlate the habitus of PFP crystallites to their crystalline structure, showing that the spicular PFP islands are limited by planar (001) edge faces at the long side and the herringbone (010) plane at the short side of the crystallites.

3.1.3 PFP and P-Tetrone thin films on HOPG surfaces of different quality

Graphite and graphene surfaces are highly interesting materials to be used in organic optoelectronic devices as they offer excellent mechanical and electronic properties, combined in the case of graphene with optical transparency. This combination of properties gives rise to the expectation, that graphene might substitute indium tin-oxide (ITO) as electrode material for opto-electronic applications.

Furthermore, it has been shown before, that PEN forms highly ordered, very smooth thin films on graphene in recumbent orientation due to the perfect match between the molecular carbon frame and the surface lattice of the graphite basal plane [44].

In the work *"Interrelation between Substrate Roughness and Thin-Film Structure of Functionalized Acenes on Graphite"* (section 5.3) it has been shown that also for PFP and pentacene-tetrone (P-TET) thin films deposited on pristine (0001)-oriented graphite,

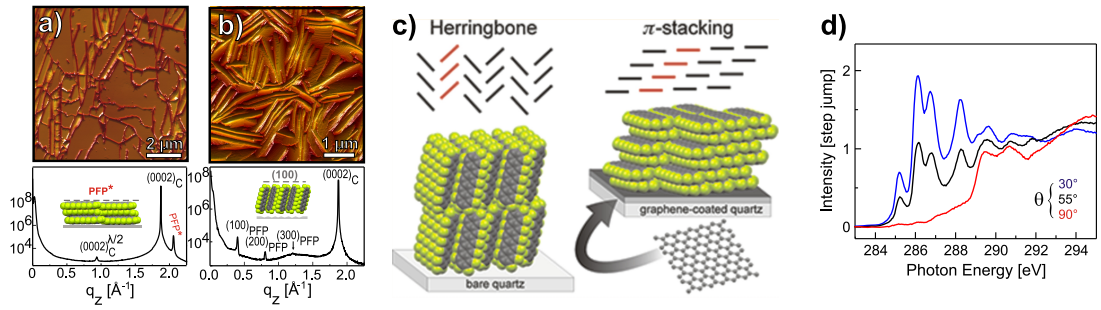

Figure 3.2: AFM micrographs and Diffractograms of PFP thin films on a) pristine HOPG and b) sputtered HOPG, c) scheme of molecular orientation and polymorphs on different substrates, d) NEXAFS spectra of PFP on pristine HOPG proving the planarity of the new polymorph

exceptionally smooth thin films in lying molecular conformation are found. Moreover, we systematically analyzed the influence of the substrate quality on the subsequently deposited thin films. We found that the growth of individual PFP crystallites is limited by monomolecular steps in the graphite surface, such that the maximum island size is determined by the coherence of the substrate. Additionally, we intentionally damaged the graphite surface by means of ion bombardment until the surface diffraction pattern monitored by *low energy electron diffraction (LEED)* had vanished. Consequently, thin films with similar preparation protocol as in case of pristine surfaces have been prepared. We found that in the case of damaged surfaces, the smooth, recumbently oriented thin films are no longer formed, but instead the molecules adopt an upright orientation and morphologies that correspond quite exactly to those of thin films deposited on oxidized silicon substrates (exemplary AFM micrographs and diffractograms presented in Fig. 3.2 a,b)). To put it in a nutshell, in this work it has been shown that pristine graphite surfaces allow the preparation of highly ordered, very smooth thin films of PFP and P-TET in lying configuration, but that this can only be achieved at high-quality surfaces without severe damages.

The aforementioned lying configuration of PFP is even more interesting from a different perspective: In its bulk structure [55], PFP exhibits a nearly perpendicular herringbone motif in the unit cell. Consequently, PFP cannot form planar recumbent thin films in its bulk phases. However these are found on graphite surfaces, as the molecules crystallize in a new polymorph (cf. Fig 3.2 c,d)), that is also found on metal surfaces like Ag(111) [105]. In this polymorph, the molecules do not exhibit any herringbone motif, but are completely planar to one another. We have analyzed this polymorph, its exact crystalline structure and its electronic properties in *"Epitaxial Growth of π-Stacked Perfluoropentacene on Graphene-Coated Quartz"* (section 5.7). Interestingly, the determination of the electron band dispersion allowed an estimate of the electron mobility, which was estimated to $> 9\ {}^{cm^2}/_{Vs}$. This value is clearly higher than the one found for the PFP bulk structure of $0.22\ {}^{cm^2}/_{Vs}$ [57]. The increase of the electron mobility compared to the bulk structure is ascribed to the vertically π-stacked molecules, of which relative orientation maximizes the vertical π-orbital overlap.

3.2 Spectroscopic characterization and phase-transitions of highly ordered organic thin films

In many cases, the spectroscopic properties of organic compounds are of interest. For example, their optical absorption spectra determine their applicability in opto-electronic devices. Furthermore, their vibrational properties are closely interconnected to their corresponding charge-transport characteristics, as the efficiency of electronic excitations strongly depends on the electron-vibration coupling (*vibronic coupling*). From a fundamental researcher's point of view, spectroscopic properties are of course also of great interest, as the detailed analysis of unknown spectroscopic properties allows to gain insight into yet

unknown systems and their monitoring as function of parameters such as temperature, time or radiation exposition allows to study the dynamics of nanoscopic processes.

Finally, also the thermal stability and the competing processes of molecule desorption and molecular decomposition are of interest as well in the framework of fundamental research as for potential applications, as material degradation is one severe reason for the nowadays quite poor lifetime of organic electronic devices.

Unfortunately, the detailed determination of spectroscopic characteristics and even more their interpretation are quite complicated. One reason for this is the poor availability of organic single crystals. Furthermore, these in many cases exhibit very strong absorption, which limits the application of transmission spectroscopy, while the quantitative analysis of reflection absorption measurements on the other hand is complicated by rotation of the polarization. The analysis of crystalline thin films allows to circumvent these issues. Another obstacle is the high sensitivity of many spectroscopic characteristics for imperfections during the preparation process. For example, non-ideal preparation protocols will most probably lead to the incorporation of undesired parasitic compounds or imperfect film structures. There is also an aspect of fundamental character: The spectroscopic properties of molecular solids are strongly anisotropic, which means that significantly different spectra are acquired for different molecular orientations or polymorphs. Therefore reliable spectroscopic characterizations can only be achieved if at the same time the homogeneity, stability and structural conformation of the sample are verified and determined. Consequently, throughout this work all spectroscopic characterizations have been supported by detailed structural investigations and the aforementioned anisotropy of spectroscopic characteristics was addressed in detail by introduction of polarization-resolution to the experimental techniques.

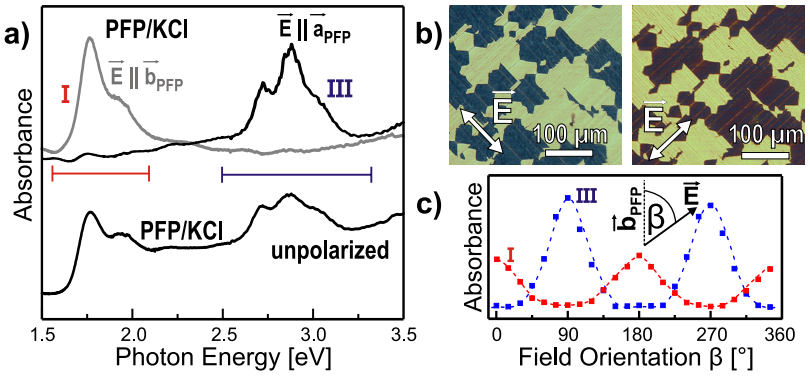

Figure 3.3: a) Optical absorption spectra of PFP thin films on KCl(100) with unpolarized light (bottom panel) and light polarized along different unit cell axes (top panels), b) polarized optical micrographs of PFP/KCl(100) thin films, c) polarization-resolved intensities of absorption bands I and III

3.2.1 Determination and modelling of optical and vibrational characteristics of perfluoropentacene thin films

As mentioned before, in the work *"Epitaxial growth of perfluoropentacene films with predefined molecular orientation: A route for single-crystal optical studies"* (section 5.1) the preparation of epitaxial thin films of PFP, which are ideally suited for polarization-resolved spectroscopic measurements has been presented. Within that work, optical absorption spectroscopy was applied to determine the optical properties of PFP. By application of XRD, the structure has been determined very accurately. As furthermore the size of individual domains with identical lateral orientation was sufficiently large, it was possible to exclusively illuminate domains with molecules in similar orientation and therefore continuously rotate the light polarization with respect to the molecular axes for PFP thin films deposited on KCl (100) surfaces (cf. Fig. 3.3). By this means, the orientation of the transition dipole moments of all corresponding optical transitions have been determined.

However, in that work the applied spectrometer featured a comparably large illumination spot with a diameter of about 3 mm and did not allow precise positioning of the spot on the sample surface. Consequently, no polarization-resolved measurements could be applied in the case of PFP / NaF (100) films, where the size of uniform domains was not sufficient for that purpose. Moreover, the spectral resonances are rather broad at room temperature conditions, which hampered the exact separation of the leading excitonic resonances (cf. UV/Vis spectroscopy Section). For that reason, these measurements have been repeated and expanded in a recent joint work with K. Kolata, J. Kunert, G. Witte and S. Chatterjee, which is currently in preparation for publication. In this study, a more sophisticated experimental set-up was used that allowed spot sizes of below 30 µm and exact microscopic positioning of the illumination spot under a microscope. Furthermore, these experiments have been conducted at temperatures of as low as 10 K, which has led to significantly sharper peak shapes (cf. Fig. 3.4 a)) and therefore allowed clear separations and identifications of the individual excitations. The detailed inspection of the polarization-resolved spectra (cf. Fig. 3.4 b,c)) revealed an exciton band X_3 additional

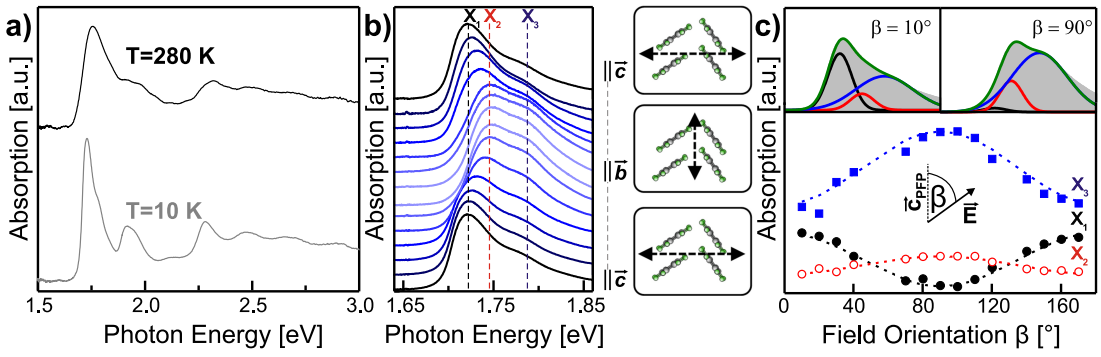

Figure 3.4: a) Optical absorption spectra of PFP thin films on NaF(100) with polarization along the PFP-$\vec{c}$-direction, b) spectra acquired at different polarization angles with denotation of excitations c) polarization-resolved intensities of the absorption bands

to the two exciton bands X_1 and X_2 arising from the Davydov splitting. While X_1 and X_2 both exhibit significant binding energies, their actual values are different due to the different resonance-interaction between the molecules within the unit cell. The additional band X_3 on the other hand emerges due to the planar stacking of PFP molecules in the $\vec{b}$-direction (cf. Fig. 2.1 c)) which leads to significant Coulomb coupling between those.

The epitaxial thin films of PFP on KCl(100) and NaF(100) have also been used to study the vibrational properties of PFP in the work *"Vibrational Davydov-Splittings and Collective Mode Polarizations in Oriented Organic Semiconductor Crystals"* (section 5.5). Comparing the spectra of both thin films in their individual structural conformation to isotropic PFP/KBr pellets and conducting also polarization-resolved measurements allowed to determine the exact energy positions, oscillator strengths and dipole moments of all IR-active vibrational modes in the energetic range above 800 cm^{-1} (cf. Fig. 3.5 a,b)). This very precise and extensive dataset was further used to benchmark different DFT functionals. Especially the correct modelling of the van-der-Waals interactions between the different molecules is a current research topic that many theoretical approaches still fail to describe accurately. For that purpose, different typical DFT methods have been applied to calculate the vibrational spectra of PFP and the results have been compared to the experimental data. The best accordance between the theoretical results and the experimental data was found for the PBE functional with consideration of dispersion effects. Due to the exact knowledge of the energetic positions and the dipole moments of all excitations, all modes which were computed by the DFT calculation have been identified in the experimental spectra. Having found an adequate theoretical modelling of the system, the computations also enabled the enlightenment of some further aspects: As

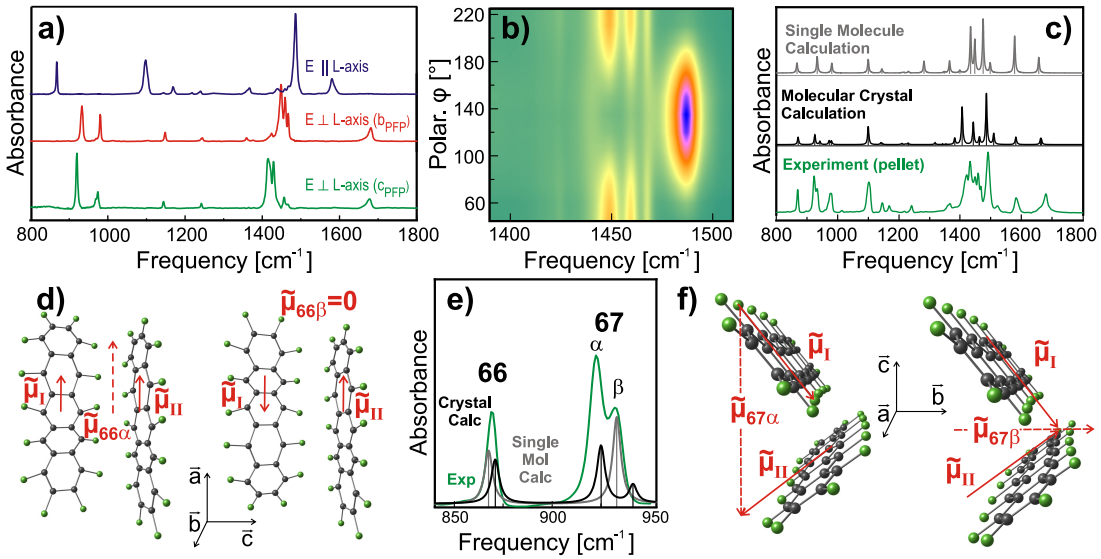

Figure 3.5: a) IR spectra of PFP thin films resolved by molecular axes, b) false-color plot of polarization-resolved IR spectra (color coding: green-yellow-red-blue (increasing intensity)), c) comparison of experimental data, single molecule calculation and crystal calculation, magnified in e). d), f) visualization of displacement patterns for different coupled vibrations and corresponding dipole moments.

the computations also embrace the actual displacement patterns of the vibrations, those could be visualized which allowed interesting and very concrete insights. Furthermore, the computations can not only model the molecular crystal but also individual, isolated molecules and compute their vibrational spectra, which are not easily accessible by the experiment. These spectra do - different from the crystal calculations - not embrace the Davydov-Splitting arising from the two non-translationally equivalent molecules in the PFP unit cell. Therefore, the comparison of these two spectra have allowed the identification and assignment of the different Davydov-split modes (cf. Fig. 3.5 c),e)). Finally, this allowed to understand, why some of the fundamental modes exhibit such a Davydov-Splitting into two vibrational modes with non-zero intensity, while others split into one mode with finite and one without intensity. The reason for this behavior is the different dipole moment of the fundamental modes: As exemplarily visualized in Fig. 3.5 d),f) those modes with polarization along the long axis of the PFP molecule (L-polarized modes) exhibit an exact cancellation of the individual dipole moments when the vibrations have a phase relation of π, while in-phase vibrations lead to a total dipole moment in L-direction. Fundamental modes with polarization within the molecular plane (M-polarized modes) on the other hand, can not cancel each other out in any phase relation in the molecular crystal due to the herringbone motif within the unit cell. In this work we have shown that the vibrational spectra of conjugated aromatic molecules are not describable by fingerprint identification of individual chemical bonds, but the actual displacement patterns are distributed over the entire molecule. Due to its novel approach, that has combined the advantages of experimental and theoretical methods and addressed a number of fundamental questions, we are convinced that this work will be of general interest within the field of molecular solid spectroscopy.

3.2.2 Phase-transitions and thermal decomposition of perfluoropentacene monolayers on coinage metal surfaces

The interaction between organic compounds and metal surfaces is of great importance, as in device applications such interfaces often occur and the electronic interplay at this interface strongly influences the performance of such devices. Because metal surfaces are often highly reactive, the interaction is typically stronger than in the case of non-metallic substrates or organic-organic interfaces. In many cases, especially in the first layers the adsorbed molecules are chemically modified, which is called *chemisorption*. As a consequence, the spectroscopic characteristics as well as the stability of the corresponding molecules can be strongly modified. On the one hand, this can be utilized to prepare exact monolayers of the organic compound on the metal surface by preparation of multilayers and subsequent thermal desorption of all layers except for the first monolayer. On the other hand this may lead to unexpected, undesired side-effects, as for example electronic modification of the compound or catalytic reactions might occur.

In the work *"Temperature Dependent Structural Phase Transition at the Perfluoropentacene/Ag(111) Interface"* (section 5.4), we have analyzed the interface between PFP and

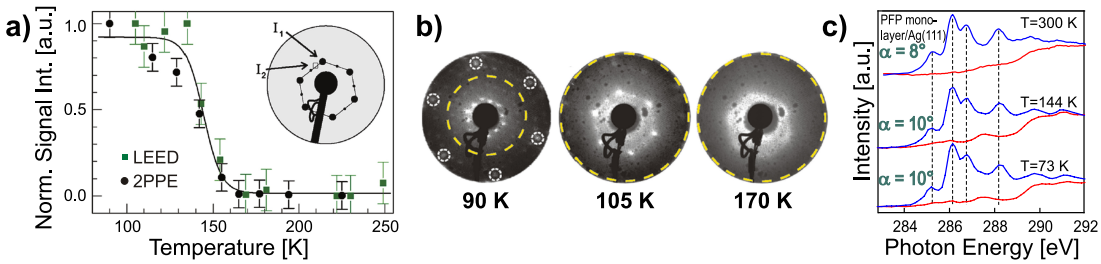

Figure 3.6: a) Evolution of 2PPE signal intensity corresponding to free silver surface areas and contrast of LEED pattern over temperature, b) exemplary LEED patterns and c) NEXAFS spectra of PFP-monolayer on Ag(111) at different temperatures below and above phase transition temperature

the silver (111) surface. Due to the high polarizability of the silver surface, the molecules adopt a flat-lying orientation in the polymorph that is also found on HOPG and has been discussed in the previous section. Careful heating of the sample to temperatures of about 400 K allows to selectively desorb the multilayers, leaving behind a monolayer of PFP, which also exhibits a flat-lying orientation and which is expected to be a closed monolayer without residual uncovered regions. However, the microscopic structure is more complex. By variation of the sample temperature we found, that at a temperature of about 145 K a phase-transition occurs. Below this temperature, *two-photon-photoemission (2PPE)*-signatures are found that correspond to non-covered silver surface areas. Moreover, an analysis of the actual microscopic structure by means of low energy electron diffraction showed that at low temperatures a crystalline (6 x 3) PFP phase is formed, which transforms into a disordered phase at higher temperatures (cf. Fig 3.6 b)). Furthermore, we have shown that this phase-transition as monitored by 2PPE and LEED is completely reversible. To find out, whether this phase transition also affects the molecular orientation with respect to the surface normal, e.g. whether the molecules undergo a conformational modification, we have applied NEXAFS spectroscopy. The results presented in Fig. 3.6 c), have shown, that in both cases, at temperatures below and above the critical temperature, the conformation remains unchanged. These results also explain, why attempts to image PFP monolayers by means of scanning tunneling microscopy at room temperature have failed: Due to the high mobility of the disordered phase, imaging is only possible at temperatures below the phase transition temperature as applied in [106].

The interplay between organic compounds and metal surfaces has also been the main aspect of the study *"Substrate induced thermal decomposition of perfluoro-pentacene thin films on the coinage metals"* (section 5.6). Here, monolayers of PFP have been prepared on gold, silver and copper (111) surfaces and their thermal stability has been analyzed by means of XPS and NEXAFS. We have shown that the thermal stability and the evolution of the electronic properties strongly depend on the chemical reactivity of the substrate. While on gold surfaces the electronic properties remain unchanged upon heating and intact desorption of the monolayer occurs, the PFP molecules are strongly modified regarding their electronic properties on copper surfaces even at room temperature. In the case of monolayers prepared at that surfaces, the NEXAFS resonances are found

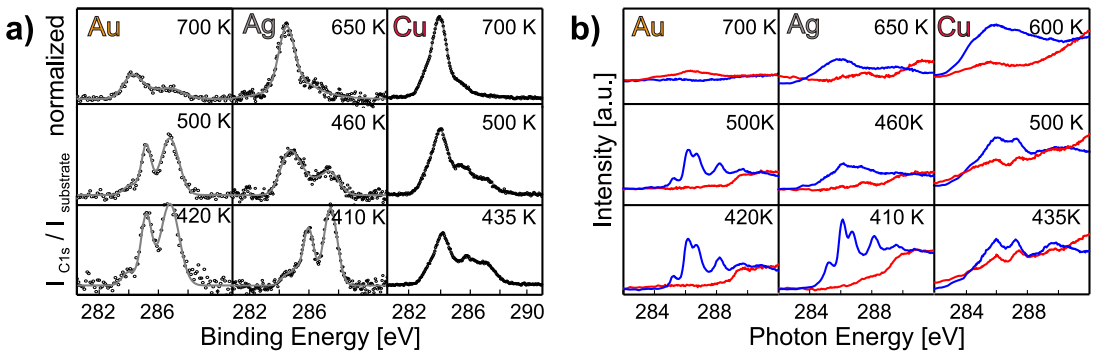

Figure 3.7: a) Series of Temperature-Dependent XP-Spectra and b) NEXAFS-Spectra of PFP-Monolayer on Ag(111), Au(111) and Cu(111)

to be strongly broadened compared to the multilayer (cf. Fig 3.7b)), which indicates strong electronic interaction between the PFP monolayer and the copper surface. Upon heating, this becomes even more pronounced and new resonances which are attributed to decomposed PFP arise. By analyzing the temperature-resolved XP-spectra shown in Fig. 3.7 a) regarding the relative intensities of the carbon atoms in different chemical vicinity, we have shown that the PFP molecules break apart at the carbon-fluorine bonds, leading to decomposition of the PFP molecules. Moreover we found evidence that the detached fluorine atoms react with the copper surface to form copper-fluoride. The thermal evolution of PFP monolayers on silver surfaces is inbetween those on gold and copper surfaces. By comparing the results of PFP monolayers on smooth Ag (111) surfaces to those deposited on the vicinal Ag (221) surface we have identified surface steps as promoters for the catalytic reactions. Our findings have further been supported by DFT-calculations, in which the adsorption and dissociation energies of PFP on the different surfaces have been compared, revealing the same trend as observed experimentally.

3.3 Preparation and spectroscopic and thermal characterization of organic heterostructures

While the preparation and characterization of single-component organic thin films already poses a number of challenges and the actual structure of processed thin films strongly depends on a number of parameters, the situation becomes a lot more complicated, when multinary systems are considered. Here, one additional complex parameter comes into play: The mutual interaction between both components. Obviously, two or more[1] different compounds may interact in different ways: Depending on their sterical and chemical compatibility they may favor molecular intermixture or prefer phase-separation. Though some efforts have been made [107, 108], up to now no embracive explanations

1 To improve the readability, during the discussion the situation of two compounds is described. However, all considerations are of course also valid - and in many cases even to a higher extent - for combinations of more than two compounds

or theoretical models exist that allow reliable predictions on the mixture behavior of two organic compounds. Specifically, the mentioned approaches only embrace the case of thermodynamic equilibrium and therefore fail to describe metastable processes, like intermixture of two compounds at low temperature, which at higher temperatures favor phase-separation. For that reason, fundamental experiments have to be conducted to provide knowledge on those molecular mixtures. The analysis of such mixtures is simple in principle. By comparing the structural and spectroscopic fingerprints of the single compounds to those of the molecular mixture, the different scenarios can be discriminated: In the case of no interaction, the spectroscopic properties of the mixture will be exact superpositions of the pure compounds, while significant deviations from such a superposition prove interaction on a molecular level. However, the nature of the different spectroscopic techniques has to be accounted for to drawback correct conclusions. Aside from the fundamental interest in gaining knowledge about the mixture behavior of two components, such knowledge is also of interest for practical applications. To give an example, in organic solar cells two different organic compounds are necessary to harvest the incident light efficiently: One with high electron affinity (*acceptor*) and one with low ionization potential (*donor*). In such heterojunction organic solar cells, the device characteristics depend strongly on the combined structure that is formed in the active layer by both compounds.

3.3.1 Thermally activated intermixture of pentacene-perfluoropentacene heterostructures and optical properties of those

Due to their high sterical compatibility and their inverted charge carrier distribution which results in effective mutual quadrupole attraction, PEN and PFP constitute an ideal model system for heterostructures of organic semiconductors. As has been shown in previous works, both molecules form a co-crystal upon co-evaporation in stoichiometrically equivalent ratio [58, 59]. Furthermore, first observations have been made that prove electronic interaction, as in the optical absorption spectra as well as in the fluorescence spectra new resonances appeared, which have been attributed to *charge-transfer excitations*

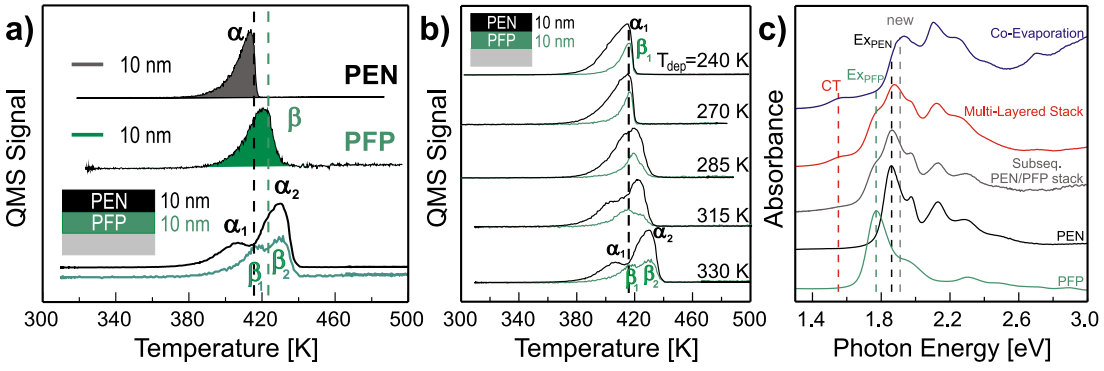

Figure 3.8: a) TD-spectra of pure PEN (top panel), pure PFP (medium panel), PEN/PFP stack, b) TD-spectra of PEN/PFP stacks prepared at different substrate temperature, c) optical absorption spectra of differently prepared heterostructures of PEN and PFP

(CT) between the highest occupied molecular orbital (HOMO) of PEN and the lowest unoccupied molecular orbital (LUMO) of PFP [60, 61].

Within the study *"Thermally activated intermixture in pentacene-perfluoropentacene heterostructures"* (section 5.8) the question has been addressed, whether the attraction between PEN and PFP not only leads to joint structure motifs and electronic interaction, but also results in enhanced thermal stability. By applying thermal desorption spectroscopy we have shown that indeed the thermal stability of the heterostructure is enhanced by about 20 K compared to the single compounds (cf. Fig. 3.8 a)), reflecting an increased enthalpy of sublimation. By monitoring the degree of thermal stabilization, we have been able to compare different preparation protocols of such heterostructures in great detail. These observations have led to unexpected results: The thermal stabilization of both compounds and therefore effective molecular intermixture occurs not only upon co-evaporation but also after subsequent deposition of both compounds. However, this effect is restricted to individual layer thicknesses of about 5 nm and furthermore occurs only in one of both possible sequences: While PFP deposition on top of PEN layers does not lead to enhanced thermal stability of the heterostructure, such stabilization is found after deposition in reverse sequence. By comparing the morphologies of these different subsequently prepared stacks and of the pure phases and by consideration of previous literature work, where PEN deposition has been shown to smoothen the comparably rough PFP interface [109], we have attributed this behavior to an enhanced contact area in the case of PEN/PFP stacks (PEN deposited on PFP) compared to the reverse stack. Moreover, we have discriminated between the possible scenarios of molecular intermixture during deposition and during the post-annealing process applied in the TDS measurement by variation of the deposition conditions (cf. Fig. 3.8 b)), showing that the first takes place and have identified the substrate temperature during the deposition of the top PEN layer as crucial parameter that determines, whether or whether not the PEN molecules can interdiffuse into the bottom PFP layer. In the case of co-evaporated heterostructures as well as multi-layered stacks prepared by alternate deposition of monolayers of both compounds, the thin films were also found to be thermally stabilized. The analysis of thermal desorption spectra of the heterostructures have furthermore shown that the mutual stabilization only occurs in the case of stoichiometrically equivalent mixtures, while excessive amounts of one compound are desorbed non-stabilized. This finding enables the exact preparation of ideally intermixed heterostructures even if the preparation process has been non-ideal and will allow the acquisition of high-quality spectra of the molecular intermixture in future studies. Finally, the inspection of the electronic properties of the differently prepared heterostructures by means of optical absorption spectroscopy has revealed results in good congruence with the findings from thermal desorption spectroscopy measurements: As presented exemplarily in Fig. 3.8 c), the CT-related excitation is found for those heterostructures, that also exhibit the thermal stabilization and can therefore be used as to judge the efficiency of the molecular intermixture. However, we have also shown that additionally to the CT-excitation another striking difference between the spectra of

ideally intermixed and phase-separated heterostructures occurs, which had not yet been reported in literature: The absorption bands which are related to the pure-phase excitons are completely suppressed in the case of ideally intermixed heterostructures. Consequently, the combination of these three spectroscopic benchmarks allows to very precisely judge on the intermixture efficiency in molecular mixtures of PEN and PFP and can be expected to be applicable and of interest also for other molecular heterostructures. Finally, the high quality of the acquired spectra, which clearly exceeds that of the previous experiments performed by other groups, may be expected to render them important references for theoretical approaches to this system.

3.3.2 Dimensional control over C_{60} nanostructures on pentacene templates

Heterostructures of PEN and C_{60} fullerene have gained significant interest in both, theoretical [110–115] and experimental [116–120] works. This is not only due to their potential application in solar cells [121, 122] and ambipolar organic field-effect transistors [123], but also due to their model character, which facilitates them an interesting material combination.

In the framework of the study *"Diffusion-controlled growth of molecular hetero-structures: fabrication of 2-D, 1-D and 0-Dimensional C60-nanostructures on pentacene templates"* (section 5.9) the interface between these two materials has been precisely analyzed. As bottom layer PEN multilayers have been chosen which can be prepared in high quality and have been studied before in detail. This allowed to chose preparation conditions at which uncovered surface areas and therefore undesired interaction between the afterwards deposited C_{60} molecules and the substrate could be excluded. As presented in Fig. 3.9 a), deposition of small amounts of C_{60} (d_{nom}=0.25 and 0.5 nm) onto the PEN multilayer at room temperature leads to the formation of C_{60} clusters pinned at the PEN step edges, which represents surprisingly high mobility of C_{60} on the PEN surface as well as remarkable interaction between C_{60} and the PEN edge faces. As the AFM micrographs in Fig. 3.9 b) show, variation of the substrate temperature during the C_{60} evaporation process allows to control the structure and dimensionality of the C_{60} nuclei. While at low

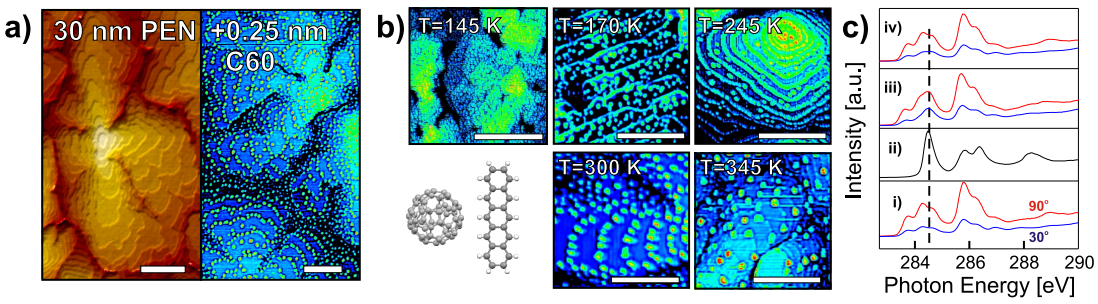

Figure 3.9: AFM micrographs of a) 30 nm pure PEN and 0.25 nm C_{60} deposited on top, b) C_{60} nanostructures deposited at different substrate temperatures on PEN multilayers (all of which prepared at room temperature, all measurements conducted at room temperature) and c) NEXAFS spectra of bare PEN bottom layer (i), pure C_{60} (ii), 0.5 nm C_{60} deposited on PEN multilayer (iii), additional 5 nm PEN deposited on top (iv)

temperatures, rather homogenous, two-dimensional coating of the PEN surface by the C_{60} molecules occurs, at somewhat elevated temperatures (240 K), one-dimensional nanowires of C_{60} that continuously decorate the PEN step edges are found. At even higher elevated temperatures, the cohesion between C_{60} has been found to completely outrule the adhesion of C_{60} at PEN: Here, 0-dimensional clusters of increased size are found, which are pinned at the PEN step edges. Interestingly, all interfaces are stable at room temperature and exhibit no post-growth dewetting. Furthermore we have shown, that subsequent deposition of additional PEN onto these interfaces allows the burial of the C_{60} clusters and nanowires and therefore to prepare low dimensional buried organic hetero-structures. Applying x-ray diffraction and NEXAFS and utilizing their different probe depths, we have finally shown that the orientation of the subsequently deposited PEN remains unchanged compared to the bottom layer in upright orientation (cf. 3.9 c)).

CHAPTER 4

Summary and Outlook

In this thesis the structural and spectroscopic properties of the organic semiconductor perfluoropentacene (PFP) have been studied in detail. By variation of the preparation conditions and well-considered choice of substrates, highly ordered thin films have been prepared. Moreover, different preparation protocols have been identified that allow comprehensive structural control over the thin film formation regarding the molecular orientation, the lateral ordering and the crystal structure. The structural conformation of the thin films has been determined by a wide combination of different techniques: Atomic Force Microscopy (AFM) and Polarized Optical Microscopy allowed to analyze the morphology, while Near-Edge X-Ray Absorption Fine Structure Spectroscopy (NEXAFS) and X-Ray Diffraction Spectroscopy (XRD) were utilized to determine the molecular orientation and their crystallinity. A number of these findings as the utilization of alkali halide surfaces with congruence between their surface structure and the lattice geometry of the deposited material as well as the strong correlations between the substrate temperature during deposition and the resulting thin film morphology are expected to be useful to gain structural control also over other organic compounds. First attempts of applying this to compounds like pentacene-tetrone and copper-phtalocyanine have already yielded promising results.

The precise control over the molecular conformation allowed to conduct detailed spectroscopic measurements regarding the optical, vibrational, chemical and electronic properties of PFP by application of UV/Vis absorption spectroscopy, Fourier-Transform Infrared Spectroscopy (FTIR), X-ray Photoelectron Spectroscopy (XPS) and NEXAFS spectroscopy. Moreover, the exact knowledge about the thin film structure enabled polarization-dependent measurements with respect to the molecular axes. Consequently, the highly anisotropic optical and vibrational properties of PFP have been determined and correlated to the molecular packing motifs. Furthermore, the extensive datasets have served as benchmarks for theoretical calculations and enabled the comparison of different functionals. This allowed to identify computational methods which have reproduced the experimental results to a very good extent and further provided additional information that helped to visualize the actual displacement patterns in molecular vibrations and to understand the different coupling mechanisms in Davydov-split vibrational modes. The preparation of PFP mono-

layers on different metal surfaces has allowed to characterize the chemical interaction of PFP with these surfaces. By that means, it has been shown that despite its proposed high chemical stability due to the fluorination of the outer rim, significant catalytic reactions occur upon thermal heating which strongly modify the electronic properties of PFP. These issues pose significant challenges for possible device applications, as in those the actual electronic structure and possible degradation processes of the organic-metal-interface are crucial, which therefore have to be analyzed in detail to understand the actual device characteristics instead of only considering the bulk properties of the organic compound. Similar to the aforementioned strategies to gain control over the structural conformation of the thin films, the applied spectroscopic characterizations, especially the approach to precisely correlate the structural orientations to the spectroscopic anisotropies have the potential to be used in numerous further studies to achieve spectroscopic details for future compounds.

Finally, two complementary organic heterostructures have been prepared and analyzed: Blends of PEN and PFP and PEN and C_{60}. The first combination exhibits strong mutual interaction due to their high sterical compatibility and strong quadrupole interaction, which results in the formation of efficient intermixtures at the molecular level at suitable preparation protocols in stoichiometrically equivalent ratio. In contrast, the latter combination results in phase-separation of both compounds. By application of thermal desorption spectroscopy, the mutual attraction of PEN and PFP has been shown to significantly enhance the thermal stability of this heterostructure compared to the single compounds. Moreover, it was found that different preparation methods exist that allow molecular intermixture, one of which is the preparation of subsequently deposited PEN/PFP blends, where at sufficiently provided diffusivity - as varied by the substrate temperature during deposition - interdiffusion of PEN into the PFP thin film is enabled. However, the preparation of such blends in reverse order does not lead to such a behavior which has been attributed to different extents of the contact area at the corresponding interfaces by interpreting the data from atomic force microscopy and x-ray reflectivity measurements. The analysis of the electronic properties by means of optical absorption spectroscopy has led to the conclusion that the optical signatures may also be interpreted as sensitive benchmarks for the efficiency of intermixture in those blends. Specifically the appearance of the charge-transfer-related excitation and the extinction of the pure-phase excitons have been identified as the crucial indicators. Finally, it has been shown that the thermal stabilization of the heterostructure compared to the single compounds may also be used to selectively desorb the non-intermixed extents of the single compounds. This enables very precise spectroscopic characterizations and will for example allow to determine the electronic and vibrational properties of the PEN-PFP-heterostructure without undesired contributions of the pure compounds.

In contrast to the mixture of PEN and PFP where the energy gain related to intermolecular cohesion exceeds that of the formation of pure-phase clusters, the opposite is the case for the combination of PEN and C_{60}. By deposition of small amounts of C_{60} on top of PEN

multilayers, the formation of C_{60} nano-structures has been analyzed. It has been found that the aforementioned preferred cohesion of C_{60} molecules leads to the formation of separated C_{60} clusters on the PEN template. Interestingly, these clusters are not uniformly distributed on the PEN islands but instead pinned at the PEN step edges. The variation of the substrate temperature during deposition of C_{60} has allowed to control the diffusivity of the C_{60} molecules and the dimensionality of the wetting layers: While 2D-structures are found at cryogenic substrate temperatures, continuous one-dimensional decoration of the PEN step edges occurs at intermediate temperatures of 240 K, whereas at elevated temperatures the molecules form 0-dimensional clusters. Interestingly, all of these structures are stable upon post-deposition heating. Additionally, different approaches of the preparation of buried C_{60} nanoclusters have been compared by means of additional PEN deposition, which will be addressed in the future by means of spectroscopic investigations to find out about the coupling at organic acceptor/donor-interfaces.

Of course, this work does not put the demand of being all-embracing or having clarified all open questions within the field of organic semiconductors and molecular thin films. Rather, it has to be understood as a comprehensive element within this field of research which helped to approach some fundamental and practical questions. The fundamental nature of the studies however facilitates them as interesting and important within a wide range of research fields and they may be expected to influence and stimulate a number of further studies.

CHAPTER 5

Publications

5.1 Article I: Epitaxial growth of perfluoropentacene films with predefined molecular orientation: A route for single-crystal optical studies

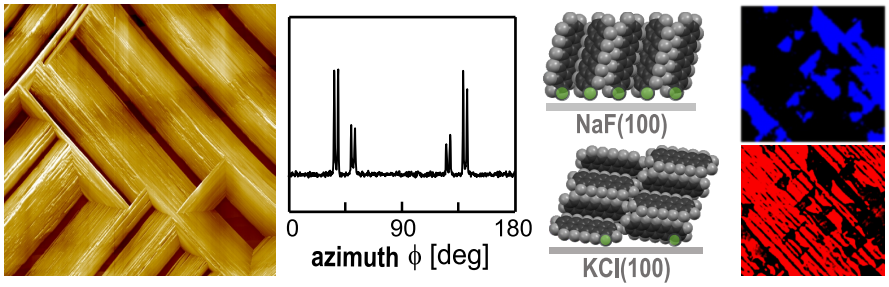

5.1.1 Abstract

Using atomic-force microscopy and x-ray diffraction we show that perfluoropentacene ($C_{22}F_{14}$, PFP) forms long-range ordered, epitaxial films on KCl(100) and NaF(100) cleavage planes. On both substrates the films adopt the same crystalline bulk phase, but surprisingly exhibit quite different molecular orientations, being upright oriented on NaF and recumbent oriented on KCl. Accompanied thermal desorption spectroscopy measurements indicate the absence of a stabilized seed layer, like on metals, hence suggesting that in both cases the PFP films are stabilized by an electrostatic point-in-line relationship between the outermost fluorine atoms and the alkali cations of the alkali halide surfaces. Furthermore, the transparency of both substrates was utilized to perform detailed transmission UV/Vis spectroscopy and polarized optical microscopy measurements along well-defined crystallographic directions. From these data the orientation of the transition dipole moments of the various optical excitations were experimentally determined and a directional anisotropic exciton coupling was observed, which is attributed to the asymmetric molecular packing motif within the (100) plane of the PFP crystal lattice.

5.1.2 Methods

Atomic Force Microscopy, Organic Molecular Beam Deposition, Polarized Optical Microscopy, Thermal Desorption Spectroscopy, UV/Vis Spectroscopy, X-Ray Diffraction.

5.1.3 Own Contribution

I have prepared all samples and planned and conducted all experiments, in case of XRD measurements Martin Zimmermann (Bruker AXS) was of assistance. I have written the

major part of the manuscript, while Gregor Witte has helped to interpret the data as well as to improve the manuscript.

Some of the AFM and XRD results had already been part of my Diploma thesis [124], however, the major part of the experiments as well as the interpretation of the data and the preparation of the manuscript have taken place within the framework of this doctoral thesis.

PHYSICAL REVIEW B **83**, 155428 (2011)

Epitaxial growth of perfluoropentacene films with predefined molecular orientation: A route for single-crystal optical studies

Tobias Breuer and Gregor Witte
Molekulare Festkörperphysik, Philipps-Universität Marburg, D-35032 Marburg, Germany
(Received 12 February 2011; published 18 April 2011)

Using atomic-force microscopy and x-ray diffraction we show that perfluoropentacene ($C_{22}F_{14}$, PFP) forms long-range ordered, epitaxial films on KCl(100) and NaF(100) cleavage planes. On both substrates the films adopt the same crystalline bulk phase, but surprisingly exhibit quite different molecular orientations, being upright oriented on NaF and recumbent oriented on KCl. Accompanied thermal desorption spectroscopy measurements indicate the absence of a stabilized seed layer, like on metals, hence suggesting that in both cases the PFP films are stabilized by an electrostatic point-in-line relationship between the outermost fluorine atoms and the alkali cations of the alkali halide surfaces. Furthermore, the transparency of both substrates was utilized to perform detailed transmission UV/Vis spectroscopy and polarized optical microscopy measurements along well-defined crystallographic directions. From these data the orientation of transition dipole moments of the various optical excitations were experimentally determined and a directional anisotropic exciton coupling was observed, which is attributed to the asymmetric molecular packing motif within the (100) plane of the PFP crystal lattice.

DOI: 10.1103/PhysRevB.83.155428 PACS number(s): 68.55.am, 61.05.cp, 68.37.Ps, 78.66.Qn

I. INTRODUCTION

Despite the recent success of using organic semiconductors as active material for device applications,[1–6] many fundamental aspects regarding the charge transport[7] or photoexcitation[8] in such materials are still not well understood. In part, this is due to the fact that measured material properties are largely affected by extrinsic factors like structural defects and impurities,[9,10] which poses a challenge for experimental studies on highly ordered molecular crystals to derive the intrinsic properties.[11] Though transport measurements and optical spectra are available for some organic single crystals,[10,12–14] they are commonly restricted to specific crystallographic directions because many crystals exhibit a flaky habitus. Moreover, a systematic broadening of such single-crystal studies toward other molecular materials in many cases is hampered by the lack of sufficiently sized crystals.

Therefore, organic thin films have been considered as an alternative approach to study optoelectronic properties of molecular solids. Due to a large mismatch in symmetry and lattice parameters between organic crystals and inorganic substrates, however, mostly poly-crystalline films are obtained, often also revealing a coexistence of different crystalline orientations or phases.[15–17] Nevertheless, epitaxially ordered heterostructures have been observed for some organic thin films upon deposition on inorganic substrates which are stabilized by an accordance of characteristic lengths yielding, for example, a point-in-line epitaxy.[18] Remarkably, epitaxially ordered organic thin films have been obtained almost exclusively on weakly interacting substrates like insulators or half metals, for example, for para-phenylene on mica,[19,20] TiO_2(110)[21] and KCl(100)[22–24] pentacene on Bi(0001)[25] and KBr(100),[26] phthalocyanines on alkali halides,[27,28] and TTF/TCNQ (charge transfer salt) on KCl(100).[29,30] In this regard it should, however, be mentioned that these films usually appear not uniformly oriented but exhibit different coexisting crystalline orientations and lateral alignments, which strongly depend on growth temperature, film thickness, and substrate roughness.[17,31] By contrast chemisorbed wetting layers of planar-oriented molecules are typically formed on metal surfaces while subsequent film growth is accompanied by molecular reorientation and pronounced islanding, leading to a considerable film roughness.[31,32] Regarding optical absorption measurements metal substrates appear rather unfavorable because they induce screening and quenching effects, while detailed optical spectroscopy of crystalline organic adlayers have been carried out on electronically decoupled insulating substrates.[20,28]

One of the key features of organic electronics is the versatile tailoring of electronic properties by means of chemical modifications of the π-conjugated molecular materials.[33–35] One approach along this direction is based on fluorination. In case of the prototypical pentacene this yields perfluoropentacene (PFP, $C_{22}F_{14}$),[36] a promising new organic semiconductor with *n*-type charge transport behavior and enhanced chemical robustness against oxidation. Revealing the same symmetry and a similar molecular packing motif in the crystalline phase as the nonfluorinated analog but exhibiting an inverted quadrupole moment it constitutes an interesting model system to study the effect of this molecular modification on the electronic and optical properties of the molecular solid. Unfortunately, no macroscopic sized crystals or epitaxially ordered films of PFP have yet been observed. Furthermore, attempts to grow epitaxial PFP films on Bi(0001), like for the nonfluorinated analog, failed.[37] As regards the optical properties of PFP solids they have so far been restricted to polycrystalline films prepared on SiO_2. In that case films reveal a pronounced texturing, forming (100)-oriented layers, but consist of azimuthally isotropically distributed needles,[38] hence limiting the optical analysis only to in-plane and out-of-plane components.[39]

In this study we have investigated the growth of PFP films on various alkali halide substrates by using atomic force microscopy (AFM) and x-ray diffraction (XRD) and demonstrate that particularly well-ordered epitaxial films are formed on NaF(100) and KCl(100) substrates. Although these films adopt the same crystalline bulk phase quite different molecular orientations (recumbent vs upright) were observed

for both substrates. Additional information on the adsorption energetics was obtained from thermal desorption spectroscopy (TDS) measurements while the morphology of the bottom side of films grown on the different substrates was studied after dissolving the water-soluble substrates. In a next step the fortunate growth situation of different molecular orientations in combination with the optical transparency of the alkali halide substrates was utilized to perform optical absorption measurements along different crystallographic directions of PFP. These data make it possible, in particular, to determine the orientation of transition dipole moments for the various optical excitations.

II. EXPERIMENTAL

The PFP films were grown under ultrahigh-vacuum (UHV) conditions onto KCl(100) and NaF(100) substrates. All substrate surfaces have been prepared by cleaving slices of about 2 mm from the single-crystal rods (Korth Kristalle GmbH) in air. Subsequently, the samples were quickly transferred into the vacuum system using a load-lock system and heated at 450 K in vacuum to remove adsorbed water. All PFP (Kanto Denka Kogoyo Co., Ltd.) films were deposited by organic molecular beam deposition from an aluminum crucible of a resistively heated Knudsen cell at a deposition rate of 8 Å/min, monitored by quartz crystal microbalance. To characterize the thermal stability of the films thermal desorption experiments were conducted employing a quadrupole mass spectrometer (Balzers QMA 200) with a Feulner cup positioned close to the sample surface. TD spectra were acquired by recording the mass signal of the double-charged molecule ion (M^{2+}, $m/z = 265$ amu) during a computer-controlled linear increase of the substrate temperature from 290 K to 550 K with a heating rate of $\beta = 0.5$ K/s. Temperatures were measured via thermocouples directly attached to the samples' surfaces. The film morphology was characterized by AFM (Agilent SPM 5500) operated in tapping mode at ambient conditions. The crystalline structure and orientation of the films were analyzed by means of XRD (Bruker AXS Discover D8) using monochromatized Cu $K\alpha$ radiation ($\lambda = 1.5406$ Å) and a LynxEye silicon strip detector. A UV/Vis spectrophotometer (Agilent 8453) and optical microscopy in combination with spectral and polarization filters were utilized to characterize the optical properties of the films.

III. RESULTS

A. Film morphology

In Fig. 1 we present AFM data showing the morphology of PFP films prepared by molecular beam deposition onto NaF(100) and KCl(100) surfaces. On sodium fluoride PFP forms spicular islands whose size and azimuthal ordering depend on the substrate temperature upon growth. As illustrated in Fig. 1(a), deposition of PFP on NaF at substrate temperatures of 310 K yields only small fibroid islands with lengths of about 500 nm. Though some islands are aligned in parallel with their neighbors, no global ordering occurs. Raising the growth temperature to 343 K, however, yields largely increased islands with typical lengths of more than 10 μm and a width of about 300 nm that are uniformly aligned along ⟨001⟩

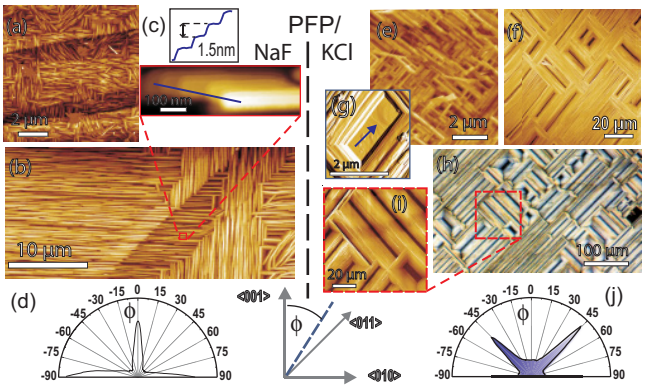

FIG. 1. (Color online) Comparison of AFM data showing the morphology of PFP films deposited on NaF(100) (left panels) and on KCl(100) (right panels). (a),(e) Deposition at $T = 310$ K; (b),(f) deposition at $T = 343$ K; (d),(j) statistical analysis of the island orientation of latter samples. Panel (c) reveals a magnified micrograph of (b) with accompanied line scan and panel (g) displays a magnified detail showing an uncovered KCl substrate region. Panel (h) shows an optical micrograph of a PFP film deposited at $T = 363$ K on KCl together with (i) a corresponding AFM micrograph.

substrate directions appearing in two orthogonal rotational domains according to the substrate symmetry [Fig. 1(b)]. This is made particularly clear by a statistical analysis of the azimuthal ordering carried out for several large-area AFM micrographs which is shown in Fig. 1(d). At these conditions domains with same azimuthal island orientation of about 75×75 μm were observed for a nominal film thickness of 30 nm. Corresponding line profiles perpendicular to the needle axis [see inset Fig. 1(c)] reveal distinct molecular steps of 1.5 nm that agree favorably with the (100)-layer spacing of PFP, hence indicating an upright molecular orientation in these needles like in the case of PFP films on SiO_2.[38]

PFP films on KCl(100) also consist of elongated islands which are, however, oriented along the ⟨011⟩ substrate azimuth and again appear in two rotational domains. In contrast to NaF a considerable azimuthal ordering occurs on KCl already upon deposition at 310 K [Fig. 1(e)]. Also on this substrate the long-range ordering and grain size can be largely improved by raising the growth temperature, yielding an optimal temperature of 363 K. At these conditions crystalline islands of more than 200 μm are formed which could easily be imaged by optical microscopy [see Fig. 1(h)]. Similar images were observed throughout the entire sample and thus prove the excellent global ordering of such films. In addition, AFM data indicate that PFP islands on KCl(100) exhibit particular straight lateral edges [see Fig. 1(i)] without any waviness as it was found for PFP fibers on NaF(100) [cf. Fig. 1(b)]. Interestingly, no molecular steps were found on the PFP films on KCl. Instead, the individual islands reveal a height of more than 120 nm at a nominal film thickness of 30 nm, hence reflecting a poor wetting of this substrate and a pronounced islanding. As shown in Fig. 1(g) even noncovered KCl regions were found that exhibit characteristic step bunches associated with surface steps of the bare KCl substrate.

Attempts to also increase the size of PFP islands on NaF(100) by raising the growth temperature to 363 K failed.

Instead, no adsorption took place at all, and the substrate remained completely uncovered and leads to the conclusion that the sticking coefficient of PFP on NaF is drastically reduced at this substrate temperature.

Furthermore, to compare the initial stage of PFP film growth on both substrates the morphology of 3-nm films deposited at 343 K was analyzed. As shown in Fig. 2(a) thin PFP films on NaF reveal similar characteristics except a reduced fiber size than the thicker layers. By contrast, a rather different morphology was found for such films on KCl where large surface areas of more than 20 μm^2 remain uncovered and rather tall islands appear, thus suggesting poorer wetting than on NaF [Fig. 2(b)]. Interestingly, not all of these islands are oriented along the $\langle 011 \rangle$ azimuth of KCl like the islands in thicker films, but some of them adopt an orientation along the $\langle 001 \rangle_{KCl}$ directions. While the former islands exhibit heights of more than 50 nm the latter fibers are much longer and have typical heights of 10–15 nm. Comparison with the orientation of substrate steps of the bare KCl(100) surface suggests that these fibers oriented along $\langle 001 \rangle_{KCl}$ can be attributed to step decoration effects and are overgrown during further deposition. Findings showing distinct differences in the interface structure of PFP films on both substrates are further supported by an inspection of the bottom side of the films. For this purpose the water solubility of the alkali halide substrates was utilized and the substrate was dissolved after the PFP films were fixed by an elastomer glued onto the top side. Figures 2(c) and 2(d) compare AFM data showing the backside of PFP films on both substrates. Beside the different epitaxial orientation of the islands also different film roughnesses were found in topographical line profiles for films grown on the various substrates. The back side of PFP films on NaF reveals a roughness of less than 10 nm while height differences of more than 100 nm are found for films on KCl, again indicating the presence of completely uncovered regions.

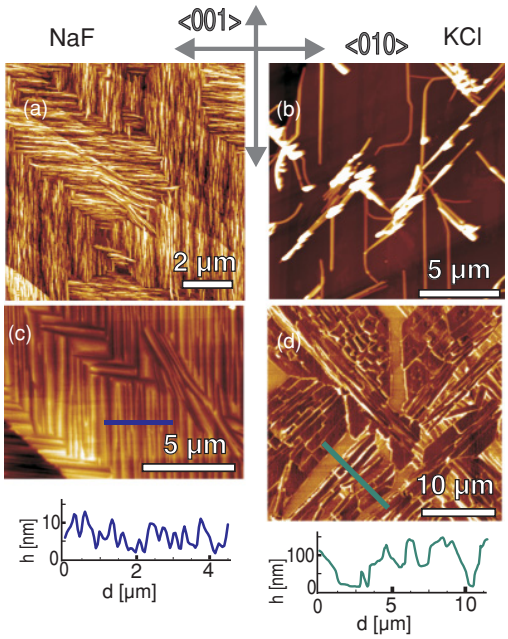

FIG. 2. (Color online) AFM data of PFP films on NaF(100) and KCl(100) showing (a),(b) the initial growth (nominal thickness 3 nm) and (c),(d) the back side of 50-nm PFP films after the substrate was dissolved in water. All samples were prepared at temperatures of 343 K.

B. Thermal stability

To compare the thermal stability of PFP films grown on the different alkali halide substrates TDS measurements were carried out. As shown in Fig. 3 all TD spectra reveal only one distinct desorption peak around about 425 K for the mass of the molecule ion. Since the peak area increases with the respective film thickness while the ascending peak flank remains identical on each substrate, it can be assigned to multilayer desorption. A precise comparison of the thermal stability of PFP films on the various substrates is rather difficult because the apparent position of the peak maxima depends on the actual film thickness. Therefore, we considered the onset of desorption that was determined from the intersection of an exponential ascending peak flank and a background signal. As shown in the inset of Fig. 3 this analysis yields somewhat different onset temperatures for PFP desorption of about 380 K for KCl and 390 K for NaF, respectively. We note that although the low thermal conductivity of alkali halides makes it rather difficult to precisely measure surface temperatures, the present data indicate that the differently oriented PFP films (described in the next section) exhibit slightly different thermal stabilities.

No further desorption peak even at the mass of characteristic fragments could be detected at higher temperatures, hence indicating the absence of a firmly bound first monolayer. The present system thus parallels the situation observed for pentacene on SiO_2 (Ref. 40) or graphite,[41] where, in contrast to pentacene adsorption on various metal substrates such as Cu, Ag, Au (Refs. 42–44), or PFP on Ag (Ref. 45), no specific monolayer can be prepared by heating.

C. Crystalline orientation

Though a preferential azimuthal alignment of the PFP islands is clearly inferred from the AFM data additional

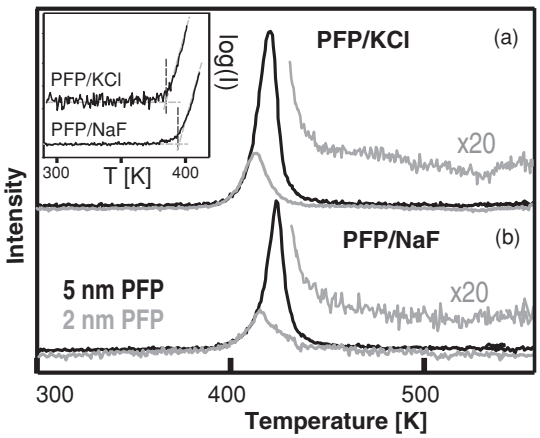

FIG. 3. Thermal desorption spectra of PFP films of different thickness deposited (a) on KCl(100) and (b) on NaF(100). All spectra were recorded for the molecule ion and a heating rate of $\beta = 0.5$ K/s.

XRD measurements were carried out to derive more precise information about the crystalline ordering and orientation. Typical $\theta/2\theta$ scans that were recorded in Bragg-Brentano geometry are shown in Fig. 4(a). To verify the surface alignment and to compensate a possible angular offset of the diffractometer the simultaneously measured (200) substrate reflex was used as an intrinsic reference. For PFP/NaF(100) distinct reflexes were found at scattering angles of 5.74°, 11.42°, 17.14°, and 22.86° which are in good compliance with the positions expected for the (n00) peaks of the PFP bulk structure[36] [5.71°, 11.41°, 17.14°, 22.92°] with a layer spacing of $d_{(100)} = 15.50$ Å, thus proving the formation of (100)-oriented PFP films on NaF(100).

Further information about the azimuthal orientation of the crystalline PFP films was obtained from ϕ scans. For (100)-oriented PFP films on NaF(100), where molecules adopt an upright orientation, the $(112)_{\mathrm{PFP}}$ reflex was chosen because it reveals a high intensity in the powder spectrum and represents a lattice plane that is largely tilted with respect to the $(100)_{\mathrm{PFP}}$ plane, hence providing a clear signature of the in-plane orientation. In total, 16 peaks were observed which can be reduced according to the substrate symmetry to 4 different peaks positioned at $\phi = 36.7°$, 39.8°, 50.2°, and 53.3° in the first quadrant as shown in Fig. 4(b). The latter two peaks can be identified as $(11\bar{2})_{\mathrm{PFP}}$ reflexes which are simultaneously detected because of their very similar interplanar spacing [$d_{(112)} = 3.43$ Å, $d_{(11\bar{2})} = 3.46$ Å]. Like the $(112)_{\mathrm{PFP}}$ reflex, they appear symmetrically distributed by $\Delta\phi_1 = \pm 6.8°$ around the ⟨011⟩ substrate azimuth and indicate the presence of mirror domains. In addition, they exhibit a splitting of $2\delta\phi = 3.1°$, which is attributed to an appreciable mosaicity within the fibers. To obtain the lateral alignment of the molecules from the ϕ scans we have considered the line of intersection between the (100) surface plane and the monitored (112) plane of the PFP film to get a projection of the Bragg condition onto the surface plane [blue dashed line in Fig. 5(a)]. Afterward, we used the PFP bulk structure to calculate the angle α between this intersection line and a suitable unit cell axis. Using the b axis of the PFP lattice, this yields an angle of $\alpha = 51.8°$. This value has to be subtracted from measured ϕ angles to extract the molecules' orientation relative to the high-symmetry direction of the substrate (cf. Fig. 5). This analysis shows that the **b** vector (4.49 Å) of the PFP lattice almost coincides with the ⟨010⟩ lattice vector of the NaF(100) surface (4.62 Å), hence suggesting a stabilization of PFP films due to a point-in-line relation between the lowermost fluorine atoms of the upright-oriented PFP molecules and the underlying sodium atoms of the NaF(100) surface as depicted in Fig. 5(a). The small mosaicity of $\delta\phi = \pm 1.55°$ may be attributed to the slight mismatch (3%).

Quite surprisingly, a rather different orientation was observed for PFP films grown on KCl(100). In that case only one distinct peak at 16.65° was found in the $\theta/2\theta$ scans while no $(n00)_{\mathrm{PFP}}$ diffraction peaks appear [cf. second curve in Fig. 4(a)]. The observed peak has been identified as $(102)_{\mathrm{PFP}}$ reflex, hence indicating a recumbent orientation of PFP molecules as depicted schematically in Fig. 5(b). The

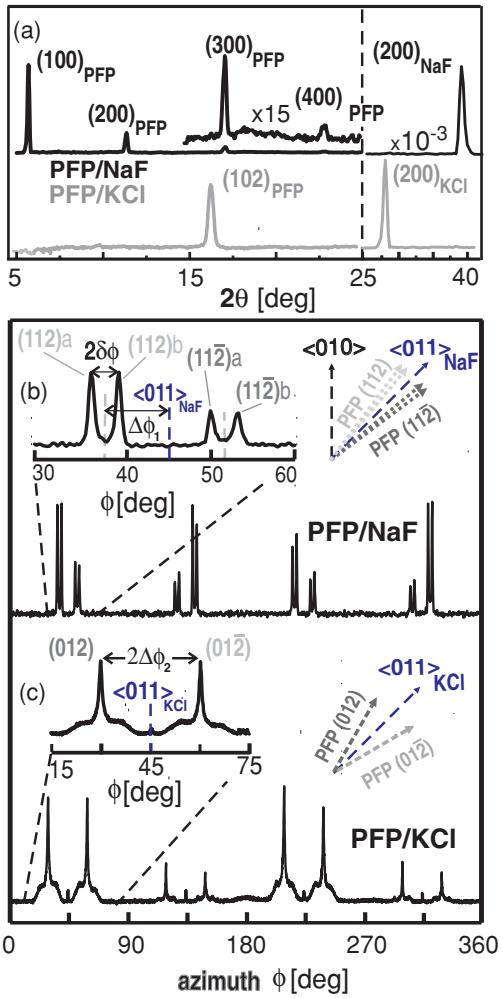

FIG. 4. (Color online) X-ray diffraction data of 50-nm PFP films grown on NaF(100) and KCl(100). (a) $\theta/2\theta$ scans and azimuthal ϕ scans recorded for (b) the $(112)_{\mathrm{PFP}}$ reflex on NaF and (c) the $(012)_{\mathrm{PFP}}$ reflex on KCl together with magnified ϕ scans (insets) showing the corresponding fine structure.

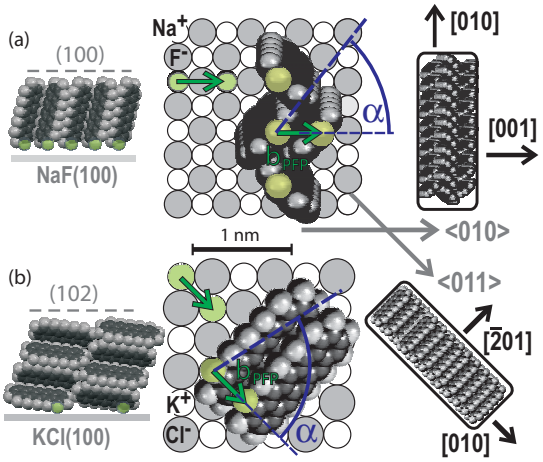

FIG. 5. (Color online) Hard-sphere model illustrating the molecular structure of epitaxial PFP films (a) on NaF(100) and (b) on KCl(100). The green balls represent the outermost fluorine atoms that are in contact with the substrate. For clarity only one rotational domain is shown. The right-handed sketches show the molecule orientation within the PFP needles (those not true to scale).

corresponding azimuthal ϕ scans that were recorded for the $(012)_{PFP}$ and $(01\bar{2})_{PFP}$ reflexes (having the same interlayer distance) reveal in total eight peaks as shown in Fig. 4(c). According to the substrate symmetry, this number can be reduced and yields one of each reflex per ϕ quadrant appearing symmetrically at $\Delta\phi_2 = \pm 14.8^\circ$ around the $\langle 011 \rangle$ substrate azimuth. The further analysis of the molecular arrangement in these planes projected onto the surface [dashed line in Fig. 5(b) denoting the intersection between the $(102)_{PFP}$ and $(012)_{PFP}$ planes] shows that the **b** vector is aligned along the $\langle 011 \rangle$ direction of the substrate. This alignment yields a rather close match between the **b** vector and the $\langle 011 \rangle$ vector of KCl (4.45 Å) with a lattice mismatch of less than 1%.

D. Optical properties

PFP films on both alkali halide substrates also show strikingly different optical properties such as their color appearance: PFP films on NaF exhibit a blue color while they appear green on KCl independent of film thickness. UV/Vis transmission absorption spectra allow a more detailed analysis [shown in Fig. 6(a)] which are possible due to the transparency of both substrates. Spectra of PFP films on NaF reveal an intense absorption band at 1.75 eV and a weaker band at about 2.3 eV (denoted as I and II). Both absorption maxima are accompanied by weaker replica appearing shifted by $\Delta E = 0.18$ eV toward higher energies and might be attributed to vibrational progressions of the photoexcitations. Note that in a previous high-resolution electron-energy-loss spectroscopy study of PFP films various in-plane stretching modes with energies between 178 and 185 meV were observed.[46] Alternatively, the fine structure could be assigned to an exciton excitation with a Davydov splitting, which is expected for crystalline molecular materials with nonprimitive unit cells like in the case of pentacene.[47–49] For PFP films on KCl the second absorption band was not observed but instead an intense third band (III) appears at 2.75 eV, which exhibits the largest intensity at the first replica.

Correlating the measured absorbances with the different molecular orientations within the crystalline films on both substrates makes it possible to derive information on the orientation of the corresponding transition dipole moments (TDMs) by employing the selection rule $I_{abs} \sim |\vec{E} \cdot \overrightarrow{TDM}|^2$. The absence of absorption band III for films with upright-oriented molecules indicates that TDM_{III} is oriented perpendicular to the $(100)_{PFP}$ plane, hence proceeding essentially along the molecular long axis. Similarly, the disappearance of band II for PFP/KCl shows that TDM_{II} is mainly oriented perpendicular to the $(102)_{PFP}$ plane while its appearance for PFP/NaF implies a significant component within the $(100)_{PFP}$ plane, hence indicating that its main component is oriented along $[001]_{PFP}$. Note that a distinct polarization dependence of absorption spectra has also been observed for PFP films on SiO_2 (Ref. 39) by spectroscopic ellipsometry measurement, which are shown likewise in Fig. 6(a) for comparison. In that case, however, a detailed analysis is hampered by an isotropic in-plane distribution of PFP islands,[38] whereas the epitaxial ordering in addition enables an azimuthal analysis. The extended crystalline domains that are observed in the AFM data of PFP films [cf. Fig. 1(i)] could also be visualized

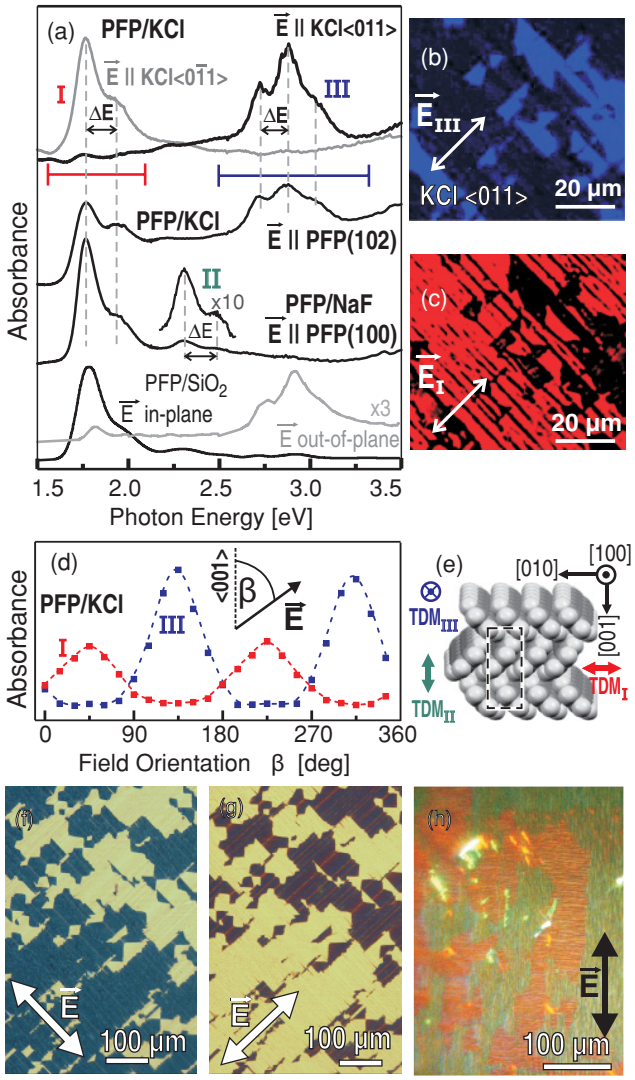

FIG. 6. (Color online) Summary of optical properties of PFP films. (a) UV/Vis transmission absorption spectra of 50-nm PFP grown on NaF(100) and KCl(100), compared to PFP on SiO_2 (Ref. 39) (lowermost spectra). The uppermost spectra of PFP/KCl were recorded by using linear polarized light oriented along the $\langle 0\bar{1}1 \rangle$ and $\langle 011 \rangle$ azimuth directions of KCl. Panels (b) and (c) display polarized optical micrographs for PFP/KCl with polarization plane oriented along the $\langle 011 \rangle$ azimuth illuminated with (b) blue light (spectral region III) and (c) red light (spectral region I). Panel (d) shows absorption intensities of PFP/KCl in spectral regions I and III as functions of polarization direction. Panel (e) displays the orientation of transition dipole moments with respect to the PFP lattice derived for the different spectral excitations. Corresponding optical micrographs with linear polarized light are shown (f),(g) for PFP/KCl and (h) for PFP/NaF.

by optical microscopy in combination with polarization and spectral filters. Figure 6(b) displays an optical micrograph of a 50-nm PFP film on KCl(100) obtained with linear polarized ($\vec{E} \| \langle 011 \rangle_{KCl}$) blue transmitted light by using a color filter with pass-band in region III. The bright- and dark-appearing domains change their contrast when azimuthally rotating the polarization plane by 90° (not shown). Moreover, by changing

the pass band and illuminating the film with red light (region I) but the same polarization, the absorption contrast also changes, as shown in Fig. 6(c), which proves the orthogonality of the TDM of absorption bands I and III. The excitation of band I occurred at light polarization perpendicular to the needles' long axis, while band III was excited when the polarization was parallel to this axis. A similar effect was observed in the polarization micrographs of PFP films on NaF(100). In that case absorption of band I occurs if the light is polarized along the spicular axis of the islands while band II becomes excited if the polarization plane is perpendicular to this axis (not shown).

Figures 6(f) and 6(g) show optical micrographs of 150-nm PFP films grown at $T_{\mathrm{Dep}} = 343$ K onto KCl(100) that were illuminated with linear polarized white light. Evidently, the effective colors of the islands depend on the direction of light polarization. While islands that are oriented with their long axis parallel to $\vec{E}$ appear blue, the ones aligned normal to $\vec{E}$ appear in a green-red fashion. A similar effect was also found for PFP layers on NaF(100), as shown in Fig. 6(h) for 150-nm film grown at $T_{\mathrm{Dep}} = 343$ K. In this case light polarization along the islands' long axis yields a turquoise color appearance, and crystallites that are rotated by 90° appear pink.

Optical polarization micrographs show further that symmetry-equivalent rotational domains of PFP films on KCl(100) are not uniformly distributed across the sample. Actually, areas with lateral extensions of more than 1 mm were found that exhibit only one domain orientation. In combination with an aperture and a polarization filter this made it possible to acquire UV/Vis spectra of one specific crystalline phase, hence enabling the characterization of a locally uniform crystalline region with well-defined polarization. The uppermost spectra in Fig. 6(a) show two typical absorption spectra that were obtained for polarization planes oriented along $\langle 011\rangle$ and $\langle 0\bar{1}1\rangle$ directions of the KCl(100) surface and exhibit a complementary azimuthal anisotropy for the absorption bands I and III. Figure 6(d) shows the intensity of absorption bands I and III as function of polarization direction β. The observed twofold symmetry is due to the equivalence of light polarization along β and $\beta + 180°$. The peak positions of band I at 45° and of band III at 135° are in perfect concordance with the optical micrographs.

From the conditions that TDM_{I} is located within the $(102)_{\mathrm{PFP}}$ plane and also orthogonal to TDM_{III}, which in turn is progressing along the [100] direction of PFP, leads to the conclusion that TDM_{I} has a main component oriented along $[010]_{\mathrm{PFP}}$. By combining the results of the in-plane XRD scans and optical micrographs we can conclude further that absorption band III represents an excitation perpendicular to band I along the long axis of PFP islands on KCl, showing that this axis is oriented along the [010] direction of PFP. We note that the observed TDM directions of bands I and II differ strongly from the single-molecule axes. For example, TDM I is oriented along $[010]_{\mathrm{PFP}}$ and therefore rotated by 45° relative to both single molecules in the PFP unit cell [cf. Fig. 6(e)].

IV. DISCUSSION

The present AFM and XRD data yield a pronounced epitaxial growth of PFP films on KCl(100) and NaF(100) surfaces. Although molecules are only weakly adsorbed on both alkali halide substrates, and in particular reveal no firmly bound wetting layer, like on metal surfaces,[45] which is inferred from the absence of any monolayer-related thermal desorption peak, quite surprisingly they adopt rather different molecular and crystalline orientations on both substrates. On sodium fluoride PFP molecules exhibit an upright orientation like films grown on SiO_2 (Ref. 38). The epitaxial alignment of the formed spicular islands along the $\langle 010\rangle$ azimuth of the substrate can be attributed to the good accordance of this NaF lattice vector and the **b** vector of PFP.

In contrast, PFP molecules adopt a rather recumbent orientation on KCl and form $(102)_{\mathrm{PFP}}$-oriented films that also consist of spicular islands. Within the $(102)_{\mathrm{PFP}}$ contact plane the PFP molecules are slightly tilted so that actually only one outermost fluorine atom [indicated by green balls in Fig. 5(b)] is in direct contact with the substrate. The PFP islands on KCl(100) are oriented along the $\langle 011\rangle$ substrate azimuth and again are stabilized by a close match of the corresponding lattice constant with the **b** vector of PFP. A closer inspection reveals further that along the direction perpendicular to the **b** vector such contact points exhibit also a perfect higher-order commensurability with the nearest K^+–K^+ distance, $d_{K^+K^+}$, within the KCl(100) surface ($15 \times d_{KK} = |4\mathbf{a} - 2\mathbf{c}|$), thus providing an additional stabilization. We attribute the epitaxial ordering that is illustrated schematically in Fig. 5 to an electrostatic coupling between electronegative fluorine atoms and Na^+ or K^+ cations of both surfaces. This assignment is further evidenced by additional growth experiments carried out for PFP films on ZnO($11\bar{2}0$). Although this surface also has a rectangular unit cell and a good compliance of the nearest-neighbor Zn distance ($d_{Zn-Zn} = 4.58$ Å) with the **b** vector of PFP (misfit 2%) no epitaxial ordering was observed which is attributed to the smaller ionicity of Zn compared to the alkali metal ions.

Comparing the quality of PFP islands formed on both substrates reveals that fibers on NaF exhibit a noticeable waviness while they appear rather straight on KCl. This observation can be related to the peak splitting of $2\delta\phi = 3.1°$ found in the polar x-ray scans [cf. Fig. 4(b)] and indicates an appreciable mosaicity within the crystalline fibers.

Besides a different crystalline orientation of PFP films adopted on both alkali halide substrates differences were also obtained with regard to their wetting and sticking properties. As shown in Fig. 2 deposition of 3-nm PFP leads to covering of a large fraction of the NaF(100) surface, but an equivalent deposition yields tall islands on KCl(100) while the most part of the substrate surface remains uncovered. This reflects rather different wetting properties and most likely also different diffusion lengths of the unequally oriented molecules yielding various apparent film roughnesses. To verify that the different roughness obtained for the initial stage of film growth is characteristic of the respective PFP/alkali halide interfaces also the bottom side of thicker PFP films was inspected after the soluble substrates had been dissolved. Corresponding AFM data [cf. Figs. 2(c) and 2(d)] reveal the same morphology

as the upper sides. In particular, the pronounced azimuthal ordering of the islands can be recognized which exhibit a very different roughness, yielding tall but laterally extended islands on KCl, while PFP fibers on NaF are more narrow, yielding smaller grooves in between. A comparison of temperature-dependent film depositions showed that the size of the formed islands could be largely improved and yielded the largest PFP islands upon growth at 363 K on KCl. Interestingly, at this temperature PFP does not adsorb on the NaF surface, which instead remained uncovered and thus indicates distinct differences in the initial sticking coefficient at elevated temperatures.

Comparing the onset of multilayer desorption determined from the present TDS measurements indicates a slightly larger thermal stability for the (100) surface of PFP than for the $(102)_{PFP}$ surface which might be attributed to differences in the respective surface energies. As the molecules are upright oriented and closely packed within the $(100)_{PFP}$ surface, they have a larger coordination compared to those within the $(102)_{PFP}$ surface, which adopt a recumbent orientation (cf. Fig. 5).

Epitaxially ordered films have been observed before at the growth of various organic compounds on alkali halide surfaces, such as, for example, para-phenylene,[22–24] pentacene,[26] phthalocyanines,[27,28] or TTF/TCNQ.[29,30] In those cases, however, coexisting other phases also appeared or similar orientational growths were found on different alkali halide substrates. By contrast the presently studied PFP films adopt different orientations on the various alkali halides but in each case appear in one exclusive phase. This behavior is distinctly different from the well-known growth scenario of organic compounds on metals and insulators, where strong adsorbate-substrate interaction often leads to recumbently oriented molecules, while weakly interacting insulator substrates normally induce upright-standing molecules. Apparently, a weak substrate interaction combined with a large diffusion length is an important prerequisite to achieve long-range ordered organic films like in the case of PFP films on KCl(100). On the contrary, on metals such an adjustment is not possible and the stress release between a chemisorbed seed layer and subsequently grown multilayers typically lead to dewetting and molecular reorientation.[31]

The fortunate situation that crystalline PFP films with different orientations are formed on the various alkali halide substrates enabled rather detailed directional and polarization-dependent optical absorption measurements. This data allowed in particular to determine the spatial orientation of transition dipole moments (TDMs) of the various optical excitation bands that are summarized in Fig. 6(e).

The analysis shows that the TDMs of bands I and II are both oriented parallel to the (100) plane of PFP. Considering furthermore that both PFP molecules of the unit cell are aligned nearly perpendicular to each other, a similar angular azimuthal dependence is expected for these two absorption bands since both molecules have nearly the same projection with respect to the [010] and [001] directions of the PFP lattice. In contrast to this expectation our data show, however, a strong anisotropy, as band I is excited when light polarization is parallel to $[010]_{PFP}$ and band II is excited by light polarized along $[001]_{PFP}$. [cf. 6(g)]. The observed difference thus suggests that the asymmetric packing motifs that is, coplanar stacks along [010] vs herring-bone piles along [001] directions of the PFP lattice have a wide influence on the photoexcitation in such materials.

By combining the optical micrographs and the determined TDM information, the molecule orientation within the needle-like PFP islands on NaF and KCl could be analyzed. On both substrates the molecules coordinate with their *b* axis parallel to the needles' long axis. The orientation perpendicular to the long axis differs on both substrates. On NaF the molecules align with the [001] direction along the short axis, while they arrange in the $[\bar{2}01]$ direction along this axis on KCl.

The different color appearance of PFP thin films that was mentioned above can easily be explained by means of these thoughts. For example, since TDM_I is oriented along $[001]_{PFP}$, the areas of the PFP film that are oriented with their $[001]_{PFP}$ direction parallel to $\vec{E}$ absorb the red part of the incident light spectrum, thus appearing blue, as demonstrated by the optical micrograph shown in Fig. 6(g).

V. CONCLUSION

In summary, we have observed a peculiar growth mode for PFP films on NaF(100) and KCl(100) surfaces. On both substrates epitaxially ordered, crystalline PFP films are formed but exhibit different molecular and crystalline orientations. In combination with the optical transparency of the alkali halide substrates this enabled detailed optical transmission measurements along various crystal axes of the PFP lattice. Moreover, from polarization-dependent measurements we were able to determine the spatial orientation of the transition dipole moments of various optical excitations and found evidence of a directional anisotropic exciton coupling in PFP. The present study provides rather detailed experimental data on the optical properties of PFP crystals and hopefully will stimulate future theoretical studies that help to understand the exciton dynamics in such organic semiconducting materials.

ACKNOWLEDGMENTS

The authors thank M. Zimmermann (Bruker AXS, Karlsruhe) for his assistance with the XRD measurements and W. Parak (Universität Marburg) for providing access to the UV/Vis spectrometer. Tobias Breuer thankfully acknowledges financial support by the Friedrich-Ebert-Stiftung.

[1] Y. Shirota, J. Mater. Chem. **10**, 1 (2000).
[2] H. E. Katz, Z. N. Bao, and S. L. Gilat, Acc. Chem. Res. **34**, 359 (2001).
[3] C. D. Dimitrakopoulos and P. R. L. Malenfant, Adv. Mater. **14**, 2 (2002).
[4] S. R. Forrest, Nature (London) **428**, 911 (2004).

[5]G. Hadziioannou and G. G. Malliaras, *Semiconducting Polymers* (Wiley-VCH, Weinheim, Germany, 2007), Vol. 1.
[6]Z. Bao and J. Locklin, *Organic Field-Effect Transistors* (CRC Press, Boca Raton, FL, 2007).
[7]V. Coropceanu, J. Cornil, D. A. da Silva Filho, Y. Olivier, R. Silbey, and J-L. Brédas, Chem. Rev. **107**, 926 (2007).
[8]M. Pope, *Electronic Processes in Organic Crystals and Polymers* (Oxford University Press, Oxford, 1999).
[9]N. Karl, in *Organic Electronic Materials*, edited by R. Farchioni and G. Grosso (Springer, New York, 2001).
[10]N. Karl, Synth. Metals **133**, 649 (2003).
[11]Z. T. Jiang, Q. F. Sun, X. C. Xie, and Y. Wang, Phys. Rev. Lett. **93**, 076802 (2004).
[12]V. Sundar, J. Zaumseil, V. Podzorov, E. Menard, R. Willett, T. Someya, M. Gershenson, and J. Rogers, Science 303 **5664**, 1644 (2004).
[13]M. Dressel, B. Gompf, D. Faltermeier, A. K. Tripathi, J. Pflaum, and M. Schubert, Opt. Express **16**, 19970 (2008).
[14]R. W. I. de Boer, M. E. Gershenson, A. F. Morpurgo, and V. Podzorov, Phys. Stat. Sol. A **201**, 1302 (2004).
[15]G. Witte and Ch. Wöll, J. Mater. Res. **19**, 7 (2004).
[16]R. Ruiz, D. Choudhary, B. Nickel, T. Toccoli, K.-C. Chang, A. C. Mayer, P. Clancy, J. M. Blakely, R. L. Headrick, S. Iannotta, and G. G. Malliaras, Chem. Mater. **16**, 4497 (2004).
[17]R. Resel, J. Phys. Condens. Matter **20**, 184009 (2008).
[18]D. E. Hooks, T. Fritz, and M. D. Ward, Adv. Mater. **13**, 227 (2001).
[19]A. Andreev, G. Matt, C. Brabec, H. Sitter, D. Badt, H. Seyringer, and N. S. Sariciftci, Adv. Mat **12**, 629 (2000).
[20]F. Balzer and H. G. Rubahn, Adv. Funct. Mater. **15**, 17 (2005).
[21]G. Koller, S. Berkebile, J. Krenn, G. Tzvetkov, G. Hlawacek, O. Lengyel, F. Netzer, C. Teichert, R. Resel, and M. Ramsey, Adv. Mater. **16**, 2159 (2004).
[22]T. Mikami and H. Yanagi, Appl. Phys. Lett. **73**, 563 (1998).
[23]R. Resel, Thin Solid Films **433**, 1 (2003).
[24]Detlef-M. Smilgies and E. J. Kintzel Jr., Phys. Rev. B **79**, 235413 (2009).
[25]G. E. Thayer, J. T. Sadowski, F. Meyer zu Heringdorf, T. Sakurai, and R. M. Tromp, Phys. Rev. Lett. **95**, 256106 (2005).
[26]T. Kiyomura, T. Nemoto, K. Yoshida, T. Minari, H. Kurata, and S. Isoda, Thin Solid Films **515**, 810 (2006).
[27]M. Ashida, Bull. Chem. Soc. Jpn. **39**, 2632 (1966).
[28]H. Yanagi, T. Kouzeki, M. Ashida, T. Noguchi, A. Manivannan, K. Hashimoto, and A. Fujishima, J. Appl. Phys. **71**, 5146 (1992).
[29]P. Chaudhari, B. A. Scott, R. B. Laibowitz, Y. Tomkiewicz, and J. B. Torrance, Appl. Phys. Lett. **24**, 439 (1974).
[30]E. E. Simonyi, B. A. Scott, and E. A. D. White, Mater. Res. Bull. **11**, 347 (1976).
[31]G. Witte and Ch. Wöll, Phys. Stat. Sol. A **205**, 497 (2008).
[32]A. Gerlach, S. Sellner, S. Kowarik, and F. Schreiber, Phys. Status Solidi A **205**, 461 (2008).
[33]J. E. Anthony, Chem. Rev. **106**, 5028 (2006).
[34]J. S. Wu, Curr. Org. Chem. **11**, 1220 (2007).
[35]M. Mas-Torrent and C. Rovira, Chem. Soc. Rev. **37**, 827 (2008).
[36]Y. Sakamoto, T. Suzuki, M. Kobayashi, Y. Gao, Y. Fukai, Y. Inoue, F. Sato, and S. Tokito, J. Am. Chem. Soc. **126**, 8138 (2004).
[37]J-Z. Wang, J-T. Sadowski, Z-H. Xiong, Y. Fujikawa, Q-K. Xue, T. Sakurai, Nanotechnology **20**, 095704 (2009).
[38]S. Kowarik, A. Gerlach, A. Hinderhofer, S. Milita, F. Borgatti, F. Zontone, T. Suzuki, F. Biscarini, F. Schreiber, Phys. Status Solidi RRL **2**, 120 (2008).
[39]A. Hinderhofer, U. Heinemeyer, A. Gerlach, S. Kowarik, R. Jacobs, Y. Sakamoto, T. Suzuki, and F. Schreiber, J. Chem. Phys. **127**, 194705 (2007).
[40]D. Käfer, C. Wöll, and G. Witte, Appl. Phys. A **95**, 273 (2009).
[41]J. Götzen, D. Käfer, C. Wöll, and G. Witte, Phys. Rev. B **81**, 085440 (2010).
[42]S. Söhnchen, S. Lukas, and G. Witte, J. Chem. Phys. **121**, 525 (2004).
[43]D. Käfer, L. Ruppel, and G. Witte, Phys. Rev. B **75**, 085309 (2007).
[44]D. Käfer and G. Witte, Chem. Phys. Lett. **442**, 376 (2007).
[45]J. Götzen, C. H. Schwalb, C. Schmidt, G. Mette, M. Marks, U. Höfer, and G. Witte, Langmuir **27**, 993 (2011).
[46]K. Fujii, C. Himcinschi, M. Toader, S. Kera, D. R. T. Zahn, and N. Ueno, J. Elect. Spectrosc. Relat. Phenom. **174**, 65 (2009).
[47]J. Lee, S. S. Kim, K. Kim, J. H. Kim, and S. Im, Appl. Phys. Lett. **84**, 1701 (2004).
[48]O. Ostroverkhova, S. Shcherbyna, D. G. Cooke, R. F. Egerton, and F. A. Hegmann, R. R. Tykwinski, S. R. Parkin, and J. E. Anthony, J. Appl. Phys. **98**, 033701 (2005).
[49]D. Faltermeier, B. Gompf, M. Dressel, A. K. Tripathi, and J. Pflaum, Phys. Rev. B **74**, 125416 (2006).

5.2 Article II: Application of transmission electron microscopy for microstructural characterization of perfluoropentacene thin films

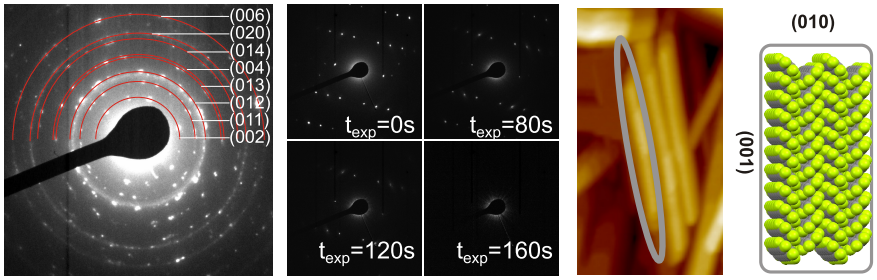

5.2.1 Abstract

The crystalline structure and orientation of perfluoropentacene ($C_{22}F_{14}$, PFP) fibers formed upon thin-film deposition onto SiO_2 substrates have been studied by means of transmission electron microscopy (TEM), atomic force microscopy (AFM), and x-ray diffraction. The synopsis of TEM micrographs and diffraction patterns enhances the understanding of local crystal orientation on small length scales. The relationship of the PFP fiber morphology with the crystalline arrangement of PFP molecules within single fibers was established using this technique. Radiation damage, which is a critical problem for TEM investigations of organic materials, is described and the sample morphology after TEM investigations is correlated with AFM measurements of samples previously examined by TEM.

5.2.2 Methods

Atomic Force Microscopy, Organic Molecular Beam Deposition, Transmission Electron Microscopy, X-Ray Diffraction

5.2.3 Own Contribution

The general idea for this experiment was developed in discussion with Wiebke Witte, Andreas Beyer, Kerstin Volz and Gregor Witte. I have prepared all samples, conducted all AFM and XRD measurements and interpreted the data as well as prepared them for publication. The TEM data was acquired by Benedikt Haas, Wiebke Witte and Andreas Beyer. The manuscript was written in close cooperation and discussion between Benedikt Haas, Kerstin Volz, Gregor Witte and myself.

Application of transmission electron microscopy for microstructural characterization of perfluoropentacene thin films

Benedikt Haas, Andreas Beyer, Wiebke Witte, Tobias Breuer, Gregor Witte, and Kerstin Volz
Faculty of Physics and Materials Science Center, Philipps-University Marburg, D-35032 Marburg, Germany

(Received 28 June 2011; accepted 20 August 2011; published online 7 October 2011)

The crystalline structure and orientation of perfluoropentacene ($C_{22}F_{14}$, PFP) fibers formed upon thin-film deposition onto SiO_2 substrates have been studied by means of transmission electron microscopy (TEM), atomic force microscopy (AFM), and x-ray diffraction. The synopsis of TEM micrographs and diffraction patterns enhances the understanding of local crystal orientation on small length scales. The relationship of the PFP fiber morphology with the crystalline arrangement of PFP molecules within single fibers was established using this technique. Radiation damage, which is a critical problem for TEM investigations of organic materials, is described and the sample morphology after TEM investigations is correlated with AFM measurements of samples previously examined by TEM. © *2011 American Institute of Physics*. [doi:10.1063/1.3646549]

I. INTRODUCTION

Organic semiconductors have attracted considerable attention because of their promising potential for the fabrication of thin-film organic electronic devices.[1–5] Among the molecular materials used for such applications, polycyclic aromatic hydrocarbons are of particular interest because they form crystalline films that exhibit high charge carrier mobilities. Previous studies have shown that the resulting device characteristics critically depend on the degree of crystalline ordering of the organic layers.[6] Moreover, the shape anisotropy of the molecular entities also causes a pronounced directional ordering and packing in the crystalline phase[7] and commonly leads to rather anisotropic charge transport along the various crystallographic directions.[8,9] Therefore, a precise characterization of the microstructure of organic thin films[10,11] is of vital interest for a detailed understanding of the properties of such molecular materials.

Because organic thin films are usually polycrystalline, x-ray diffraction (XRD) measurements can provide precise information about lattice constants and crystal structure, but hardly determine in-plane ordering. Although micro-spot diffraction has become available in some synchrotron facilities of the third generation,[12,13] a precise relation of local diffraction and corresponding morphology remains problematic because of the lack of simultaneous imaging. By contrast, transmission electron microscopy (TEM) offers the unique advantage that micrograph and corresponding local diffraction pattern can be acquired at the same positions, and the possibility to collect diffraction data from submicron-sized areas is unmatched by XRD. Though complicated by electron-induced radiation damages of organic materials, TEM has been successfully used to characterize polycrystalline organic semiconductor films.[14–17] In that way, for example, rather detailed information on the local structural transformation between different crystalline phases has been obtained for pentacene thin films.[18]

Here we report for the first time a TEM characterization of perfluoropentacene (PFP) films grown on SiO_2. A previous XRD study of PFP on SiO_2 has shown that deposition of this newly available n-type organic semiconductor[19] on silicon oxide yields crystalline fibers that exhibit a distinct (100) texture but with an isotropic azimuthal distribution.[20]

Two different crystalline phases have been determined for PFP; a bulk phase ($a = 15.51$ Å, $b = 4.49$ Å, $c = 11.45$ Å, $\alpha = 90°$, $\beta = 91.567°$, $\gamma = 90°$),[19] which is slightly modified in thin films on some substrates ($a = 15.76$ Å, $b = 4.51$ Å, $c = 11.48$ Å, $\alpha = 90°$, $\beta = 90.4°$, $\gamma = 90°$) (Ref. 27) (both structures exhibit the monoclinic space group $P2_1/c$) and a new polymorph on Ag(111) that reveals an interlayer spacing of 3.16 Å, thus indicating a rather declined molecular orientation. Because of their strong similarity, the bulk and thin-film phases could not be told apart by TEM electron diffraction.

In the present work we have studied the crystalline structure of such fibers by using TEM in combination with atomic force microscopy (AFM) and XRD. First, damage because of electron irradiation has been characterized for the studied films concerning interior and exterior changes of the fibers. The degradation of organic materials in the TEM is a serious issue and a complex process that is not fully understood.[21] In principle, the highly accelerated electrons break chemical bonds, leaving radicals. These radicals form new bonds, changing the local structure of the compound and destroying the crystalline order. Empirical formulas describe the exponential decline of diffraction intensities of irradiated polymers of different kinds to some extent (Kumar and Adams[22]). More sophisticated models are obtained by taking into account not only the irradiation dose, but also the dose rate.[23] However, the stability of the sample also depends on the geometry; thicker, larger samples that are only partially illuminated are able to spread the heat.[21] Good contact to the substrate allows for better electrical and thermal transport away from the irradiated area. Furthermore, sputter-coating with a nanometer-thick carbon film and cooling of the specimen enhances this effect.[24] Other authors attribute the positive influence of carbon-coatings to diminished diffusion of split-off peripheral atoms, thus recombining more likely in the original configuration.[25] In addition to this unclarity, the

degradation process itself is not fully characterized by the decay of diffraction intensities. As changes in electrical conductivity, thermal expansion coefficients, and strain properties in polymers indicate, microscopic rearrangements take place that might be not fully correlated to the overall diffraction intensities.[22] Nevertheless, the determination of diffraction decay is an admissible indicator for the loss of basic material parameters. For samples with anisotropic topography, an individual behavior in degradation dynamics is expected. This is particularly true for films that strongly vary in thickness, as the critical electron exposure is roughly proportional to the thickness of the specimen.[26]

Based on the investigations performed for the PFP films grown in this study, reliable imaging conditions for the organic material were defined, which were used for the subsequent analysis.

Data from AFM, XRD, and TEM are in agreement, confirming the (100) orientation of PFP on SiO_2. Furthermore, the monocrystallinity and molecular arrangement of single fibers is demonstrated by correlating real and reciprocal space information available in a TEM.

II. EXPERIMENTAL

All PFP films were grown onto (100)-oriented silicon wafers covered by a native oxide layer. The samples were cleaned by rinsing in absolute ethyl alcohol and acetone, followed by heating at 475 K after transfer into the vacuum system. To provide electron transparent samples, the wafers had been thinned by dimpling and ion milling until a defined hole with a diameter of about 10 μm was obtained prior to the transfer into the vacuum system. The PFP (Kanto Denka Kogyo Co., Ltd.) thin films were prepared under high vacuum conditions (base pressure $\leq 10^{-8}$ mbar) by organic molecular beam deposition (OMBD) from a resistively heated Knudsen cell at typical deposition rates of 6 Å/min as determined by a quartz-crystal microbalance. The sample surface temperatures were controlled with a K-type thermocouple attached to the sample holder. JEOL 2100-Cryo and JEOL 3010-UHR transmission electron microscopes at acceleration voltages between 100 and 300 kV were used to acquire the electron micrographs and micro-spot diffraction patterns. The TEM samples were cooled to a temperature of 90 K during the investigations to minimize the radiation damage caused by the electron beam. These data were completed by *ex situ* measurements of the morphology and crystallography of the PFP films. The film morphology was characterized by AFM (Agilent SPM 5500) operated in tapping mode at ambient conditions, whereas the average crystalline orientation of the films was determined from XRD data acquired with a diffractometer (Panalytical X'Pert Pro) using Cu $K\alpha$ radiation ($\lambda = 1.5405$ Å) and a PiXcel detector.

III. RESULTS

The paper is organized as follows: first we describe investigations on the electron radiation damage of the PFP films used for this study. From these experiments, experimental conditions in the TEM were derived, which were used for the subsequent investigations of the morphology and structure of PFP films deposited onto SiO_2 substrates under different conditions.

A. Beam damage

To optimize imaging conditions for the PFP films investigated, the acceleration voltages of the various microscopes were varied in a range between 100 kV and 300 kV. Moreover, the sample temperature during the TEM measurements was varied between liquid nitrogen and room temperature. For each set of conditions, diffraction as well as image data was acquired and the time was measured, after which the crystalline structure of the PFP films was destroyed. For this information, the disappearance of crystalline Bragg reflections was used. Figure 1 shows a series of electron diffraction patterns taken under low-dose conditions, exhibiting the typical decay of diffraction intensity. The intensity in the Bragg reflections vanishes with time, whereas the spots remain at their respective positions, indicating that the crystal structure of the undisturbed material stays unchanged. The disappearance of the Bragg reflections is, of course, also a strong function of the electron density as well as of the sample parameters, as summarized in the introduction above.

By comparison, a sequence of consecutive dark-field images is shown in Fig. 2. Two effects are superimposed; in addition to the slow degradation (indicated by the decrease of overall intensity), the strongly diffracting areas seem to gradually move in certain directions (see markers in Fig. 2). This second effect can be attributed to a small bending of the fibers because of heat transferred into the material during electron irradiation or because of strain generated as a result of expansion during the amorphization process. This bending results in the non-fulfillment of Bragg-conditions for selected sample regions and hence a darker contrast in dark-field images.

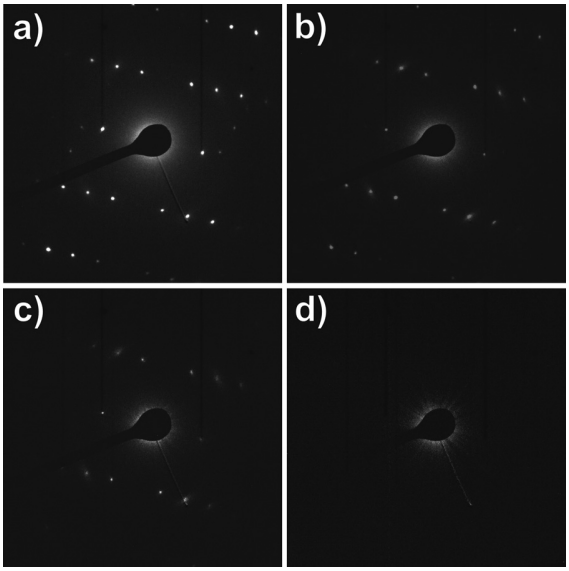

FIG. 1. Electron diffraction patterns showing the stepwise degradation of a PFP film in (100) orientation (cooled to liquid-nitrogen temperatures, 300-kV acceleration voltage): (a) initial image, (b) after about 80 s, (c) irradiated for a total time of ~120 s, and (d) no spots are visible after ~160 s.

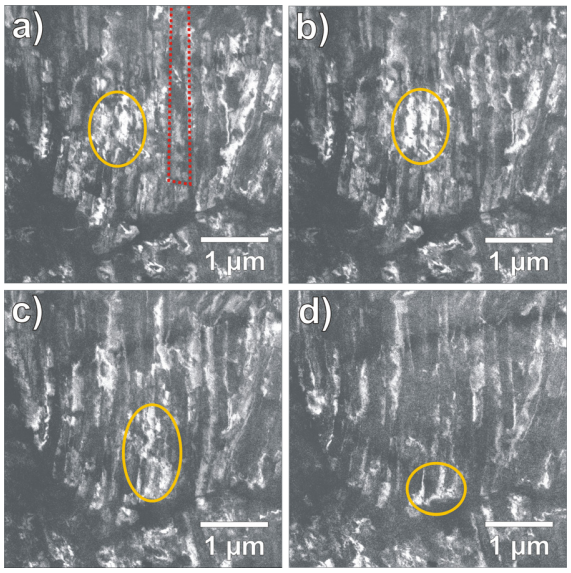

FIG. 2. (Color online) Sequential dark-field images of PFP fibers (contour of one fiber schematically marked in (a). As time passes, the location of strong diffraction contrast (e.g., marker) drifts (a) to (d). Simultaneously, the integrated intensity decreases during the ~2 min of irradiation by 200 keV electrons between (a) and (d).

We conducted systematic experiments to determine the influence of the electron energy and the sample temperature on the stability. The time depicted in Fig. 3 is the duration for which Bragg reflections could be observed by the naked eye (i.e., minimum contrast in the range of 5%). Because of the reasons given in the introduction, which explain that critical dose rates for destruction of the material depend on several conditions, and because of the lack of a (screened) Faraday cup (which is crucial to reliably determine the current density), the dose rate in Fig. 3 is given in arbitrary units and not in units of $e/Å^2$ (as a very rough estimate the critical dose was evaluated to be around 100 $e/Å^2$). Despite the errors that arose with this method (sample thickness dependence, etc.), a clear trend can be observed: Lower sample temperatures and, more interestingly, higher electron energies enhance the stability. Hence, the reduction in effective cross section is more important than the higher kinetic energy of the electrons. This result holds for a destruction mechanism by separating peripheral atoms.[25]

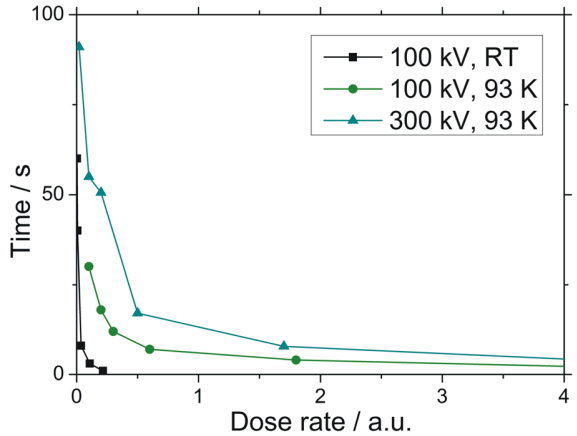

FIG. 3. (Color online) Stability of PFP during electron irradiation for different acceleration voltages and sample temperatures.

Following this study, the investigations summarized in the remainder of this paper were carried out under low-dose conditions at acceleration voltages of 200 kV and 300 kV, respectively, and at liquid-nitrogen sample temperature.

To complement this characterization and to also study the impact of radiation exposure on the morphology of the PFP films, a series of AFM data was taken before and after the TEM measurements. As shown in Fig. 4 the morphological motif of the film remains the same, but the spicular islands show a pitted surface after the electron irradiation, whereas they had been rather smooth before. This finding is in agreement with high-resolution investigations of various organic crystals, including polycyclic compounds.[26] The irradiation damage seems to occur and progress inhomogeneously; the compound degrades pointwise. While the damaged areas spread, the surrounding material stays crystalline until it is reached by the expanding amorphous regions.

B. PFP film morphology and crystallinity

PFP films that are grown on silicon dioxide consist of spicular islands as shown in Fig. 5. Upon room-temperature deposition, these fibers exhibit typical sizes of about 1 μm×150 nm. Though some neighboring fibers reveal a parallel alignment, the islands are azimuthally isotropic distributed on the amorphous substrate, yielding a typical film roughness (rms) of 5.47 nm for 30-nm films. Nevertheless, the fibers exhibit a pronounced texturing that is evidenced by corresponding x-ray diffraction data shown in Fig. 5(e). The $\theta/2\theta$ scan reveals distinct peaks at 5.65°, 11.32°, 16.99°, and 22.7° that correspond well to the (h00) peaks of the PFP bulk lattice,[19] consequently proving the expected (100) orientation of PFP islands as observed before by Kowarik *et al.*[20] By raising the substrate temperature during deposition to 343 K, the crystallites become distinctly larger and reach lateral dimensions of up to 6 μm × 400 nm (cf. Fig. 5(c)). This ripening effect is attributed to the enhanced diffusion of the molecules at the higher substrate temperature. On the

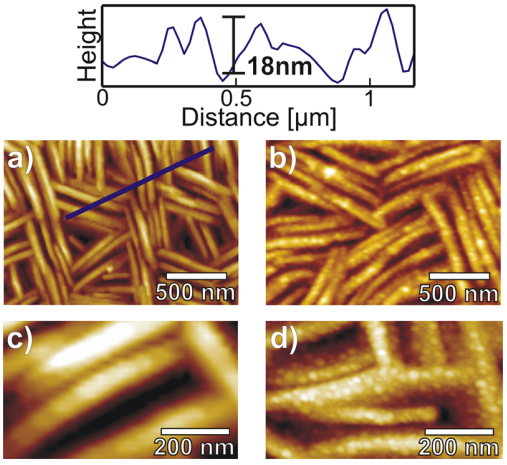

FIG. 4. (Color online) Comparison of AFM micrographs of a 30-nm PFP film grown onto a dimpled SiO_2 substrate before (lhs) and after (rhs) TEM measurements.

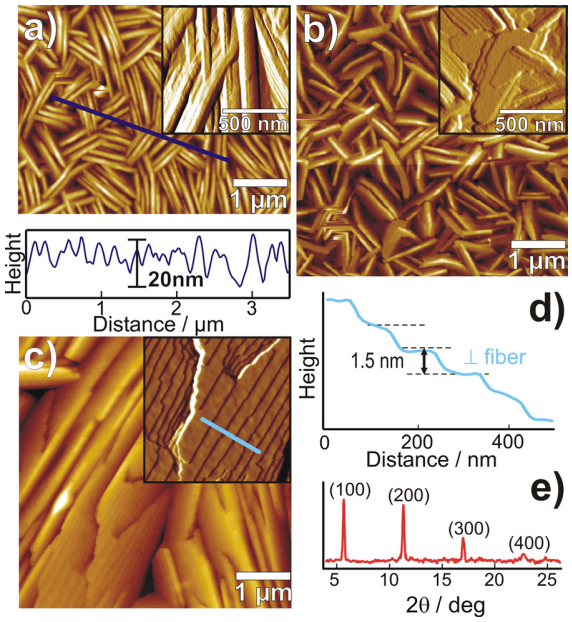

FIG. 5. (Color online) AFM micrographs showing the morphology of 30-nm PFP films on SiO_2: (a) grown at 300 K, (b) after subsequent heating at 343 K for 17 h, (c) grown at 343 K, together with (d) corresponding line-scan. The insets reveal amplitude images of a zoomed area and panel (e) shows a $\theta/2\theta$ x-ray scan of sample (a).

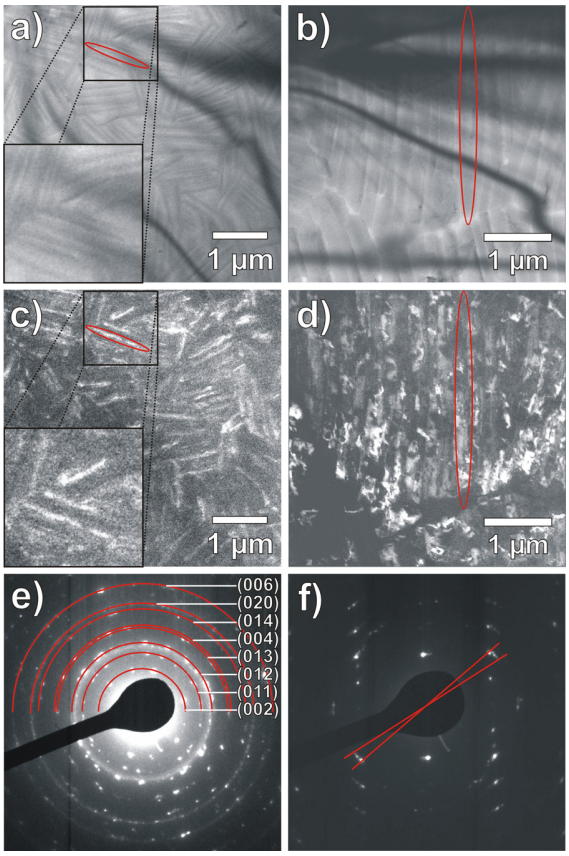

FIG. 6. (Color online) Bright-field (a) and (b), and dark-field (c) and (d) images for substrate temperatures of 300 K (a) and (c). and 343 K (b) and (d), respectively. The dark lines in the bright-field images are bending countours in the silicon substrates. In (e) a diffraction pattern of a ~10-μm sized area of (b) is shown, in (f) a diffraction pattern of the same film is shown, but from an area of ~1 μm in diameter.

extended fibers, individual monomolecular steps with a height of 1.5 nm have been clearly resolved in the AFM data (see Fig. 5(d)), which are in close agreement with (100) interlayer spacing of PFP, thus reflecting the upright orientation of PFP molecules on silicon dioxide. Interestingly, a ripening of the fibers could not be achieved by post-deposition annealing of films that were grown at room temperature. Instead, the size of the fibers almost remains constant whereas some areas of the film smooth out, leading to larger plateaus with molecular evenness as depicted in Fig. 5(b).

TEM bright-field images (Figs. 6(a) and 6(b)) show the same spicular ordering of the PFP fibers as concluded from the AFM data. Several fibers have been marked in the respective bright-field images for clarity. The crystalline PFP needles arrange themselves in bundles, where the single fibers lie parallel to each other. The dimension of the bundles as well as of the single fibers increases with increasing deposition temperature from 300 K to 343 K. Diffractograms of 10-μm sized areas show a polycrystalline structure (Fig. 6(e)), whereas small areas (about 1 μm in diameter), which contain only a few parallel fibers, give rise to monocrystalline diffraction patterns (Fig. 6(f)). From the width of the Bragg reflections in Fig. 6(f) it can be concluded that neighboring fibers in the bundles have the same orientation with an angular deviation less than 10°. Both diffraction patterns support a (100) orientation of the PFP films, as will be shown in Fig. 7. For the dark-field micrographs 7(c) and 7(d) an objective aperture diameter was chosen that led to imaging with several spots. The dark-field images indicate that the fibers are monocrystalline at both deposition temperatures with a significant amount of lattice plane bending along the single fibers, which results in inhomogeneous dark-field contrast along the fibers. This can be seen more clearly from enlargements of selected regions of Figs. 6(a) and 6(c), respectively.

To address the crystalline orientation of single fibers, microspot diffraction was carried out. In Fig. 7, two diffraction patterns are shown exemplarily and correlated to the corresponding bright-field images. These spot diffraction patterns prove that the single needles are monocrystalline. The diffraction patterns were simulated using the software package JEMS,[28] and the bulk phase of PFP,[19] as a structure input. The best fit between the experimental images and theoretical models was obtained for a (100) orientation of the PFP crystal, as already observed in an XRD study carried out by Kowarik *et al.*[20] for films deposited under similar conditions and supported by XRD measurements presented in this work. The diffraction pattern shown in Fig. 7(a) is indexed with the reflections of this orientation. In the two bright-field images the strong contrast results again from bending of the silicon substrate used. The contrast of the PFP film investigated is much weaker. For clarity, the long axes of the fibers are marked with broken lines in each bright-field image and the arrows indicate the sideways boundaries. The orientation of the real and reciprocal space images is the same and the broken lines in the diffraction patterns show the needle orientation of the bright fields as a guide to the eye. A

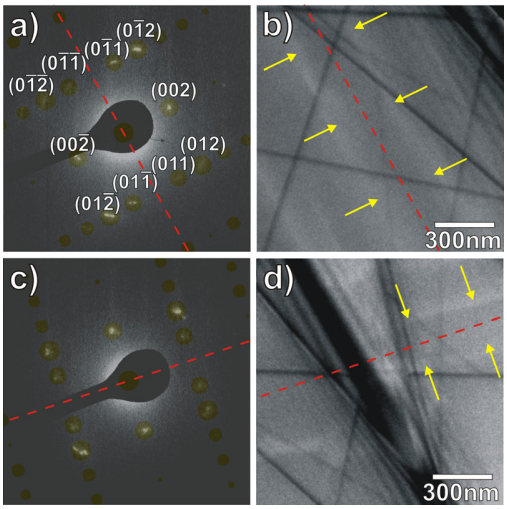

FIG. 7. (Color online) Two examples of the orientation relation of fibers and corresponding diffration patterns. The fibers are monocrystalline with constant orientation of the molecules. The broken lines indicate the direction and the arrows the boundaries of the fibers in the bright-field images (b) and (d). A parallel line is sketched in the respective diffraction patterns (a) and (c) as a guide to the eye and the transparent spots mark the locations of the simulated Bragg reflections using bulk phase data. The dark lines in (b) and (d) are bent contours from the silicon substrate.

correlation reveals that the (010) direction of the PFP crystal is always oriented along the long axis of the fibers, whereas the sideways boundaries are always parallel to the (001) planes. This orientation relationship has been found for all fibers investigated.

The results of the TEM investigations on the crystalline structure of the PFP fibers on SiO_2 substrates are summarized in Fig. 8. Note that the presented visualization of the molecular arrangement in PFP films corresponds to a rectangular unit cell. As the PFP unit cell is monoclinic, this visualization is not completely correct. Because the angle

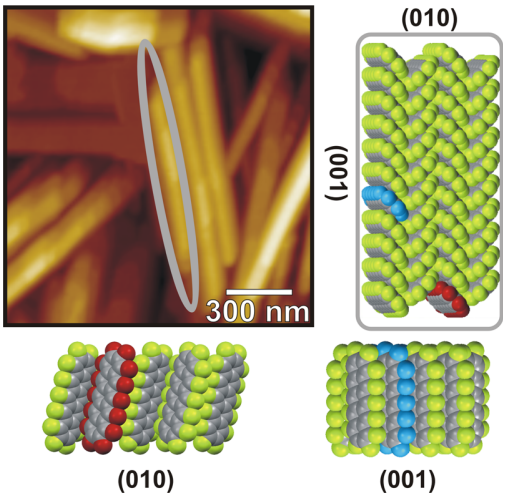

FIG. 8. (Color online) Schematic model of the crystalline orientation of the PFP fibers on SiO_2 derived from the present TEM data. The marked molecules show the difference in the effective contact area for (010) and (001) planes that could explain the shape of the needles. Note that the presented visualization of the molecular arrangement in PFP films corresponds to a rectangular unit cell. As the monoclinic angle of the PFP phases is very close to 90°, we decided to use this visualization for reasons of simplicity.

between planes (001)/(010) and (100) is 91.56° (90.4° in thin-film phase) we decided to use this visualization for reasons of simplicity. The needles have a distinct shape anisotropy with a long/short axis length-ratio in the range of 10. TEM as well as XRD data agree on the upright orientation of the PFP molecules on the surface resulting in the (100) plane of the PFP bulk phase being parallel to the Si/SiO_2 surface. A comparison of TEM diffraction with real space data confirms that the molecular arrangement in the needles is identical for all samples under investigation. The close-packed (001) planes of the PFP crystal form the sidewall of the needles, whereas the (010) plane is perpendicular to the long axis of the needles. This structure is probably favored by the large effective contact area of the stacked molecules in (010) direction compared to the small interaction area of molecules that attach to the (001) planes to form a new row (see the molecules marked in Fig. 8). This conclusion is supported by the fact that this ordering is also observed for PFP on sodium fluoride.[29]

For PFP films on other anorganic substrates, dewetting accompanied by the formation of undercut structures has been observed.[29] To address this, intensity scans perpendicular to the fibers in TEM dark-field images were performed. Under certain tilting conditions (two-beam case) and up to a maximum film thickness—which is for C-based compounds above 100 nm—the dark-field intensity increases linearly with sample thickness. In Fig. 9, a linescan across a dark-field image of PFP deposited at 343 K is shown. One observes an increasing intensity from the edge to the center of a fiber bundle. This intensity increase corresponds to the stepped profile already observed in the AFM scans, thus indicating the absence of voids underneath the surface of the PFP film. Consequently, PFP on SiO_2 wets the surface and a filled triangular structure is established for the deposition conditions used.

IV. SUMMARY

In summary, the morphology and crystalline structure of PFP films on silicon dioxide substrates were examined using a correlation of AFM, XRD, and TEM data. For the latter, imaging conditions, which minimize the radiation damage that destroys the organic material were determined and used afterward; PFP is shown to grow as monocrystalline spicular fibers on amorphous silicon dioxide with parallel needles arranging to larger bundles. Single fibers are rotated with

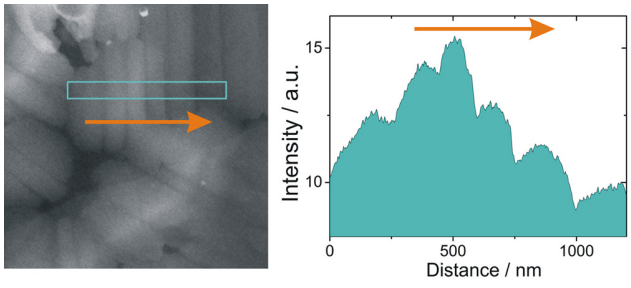

FIG. 9. (Color online) Intensity-scan perpendicular to the PFP fibers (grown at 343 K).

respect to each other around their azimuth. The PFP orientation has been determined by microspot electron diffraction in agreement with XRD to be (100) orientation. Correlation of real space micrographs and diffraction patterns revealed the crystallographic structure of the fibers; their long axis is oriented perpendicular to the (010) planes of the PFP crystal and the sidewise boundaries are formed by the (001) planes of the PFP crystal. This general orientation might arise during growth because of the large interaction area for a PFP molecule with the preexisting fiber when attached to the end of the needle on a (010) plane compared to the almost freestanding molecule that starts a new row, as it is omnipresent for PFP.

The PFP/SiO_2 system was used as a demonstration of the power of TEM measurements. Through the azimuthally isotropic distribution of PFP needles, the microscopic molecule arrangement could be determined by a combination of imaging and diffraction techniques.

ACKNOWLEDGMENTS

Support of the German Science Foundation (DFG) in the framework of the Heisenberg program (K. Volz) and support by the Friedrich-Ebert-Stiftung (T. Breuer) are gratefully acknowledged. We also thank Professor Uwe Maier (Faculty of Biology, Philipps-University) for the use of the JEOL 2100 TEM, and the Faculty of Chemistry, Department for Crystal Structure Determination, for providing access to the x-ray diffractometer.

[1]Y. Shirota, J. Mater. Chem. **10**, 1 (2000).
[2]C. D. Dimitrakopoulos and P. R. L. Malenfant, Adv. Mater. **14**, 2 (2002).
[3]S. R. Forrest, Nature **428**, 911 (2004).
[4]G. Hadziioannou and G. G. Malliaras, *Semiconducting Polymers*, Vol. 1 (Wiley VCH, Berlin, 2007).
[5]Z. Bao and J. Locklin, *Organic Field-Effect Transistors* (CRC Press, Boca Raton, 2007).
[6]N. Karl, Synth. Met. **133**, 649 (2003).
[7]J. E. Anthony, Chem. Rev. **106**, 5028 (2006).
[8]N. Karl, in *Organic Electronic Materials*, edited by R. Farchioni and G. Grosso (Springer, Berlin, 2001).
[9]J. Cornil, J. P. Calbert, and J. L. Bredas, J. Am. Chem. Soc. **123**, 1250 (2001).
[10]G. Witte and Ch. Wöll, J. Mater. Res. **19**, 7 (2004).
[11]F. Schreiber, Phys. Status Solidi A **201**, 1037 (2004).
[12]C. Riekel, Rep. Prog. Phys. **63**, 233 (2000).
[13]M. A. Marcus, A. A. MacDowell, R. Celestre, A. Manceau, T. Miller, H. A. Padmorea, and R. E. Subletta, J. Synchrotron Radiat. **11**, 239 (2004).
[14]T. Minakata, H. Imai, M. Ozaki, and K. Saco, J. Appl. Phys. **72**, 5220 (1992).
[15]L. F. Drummy, P. K. Miska, and D. C. Martin, J. Mater. Sci. **39**, 4465 (2004).
[16]D. C. Martin, J. Chen, J. Yang, L. F. Drummy, and Ch. Kübel, J. Polym. Sci., Part B: Polym. Phys. **43**, 1749 (2005).
[17]H. Qian, M. Malac, and R. F. Egerton, Philos. Mag. **87**, 253 (2007).
[18]Y. Murakami, S. Tomiya, N. Koshitani, Y. Kudo, K. Satori, M. Itabashi, N. Kobayashi, and K. Nomoto, Phys. Rev. Lett. **103**, 146102 (2009).
[19]Y. Sakamoto, T. Suzuki, M. Kobayashi, Y. Gao, Y. Fukai, Y. Inoue, F. Sato, and S. Tokito, J. Am. Chem. Soc. **126**, 8138 (2004).
[20]S. Kowarik, A. Gerlach, A. Hinderhofer, S. Milita, F. Borgatti, F. Zontone, T. Suzuki, F. Biscarini, and F. Schreiber, Rapid Res. Lett. **2**, 120 (2008).
[21]U. Kolb, T. E. Gorelik, E. Mugnaioli, and A. Stewart, Polym. Rev. **50**, 385 (2010).
[22]S. Kumar and W. W. Adams, Polymer **31**, 15 (1990).
[23]J. R. Fryer, Ultramicroscopy **23**, 321 (1987).
[24]S. M. Salih and V. E. Cosslett, Philos. Mag. **30**, 225 (1974).
[25]J. R. Fryer and F. Holland, Ultramicroscopy **11**, 67 (1983).
[26]J. R. Fryer, Ultramicroscopy **14**, 227 (1984).
[27]I. Salzmann, S. Duhm, G. Heimel, J. P. Rabe, N. Koch, M. Oehzelt, Y. Sakamoto, and T. Suzuki, Langmuir **24**, 7294 (2008).
[28]P. A. Stadelmann, Ultramicroscopy **21**, 131 (1987).
[29]T. Breuer and G. Witte, Phys. Rev. B **83**, 155428 (2011).

5.3 Article III: Interrelation between Substrate Roughness and Thin-Film Structure of Functionalized Acenes on Graphite

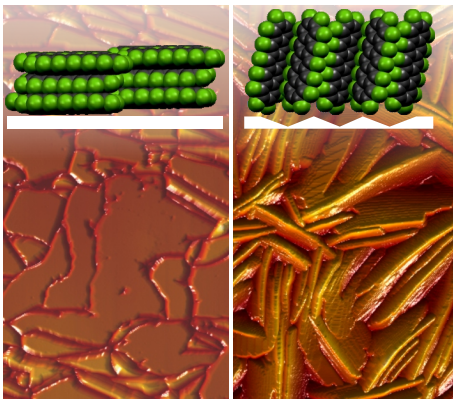

5.3.1 Abstract

Using atomic force microscopy (AFM) and X-ray diffraction (XRD), we analyzed the growth of differently modified pentacenes (perfluoropentacene and pentacenetetrone) on graphite and demonstrate that both the resulting morphology and the crystalline structure of the films critically depend on the microroughness of the substrate. On well-ordered highly oriented pyrolytic graphite (HOPG) surfaces prepared by exfoliation, both molecular materials form exceptionally smooth films, which consist of large-area molecularly flat islands yielding an overall low roughness. Interestingly, in these films molecules adopt a recumbent orientation, while on defective substrates, created by brief ion sputtering, the molecules adopt an upright orientation and form nonconnected islands exhibiting a significantly increased film roughness. Our study not only underlines the possibility to prepare very smooth films on a weakly interacting substrate but also emphasizes the importance of a proper substrate preparation and the significance of precise knowledge of substrate-surface properties to control the resulting structure of organic films.

5.3.2 Methods

Atomic Force Microscopy, Organic Molecular Beam Deposition, Polarized Optical Microscopy, Low Energy Electron Diffraction, X-Ray Diffraction

5.3.3 Own Contribution

I have prepared all samples and conducted the AFM, LEED and Polarized Optical Microscopy measurements, except for the AFM measurement of the post-heated PFP

sample on pristine HOPG (Fig. 5), which was conducted by Antonia Morherr. Jan Götzen has produced some preliminary results. Ingo Salzmann and Martin Oehzelt acquired the XRD data after my request. I prepared the data for publication and wrote the major part of the manuscript, while Ingo Salzmann, Martin Oehzelt, Norbert Koch and Gregor Witte helped to improve it.

CRYSTAL GROWTH & DESIGN

ARTICLE

pubs.acs.org/crystal

Interrelation between Substrate Roughness and Thin-Film Structure of Functionalized Acenes on Graphite

Tobias Breuer,[†] Ingo Salzmann,[‡] Jan Götzen,[†] Martin Oehzelt,[‡] Antonia Morherr,[†] Norbert Koch,[‡] and Gregor Witte*[,†]

[†]Molekulare Festkörperphysik, Philipps-Universität Marburg, D-35032 Marburg, Germany

[‡]Institut für Physik, Humboldt-Universität zu Berlin, D-12489 Berlin, Germany

Supporting Information

ABSTRACT: Using atomic force microscopy (AFM) and X-ray diffraction (XRD), we analyzed the growth of differently modified pentacenes (perfluoropentacene and pentacenetetrone) on graphite and demonstrate that both the resulting morphology and the crystalline structure of the films critically depend on the microroughness of the substrate. On well-ordered highly oriented pyrolytic graphite (HOPG) surfaces prepared by exfoliation, both molecular materials form exceptionally smooth films, which consist of large-area molecularly flat islands yielding an overall low roughness. Interestingly, in these films molecules adopt a recumbent orientation, while on defective substrates, created by brief ion sputtering, the molecules adopt an upright orientation and form nonconnected islands exhibiting a significantly increased film roughness. Our study not only underlines the possibility to prepare very smooth films on a weakly interacting substrate but also emphasizes the importance of a proper substrate preparation and the significance of precise knowledge of substrate-surface properties to control the resulting structure of organic films.

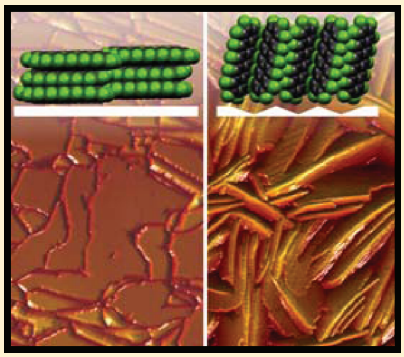

1. INTRODUCTION

Owing to the anisotropic shape of π-conjugated aromatic molecules and the related anisotropic intermolecular interactions, these compounds generally adopt complex packing motifs in the crystalline phase, like, for example, layered stacking and/or herringbone arrangements.[1] These structural features also result in a pronounced anisotropy of electronic and optical properties of organic crystals[2] and crystalline molecular films.[3−6] Therefore, precise control of molecular and crystalline orientation during film growth is inevitable to utilize and explore the remarkable optoelectronic properties of such materials. Moreover, it is also of prime importance for an optimized fabrication of organic thin-film devices. Previous studies have shown that the structure of organic films is mainly governed by a competition between intermolecular and molecule−substrate interactions. On metal substrates, this initially favors a recumbent adsorption geometry of planar π-conjugated molecules, whereas an upright orientation is frequently observed on weakly interacting substrates such as SiO_2.[7] Subsequent molecular film growth on metals is in many cases accompanied by distinct dewetting and island formation,[8−10] while the actual molecular orientation depends critically on the surface roughness. In contrast to molecular films that were grown on well-ordered single-crystalline metal surfaces, the recumbent molecular orientation of the lowermost seed-layer is not retained in multilayer films if grown on polycrystalline metals. There, a preferential upright molecular orientation has been observed for various molecular compounds including diindenoperlyene, phthalocyanines, and pentacene.[11−14] A similar situation was also reported upon growth of sexithiophene films on TiO_2(110), which exhibit distinct needles with recumbent molecular orientation mediated by the substrate, while on poorly ordered surfaces islands with upright-oriented molecules are formed.[15]

Previously, we have shown that particularly smooth pentacene films can be grown on graphite exhibiting molecularly flat islands, which extend over several micrometers.[16] Despite a rather weak molecule−graphite interaction,[17] the molecules adopt a recumbent orientation in such films, which is caused by a prealignment in the initial stage of film growth due to a perfect match between the molecular carbon frame and the surface lattice of the graphite basal plane.[16] Moreover, it could be demonstrated that the weak substrate interaction allows a small molecular reorientation in the lowermost layer and thus a relief of strain caused by the structural misfit between the molecular arrangement in the physisorbed wetting layer and the crystalline bulk phase. Finally, it was found that this particular growth mode depends sensitively on the surface quality since a quite different growth scenario occurs on defective surface regions where pentacene forms islands with upright molecular orientation.

Here, we report a comparative growth study of the two chemically modified pentacene derivatives perfluoropentacene (PFP) and 5,7,12,14-pentacenetetrone (PTET). Though both molecules are planar, they exhibit dissimilar crystal structures,[18,19] which is related

Received: July 14, 2011
Revised: September 6, 2011
Published: September 15, 2011

to distinct differences in the intramolecular charge distributions. This poses the question about the general ability of graphite to control the molecular orientation in adsorbed thin films. Combining atomic force microscopy (AFM) and X-ray diffraction (XRD) measurements, we demonstrate that, indeed, long-range ordered and exceedingly smooth films with recumbent molecular orientation can be prepared also for such functionalized acenes and that the resulting film structure depends critically on the roughness of the substrate surface. While PTET exhibits the known crystalline bulk phase,[19] PFP films adopt a new polymorph, which had been found previously also for PFP films that were deposited onto Ag(111) surfaces.[20] In contrast to this finding for pristine exfoliated highly oriented pyrolytic graphite (HOPG), on microscopically rough graphite substrates prepared by brief sputtering both materials grow in their respective bulk phases and exhibit upright molecular orientations.

2. EXPERIMENTAL SECTION

All molecular films were grown onto ZYA-grade highly oriented pyrolytic graphite (HOPG) substrates (SPI supplies, mosaicity < 0.4°), which, in each case, were prepared by exfoliation in air before loading into the ultra-high vacuum (UHV) chamber. Particular care was taken to avoid graphite flakes sticking out of the sample, which easily can adhere to the AFM tip by sleeking the cleaved surfaces. The graphite substrates were mounted onto sample holders either by conductive adhesion tape (Plano) or by metal clips, which also enable sample heating prior to deposition. To investigate the influence of surface roughness on the molecular film growth, some of the cleaved HOPG substrates were intentionally modified by Ar^+-sputtering (E = 700 eV, I = 5 μA), and the resulting surface ordering was monitored by low energy electron diffraction (LEED).

PFP (Kanto Denka Kogoyo Co. LTD) and PTET (Avocado Organics) films were deposited under high vacuum conditions (base pressure < 5×10^{-9} mbar) by organic molecular beam deposition from alumina crucibles of a resistively heated Knudsen cell at deposition rates of 6 Å/min monitored by quartz crystal microbalance.

The morphology of the various films was characterized at ambient conditions by means of atomic force microscopy (AFM, Agilent SPM 5500) operated in tapping mode at cantilever frequencies of about 300 kHz. The XRD measurements were carried out under He atmosphere at the W1 beamline at DESY-HASYLAB (Hamburg). Optical microscopy in combination with a linear polarizer was employed to obtain complementary information about the lateral size of the crystallites within the films.

3. RESULTS

3.1. PFP and PTET Films on Pristine Graphite. Figure 1 compares the morphology and crystalline orientation of PFP and PTET films with a nominal thickness of 50 nm that were deposited at room temperature onto freshly cleaved HOPG substrates. AFM data show that films of both materials consist of compact and densely packed mesa-like islands extending over several micrometers that are separated by deep and narrow trenches. High resolution AFM images yield a roughness of less than 0.2 nm for the individual island surfaces (cf. magnified line scans in Figure 1b,f), thus indicating that the islands appear to be molecularly flat. Only in the case of PTET some islands reveal characteristic depressions with a depth of about 20 nm on the otherwise flat islands (indicated by black arrows in the inset of Figure 1e). A quantitative analysis yields highly uniform island heights, thus demonstrating overall very smooth organic films. This is remarkable since previous studies have revealed a substantial roughness for PFP films grown onto SiO_2 or Ag(111) substrates.[21,10]

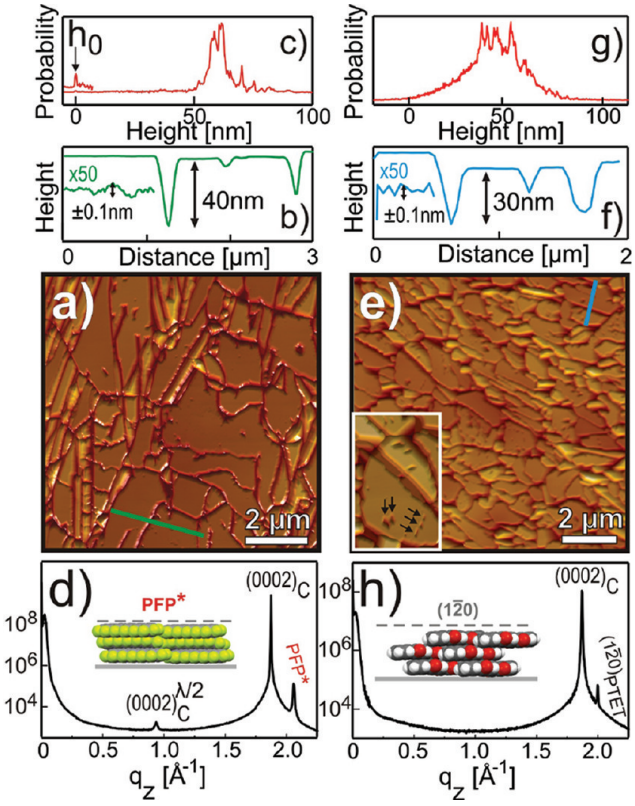

Figure 1. Comparison of PFP (lhs) and PTET films (rhs) of nominal thickness of 50 nm grown at room temperature onto freshly cleaved HOPG substrates: (a, e) AFM micrographs together with corresponding line scans and height distributions (b, c, f, g). Corresponding specular XRD-data are shown in panels (d, h) and the resulting molecular arrangements are sketched in the respective insets.

Using specular X-ray diffraction, the crystalline orientation of the molecular films was identified. Typical XRD results are depicted in Figure 1d,h and exhibit a dominating substrate related C(0002) diffraction peak at q_z = 1.87 Å^{-1} (corresponding to an interlayer spacing of the graphite basal planes of 3.36 Å). For the PTET film, an additional diffraction peak appears at q_z = 2.00 Å^{-1} (cf. Figure 1h). With a corresponding lattice plane distance of 3.142 Å, this peak can be unambiguously identified as (1 $\bar{2}$ 0) peak of the PTET bulk structure,[19] thus reflecting a recumbent molecular orientation in such films as sketched in the inset of Figure 1h.

In addition to the C(0002) substrate reflection, the diffractogram of the PFP film (shown in Figure 1d) reveals two further peaks at q_z = 0.937 Å^{-1} and q_z = 2.06 Å^{-1}. While the first is assigned to the $\lambda/2$ contribution of the substrate reflection, which is visible here due to a significantly larger thickness of the HOPG crystal used in this experiment, the peak at higher momentum transfer is assigned to PFP. It corresponds to a lattice spacing of 3.05 Å, which does not match any reflection of the PFP bulk structure[18] or the PFP thin-film phase,[22] which therefore demonstrates the presence of a new surface-mediated PFP polymorph that was already reported for Ag(111) substrates.[20] Note that there a PFP herringbone structure of (inclined) lying molecules could be deduced from XRD and photoemission data for this specific polymorph.

Though AFM data reveal the presence of very smooth islands, their lateral crystalline ordering, especially the size of single-crystalline

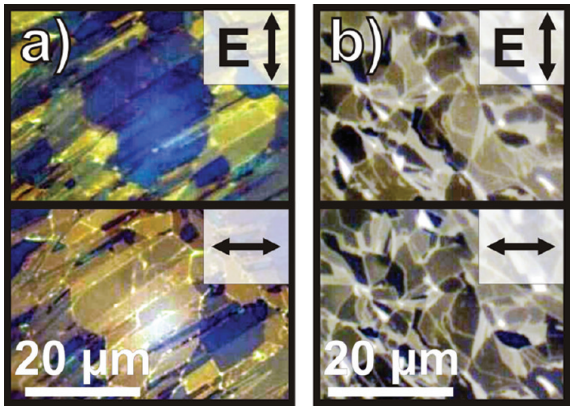

Figure 2. Polarization microscopy micrographs of (a) PFP and (b) PTET films with a nominal thickness of 50 nm grown at 325 K on pristine HOPG substrates that were recorded with linearly polarized light at different orientations as indicated by the black arrow.

regions, cannot be concluded directly because rotational domains within the islands are still possible. Similarly, the XRD Θ/2Θ scans clearly prove the crystallinity of the films but cannot judge the lateral single-crystallinity of the individual islands. Since the various optical excitations of aromatic molecules like PFP have differently oriented transition dipole moments,[6] the color appearance of the islands observed by polarization microscopy can be used to obtain complementary information about the domain size. Figure 2 displays a series of optical micrographs of PFP and PTET films taken for linear polarized light with different angles of polarization. In order to increase the size of individual islands, the films had actually been deposited at a slightly higher substrate temperature of 325 K, which yields island diameters of more than 10 μm. While the islands appear azimuthally distributed due to the polycrystallinity of the HOPG substrate, they exhibit a rather homogeneous polarization contrast within the individual islands, thus reflecting their homogeneous crystalline structure.

3.2. PFP and PTET Film Growth on Defective Graphite Surfaces. In a previous study, it was reported that the resulting morphology and crystalline orientation of pentacene films grown on HOPG depend sensitively on the actual surface roughness.[16] Therefore, we have also investigated the structure of PFP and PTET films grown onto graphite substrates, which had been intentionally roughened by sputtering. To analyze the influence of such a treatment, first of all the quality of the graphite surface and its degradation upon sputtering were characterized by means of AFM and LEED. Figure 3a,b compares two AFM micrographs that were taken at the same position of a HOPG substrate before and after Ar^+-ion sputtering (5 min, 700 eV). An inspection of these images shows that the morphology does not change dramatically. The general morphology remains unchanged, while a significant increase of surface roughness occurs. Please note that the depicted image must not be misinterpreted as a real image of atomic defects, as the resolution of the AFM is too low to resolve those defects directly. However, the increased roughness (rms of the sputtered substrate 0.17 nm compared to 0.061 nm of the defect-free surface) is a clear indication of degrading substrate quality. This finding is supported as a rapid degradation of the substrate LEED pattern with sputtering time was observed. The LEED pattern of the pristine HOPG surface prepared by exfoliation reveals a characteristic ring pattern, which reflects its

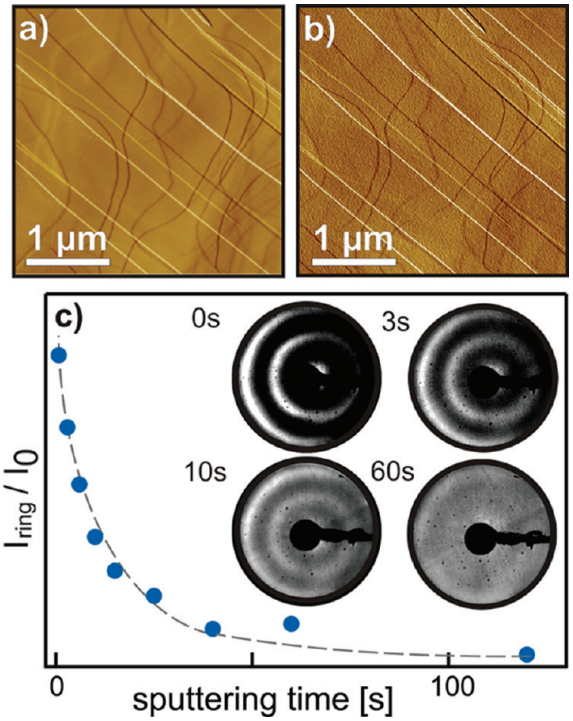

Figure 3. Surface degradation of an exfoliated HOPG surface upon subsequent Ar^+-ion sputtering (700 eV). AFM micrographs recorded (a) before and (b) after 2 min of sputtering reveals enhanced substrate roughness; electron diffraction (c) reveals a rapid disappearance of the substrate LEED pattern (E = 180 eV) as a function of the sputtering time.

high local ordering but azimuthal isotropy of the graphite flakes within the surface. Figure 3c depicts the diffraction ring to background intensity ratio, which becomes halved already after bombardment times of only 6 s, while after 2 min the ring pattern was no longer visible thus indicating severe damaging of the surface lattice. From this characterization, we conclude that room temperature sputtering essentially creates point defects, which destroy the coherence of the graphite surface lattice but does not increase the step density.

Figure 4 compares the resulting morphology and crystalline orientation of PFP and PTET films that were grown on HOPG substrates, which had been sputtered for 5 min prior to deposition. Rather different film structures are observed, which is strikingly illustrated by the AFM data recorded for a 50 nm PFP film depicted in Figure 4a−c. Instead of a smooth layer, the film consists of elongated spicular islands with a length of several micrometers and a width of 100−300 nm, that are laterally isotropically distributed along the sample yielding an overall large roughness of more than 20 nm. This morphology parallels the situation observed before for PFP films grown onto SiO_2.[21] Like in that case, characteristic steps of about 1.5 nm were identified (cf. line scan Figure 4b), which is in close agreement with the interlayer distance of (100)-planes, hence indicating an upright molecular orientation. To verify if this locally observed orientation is characteristic for the entire sample, XRD measurements were carried out for this sample. The corresponding XRD scan that is shown in Figure 4d reveals beside the (0002) diffraction peak of the substrate (at q_z = 1.873 Å^{-1}) three PFP-related peaks at q_z = 0.401 Å^{-1}, q_z = 0.805 Å^{-1}, and q_z = 1.208 Å^{-1}. These peak positions are in excellent agreement with the (n00)-reflexes of

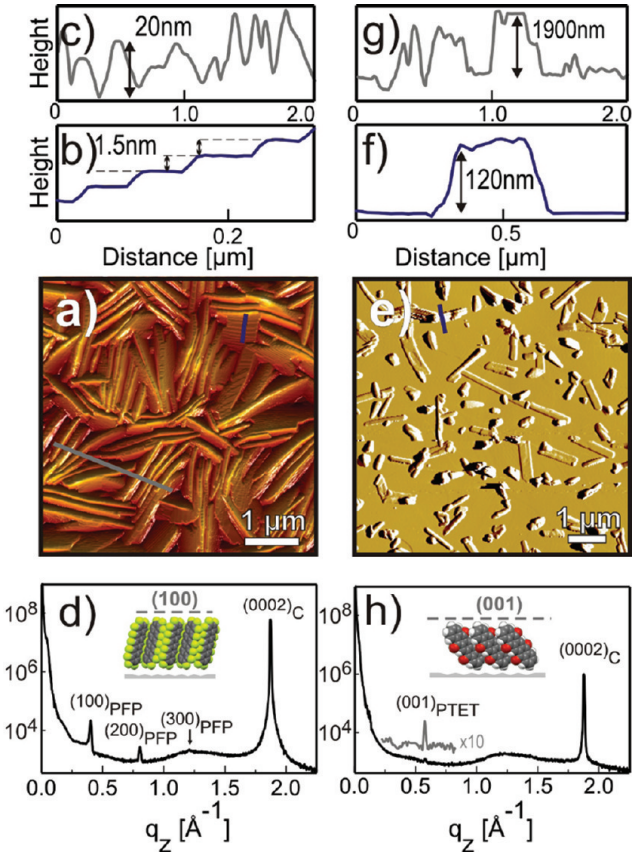

Figure 4. Morphology and crystalline structure of PFP (lhs) and PTET films (rhs) grown on HOPG substrates that were intentionally roughened by brief Ar^+ sputtering (5 min): (a) AFM micrograph of a 50 nm PFP film with (b, c) corresponding line scans, and (e) AFM micrograph (amplitude image) of a nominal 3 nm PTET film with (f) corresponding topographical line scan while (g) reveals a line scan of a 50 nm PTET film, which could not be imaged properly. Accompanying specular XRD scans are shown in panels (d) for a 50 nm PFP film and (h) for a 50 nm PTET film. The molecular orientations in the films are sketched in the insets.

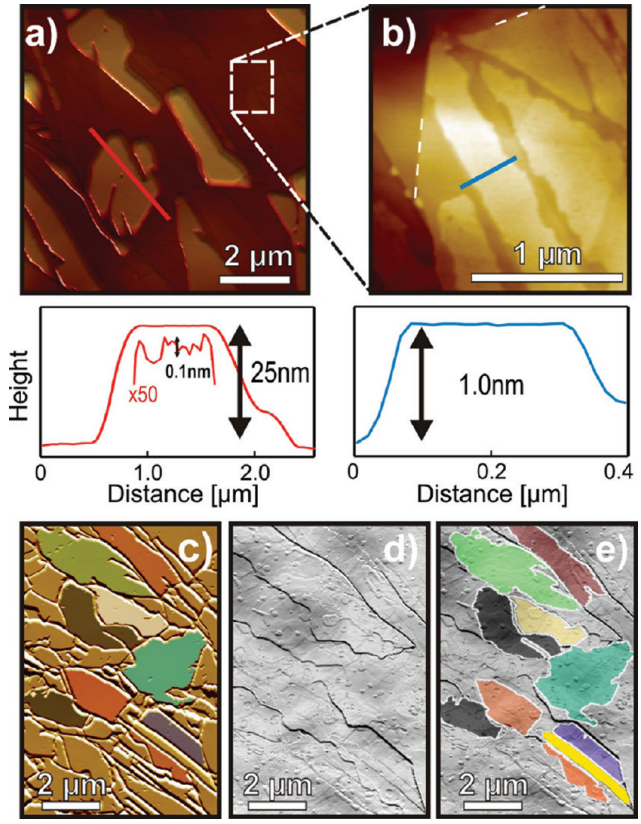

Figure 5. AFM micrograph showing the morphology of 5 nm PFP deposited (a) on pristine HOPG together with (b) magnified image and corresponding line scans. Panels (c–e) show a comparison of a 40 nm PFP film deposited on pristine HOPG and (d) the bare surface after thermal desorption of the film. In panel (e) tagged islands from (c) are superimposed onto the bare surface.

the PFP-thin film phase[22] ($q_{z,(100)}$ = 0.399 Å^{-1}, $q_{z,(200)}$ = 0.797 Å^{-1}, $q_{z,(300)}$ = 1.196 Å^{-1}), thus proving an overall upright orientation of PFP molecules on the sputtered HOPG substrate.

Supporting XRD reciprocal space mapping experiments of this film confirmed that on the rough substrate molecules actually crystallize only in this polymorph — instead of the PFP single-crystal phase[18] or the new polymorph observed for the case of pristine HOPG (data shown in Supporting Information).

Likewise, a strikingly different morphology was also observed for PTET films that were deposited onto sputtered HOPG substrates. In that case a pronounced dewetting takes place and leads to the formation of extremely elevated islands exceeding even a height of 2 μm at a nominal film thickness of 50 nm (cf. line scan Figure 4g), which, however, impeded the acquisition of satisfying AFM images. Therefore, the morphology of much thinner films was characterized. Figure 4e shows such a typical amplitude AFM image of a PTET film with a nominal thickness of 3 nm, which reveals the presence of elongated mesa-shaped islands with heights of more than 100 nm at widths of about 200 nm. Though the mentioned roughness obviated precise AFM imaging for a 50 nm thick film, XRD scans are, by nature, not affected by this limitation. The corresponding XRD scan (see Figure 4h) reveals in addition to the C(0002) substrate peak a weak but distinct diffraction peak at q_z = 0.576 Å^{-1}. The corresponding lattice spacing of d = 10.91 Å is in good agreement with the (001) lattice spacing of the PTET bulk phase. In this texture, the molecules are rather upright-oriented and their long axis adopts an angle of about 42° with respect to the sample surface, as shown schematically in the inset in Figure 4h.

3.3. Initial Stage of Film Growth. To fathom the influence of the substrate surface structure on molecular film growth and possible limitations of the island sizes additional AFM measurements were carried out for the initial stage of PFP deposition. Figure 5a shows an AFM micrograph of a PFP film with a nominal thickness of 5 nm deposited onto a pristine HOPG substrate. At this initial growth stage rather large mesa-shaped islands with a height of more than 20 nm are formed that reveal molecularly flat surfaces extending over several micrometers. In addition, they are surrounded by distinctly lower and less extended islands exhibiting a height of only 1 nm corresponding to just a few monolayers as shown by the magnified micrograph in Figure 5b. Comparing the shape of such lower islands and the position of substrate steps (cf. dashed line in Figure 5b) suggests that the size of the molecular islands is limited by steps and/or grains of the substrate. To further study this effect AFM was employed to compare the island shape occurring in a 40 nm PFP film with the corresponding morphology of the underlying HOPG

dx.doi.org/10.1021/cg200894y |*Cryst. Growth Des.* 2011, 11, 4996–5001

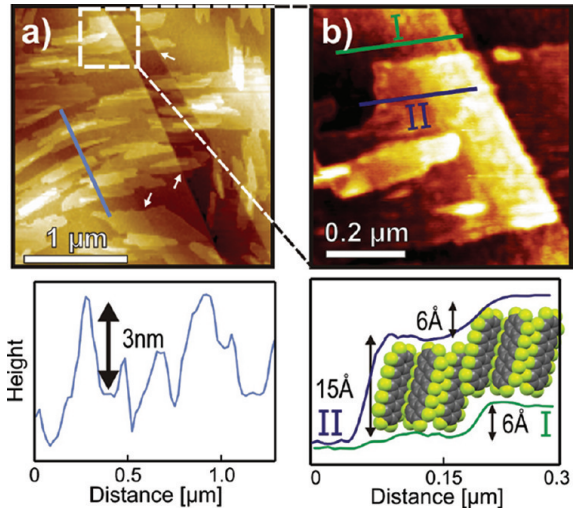

Figure 6. AFM micrographs showing the initial stage of PFP film formation on a sputtered HOPG substrate together with corresponding line scans. The magnified image b) reveals the appearance of a dislocation within the PFP film induced by an underlying substrate double-step.

substrate. For this purpose the PFP film was thermally desorbed in a vacuum chamber by heating the sample at 450 K for 10 min. Figure 5c−e shows the result of this experiment. One can easily verify that the images show the same area of the sample, as characteristic edges can be identified in both cases. Note that the visible edges represent different grain-boundaries. While they reveal a topographic contrast of PFP island-borders within the film (Figure 5c) they represent substrate edges of the bare surface, which are enhanced in the AFM amplitude image shown in Figure 5d. By superimposing the contour of individual islands, which are color tagged in Figure 5c onto the bare HOPG surface of the same position this effect becomes even more explicit (cp. Figure 5d,e). This analysis proves that the island sizes are actually limited by the density of step edges and the grain size of the substrate.

Finally, we investigated the initial growth of PFP films on sputtered HOPG surfaces. In contrast to the growth scenario on pristine HOPG the molecules nucleate in rather small, azimuthally isotropically distributed spicular islands as shown in Figure 6 for a PFP film with a nominal thickness of about 4 nm. The high nucleation density of these islands leads to a rather high coverage of the substrate surface, while thicker films (cf. Figure 4a) exhibit a substantial roughness. The observed islands again show characteristic molecular steps of 1.5 nm, which reflect the upright molecular orientation. Since again substrate steps are clearly observed, their influence on the island growth can be followed. The overview image depicted in Figure 6a exhibits many spicular islands that extend over such substrate steps (indicated by white arrows). A closer inspection (see magnified image in Figure 6b) further reveals that upright-oriented molecules are capable of overgrowing small substrate steps by creating dislocations within the molecular adlayer as illustrated by the corresponding line scans.

4. DISCUSSION

In the present study, we have analyzed the film formation of the pentacene derivatives perfluoropentacene and pentacenetetrone on HOPG substrates with particular emphasis on the influence of substrate roughness.

Previous studies have already shown that organic electronic device properties depend critically on the substrate roughness.[23,24] For instance, the grain size within organic films is affected by the quality of the dielectric surfaces and their actual chemical termination.[25] However, detailed microscopic investigations were hampered by the amorphous nature of the substrates used.

The present data demonstrate that film growth on graphite substrates of different surface quality (pristine vs sputtered) does not only result in very unequal film roughnesses but that the films also exhibit entirely different molecular and crystalline orientations. On microscopically rough HOPG surfaces, the studied molecules grow in an upright orientation and form crystalline islands exhibiting their respective bulk phase. In contrast, on pristine HOPG substrates films of recumbently oriented molecules are formed and, in case of PFP, even exhibit growth in a different polymorph. These findings are in good concordance with a former study regarding the growth of pentacene on HOPG,[16] suggesting that the observed effect is general for different acenes and not only a peculiarity of pentacene. Different molecular orientations have also been reported for acenes grown on metals of different roughness, for example, for pentacene on single and polycrystalline gold.[13] Interestingly, however, the film roughness appears to be inverted: While on single crystalline metal substrates highly ordered wetting layers are formed, which are stabilized by electronic interaction (chemisorption), the subsequent layers exhibit substantial islanding and are significantly rough. We note that the actual molecular orientation in such films can be rather different since in some cases upright-oriented molecules are found while they remain recumbently oriented in other cases.[9,13,26−28]

Most notably, although any additional chemical substrate interactions of pentacene and its derivatives can be excluded on graphite substrates, they form remarkably smooth films on pristine surfaces. We attribute this exceptional film growth to the good match of the carbon frame of the acenes with the lattice of the basal plane of graphite: A comparison between the ring diameters of PFP (2.77 Å), PTET (2.78 Å (H-terminated), 2.80 Å (O-terminated)), PEN (2.81 Å), and graphite (2.85 Å) shows a close match, which suggests a template effect by the formation of a commensurate seed layer on the HOPG surface. Moreover, as demonstrated previously for the case of pentacene on HOPG,[16] the low adsorption energy additionally allows a slight rearrangement of the adsorbed molecules, thus enabling adjustment to the packing motif of the crystalline structure. Apparently, this prealignment causes PFP molecules to grow in recumbent orientation and to form a new polymorph. While this polymorph is observed also for PFP films grown on Ag(111),[20] there, in clear contrast, the films exhibit a substantial roughness.[10] A comparison of the shape of PFP islands on pristine HOPG and the morphology of the underlying substrate shows that the island size is actually limited by the size of substrate grains, hence indicating that such grain boundaries are efficient diffusion barriers during growth. Note that such a specific nucleation and grain-limited growth was also observed before for the growth of *p*-quaterphenylene films on polycrystalline gold.[29−31]

A completely different situation occurs on sputtered HOPG substrates. Because of the lack of any templating effect, which would cause a prealignment upon nucleation, and because of a larger nucleation density on the rough surface, the film growth most likely is goverened by a minimization of surface energy. Like in the case of chemically inert substrates, for example, SiO_2, this leads to upright-oriented molecules forming fiber-textures with (100)-oriented surfaces, where molecules adopt a high coordination and, thus, a low surface energy.

On the basis of AFM data of the initial stage of growth, it was found that upright-oriented PFP molecules are able to overgrow low defect steps of the substrate by creating dislocations within the film (cf. Figure 6b). Interestingly, this ability was not observed for PTET and is attributed to the oxygen side groups whose repulsive interaction requires interdigitation, thus allowing only for specific lateral shifts of neighboring molecules.

5. CONCLUSION

The present growth study of acene derivatives on HOPG substrates of different surface quality (roughness) demonstrates that the resulting crystalline structure of such molecular films is not only controlled by the interplay of molecule−substrate and molecule−molecule interactions but also depends sensitively on the single-crystalline coherence length of the substrate. Pristine HOPG substrates with a low defect density are demonstrated to be well-suited templates for preparing particularly smooth acene films consisting of largely extended and molecularly flat islands. In such films, pentacene as well as pentacenetetrone and perfluoropentacene adopt a recumbent orientation, which, in case of PFP, is enabled by a new polymorph. The remarkable order in these films makes them interesting model systems for further optical and electronic studies to characterize the influence of packing motifs on the opto-electronic properties of such functional molecular materials.

■ ASSOCIATED CONTENT

Supporting Information. Supporting X-ray diffraction reciprocal space mapping data of a PFP thin film deposited on a sputtered HOPG substrate. This information is available free of charge via the Internet at http://pubs.acs.org/.

■ AUTHOR INFORMATION

Corresponding Author
*E-mail: gregor.witte@physik.uni-marburg.de.

■ ACKNOWLEDGMENT

We thank Wolfgang Caliebe (DESY - HASYLAB) for experimental support and A. Moser (TU-Graz, Austria) for providing computational support for RSM data analysis. T.B. acknowledges financial support by the Friedrich-Ebert-Stiftung. M.O. acknowledges financial support by the Austrian Science Fund (FWF) project P21094−N20.

■ REFERENCES

(1) Anthony, J. E. *Chem. Rev.* **2006**, *106*, 5028.
(2) Karl, N., Farchioni, R., Grosso, G., Eds. *Organic Electronic Materials*; Springer: New York, 2001.
(3) Duhm, S.; Heimel, G.; Salzmann, I.; Glowatzki, H.; Johnson, R. L.; Vollmer, A.; Rabe, J. P.; Koch, N. *Nat. Mater.* **2008**, *7*, 326.
(4) Ueno, N.; Kera, S. *Prog. Surf. Sci.* **2008**, *83*, 490.
(5) Sassella, A.; Borghesi, A.; Meinardi, F.; Tubino, R.; Gurioli, M.; Botta, C.; Porzio, W.; Barbarella, G. *Phys. Rev. B* **2000**, *62*, 11170.
(6) Breuer, T.; Witte, G. *Phys. Rev. B* **2011**, *83*, 155428.
(7) Witte, G.; Wöll, Ch. *J. Mater. Res.* **2004**, *19*, 7.
(8) Stöhr, M.; Gabriel, M.; Möller, R. *Europhys. Lett.* **2002**, *59*, 423.
(9) Käfer, D.; Witte, G. *Chem. Phys. Lett.* **2007**, *442*, 376.
(10) Götzen, J.; Schwalb, C. H.; Schmidt, C.; Mette, G.; Marks, M.; Höfer, U.; Witte, G. *Langmuir* **2001**, *27*, 993.
(11) Dürr, A. C.; Koch, N.; Kelch, M.; Ghijsen, J.; Johnson, R. L.; Pireaux, J. J.; Schwartz, J.; Schreiber, F.; Dosch, H.; Kahn, A. *Phys. Rev. B* **2003**, *68*, 115428.
(12) Peisert, H.; Biswas, I.; Zhang, L.; Knupfer, M.; Hanack, M.; Dini, D.; Batchelor, D.; Chasse, T. *Surf. Sci.* **2006**, *600*, 4024.
(13) Käfer, D.; Ruppel, L.; Witte, G. *Phys. Rev. B* **2007**, *75*, 085309.
(14) Zheng, Y.; Wee, A. T. S.; Chandrasekhar, N. *ACS Nano* **2010**, *4*, 2104.
(15) Ivanco, J.; Haber, T.; Krenn, J. R.; Netzer, F. P.; Resel, R.; Ramsey, M. G. *Surf. Sci.* **2007**, *601*, 178.
(16) Götzen, J.; Käfer, D.; Wöll, Ch.; Witte, G. *Phys. Rev. B* **2010**, *81*, 085440.
(17) Zacharia, R.; Ulbricht, H.; Hertel, T. *Phys. Rev. B* **2004**, *69*, 155406.
(18) Sakamoto, Y.; Suzuki, T.; Kobayashi, M.; Gao, Y.; Fukai, Y.; Inoue, Y.; Sato, F.; Tokito, S. *J. Am. Chem. Soc.* **2004**, *126*, 8138.
(19) Käfer, D.; El Helou, M.; Gemel, Ch.; Witte, G. *Cryst. Growth Des.* **2008**, *8*, 3053.
(20) Duhm, S.; Hosoumi, S.; Salzmann, I.; Gerlach, A.; Oehzelt, M.; Wedl, B.; Lee, T. L.; Schreiber, F.; Koch, N.; Ueno, N. *Phys. Rev. B* **2010**, *81*, 045418.
(21) Kowarik, S.; Gerlach, A.; Hinderhofer, A.; Milita, S.; Borgatti, F.; Zontone, F.; Suzuki, T.; Biscarini, F.; Schreiber, F. *Phys. Status Solidi (RRL)* **2008**, *2*, 120.
(22) Salzmann, I.; Duhm, S.; Heimel, G.; Rabe, J. P.; Koch, N.; Oehzelt, M.; Sakamoto, Y.; Suzuki, T. *Langmuir* **2008**, *24* (14), 7294.
(23) Jung, Y.; Kline, R. J.; Fischer, D. A.; Liu, E. K.; Heeny, M.; McCulloch, I.; DeLongchamp, D. M. *Adv. Funct. Mater.* **2008**, *18*, 742.
(24) Yang, H.; Yang, C.; Kim, S. H.; Jang, M.; Park, C. E. *ACS Appl. Mater. Interfaces* **2010**, *2*, 391.
(25) Ruiz, R.; Choudhary, D.; Nickel, B.; Toccoli, T.; Chang, K.-C.; Mayer, A. C.; Clancy, P.; Blakely, J. M.; Headrick, R. L.; Iannotta, S.; Malliaras, G. G. *Chem. Mater.* **2004**, *16*, 4497.
(26) Söhnchen, S.; Lukas, S.; Witte, G. *J. Chem. Phys.* **2004**, *121*, 525.
(27) Götzen, J.; Lukas, S.; Birkner, A.; Witte, G. *Surf. Sci.* **2011**, *605*, 577.
(28) Djuric, T.; Ules, T.; Flesch, H. G.; Planck, H.; Shen, Q.; Teichert, C.; Resel, R.; Ramsey, M. G. *Cryst. Growth Des.* **2011**, *11*, 1015.
(29) Müllegger, S.; Mitsche, S.; Pölt, P.; Hänel, K.; Birkner, A.; Wöll, Ch.; Winkler, A. *Thin Solid Films* **2005**, *484*, 408.
(30) Müllegger, S.; Salzmann, I.; Resel, R.; Winkler, A. *Appl. Phys. Lett.* **2003**, *83* (22), 4536.
(31) Müllegger, S.; Salzmann, I.; Resel, R.; Hlawacek, G.; Teichert, C.; Winkler, A. *J. Chem. Phys.* **2004**, *121*, 2272.

SUPPORTING INFORMATION
Interrelation between substrate roughness and thin-film structure of functionalized acenes on graphite

Tobias Breuer,[1] Ingo Salzmann,[2] Jan Götzen,[1] Martin Oehzelt,[2]
Antonia Morherr,[1] Norbert Koch,[2] and Gregor Witte[1]

[1]*Molekulare Festkörperphysik, Philipps-Universität Marburg, D-35032 Marburg, Germany*
[2]*Institut für Physik, Humboldt-Universität zu Berlin, D-12489 Berlin, Germany*

As we discussed in the main text, PFP films exhibit different polymorphs depending on the substrate quality. While they crystallize in the thin-film phase [1] on sputtered surfaces, they grow in a different polymorph on pristine HOPG. To support the specular XRD data presented in the main text we conducted additional x-ray diffraction reciprocal space mapping experiments on the PFP film deposited on a sputtered HOPG substrate (see Fig. 4d) for the related specular XRD data). As all observed reflections are in good agreement with the PFP thin-film phase (see Fig. S 1) this data prove that PFP grows in its thin-film phase on defective (sputtered) HOPG surfaces. In future work we will conduct additional RSM experiments, accompanied by further measurements, e.g., of PFP films on pristine HOPG.

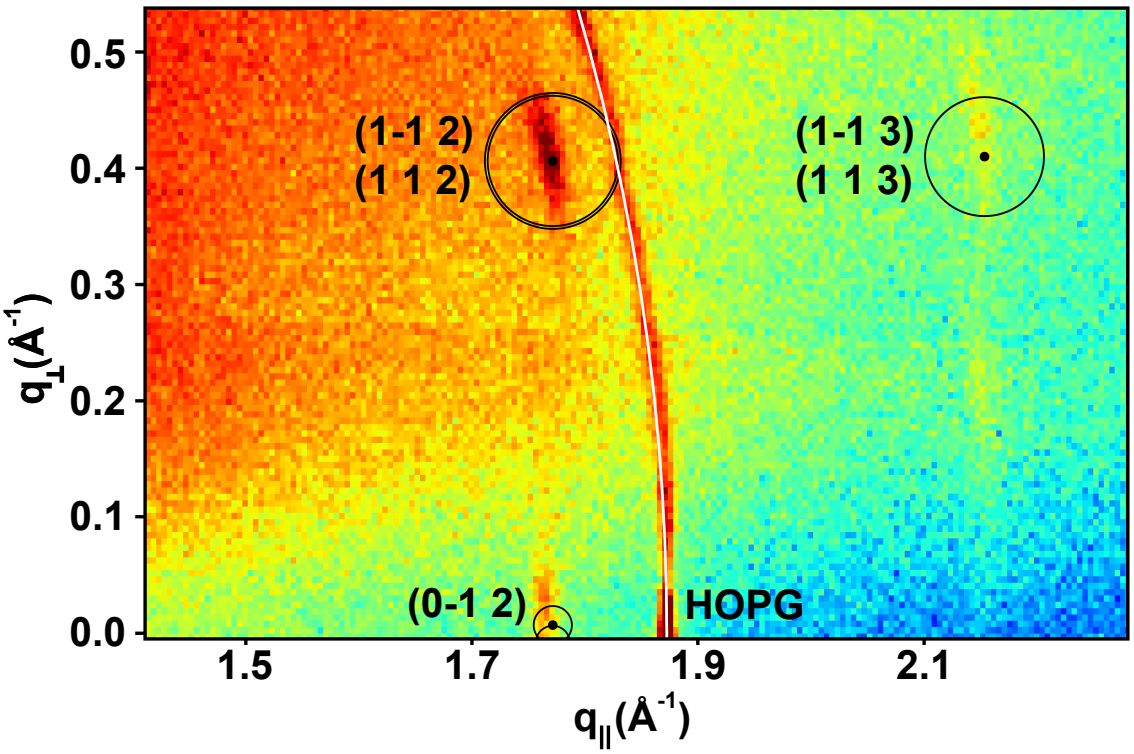

Figure S 1: X-ray diffraction reciprocal space map (RSM) of a nominally 50 nm thick perfluorpentacene (PFP) film on a HOPG substrate roughened by Ar^+ sputtering [cf. Fig. 4 a-d) in the main text]. Radii of the black circles correspond to the calculated structure factors of the respective PFP thin-film phase reflections; the white circle indicates a (weak) contribution of the HOPG (0002) substrate reflection. RSM data was recorded under an incident angle of the primary beam of 0.15° with respect to the sample surface; the map consists of two scans along $q_{||}$ using a 1D detector (1280 channels, 10 channels vertically averaged).

[1] Salzmann, I.; Duhm, S.; Heimel, G.; Rabe, J.P.; Koch, N.; Oehzelt, M.; Sakamoto, Y.; Suzuki, T. *Langmuir* **2008**, *24 (14)*, 7294

5.4 Article IV: Temperature Dependent Structural Phase Transition at the Perfluoropentacene/Ag(111) Interface

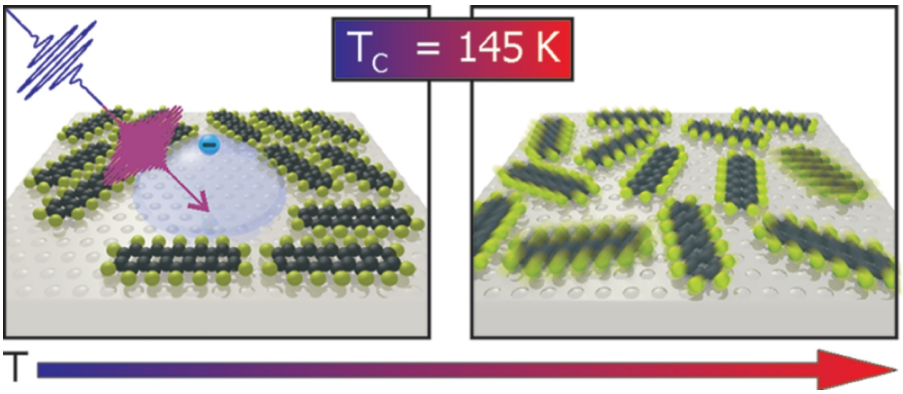

5.4.1 Abstract

Monolayers of perfluoropentacene (PFP) on Ag(111) undergo a reversible structural transition from a crystalline (6 × 3) phase at low temperatures to a disordered phase at room temperature. Two-photon photoemission (2PPE) of the low temperature phase revealed a distinct signal of the first image-potential state (n = 1) of Ag(111), thus showing the presence of bare substrate regions between the crystalline PFP islands. At higher temperatures, the entire surface is covered by a disordered phase of diffusing molecules causing a complete suppression of the (n = 1) signal and the electron diffraction (LEED) pattern. X-ray absorption spectroscopy showed that neither a change of the weak chemical interaction nor a change of the molecular tilt angle occurs during this phase-transition. The quantitative analysis of the 2PPE signal and the LEED contrast yields a transition temperature of $T_C = 145 \pm 5$ K. The present experiment shows that desorption of excess multilayers leads to an effective coverage of less than a dense monolayer.

5.4.2 Methods

Low Energy Electron Diffraction, Organic Molecular Beam Deposition, Near-Edge X-Ray Absorption Fine Structure Spectroscopy, Two-Photon-Photo-Emission (2PPE)

5.4.3 Own Contribution

The 2PPE and LEED experiments have been performed by Manuel Marks and Christian Schwalb. I have helped Christian Schmidt to plan, perform and evaluate the NEXAFS

measurements and to prepare the samples as well as to improve the manuscript. Gregor Witte and Ulrich Höfer have helped to interpret the data and to improve the manuscript.

THE JOURNAL OF PHYSICAL CHEMISTRY C

ARTICLE

pubs.acs.org/JPCC

Temperature Dependent Structural Phase Transition at the Perfluoropentacene/Ag(111) Interface

Manuel Marks, Christian Schmidt, Christian H. Schwalb, Tobias Breuer, Gregor Witte,* and Ulrich Höfer*

Fachbereich Physik und Zentrum für Materialwissenschaften, Philipps-Universität Marburg, D-35032 Marburg, Germany

ABSTRACT: Monolayers of perfluoropentacene (PFP) on Ag(111) undergo a reversible structural transition from a crystalline (6 × 3) phase at low temperatures to a disordered phase at room temperature. Two-photon photoemission (2PPE) of the low temperature phase revealed a distinct signal of the first image-potential state (n = 1) of Ag(111), thus showing the presence of bare substrate regions between the crystalline PFP islands. At higher temperatures, the entire surface is covered by a disordered phase of diffusing molecules causing a complete suppression of the (n = 1) signal and the electron diffraction (LEED) pattern. X-ray absorption spectroscopy showed that neither a change of the weak chemical interaction nor a change of the molecular tilt angle occurs during this phase-transition. The quantitative analysis of the 2PPE signal and the LEED contrast yields a transition temperature of T_C = 145 ± 5 K. The present experiment shows that desorption of excess multilayers leads to an effective coverage of less than a dense monolayer.

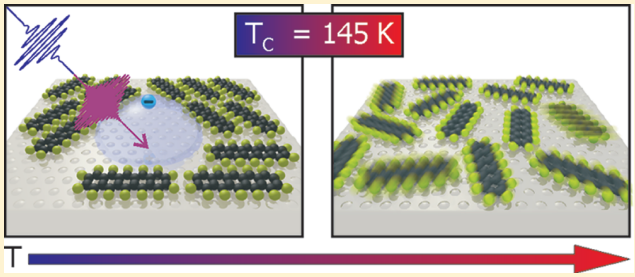

INTRODUCTION

Despite the recent success of organic electronics, a detailed understanding of fundamental physical processes occurring at metal−organic interfaces still remains challenging. In particular, processes determining the transfer and decay of free charge carriers are still not well characterized. Since the injection of charge carriers at molecule−metal contacts is decisive for the performance of organic electronic devices, significant efforts have been made to investigate the energy level alignment between molecular semiconductors and metal electrodes.[1−4] In order to achieve small injection barriers, a close match between the highest occupied molecular level and the Fermi level of the electrode is required in case of p-type organic semiconductors. For n-type semiconductors the energetic position of unoccupied molecular orbitals and their overlap with metallic states determine the charge injection dynamics.

Like the lifetime of excited electrons, the efficiency of charge injection critically depends not only on the level alignment, but also on the electronic coupling between metal and organic states.[5] In addition, a number of structural and chemical factors, such as the emergence of new interface states,[6,7] can affect the charge injection processes significantly. Clearly, all of these factors, not only the position of interfacial energy levels,[8−10] depend on the interface morphology.[11,12] Temperature dependent structural transitions, which are reported for several interfaces between conjugated molecules and metal substrates,[8,10,13,14] are therefore expected to have a strong influence on the excitation of charge carriers across a metal−organic interface.

In this article, combining LEED, X-ray absorption spectroscopy (NEXAFS), and time-resolved two-photon photoemission (2PPE), we demonstrate a reversible, temperature dependent structural phase transition from a two-dimensional crystalline phase to a disordered phase for perfluoropentacene (PFP, $C_{22}F_{14}$) monolayers adsorbed on Ag(111). PFP is a particular interesting n-type semiconductor[15] because it renders possible a comparison with the nonfluorinated and widely studied analogue p-type semiconductor pentacene ($C_{22}H_{14}$).[14,16] For low temperatures, the commensurate, highly ordered film structure of PFP monolayer films on Ag(111) has been identified using scanning-tunnelling microscopy (STM) and low energy electron diffraction (LEED).[17,18] Moreover, the vertical layer−substrate distance and the occupied electronic structure are well studied.[19,20]

In recent years, 2PPE has proven to be a very powerful tool to investigate unoccupied states and the dynamics of adsorbates at surfaces.[21−29] Here, we employ this technique as a monitor of the phase transition by using image-potential states as a local probe of extended clean Ag(111) areas that appear upon ordering of PFP/Ag(111). Since image-potential states are located directly in front of the surface,[30−32] adsorbate layers have a strong influence on their binding energies and the electronic lifetimes.[33−38] Moreover, small substrate areas of a few nanometers in diameter are required for the formation of image-potential states,[39] thus electrons in image-potential states can be utilized as sensitive probes for adlayer coverages. Berthold et al. monitored the photo-induced desorption of Ar/Cu(100) using the signal of the first image-potential state (n = 1) to quantify the proportion of Ar-covered and clean substrate areas.[40] Following this idea, we have employed the (n = 1) image-potential state to noninvasively monitor the coexistence and proportion of covered and bare substrate areas during the structural phase transition of the PFP film.

Received: October 6, 2011
Revised: November 24, 2011
Published: December 05, 2011

The article is organized as follows: after separately presenting the results of the three complementary experimental techniques, the origin of the structural transition within the PFP thin film will be discussed. Among others, our results explain why no structural information on the adlayer structure of PFP/Ag(111) is observed at elevated temperatures.

EXPERIMENTAL SECTION

The 2PPE and LEED experiments were performed in an ultrahigh vacuum (UHV) chamber with a base pressure of 4×10^{-11} mbar.[41] The chamber is equipped with an X-ray source, a four grid LEED, and a hemispherical energy analyzer with a five-channeltron-array detector. A Ti:sapphire oscillator with a repetition rate of 82 MHz serves as the laser source. The fundamental Gaussian pulses (τ_{IR} = 42 fs, $\hbar\omega_{IR}$ = 1.56 eV) are split using a 50/50 beam splitter. One part is frequency doubled by second-harmonic generation (SHG), while the second part is frequency tripled by subsequent SHG and sum-frequency generation (SFG). The resulting *p*-polarized laser pulses (τ_{blue} = 45 fs, $\hbar\omega_{blue}$ = 3.10 eV and τ_{UV} = 70 fs, $\hbar\omega_{UV}$ = 4.69 eV) are aligned collinearly and focused to a 100 μm spot onto the sample at an incident angle of 75° with respect to the surface normal. The overall energy resolution was 65 meV with an angular resolution of 1.2°.

The NEXAFS measurements were performed at the HE-SGM dipole beamline of the synchrotron storage ring BESSY II in Berlin (Germany) that provides linear polarized synchrotron light with a polarization factor of 0.91 and an energy resolution of about 300 meV at the carbon K-edge. All NEXAFS spectra were recorded in partial electron yield mode using a channel plate detector with a retarding field of −150 V. In order to calibrate the absolute energy scale of the X-ray absorption spectra, the photocurrent from a carbon coated gold grid in the incident beam that exhibits a distinct absorption maximum at 284.9 eV was recorded simultaneously. The NEXAFS raw data were normalized with respect to the transmission of the clean substrate and the incident photon flux.

The Ag(111) sample (MaTeck) was cleaned by repeated cycles of sputtering (E_{kin} = 0.7 eV, $I_{sputter}$ = 3 μA, T_{sample} = 373 K for 20 min) and subsequent annealing (T_{sample} = 773 K for 5 min) until no contaminations were observed in the XPS and 2PPE spectra and a sharp LEED pattern with low background signal was observed. Perfluoropentacene (Kanto Denka Kogoyo, purity >99%), was deposited with a rate of 0.25−0.3 ML/min from a resistively heated Knudsen cell onto the sample that was held between 270 and 290 K during thin film growth.

Previous studies have shown that upon molecular beam deposition, bi- and multilayers start to grow already before completion of the first monolayer, which complicates the preparation of defined monolayer films.[42] Following ref 18, a nominal monolayer coverage was achieved by first depositing a thin multilayer film and subsequently desorbing the excessive multilayers by heating the sample to 403 K for five minutes.

RESULTS

Two-Photon Photoemission. Figure 1 depicts a series of 2PPE spectra of a nominal PFP monolayer adsorbed on Ag(111), which were recorded at different temperatures during cooling-down from room temperature to 90 K. The energy is given as intermediate state energy with respect to E_F. It is calculated by subtracting the photon energy $\hbar\omega_{blue}$ used in the photoemission step from the final state energy of the photoelectrons after photoemission (Figure 1, top abscissa). At 90 K, four separated peaks can be observed in the 2PPE spectrum. As discussed later, two of the peaks (n = 1 and SS) originate from areas of the uncovered Ag(111) substrate, while signals (A) and (B) appear in the spectrum after adsorption of a nominal PFP monolayer. A spectrum of a bare Ag(111) surface is shown in Figure 3 for comparison, and the modifications due to PFP adsorption will be discussed later. Interestingly, the 2PPE spectra of a nominal monolayer PFP on Ag(111) reveal a strong temperature dependence. With increasing temperature, the intensity of the peaks (n = 1) and (SS) starts to decrease until they completely vanish for temperatures above 165 K. The two remaining features, (A) and (B), undergo changes in final state energy and peak form between 130 and 165 K. Peak (A) at the low energy side of the spectrum shows a shift toward higher final state energies, whereas the line width of signal (B) decreases. The shift of peak (A) is not gradual. Instead, a second peak arises at the high energy side that takes over the entire intensity and the original peak vanishes. Similarly, the line width of peak (B) abruptly decreases around 155 K but reveals only minor changes in energy. Above temperatures of 165 K, the spectra remain almost unaltered. All observed changes in the 2PPE spectra are completely reversible.

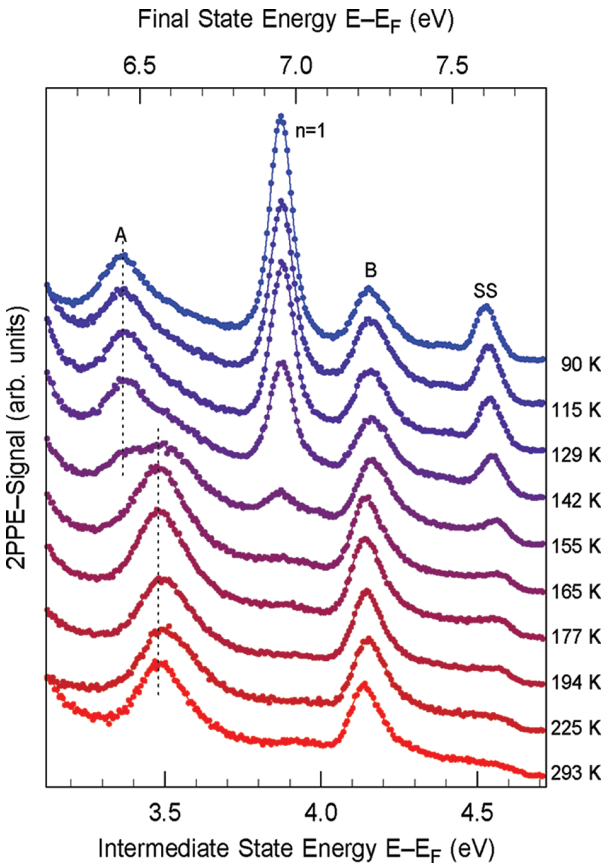

Figure 1. 2PPE spectra of a nominal PFP monolayer on Ag(111) recorded during repeated cooling-down from room temperature down to 90 K. For temperatures around 150 K, the 2PPE spectra undergo significant changes that are completely reversible. With increasing temperature the substrate signals, (n = 1) and (SS) decrease, while the PFP induced signal (A) experiences a shift in energy. Analogously, the line width of peak (B) decreases, and its maximum shifts to slightly lower final state energies.

dx.doi.org/10.1021/jp2094577 |J. Phys. Chem. C 2012, 116, 1904–1911

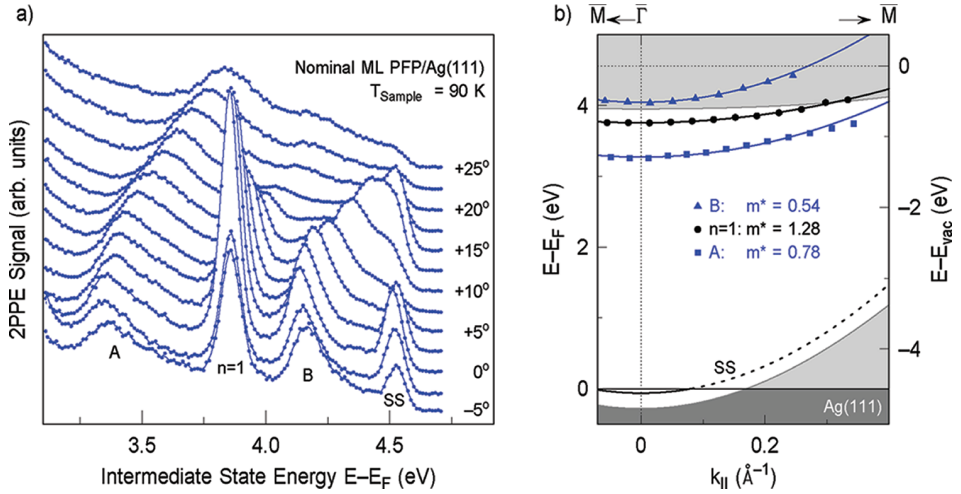

Figure 2. (a) Series of angle-resolved 2PPE spectra (normalized to peak A) of a nominal PFP monolayer recorded at 90 K (the exit angle is given with respect to the surface normal). (b) Positions of the peak maxima of (A), (B), and ($n = 1$) shown in a dispersion diagram in front of the projected band structure of the bare substrate. The occupied projected bulk bands are indicated in dark gray, the unoccupied bands in light gray, and the projected band gap in white. The dispersion of (A), (B), and ($n = 1$) can be approximated by free-electron like parabolas with effective masses of $0.78m_e$, $0.54m_e$, and $1.28m_e$, respectively.

Actually, the spectrum at 90 K had been recorded after cooling the prepared nominal monolayer, while the remaining spectra were taken after thawing the sample and again cooling down to 90 K. This leads to a full recovery of the peaks ($n = 1$) and (SS) while signals (A) and (B) reobtain their original energetic position, peak form, and intensity. As no deviations are observed, a significant decomposition or desorption of PFP molecules is excluded, hence indicating a change in the interface morphology.

The bandstructure of unoccupied electronic states can be investigated by angle-resolved 2PPE. The dispersion of the resolved states allows us to deduce the degree of delocalization of the excited electrons in a direction parallel to the surface. The parallel momentum is calculated via $k_{||} = (2m_eE_{kin}/\hbar^2)^{1/2}\sin(\theta)$, where E_{kin} is the kinetic energy and θ the emission angle of the electrons. Figure 2a depicts a series of angle-resolved 2PPE spectra of a nominal PFP monolayer that was recorded at 90 K. All observed peaks in the spectrum are strongly dispersing and shift to higher energies with increasing emission angle. As expected for delocalized surface states, e.g., image-potential states, the dispersion of the ($n = 1$) state can be approximated using a free-electron like parabola $E(k_{||}) = (\hbar k_{||})^2/2m_{eff} + E_0$ with an effective mass $m_{eff} = m^*m_e$. A fit of the position of the peak maxima yields an effective mass factor of $m_{n=1}{}^* = 1.28 \pm 0.10$ at the $\bar{\Gamma}$-point. The respective data and the fit are shown in Figure 2b together with the projected band structure of the clean Ag(111) substrate. Similarly, states (A) and (B) reveal a delocalization in the surface plane with effective mass factors of $m_A{}^* = 0.78 \pm 0.20$ and $m_B{}^* = 0.54 \pm 0.10$, which are independent of temperature within our experimental error.

In order to identify the observed peaks, in particular the peak ($n = 1$), 2PPE spectra of clean and PFP covered Ag(111) are compared in Figure 3. For the clean substrate, four distinct peaks are observed (black diamonds). The predominant signal originates from the ($n = 1$) image-potential state. Additionally, a nonresonant 2PPE transition from the lower to the higher sp-band,[43] the image-potential resonance ($n = 2$), and a superposition of the higher image-potential resonances and direct nonresonant 2PPE from the Shockley surface state (SS) can be observed.[44] As shown in the excitation scheme (inset Figure 3), the ($n = 1$)

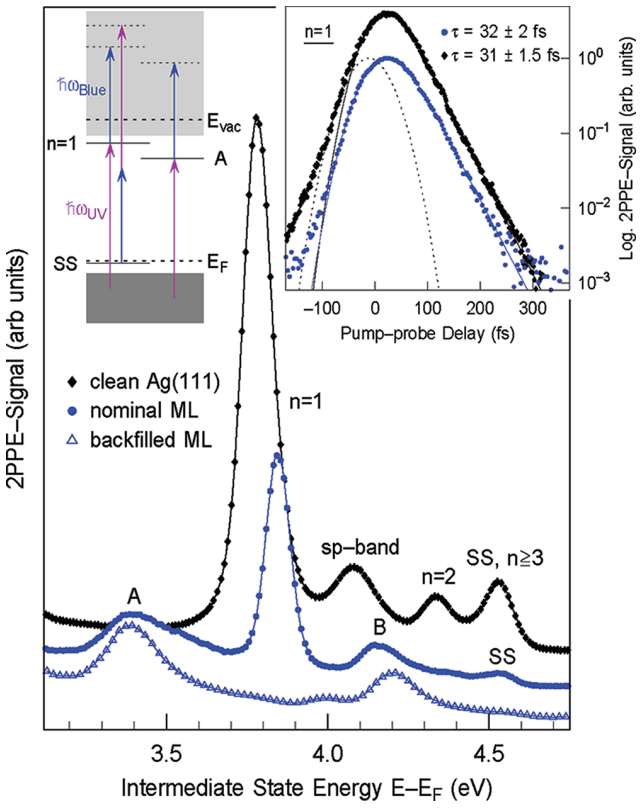

Figure 3. Coverage dependent 2PPE spectra of PFP films on Ag(111). For clean Ag(111) (black diamonds, measured at 293 K), ($n = 1$),2 image-potential states, Shockley surface state, and *sp*-band transition are visible. For a nominal PFP monolayer measured at 90 K, peaks (A) and (B) appear in the spectrum, while the ($n = 1$) and (SS) signals are attenuated (blue dots). Deposition of an additional 0.35 ML onto the nominal monolayer leads to suppression of the ($n = 1$) and slight changes of peaks (A) and (B) (triangles). The insets depict excitation schemes (left) and pump−probe traces of the ($n = 1$) image-potential state on a semilogarithmic scale (right).

dx.doi.org/10.1021/jp2094577 |J. Phys. Chem. C 2012, 116, 1904–1911

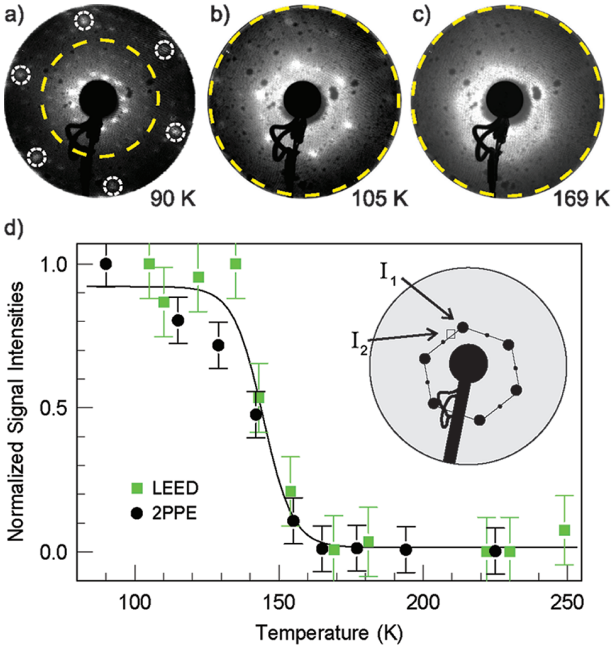

Figure 4. LEED patterns of a nominal PFP monolayer on Ag(111) taken at: (a) T_{sample} = 90 K, E_{kin} = 43.0 eV; (b) 105 , 15.4 eV; and (c) 169 K, 14.0 eV. In panel a, dotted lines indicate substrate spots, and the dashed circle marks the section observed at lower beam energies. Panel d depicts the normalized contrast of the LEED patterns (green squares) and normalized (n = 1) intensity (black dots) as function of sample temperature together with a corresponding fit using a Boltzmann sigmoidal (black line). The inset sketches the determination of the diffraction contrast (I_1 spot intensity; I_2 diffuse background signal for an area of identical size between the spots).

image-potential state is populated from states below E_F using UV photons $\hbar\omega_{UV}$. Subsequently, this transient population is photoemitted by photons of the frequency-doubled laser pulses $\hbar\omega_{blue}$. The (SS) and sp-band are emitted in a direct nonresonant 2PPE process and the intermediate state energy scale does not apply for these signals.

After preparation of a nominal PFP monolayer, the signals of the (n = 1) image-potential state and the Shockley surface state diminish compared to the clean substrate but are still clearly visible (blue dots). Additional dosing of about 0.35 ML PFP at 273 K completely suppresses the (n = 1) signal even when measured at 90 K (Figure 3, blue triangles). By contrast, the two PFP related peaks (A and B) can still be observed for the thicker PFP film, although slightly modified. A subsequent annealing step leads, however, to a recurrence of the (n = 1) signal. This proves that the predominant signal originates from the (n = 1) image-potential state of bare substrate areas, which re-emerge due to the annealing procedure. As mentioned before, surface areas of a few nanometers in diameter are required for the formation of image-potential states,[39] and therefore, these states can be used to monitor the surface coverage.[40] In order to quantify the proportion of clean substrate areas, we compare the integrals of the (n = 1) signals for the clean and PFP covered substrate. The signal decreases to about one-third of the intensity of clean Ag(111). Assuming a linear decrease of the (n = 1) signal with PFP surface coverage, we estimate that at 90 K about one-third of the silver substrate remains uncovered after preparation of the annealed PFP monolayer.

This interpretation is further corroborated by the electron lifetime because the decay of excited electrons in image-potential states is extremely sensitive to a modification of the wave function by adsorbate layers.[33,36,37] Pump−probe traces for the (n = 1) image-potential state for clean and PFP covered Ag(111) are shown in the inset of Figure 3. They are recorded by measuring the peak intensity for successively delayed laser pulses. Negative values denote a delayed UV-pulse, while for positive delays, the UV photons arrive on the sample first. The temporal resolution of the 2PPE experiment is limited by the width of the cross-correlation of the laser-pulses (dashed line). A fit of the pump−probe trace using a rate equation model that includes two Gaussian laser-pulses and an exponential decay $\propto \exp(-1/\tau)$ is used to extract the lifetime τ of the excited electrons. For the (n = 1) image-potential state of clean Ag(111), an inelastic electron lifetime of $\tau_{n=1}$ = 31 ± 1.5 fs can be observed at 90 K in agreement with previous studies.[33,44] The signal at negative delays is attributed to hot electrons close to E_F[45] that will not be further discussed here. As can be seen in the pump−probe traces, the lifetime of the (n = 1) shows no influence of adsorbed PFP molecules. This observation can only be explained by an (n = 1) image-potential state on preserved areas of the clean Ag(111) surface after preparation of the PFP film. The small energetic shift of the (n = 1) signal after adsorption of PFP is attributed to the temperature dependence of the binding energy of image-potential states that originates from the narrowing of the sp-band gap due to the thermal expansion of the crystal lattice.[46] The clean spectrum was recorded at room temperature prior to film adsorption, while the spectra for PFP/Ag(111) were taken at 90 K.

Low Energy Electron Diffraction. In order to elucidate the underlying mechanisms of the observed transitions, the change of the long-range order of the PFP/Ag(111) system with temperature was investigated using LEED. Representative LEED patterns of the nominal PFP monolayer above and below the transition temperature are shown in Figure 4.

At 90 K, a distinct diffraction pattern is clearly visible for an electron energy of 43.0 eV in Figure 4a. This reflects the commensurate (6 × 3) superstructure of the PFP monolayer on Ag(111). Previous low temperature STM studies have shown that in this adlayer the PFP molecules are uniformly oriented with their long axis along the ⟨110⟩ azimuth and densely packed according to their van der Waals width.[17,18] Reducing the incident electron energy to about 14−15 eV allows a better resolution of the inner spots of the diffraction pattern. This is indicated by the dashed circle, and the respective LEED pattern is shown in Figure 4b. At 169 K, however, the spot pattern has completely disappeared. As shown in Figure 4c, it is replaced by a hexagonally shaped, streaky pattern comparable in size, hence indicating a transition from the crystalline PFP monolayer into a rather disordered phase at elevated temperatures. The latter phase still exhibits the characteristic minimum molecule distance as found in the ordered phase as well as a preferential azimuthal alignment. A further increase of the temperature leads to the disappearance of this azimuthal alignment. Subsequent cooling of the sample back to low temperatures re-establishes the long-range order of the commensurate (6 × 3) superstructure. This reveals a similar reversibility for the transition as observed in the 2PPE experiments.

For a more quantitative analysis of the structural transition, LEED patterns recorded at various temperatures along the phase transition were analyzed. As sketched in the inset of Figure 4, we defined a diffraction contrast as the intensity ratio of a distinct LEED spot and the diffuse background signal (I_1/I_2) and

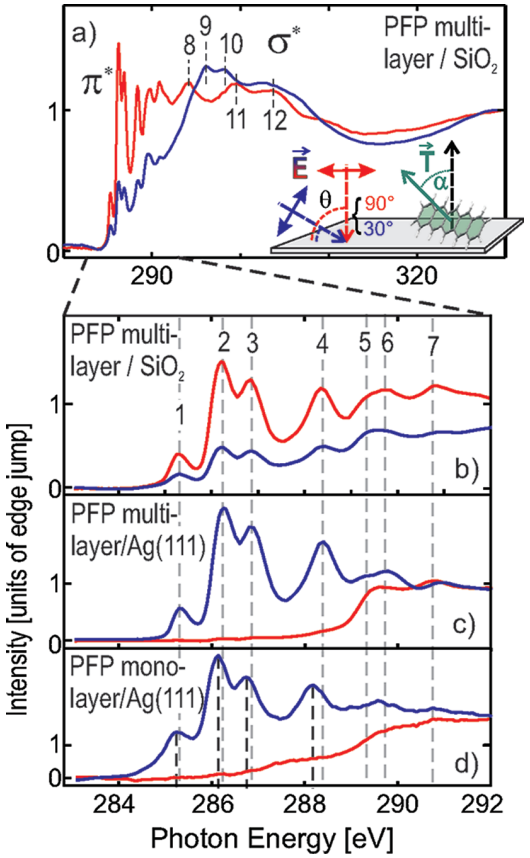

Figure 5. Series of C1s NEXAFS spectra recorded for PFP films of different thicknesses deposited onto Ag(111) and SiO_2. (a) Overview spectra of a multilayer film on SiO_2. Panels b−d reveal the magnified π^* region of the NEXAFS spectra of different films: (b) 2 nm on SiO_2, (c) 10 nm on Ag(111), and (d) nominal monolayer on Ag(111). All spectra were recorded for different orientations of the incident electrical field vector relative to the surface normal as depicted schematically in the inset of panel a.

normalized it to the contrast at 90 K. The resulting contrast curve is shown in Figure 4 and clearly reveals the vanishing crystalline phase of the nominal monolayer between 130 and 160 K.

As stated before, the intensity of the $(n = 1)$ image-potential state can be taken as fingerprint of clean, uncovered Ag(111) areas. For a more quantitative analysis of the proportion of bare surface areas during the transition, the integral of the $(n = 1)$ peak of the spectra from Figure 1 has been analyzed. Figure 4 depicts the intensity normalized to the value at 90 K as a function of sample temperature together with the LEED contrast. This clearly shows that both curves exhibit the identical temperature dependence. It thus demonstrates that the uncovered surface areas, which are present in the crystalline layer at 90 K, become effectively covered during formation of the disordered phase. In order to quantify a transition temperature T_C of the PFP adlayer, a Boltzmann sigmoidal $\propto 1/[1 + \exp(\alpha(T - T_C))]$ was fitted to both experimental data sets simultaneously. The fit gives a critical temperature of $T_C = 145 \pm 5$ K.

Near-Edge X-ray Absorption Spectroscopy. The 2PPE experiments discussed above reveal an entirely covered surface for the disordered phase at elevated temperatures, while crystalline PFP-covered and bare substrate areas coexist below T_C. In order to answer the question, how the identical amount of molecules can occupy different substrate areas, carbon edge NEXAFS measurements were carried out. They provide information on the molecular orientation and allow us to decide whether the area per molecule changes with temperature by molecular tilting or molecules are diffusing in the disordered phase.

Though first NEXAFS data have been reported previously for PFP,[47,48] a precise assignment of the various spectral features has not yet been possible. Neither systematic polarization dependent measurements nor a theoretical analysis like in the case of the nonfluorinated acenes have been carried out so far.[49] Therefore, at first, carbon edge NEXAFS spectra were recorded for PFP multilayers grown on SiO_2 to provide reference data of a system without noticeable electronic substrate interaction but uniform crystalline texture and defined orientational ordering. As shown in Figure 5a, the NEXAFS spectra reveal a number of sharp resonances at energies between 285 and 289 eV followed by some broader resonances at higher energies. At least 12 distinct resonances were identified at photon energies of 285.3 eV, 286.2 eV, 286.8 eV, 288.3 eV, 289.4 eV, 289.8 eV, 290.8 eV, 294.3 eV, 296.2 eV, 298.2 eV, 299.5 eV, and 303.8 eV (labeled by 1−12). On the basis of their energetic position relative to the absorption edge and the obtained dichroism (which is discussed later), at least the first four resonances are clearly identified as excitations of C1s electrons into closely spaced unoccupied molecular π^* orbitals. Note that due to different ionization potentials of the carbon atoms (C(C): ∼291.4 eV and C(F): ∼293.6 eV),[50] two C1s absorption edges have to be considered in case of PFP. However, for a quantitative analysis, only the first three π^* resonances are employed, which are located below both absorption edges so that their intensities can be evaluated without any background corrections. The theoretical analysis shows that the intensity of the π^* resonances depends on the orientation of the electrical field vector, $\vec{E}$, of the incident synchrotron light relative to the transition dipole moment, $\vec{T}$. In the case of aromatic molecules, $\vec{T}$ is oriented normal to the ring plane (see inset of Figure 5a).[51] Thus, from NEXAFS measurements recorded for different angles of incidence of incoming light, θ, the average tilt angle of $\vec{T}$ relative to the sample normal, α, can be determined. For vector-type π^* orbitals occurring for aromatic systems, a surface of 3-fold symmetry and linear polarized light with a degree of polarization, P, the intensity variation (linear dichroism) can be expressed as $I_{\pi^*} \propto 1/2(P \cos^2 \theta(3 \cos^2 \alpha - 1) + 1 - \cos^2 \alpha)$.[51]

In order to determine the molecular orientation, repeated NEXAFS spectra were taken at 3 different angles of incidence ($\theta = 90°$, 55°, and 30°), but for clarity, only spectra recorded at grazing (blue curve) and normal incidence (red curve) are shown in Figure 5. A quantitative analysis of the dichroism of the first three π^* resonances of the PFP film on SiO2 (see Figure 5b) yields an angle relative to the surface normal of $\alpha = 77 \pm 5°$. This value is in excellent agreement with XRD data of PFP films on SiO_2 showing the presence of (100)-oriented films where molecules adopt a uniform upright orientation with an angle of $\alpha = 76°$.[15,52]

NEXAFS spectra of a 10 nm PFP film on Ag(111), which has been prepared for comparison to the monolayer spectra, revealed very similar NEXAFS resonances but exhibited an inverted dichroism as depicted in Figure 5c. The quantitative analysis yields a tilt angle of $\alpha = 11 \pm 6°$, thus indicating a recumbent, almost flat lying molecular orientation. This geometry is in agreement with the PFP polymorph reported by Duhm et al. for PFP films on silver where a rather small interlayer spacing of

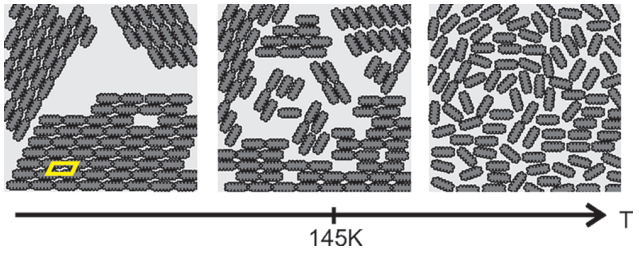

Figure 6. Schematic representation of structural phases of the PFP monolayer on Ag(111) adopted at different temperatures. The disordered layer formed at room temperature condenses upon cooling and forms a densely packed (6 × 3) structure below 145 K coexisting with uncovered regions of the silver substrate. Note that all displayed phases exhibit the same coverage.

3.06 Å was derived from XRD measurements.[19] This small spacing suggests that the long molecular axis is almost parallel to the substrate surface. We note that the NEXAFS based orientational analysis of these two limiting cases of molecular orientations well corroborates our assignment of the leading resonances as π^* resonances.

Interestingly, the NEXAFS spectra of PFP monolayer and multilayer films on Ag(111) are very similar. This is also found for films prepared by careful thermal desorption of beforehand grown multilayers as well as for submonolayers of only 0.2 nm (data not shown). The NEXAFS resonances of the monolayer appear shifted by less than 0.2 eV toward lower energies, which is attributed to screening of the core holes by the underlying metal substrate. A similar effect was also observed for the C1s and F1s photoelectron core lines of mono- and multilayer films of PFP.[18] However, only a very small broadening (~0.1 eV) of the NEXAFS resonances occurs (cf. Figure 5d) in contrast to PFP adsorbed on Cu(100), where the fine structure of the π^* resonances is no longer separated.[47] This finding reflects the absence of any distinct modification of the unoccupied molecular orbitals of PFP due to chemical interaction with the underlying silver substrate. This is remarkable since for monolayer films of the nonfluorinated pentacene adsorbed on Ag(111) and even on Au(111), a substantial broadening of the π^* resonances was found.[53,54] It indicates an almost pure van der Waals type interaction with the silver substrate, which is in line with a rather large molecule−substrate distance of 3.16 Å derived from XSW measurements.[19] The quantitative analysis of the dichroism of the PFP monolayer yields a tilt angle of $\alpha = 8 \pm 6°$, which corroborates the planar adsorption on Ag(111) concluded before on the basis of XSW and low temperature STM data.[17−19]

Additional NEXAFS measurements that were carried out for a PFP monolayer after cooling the sample down to 75 K revealed no noticeable change in the spectra, neither in peak position and width nor in dichroism (spectra not shown). This finding thus indicates that the ordered−disordered transition is not accompanied by a noticeable molecular tilting.

DISCUSSION

By combining temperature dependent 2PPE, LEED, and NEXAFS measurements, we observe a structural phase transition of a nominal PFP monolayer on Ag(111). At low temperatures an ordered crystalline phase with a (6 × 3) structure occurs, which transforms into a disordered phase of diffusing molecules at room temperature. This reversible transition proceeds in a rather small temperature regime between 130 and 160 K. NEXAFS data reveal no orientational modification and yield an almost planar adsorption geometry for all phases. In addition to the two PFP related peaks (A and B), the 2PPE spectra recorded for the ordered crystalline phase show a distinct signal from the (n = 1) image-potential state of the bare Ag(111) surface. This signal is a clear indication for the presence of uncovered surface regions and vanishes upon heating as the crystalline ordering of the adlayer is lost. This indicates a redistribution of larger uncovered regions at low temperature toward plenty but smaller voids at elevated temperatures as schematically shown in Figure 6. From the intensity of the (n = 1) signal relative to that of the clean Ag(111) surface, we estimate that about 30% of the silver substrate remains uncovered. This implies that the preparation of a PFP monolayer by thermal desorption of multilayers actually does not lead to a closed adlayer.

Disordered adlayers are common phenomena for inert, mostly nonpolar polycyclic aromatic hydrocarbons (PAH) adsorbed on weakly corrugated single crystal surfaces. So far, disorder−order transitions have been observed mostly in coverage dependent studies where a steric ordering of flat lying molecules according to their molecular van der Waals dimensions only occurs upon completion of a densely packed monolayer.[55−60] Only a few studies reveal a temperature dependence of such transitions in (sub)monolayer films.[10,13,14,61] Structural transitions have also been found upon melting of saturated monolayers of alkanes.[62,63] In that case, it was demonstrated that the structural changes are accompanied by the formation of conformational defects (gauche defects), which do not occur in the rigid acenes.

Condensation of an ordered monolayer at low temperature and formation of a disordered adlayer at room temperature were also reported for pentacene on Ag(111) but with an at least 50 K higher transition temperature.[14] Interestingly, in contrast to PFP, which is only weakly adsorbed on Ag(111), the nonfluorinated analogue is chemisorbed on that surface. This leads to a distinct broadening of the NEXAFS resonances and enhanced thermal stability of a monolayer up to more than 500 K.[53] The comparison with PFP indicates that the corrugation of the substrate holding potential, which is decisive for diffusion, apparently is quite low for both molecules despite a different desorption behavior. At this point, it is important to stress that on Ag(111), a direct comparison of the adsorption energy of PEN and PFP monolayers based on thermal desorption spectroscopy is impossible. The sharper NEXAFS resonances clearly indicate a weaker molecule−substrate interaction for PFP, hence, suggesting a lower hypothetic activation energy for desorption. However, because of a competing pathway of chemical decomposition of the fluorinated compound, an intact desorption does not proceed. Therefore, the activation energy for desorption cannot be measured. Planar, extended aromatic molecules experience a rather low corrugation potential on metal substrates due to simultaneous interaction between different parts of the adsorbed molecule and the surface. This effect is particularly pronounced for the absence of any geometrical match between the aromatic ring diameter (~2.5 Å)[64] and the nearest neighbor distance of the underlying silver substrate (2.89 Å).

In many cases, organic molecules are stronger bound to metal surfaces than in multilayer films. This has been utilized to prepare defined monolayer films by selective thermal desorption of excessive multilayers. By contrast, this approach is not applicable in the case of weakly interacting substrates such as, e.g., SiO_2 or graphite.[65,66] Apparently, this strategy is also of limited use for

preparation of densely packed monolayers of molecules with pronounced form-anisotropy adsorbed on substrates with low corrugation. In that case, competing diffusion and entropic effects favor the formation of disordered adlayers at elevated temperature. Upon subsequent cooling, the molecular motion is frozen out, and densely packed crystalline regions are formed, which coexist with uncovered regions of the substrate as depicted schematically in Figure 6. In principle, such an incomplete film can be backfilled by additional dosing as shown in Figure 3. However, this approach may lead to unwanted bi- or multilayer growth, hence again requiring an annealing step. Interestingly, this annealing step leads back to an incomplete monolayer. Therefore, the preparation of a saturated densely packed monolayer of such anisotropic molecules on weakly corrugated substrates appears to be virtually impossible. Instead, either a less densely packed monolayer is achieved or multilayer islands are present.

CONCLUSION

In conclusion, we find a temperature dependent structural transition of the PFP monolayer adsorbed on Ag(111). Between 130 and 160 K, the adsorbed PFP undergoes a change from the low-temperature densely packed crystalline phase, that coexists with bare Ag(111) regions, to a disordered phase of diffusing molecules. This finding explains why previous studies have not been able to image such PFP monolayers at room temperature by means of STM.[17,18] Moreover, it highlights a fundamental problem of preparing densely packed adlayers by thermal desorption of multilayer films. In the case of shape anisotropic molecules adsorbed on weakly corrugated substrates, diffusion hampers a dense packing and could favor interdiffusion of molecules from the first to higher layers. Structural transitions, as observed in the case of PFP on Ag(111), are important in particular for a controlled preparation of heterostructures. For disordered template layers with highly mobile molecules, interdiffusion may lead to undefined interface structures. Since the film geometry is decisive for the interfacial electronic structure, studies of charge transfer dynamics have to consider not only the crystal structure determined at low temperatures but also coverage and temperature dependent effects.

AUTHOR INFORMATION

Corresponding Author

*E-mail: Gregor.Witte@physik.uni-marburg.de (G.W.); Hoefer@physik.uni-marburg.de (U.H.).

ACKNOWLEDGMENT

It is a pleasure to thank Jan Götzen and Martin Galbraith for helpful remarks and inspiring discussions. We acknowledge the Helmholtz-Zentrum Berlin-Electron storage ring BESSY II for provision of synchrotron radiation at beamline HE-SGM and travel support. Financial support by the Deutsche Forschungsgemeinschaft through GK790, Ikerbasque foundation, and by Friedrich-Ebert-Stifung (T.B.) is also gratefully acknowledged.

REFERENCES

(1) Hill, I. G.; Rajagopal, A.; Kahn, A.; Hu, Y. *Appl. Phys. Lett.* **1998**, *73*, 662–64.
(2) Ueno, N.; Kera, S. *Prog. Surf. Sci.* **2008**, *83*, 490–557.
(3) Scott, J. C. *J. Vac. Sci. Technol., A* **2003**, *21*, 521–31.
(4) Koch, N. *J. Phys.: Condens. Matter* **2008**, *20*, 184008.
(5) Zhu, X. Y. *Surf. Sci. Rep.* **2004**, *56*, 1–83.
(6) Temirov, R.; Soubatch, S.; Luican, A.; Tautz, F. S. *Nature* **2006**, *444*, 350–53.
(7) Schwalb, C. H.; Sachs, S.; Marks, M.; Schöll, A.; Reinert, F.; Umbach, E.; Höfer, U. *Phys. Rev. Lett.* **2008**, *101*, 146801.
(8) Kilian, L.; Hauschild, A.; Temirov, R.; Soubatch, S.; Schöll, A.; Bendounan, A.; Reinert, F.; Lee, T. L.; Tautz, F. S.; Sokolowski, M.; Umbach, E. *Phys. Rev. Lett.* **2008**, *100*, 136103.
(9) Yamane, H.; Kanai, K.; Ouchi, Y.; Ueno, N.; Seki, K. *J. Electron Spectrosc. Relat. Phenom.* **2009**, *174*, 28–34.
(10) Schöll, A.; Kilian, L.; Zou, Y.; Ziroff, J.; Hame, S.; Reinert, F.; Umbach, E.; Fink, R. H. *Science* **2010**, *329*, 303–05.
(11) Yang, A.; Shipman, S. T.; Garrett-Roe, S.; Johns, J.; Strader, M.; Szymanski, P.; Muller, E.; Harris, C. *J. Phys. Chem. C* **2008**, *112*, 2506–13.
(12) Marks, M.; Zaitsev, N. L.; Schmidt, B.; Schwalb, C. H.; Schöll, A.; Nechaev, I. A.; Echenique, P. M.; Chulkov, E. V.; Höfer, U. *Phys. Rev. B* **2011**, *84*, 081301.
(13) Stadler, C.; Hansen, S.; Kröger, I.; Kumpf, C.; Umbach, E. *Nat. Phys.* **2009**, *5*, 153–58.
(14) Dougherty, D. B.; Jin, W.; Cullen, W. G.; Reutt-Robey, J. E.; Robey, S. W. *J. Phys. Chem. C* **2008**, *112*, 20334–39.
(15) Sakamoto, Y.; Suzuki, T.; Kobayashi, M.; Gao, Y.; Fukai, Y.; Inoue, Y.; Sato, F.; Tokito, S. *J. Am. Chem. Soc.* **2004**, *126*, 8138–40.
(16) Ruiz, R.; Choudhary, D.; Nickel, B.; Toccoli, T.; Chang, K. C.; Mayer, A. C.; Clancy, P.; Blakely, J. M.; Headrick, R. L.; Iannotta, S.; Malliaras, G. G. *Chem. Mater.* **2004**, *16*, 4497–4508.
(17) Wong, S. L.; Huang, H.; Huang, Y. L.; Wang, Y. Z.; Gao, X. Y.; Suzuki, T.; Chen, W.; Wee, A. T. S. *J. Phys. Chem. C* **2010**, *114*, 9356–61.
(18) Götzen, J.; Schwalb, C. H.; Schmidt, C.; Mette, G.; Höfer, U.; Witte, G. *Langmuir* **2011**, *27*, 993.
(19) Duhm, S.; Hosoumi, S.; Salzmann, I.; Gerlach, A.; Oehzelt, M.; Wedl, B.; Lee, T. L.; Schreiber, F.; Koch, N.; Ueno, N.; Kera, S. *Phys. Rev. B* **2010**, *81*, 045418.
(20) Toyoda, K.; Hamada, I.; Lee, K.; Yanagisawa, S.; Morikawa, Y. *J. Phys. Chem. C* **2011**, *115*, 5767–72.
(21) Ge, N. H.; Wong, C. M.; Lingle, R. L.; McNeill, J. D.; Gaffney, K. J.; Harris, C. B. *Science* **1998**, *279*, 202–05.
(22) Velic, D.; Hotzel, A.; Wolf, M.; Ertl, G. *J. Chem. Phys.* **1998**, *109*, 9155–65.
(23) Petek, H.; Weida, M. J.; Nagano, H.; Ogawa, S. *Science* **2000**, *288*, 1402–04.
(24) Cinchetti, M.; Heimer, K.; Wüstenberg, J.; Andreyev, O.; Bauer, M.; Lach, S.; Ziegler, C.; Gao, Y.; Aeschlimann, M. *Nat. Mater.* **2008**, *10*, 1.
(25) Rohleder, M.; Berthold, W.; Güdde, J.; Höfer, U. *Phys. Rev. Lett.* **2005**, *94*, 017401.
(26) Muntwiler, M.; Yang, Q.; Tisdale, W. A.; Zhu, X. Y. *Phys. Rev. Lett.* **2008**, *101*, 196403.
(27) Stähler, J.; Gahl, C.; Bovensiepen, U.; Wolf, M. *J. Phys. Chem. B* **2006**, *110*, 9637–44.
(28) Hagen, S.; Luo, Y.; Haag, R.; Wolf, M.; Tegeder, P. *New J. Phys.* **2010**, *12*, 125022.
(29) Shibuta, M.; Yamamoto, K.; Miyakubo, K.; Yamada, T.; Munakata, T. *Phys. Rev. B* **2010**, *81*, 115426.
(30) Echenique, P. M.; Pendry, J. B. *J. Phys. C: Solid State Phys.* **1978**, *11*, 2065–75.
(31) Giesen, K.; Hage, F.; Himpsel, F. J.; Riess, H. J.; Steinmann, W. *Phys. Rev. Lett.* **1985**, *55*, 300–03.
(32) Höfer, U.; Shumay, I. L.; Reuß, C.; Thomann, U.; Wallauer, W.; Fauster, T. *Science* **1997**, *277*, 1480–1482.
(33) Harris, C. B.; Ge, N. H.; Lingle, R. L.; McNeill, J. D.; Wong, C. M. *Annu. Rev. Phys. Chem.* **1997**, *48*, 711–44.
(34) Hotzel, A.; Ishioka, K.; Knoesel, E.; Wolf, M.; Ertl, G. *Chem. Phys. Lett.* **1998**, *285*, 271–77.
(35) Reuß, C.; Shumay, I. L.; Thomann, U.; Kutschera, M.; Weinelt, M.; Fauster, T.; Höfer, U. *Phys. Rev. Lett.* **1999**, *82*, 153–156.

(36) Güdde, J.; Berthold, W.; Höfer, U. *Chem. Rev.* **2006**, *106*, 4261–4280.
(37) Schwalb, C. H.; Marks, M.; Sachs, S.; Schöll, A.; Umbach, E.; Höfer, U. *Eur. J. Phys. B* **2010**, *75*, 23.
(38) Muller, E. A.; Johns, J. E.; Caplins, B. W.; Harris, C. B. *Phys. Rev. B* **2011**, *83*, 165422.
(39) Fischer, R.; Schuppler, S.; Fischer, N.; Fauster, T.; Steinmann, W. *Phys. Rev. Lett.* **1993**, *70*, 654–57.
(40) Berthold, W.; Feulner, P.; Höfer, U. *Surf. Sci.* **2004**, *548*, L13.
(41) Sachs, S.; Schwalb, C. H.; Marks, M.; Schöll, A.; Reinert, F.; Umbach, E.; Höfer, U. *J. Chem. Phys.* **2009**, *131*, 144701.
(42) Lukas, S.; Söhnchen, S.; Witte, G.; Wöll, C. *ChemPhysChem* **2004**, *5*, 266–270.
(43) Pontius, N.; Sametoglu, V.; Petek, H. *Phys. Rev. B* **2005**, *72*, 115105.
(44) Marks, M.; Schwalb, C. H.; Schubert, K.; Güdde, J.; Höfer, U. *Phys. Rev. B* **2012**, *84*, 245402.
(45) Shumay, I. L.; Höfer, U.; Thomann, U.; Reuß, C.; Wallauer, W.; Fauster, T. *Phys. Rev. B* **1998**, *58*, 13974–13981.
(46) Knoesel, E.; Hotzel, A.; Wolf, M. *J. Electron Spectrosc. Relat. Phenom.* **1998**, *88*, 577–84.
(47) de Oteyza, D. G.; Wakayama, Y.; Liu, X.; Yang, W.; Cook, P. L.; Himpsel, F. J.; Ortega, J. E. *Chem. Phys. Lett.* **2010**, *490*, 54–57.
(48) Kowarik, S.; Broch, K.; Hinderhofer, A.; Schwartzberg, A.; Osso, J. O.; Kilcoyne, D.; Schreiber, F.; Leone, S. R. *J. Phys. Chem. C* **2010**, *114*, 13061–67.
(49) Alagia, M.; Baldacchini, C.; Betti, M. G.; Bussolotti, F.; Carravetta, V.; Ekstrom, U.; Mariani, C.; Stranges, S. *J. Chem. Phys.* **2005**, *122*, 124305.
(50) Robin, M. B.; Ishii, I.; McLaren, R.; Hitchcock, A. P. *J. Electron Spectrosc. Relat. Phenom.* **1988**, *47*, 53–92.
(51) Stöhr, J. *NEXAFS Spectroscopy*; Springer: Berlin, Germany, 1992.
(52) Kowarik, S.; Gerlach, A.; Hinderhofer, A.; Milita, S.; Borgatti, F.; Zontone, F.; Suzuki, T.; Biscarini, F.; Schreiber, F. *Phys. Status Solidi RRL* **2008**, *2*, 120–22.
(53) Käfer, D.; Witte, G. *Chem. Phys. Lett.* **2007**, *442*, 376–83.
(54) Käfer, D.; Ruppel, L.; Witte, G. *Phys. Rev. B* **2007**, *75*, 085309.
(55) Eremtchenko, M.; Temirov, R.; Bauer, D.; Schaefer, J. A.; Tautz, F. S. *Phys. Rev. B* **2005**, *72*, 115430.
(56) Seidel, C.; Ellerbrake, R.; Gross, L.; Fuchs, H. *Phys. Rev. B* **2001**, *64*, 195418.
(57) Manandhar, K.; Parkinson, B. A. *J. Phys. Chem. C* **2010**, *114*, 15394–402.
(58) Chizhov, I.; Scoles, G.; Kahn, A. *Langmuir* **2000**, *16*, 4358–61.
(59) Langner, A.; Hauschild, A.; Fahrenhoz, S.; Sokolowski, M. *Surf. Sci.* **2005**, *574*, 153–165.
(60) Soubatch, S.; Temirov, R; Tautz, F. S. *Phys. Status Solidi A* **2008**, *205*, 511.
(61) Stadtmüller, B.; Kröger, I.; Reinert, F.; Kumpf, C. *Phys. Rev. B* **2011**, *83*, 085416.
(62) Fuhrmann, D.; Wöll, C. *Surf. Sci.* **1997**, *377*, 544.
(63) Hansen, F. Y.; Herwig, K. W.; Matthies, B.; Taub, H. *Phys. Rev. Lett.* **1999**, *83*, 2362–2365.
(64) Sakamoto, Y.; Suzuki, T.; Kobayashi, M.; Gao, Y.; Fukai, Y.; Inoue, Y.; Sato, F.; Tokito, S. *J. Am. Chem. Soc.* **2004**, *126*, 8138–8140.
(65) Käfer, D.; Wöll, C.; Witte, G. *Appl. Phys. A: Mater. Sci. Process.* **2009**, *95*, 273–284.
(66) Götzen, J.; Käfer, D.; Wöll, C.; Witte, G. *Phys. Rev. B* **2010**, *81*, 085440.

5.5 Article V: Vibrational Davydov-Splittings and Collective Mode Polarizations in Oriented Organic Semiconductor Crystals

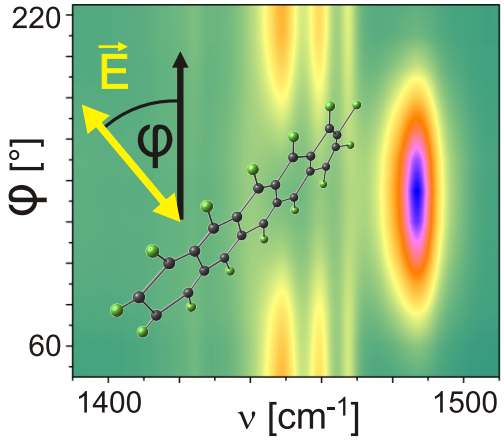

5.5.1 Abstract

Vibrational properties of highly ordered crystalline perfluoropentacene (PFP) films epitaxially grown on KCl(100) and NaF(100) substrates have been studied by means of transmission infrared spectroscopy and density functional theory. The different molecular orientations adopted by PFP on both substrates (standing vs lying) and their epitaxial ordering enable precise polarization-resolved measurements along individual crystallographic directions and thus allow an unambiguous experimental determination of the polarization of the IR modes. Computations of the vibrational spectra beyond the single-molecule approximation were employed at the periodic dispersion-corrected density functional level (PBE-D2PBC) and compared with nonperiodic calculations (PBE-D2/def2-TZVPP). Thereby, a detailed mode assignment based on vibrational energies and polarization information was attained. A microscopic explanation for the experimentally observed Davydov splitting of some modes and the IR inactivity of others was derived based on the mutual coupling of the dynamical dipole moments of the two molecules within the unit cell. Experimentally observed modes not covered by our theoretical analysis have been identified as combination bands of IR-active modes coupled to totally symmetric modes of similar displacement patterns. These findings have important implications for future studies on structure and charge transport in organic semiconductors and the validation of theoretical approaches for the modeling of vibrational spectra.

5.5.2 Methods

Density Functional Theory, Fourier-Transform-Infrared-Spectroscopy, Organic Molecular Beam Deposition, Polarized Optical Microscopy

5.5.3 Own Contribution

All samples have been prepared by myself. I have planned and conducted all experiments by myself, with some initial assistance and experimental instructions by Peter Jakob. The DFT calculations have been performed by Ralf Tonner with assistance of Mehmet Ali Celik. I have prepared the data for publication and written the major part of the manuscript, while Peter Jakob, Ralf Tonner and Gregor Witte have helped to improve it.

THE JOURNAL OF PHYSICAL CHEMISTRY C

Article

pubs.acs.org/JPCC

Vibrational Davydov Splittings and Collective Mode Polarizations in Oriented Organic Semiconductor Crystals

Tobias Breuer,[†] Mehmet A. Celik,[‡] Peter Jakob,[†] Ralf Tonner,*[,‡] and Gregor Witte*[,†]

[†]Department of Physics and [‡]Department of Chemistry, Philipps-University Marburg, Germany

Supporting Information

ABSTRACT: Vibrational properties of highly ordered crystalline perfluoropentacene (PFP) films epitaxially grown on KCl(100) and NaF(100) substrates have been studied by means of transmission infrared spectroscopy and density functional theory. The different molecular orientations adopted by PFP on both substrates (standing vs lying) and their epitaxial ordering enable precise polarization-resolved measurements along individual crystallographic directions and thus allow an unambiguous experimental determination of the polarization of the IR modes. Computations of the vibrational spectra beyond the single-molecule approximation were employed at the periodic dispersion-corrected density functional level (PBE-D2$_{PBC}$) and compared with nonperiodic calculations (PBE-D2/def2-TZVPP). Thereby, a detailed mode assignment based on vibrational energies and polarization information was attained. A microscopic explanation for the experimentally observed Davydov splitting of some modes and the IR inactivity of others was derived based on the mutual coupling of the dynamical dipole moments of the two molecules within the unit cell. Experimentally observed modes not covered by our theoretical analysis have been identified as combination bands of IR-active modes coupled to totally symmetric modes of similar displacement patterns. These findings have important implications for future studies on structure and charge transport in organic semiconductors and the validation of theoretical approaches for the modeling of vibrational spectra.

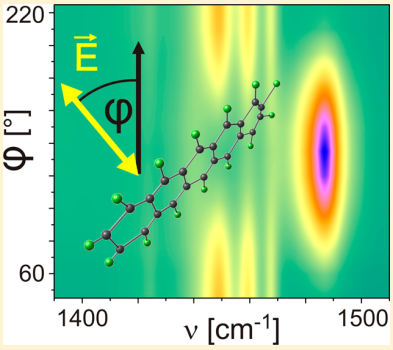

I. INTRODUCTION

Infrared (IR) spectroscopy is one of the most common spectroscopic techniques in material science used to identify molecular compounds and to detect chemical functional groups.[1] It combines nondestructiveness with high spectral resolution and sensitivity allowing us, in particular, to characterize fragile or radiation-sensitive molecular materials[2] and thus to elucidate metastable intermediates occurring, for instance, in heterogeneous catalysis.[3] Moreover, it can be utilized to determine the molecular orientation of adsorbates at interfaces[4] or to derive conformational information.[5] Beyond that, IR spectroscopy can be applied to a wide range of sample types such as gases, liquids, and solids, hence making this technique quite versatile.[6] An important basis for the analysis of IR spectra is the precise identification and assignment of the measured vibrational bands. As functional groups exhibit characteristic spectral features, they are commonly used as fingerprints to identify molecular species.[7] This approach is, however, of limited use when analyzing nonfunctionalized conjugated aromatic molecules: instead of localized vibrations of distinct chemical bonds (except some C−H stretching modes), the displacement patterns appear more distributed (delocalized) over the entire molecule hence yielding phonon-like modes.

Today, a common approach to analyze vibrational spectra of molecules is based on quantum chemical calculations. Density functional theory (DFT) has become the standard method for ab initio investigations of materials[8] and was also found to describe adequately the vibrational spectra of molecular crystals.[9] A well-known shortcoming of present-day density functionals is the inability to describe dispersion interactions correctly. (See ref 10 and references therein.) This circumstance is important not only for investigations of free molecules[11] but also even more for molecular crystals that are held together mainly by van der Waals forces. Besides other recent developments tackling the dispersion problem in DFT,[12] the semiempirical correction scheme by Grimme (DFT-D) gives promising results.[13] It was found to describe accurately molecular crystals[14] and also to be in agreement with more elaborate second-order perturbation theory (MP2) methods.[15] In particular, it promises to correct the known overestimation of lattice parameters associated with the PBE functional.[16]

In most joint experimental and theoretical studies, the assignment of vibrational modes relies on calculations of the free molecule and matching of vibrational energy levels between theory and experiment. Primarily, this provides a reasonable description, although it disregards energetic shifts due to polarization effects of surrounding molecules. It inherently fails, however, to describe the so-called Davydov splitting (also denoted as factor-group splitting)[17] occurring for molecular solids with nonprimitive basis.[18] The factor-group analysis method for the interpretation of vibrational spectra is

Received: April 27, 2012
Revised: June 8, 2012
Published: June 13, 2012

much older though.[19] By contributions from several groups,[18a,20] it became clear that these splittings cannot be neglected when an in-depth understanding of the vibrational spectra is aimed at, demanding for a theoretical description beyond the single molecule approximation. An analysis of Davydov splittings based on ab initio methods and taking into account mode polarizations has not been attempted up to now.

Polycyclic aromatic hydrocarbon (PAH) molecules have become the focus of research for various reasons. On the one hand, it was found that emission spectra of most galactic and extragalactic sources are dominated by IR features of large PAHs that had caused a vital interest in their vibrational modes to identify such extra-terrestrial organic species.[21] In addition, PAHs have attracted significant attention in recent years because their electronic properties render them promising materials for the fabrication of organic electronic devices such as organic field-effect transistors (OFETs).[22] In view of the importance of vibronic coupling for the charge-transport mechanism in such π-conjugated molecular semiconductors,[23] a detailed understanding of the vibrational properties and their coupling in molecular solids is of utmost importance.

Although IR studies have been carried out in the past for molecular solids, they were mostly limited to polycrystalline films, whereas only rather few studies of molecular single crystals have been reported.[18c,d,24] More specific, these crystal studies were essentially restricted to molecular salts or asymmetrically substituted molecules that exhibit notable electrostatic interactions. By contrast, purely van der Waals bound crystals that are of interest in connection with organic electronics have not been studied systematically. In part, this is due to difficulties in growing sufficiently sized crystals. Whereas organic semiconductor crystals have been successfully grown by physical vapor transport method, this yields, however, in many cases plate-like or flaky crystals with a thickness of few micrometers only,[25] which restricts access to one crystallographic face only. In addition, many aromatic molecular materials exhibit tremendous absorptions, which limits transmission measurements to rather thin crystals (<100 μm). By contrast, the quantitative analysis of reflection absorption measurements is complicated by rotation of the polarization. So far, these difficulties have hampered a detailed comparison of theoretical and experimental data that is required to improve theoretical descriptions further, eventually enabling exact theoretical analyses of more complicated systems, like multinary molecular crystals.

Here we report on a detailed analysis of the vibrational properties of perfluoropentacene (PFP) crystals. Whereas the molecular symmetry of this recently synthesized n-type semiconductor[26] is identical to that of the nonfluorinated analog, pentacene (PEN), the reduced masses of C−F and C−H units are quite different. As a consequence, different vibrational energies are expected, which in turn also affect the reorganization energy and thus the activation of charge transport properties.[23b] This makes PFP an interesting model system to study vibrational properties of fluorinated acenes and to compare with hydrogenated oligoacenes, which exhibit preferentially p-type conduction. Although some IR modes of polycrystalline PFP films have been previously reported,[27] no complete vibrational analysis and mode assignments are yet available. In its crystalline bulk phase, PFP exhibits a layered structure where molecules are oriented upright in such layers, whereas the aromatic planes adopt a perpendicular face-on-edge herringbone arrangement, yielding an almost rectangular unit cell (cf. Figure 1b,c). In previous works, we have demonstrated that epitaxial PFP films can be grown on

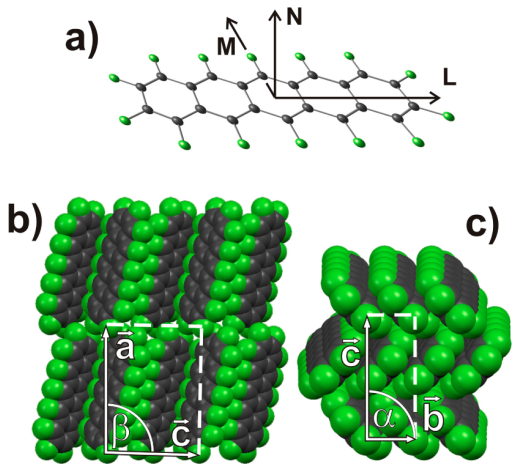

Figure 1. (a) Perfluoropentacene molecule with designation of the molecular coordinate system (LMN). (b) View onto the (**ac**)-plane (i.e., along the [010] direction) and (c) view onto the (**bc**)-plane (i.e., along the [100] direction) of the molecular PFP crystal. Note that due to the triclinic lattice the unit cell vector **a** is not exactly perpendicular to the (**bc**)-plane but forms an angle of 91.5°.

NaF(100) and KCl(100) surfaces.[28] Interestingly, on these substrates, different molecular and crystalline orientations (standing or lying) are adopted, which, in combination with the IR transparency of the supports, enable detailed polarization-resolved transmission IR measurements of crystalline PFP films. This allows, in particular, an experimental determination of the mode polarizations from the appearance and disappearance of IR modes in spectra that were recorded with the electric field vector oriented along different crystallographic directions and thus different molecular orientations. Accompanying ab initio crystal calculations reproduce the energy *and* polarization of the IR modes well and provide a detailed explanation of the observed Davydov splitting behavior of the majority of modes. Moreover, additional modes that appear in the experimental spectrum are identified as combination modes of fundamental IR-active modes and symmetric vibrational modes.

II. METHODOLOGY

II.1. Experimental Section. PFP (purity >99%) was purchased from Kanto Denka Kogoyo, whereas PEN (purity > 99.9%) was obtained from Sigma Aldrich. To provide reference samples with isotropic molecular orientation, KBr pellets of each component were fabricated by grinding a mass fraction of one thousandth into KBr powder and compressing disks with a thickness of 0.5 mm. Higher concentrations of PFP or thicker pellets led to saturation effects in the IR spectra.

Uniformly oriented and crystalline PFP films were prepared under high vacuum conditions by molecular beam deposition onto KCl(100) and NaF(100) surfaces. The layers were evaporated from a Knudsen cell at deposition rates of 6 Å/min monitored by quartz crystal microbalance.

The alkali halide surfaces have been prepared by cleaving slices of ∼2 mm from single-crystal rods (Korth Kristalle) in air. Subsequently, the samples were transferred into the vacuum system using a load-lock system and annealed at 450 K in

dx.doi.org/10.1021/jp304080g | J. Phys. Chem. C 2012, 116, 14491−14503

Table 1. Comparison of Experimental and Theoretical PFP Crystal Lattice Parameters[a]

	a	b	c	α	β	γ	V
exp.[26]	15.51(1)	4.490(4)	11.449(11)	90	91.567(13)	90	797.0(13)
PBE-D2$_{PBC}$	15.546	4.356	11.352	90	91.490	90	768.4
PBE	15.678	4.727	11.927	90	90.416	90	883.9

[a]Lengths, angles between lattice vectors, and unit cell volume are given in Å, degrees, and Å^3, respectively.

vacuum to remove adsorbed water. The resulting structure of the various films had been thoroughly analyzed in previous works by means of atomic force microscopy, X-ray diffraction, optical spectroscopy, and polarization microscopy.[28]

All IR spectra were measured with a Bruker IFS66v FTIR spectrometer using a water-cooled globar as a light source, a wire-grid polarizer, and a liquid nitrogen-cooled MCT detector that allows measurements in the spectral range of 700−5000 cm^{-1}. Because of the IR transparency of the substrates, all spectra have been recorded in transmission geometry. All data were acquired with a resolution of 2 cm^{-1} and 2000 scans were averaged to achieve adequate statistics. To minimize IR signatures due to gas-phase water and CO_2 contaminations, we evacuated the spectrometer at least 30 min before data acquisition. Afterward, the signal intensity of the corresponding absorption bands at 1300−2000 and 3500−4000 cm^{-1} (water) as well as around 2350 cm^{-1} (CO_2) had virtually vanished. To omit substrate effects as well as interference and contaminations from the used optics, we post-processed the measured spectra by rationing with spectra of uncovered alkali halide substrates or pure KBr pellets, respectively, to obtain the absorbance of PFP.

II.2. Computational Details. *a. Free Molecule.* Geometry optimizations without symmetry constraints have been carried out using the Gaussian09 optimizer (standard convergence criteria)[29] with Turbomole[30] (version 6.3.1) energies (convergence criterion 10^{-8} a.u. and grid-size m4) and gradients with the functional and basis set combination PBE[31]/def2-TZVPP[32] considering dispersion effects by applying the D2 method for the sake of consistency with the periodic calculations.[13] This level of approximation is denoted by PBE-D2 in the following. Further calculations have been carried out without dispersion correction (PBE) and with the functionals BP86[33] and B3LYP[34] as well as ab initio methods (MP2). Other basis sets (def2-SVP, def2-QZVPP)[32] were tested for convergence checks. Stationary points were characterized as minima by calculating the Hessian matrix analytically at this level of theory.[35] The resolution of identity method has been applied throughout for the approximation of four-center integrals.[36]

b. Molecular Crystal. The molecular crystal of PFP was studied by means of DFT calculations employing the Vienna Ab Initio Simulation Package (VASP 5.2),[37] which uses periodic boundary conditions (PBCs). The generalized gradient approximation (GGA) using the exchange-correlation functional proposed by Perdew, Burke, and Ernzerhof (PBE)[31] was used in combination with a plane-wave basis set. The projector-augmented wave (PAW) method[38] was used and enabled a truncation of the plane-wave basis set at a kinetic energy of 500 eV. The projection operators for the nonlocal part of the pseudopotentials were evaluated in real space (LREAL = Auto) with the exception of the linear response calculations. The Brillouin zone for the molecular crystal calculation was sampled by a 2 × 6 × 4 k-point mesh generated via the Monkhorst−Pack method.[39]

Structural optimization was performed starting from the crystal structure derived from XRD measurements[26] by means of a conjugate-gradient or quasi-Newton algorithm for ionic positions and cell parameters until the forces converged to 2×10^{-2} eV Å^{-1} and the energy during SCF cycles converged to 10^{-5} eV. Vibrational frequencies at the Γ-point of the molecular crystal were calculated through building up the force constant matrix in a linear response approach. IR intensities were calculated with a linear response approach originally formulated by Giannozzi and Baroni,[40] as implemented in VASP for the PAW formalism.[41,42]

Dispersion effects have been considered by the semiempirical correction scheme proposed by Grimme in the D2 formulation[13] as implemented in VASP,[14c] which is crucial for an accurate description of molecular crystals dominated by dispersive interactions. This methodology is abbreviated PBE-D2$_{PBC}$ in the following. All vibrational calculations were carried out in the harmonic approximation, and representations of IR spectra used a Lorentzian broadening with an fwhm of 5 cm^{-1}. To provide an easier access to comparing the computed and the experimental spectrum, we applied a scaling factor close to unity for all spectra (exact value discussed in Results section). The intensity of IR-active modes depends on the magnitude of the dynamical dipole moment $\tilde{\mu} = \partial\mu/\partial q$ (i.e., the derivative of the molecular dipole moment μ with respect to the normal coordinate q) according to ($I \propto \tilde{\mu}^2$)[43] and is given relative to the most intense mode. The measured absorbance spectra were likewise normalized to the most intense mode and are presented in units of intensity ($I \propto A$), which is a measure for the oscillator strength of the corresponding modes.

c. Validation of Computational Methods. Because the simulation of vibrational spectra is strongly dependent on an accurate reproduction of the molecular structure, the obtained optimal geometries are briefly discussed in this section. The experimental structure is reproduced sufficiently accurate with both theoretical approximations, resulting in a root-mean-square error of 0.011 (PBE-D2) and 0.013 Å (PBE-D2$_{PBC}$), respectively, for all bond lengths (Figure S1 in Supporting Information). Comparison with other methods (PBE, BP86, B3LYP, MP2) and basis sets (def2-SVP, def2-QZVPP) showed that all methods are comparable in their accuracy, but a basis set of triple-ζ quality is necessary to obtain accurate geometries. (Details can be found in Table S1 in the Supporting Information.) Deviations of up to 12 cm^{-1} are found between PBE and PBE-D2 calculations of vibrational frequencies.

Whereas the free molecule exhibits the full D_{2h} point-group symmetry, PFP in the solid state only shows C_i symmetry due to site symmetry constraints that are reproduced in the calculation. For the crystal calculation, the lattice parameters obtained in the optimization can also be compared with experimental results, as shown in Table 1. In agreement with the literature, we find that PBE overestimates the volume of the unit cell by ∼11%;[14c,44] PBE-D2$_{PBC}$ deviates by only 3.6%. The overbinding observed for the latter method has also been previously found and might be explained with temperature

dx.doi.org/10.1021/jp304080g | J. Phys. Chem. C 2012, 116, 14491−14503

effects in the experimental structure, as calculations were performed for T = 0 K, whereas the X-ray measurements were carried out at T = 173 K.[44] This indicates that our computational methodology delivers accurate structures and suggests reliable calculations of the vibrational spectra.

III. RESULTS

III.1. IR-Spectra of PEN and PFP Pellets. Figure 2 shows a comparison of IR spectra recorded for PFP and PEN pestled in KBr-pellets. Besides the characteristic C−H modes of the stretching region around 3050 cm^{-1}, PEN exhibits only very few intense vibrational modes between 750 and 1400 cm^{-1}. This appears to be a characteristic signature of polycyclic hydrocarbons (PAHs) that have been systematically studied in the past by means of matrix isolation techniques.[45] By contrast, for the perfluorinated species, no modes occur above 1700 cm^{-1} that can be attributed to the distinctly different reduced masses of $C-H$ and $C-F$ yielding an expected frequency reduction by a factor of 0.36. Beyond that, the IR spectrum of PFP reveals a large number of modes appearing in the same frequency range as for the nonfluorinated analog, but they are distinctly more intense. To quantify the integral absorbance of PEN and PFP, we compared IR spectra of stoichiometrically equivalent amounts of both compounds. In this context, we note that the small portions of PEN and PFP used in the pellets limit the weighing of equivalent amounts of both materials within an error of ~20%. In comparison, the integrals over these spectra in the spectral range from 700 cm^{-1} to 3200 cm^{-1} yield, however, values of 25.8 (PEN) and 315.6 (PFP), thus proving a clearly stronger absorbance of IR radiation in the case of PFP compared with PEN. Similar findings have been reported before for smaller acenes such as perfluoronaphthalene.[45] These properties cannot be explained by a simple mass loading and instead represent characteristic differences in the vibrational properties between hydrogenated and fluorinated PAHs. As will be discussed below in combination with our theoretical analysis, perfluorination causes a distinct modification of the displacement pattern. In the case of PEN, essentially the hydrogen atoms are vibrating with respect to the rather motionless carbon frame, whereas in PFP the carbon frame is largely displaced relative to the heavier F-hemline.

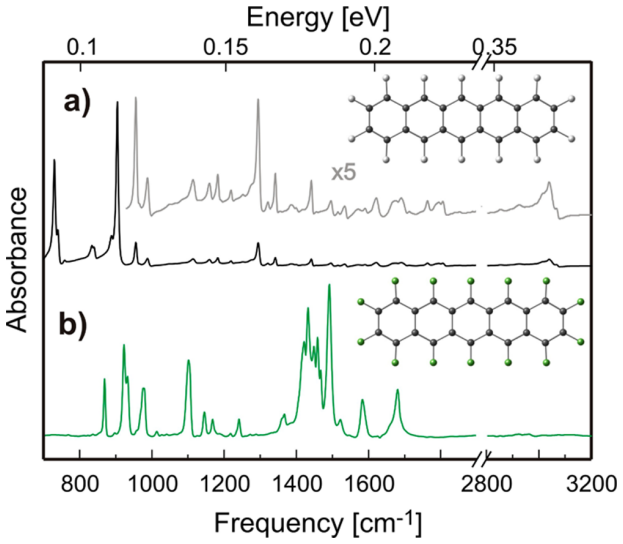

Figure 2. IR absorption spectra of (a) pentacene (PEN) and (b) perfluoropentacene (PFP) pestled in KBr pellets recorded with the same detection sensitivity.

III.2. Oriented PFP Thin Films. The isotropic molecular orientation in pellets allows the excitation of all IR-active modes; the pellet spectrum, however, does not provide any information on the mode polarization. To also determine the polarization of the various vibrational modes, we carried out additional measurements on PFP films with well-defined molecular orientations. Utilizing the exceptional epitaxial growth of PFP films on NaF(100) and KCl(100) substrates yields characteristic crystalline orientations: on sodium fluoride, (100)-oriented films are grown, where PFP molecules adopt a uniform upright orientation, whereas (102)-oriented films are formed on potassium chloride displaying a recumbent molecular orientation.[28] Considering the crystal structure of PFP,[26] these different film orientations yield tilt angles of the long molecular axis (**L**, cf. Figure 1a) with respect to the surface plane of $\theta_{(100)}$ = 79° on NaF and $\theta_{(102)}$ = 8° on KCl, as shown schematically in Figure 3. The intensity, determined from the measured absorbance, of IR-active modes depends on the orientation of the respective dynamical dipole moments, $\tilde{\mu}$, relative to the electric field vector **E** of the incident light, that is, $I \approx |\mathbf{E}\cdot\tilde{\mu}|^2$. Therefore, the intensity of PFP modes polarized along the long molecular axis scales proportional to $(\cos\alpha)^2$, with α being the angle between **E** and $\tilde{\mu}$. This yields an almost complete polarization contrast (0.04 vs 0.98) for PFP films deposited on the two substrates. Therefore, from the appearance and disappearance of IR modes, a clear distinction between polarizations along (on KCl) or perpendicular to the long molecular axis (on NaF) can be concluded.

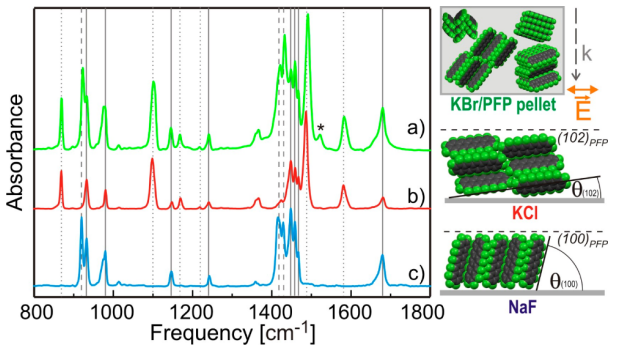

Figure 3. Transmission IR spectra recorded for differently oriented PFP molecules: (a) isotropic orientation in KBr pellet, (b) recumbent orientation in thin films on KCl(100), and (c) upright orientation in thin films on NaF(100) together with schematic representations of the molecular orientation relative to the incident light shown on the right-hand side. Solid lines mark modes that appear in both orientations, dotted lines mark those only active in PFP/KCl (100), and dashed lines mark those that exclusively appear in PFP/NaF (100) films.

Figure 3 shows a comparison of the PFP/KBr pellet spectrum with the IR-transmission spectra recorded for 150 nm PFP films grown on KCl(100) and NaF(100), respectively. The spectra of PFP/NaF and PFP/KCl have some modes in common (marked by solid lines in Figure 3), whereas others are active only on the one substrate and inactive on the other one and vice versa. For example, the vibrational modes at 869, 1169, 1486, and 1581 cm^{-1} are active in the PFP/KBr-pellet

dx.doi.org/10.1021/jp304080g | J. Phys. Chem. C 2012, 116, 14491−14503

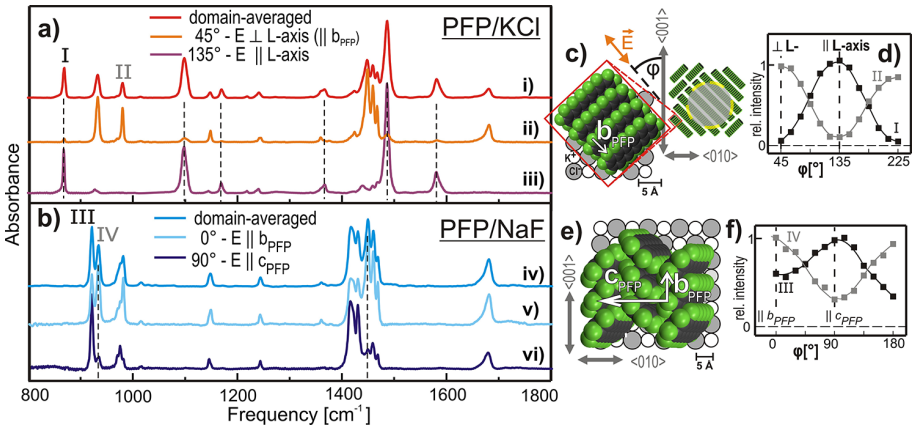

Figure 4. Polarization-resolved IR absorption spectra of epitaxial PFP films on (a) KCl(100) and (b) NaF(100). (c) Sketch of the aperture setup on single-crystalline domains on KCl(100). (d) Intensity of two IR modes (869 and 979 cm^{-1}) at different light polarizations in 15° steps (in PFP/KCl film). (e) Top-view of the PFP(100) plane, which is adopted in thin film growth of PFP on NaF, including unit cell axes and azimuth directions of the substrate. (f) Same as panel d for IR modes at 919 and 933 cm^{-1} (PFP/NaF film).

and in the PFP/KCl thin film (dotted lines), whereas they are inactive in the case of PFP/NaF, hence reflecting a polarization along the molecular **L**-axis. Other modes, like those at 919 and 1419 cm^{-1}, disappear only for PFP films on KCl (dashed lines) and thus indicate a polarization perpendicular to the **L**-axis. We note that such a polarization assignment was also achieved for the closely spaced vibrational bands between 1400 and 1500 cm^{-1} (cf. Figure S3 in the Supporting Information). A superposition of IR-spectra obtained for PFP-films on the two substrates actually reproduces all modes appearing in the PFP pellet spectrum. Only small variations in the mode energies of <3 cm^{-1} are found for the various films, which are attributed to slight lattice relaxations due to varying degrees of lattice match between the substrate and differently oriented epitaxial PFP films.[28] Merely the mode at 1486 cm^{-1} is shifted by as much as 5 cm^{-1} when comparing the crystalline PFP film on KCl and the pellet spectrum (cf. Figure S3, Supporting Information). We note further that the mode at 1522 cm^{-1} was only detected in the PFP pellet spectrum, whereas it is missing in the crystalline films on the alkali halides and thus is attributed to an impurity, as film preparation by evaporation leads to an additional purification.

The PFP lattice has a nonprimitive unit cell containing $z = 2$ molecules, each consisting of n atoms. As a consequence, each of the $(3n - 6)$ vibrations of the free molecule splits into z modes in the crystal (so-called *Davydov* splitting; we do not consider librations and translational vibrations in the crystal here because they arise in a different energy window, not accessible to our experiment) so that a larger number of dipole active modes occurs for the crystalline phase[19c] compared with the free molecule. The fact that the number of IR-active modes observed in the PFP-KBr pellet equals that of a superposition of the PFP/KCl and PFP/NaF spectra thus directly proves that the IR spectrum of PFP powder grinded in KBr does not represent a *single-molecule* IR spectrum like it is obtained by gas-phase or matrix spectroscopy. Instead, the PFP powder actually consists of small microcrystallites isotropically oriented within the KBr matrix, leading to the appearance of modes exhibiting Davydov splitting, like, for example, the modes at 919 and 933 cm^{-1}, as will be discussed later.

III.3. Polarization-Dependent Measurements. Further information on the polarization of the IR-active modes can be obtained by taking advantage of the epitaxial alignment of PFP on both alkali halide substrates, which yields an alignment of the **b**-axis of the PFP lattice along the $\langle 010\rangle_{NaF}$ and $\langle 011\rangle_{KCl}$ directions, respectively.[28] Because of the four-fold symmetry of the (100) substrate surfaces, such epitaxial PFP layers appear, however, in 90° rotational domains. As a consequence, the polarization contrast is reduced to $A\cos(\varphi)^2 + A'\cos(\varphi + 90°)^2$, where φ denotes the angle between the in-plane projection of the dipole moment and a high symmetry azimuth of the substrate, for example, the $\langle 001\rangle$ direction. Note that in the case of local majorities where only one rotational domain appears, this dependency simplifies to $\cos(\varphi)^2$, whereas equally distributed domain sizes A and A' lead to a cancellation of the in-plane contrast. To avoid such a domain averaging and still enable precise azimuthally resolved IR-measurements, we positioned apertures of 1000 (PFP/KCl thin films) and 500 μm (PFP/NaF thin films) above one rotational domain with the help of a polarization microscope (cf. Figure S2, Supporting Information) by exploiting the optical anisotropy of crystalline PFP.[28] Note that this approach is only possible because PFP films on KCl form rather large uniformly oriented domains extending over several square millimeters.

Figure 4a compares domain-averaged IR spectra (without an aperture) of PFP films on KCl(100) and those of a single domain that were recorded for different azimuthal in-plane orientations of the electric-field vector of the incident linearly polarized light. The largest intensity variation occurs at angles of φ = 135 and 45° between the polarization plane and the $\langle 001\rangle_{KCl}$ direction. In those cases, the incident field vector **E** is aligned essentially parallel to the molecular **L**-axis or perpendicular, that is, along the **b**-axis of the PFP-lattice (as shown schematically in Figure 4c). A more precise characterization of the in-plane orientation of the dynamical dipole moments of the various vibrational modes was achieved by systematically acquiring IR spectra at different azimuthal positions by rotating the sample in steps of $\Delta\varphi$ = 15°. For example, the modes at 869, 1098, 1169, and 1486 cm^{-1} exhibit maximal intensity for light polarization mainly along the PFP **L**-axis (φ = 135°), whereas the modes at 933, 979, 1148, 1448, and 1459 cm^{-1} almost vanish; for light polarized along the **b**-axis (φ = 45°), the intensity of these modes is reversed. The corresponding curve progression of the modes at 869 and 933

dx.doi.org/10.1021/jp304080g | J. Phys. Chem. C 2012, 116, 14491−14503

cm^{-1}, which is shown in Figure 4d, clearly reflects the expected $(\cos \varphi)^2$-dependency. A similar behavior was also observed for other modes (marked by dashed lines in Figure 4a), thus indicating a distinct mode polarization along the **L**-axis. We note that the noncomplete vanishing of the excitation probability at the minimum is due to the fact that despite precise positioning of the aperture a small minority of the inverted rotational domain and thus orthogonal molecular orientation is simultaneously illuminated (cf. Figure S2a, Supporting Information).

The upright orientation of PFP molecules on NaF(100) substrates allows us furthermore to study also the polarization dependency of IR modes within the **bc**-plane of the PFP-lattice. Although corresponding measurements are impeded by the distinctly smaller domain sizes, which hampers exclusive illumination of only one rotational domain, a distinct in-plane polarization contrast is observed. (Positioning of the aperture is shown in Figure S2b of the Supporting Information.) As depicted in Figure 4b, for example, the modes at 933 and 1448 cm^{-1} (dashed lines) appear most intense, if the polarization plane is oriented parallel to the **b**-vector of the PFP lattice, whereas they are much weaker if **E** is perpendicular to **b** (i.e., parallel to the **c**-axis of the PFP lattice).

Interestingly, the condition that the exciting **E**-field is oriented parallel to the **b**-vector of the PFP lattice and simultaneously perpendicular to the molecular **L**-axis can be fulfilled for either PFP/KCl or PFP/NaF films if the polarization of light is adjusted appropriately. In fact, this condition is met for the second spectra of Figure 4a,b, hence explaining their similarity. Additional modes appearing in the IR spectrum of PFP/NaF can be attributed to the minority domains, which have been visualized by polarization microscopy (cf. Figure S2b, Supporting Information). Figure 4f shows the consequences of this nonideal contrast using the example of the vibration modes at 919 and 933 cm^{-1}. The mode intensity is, for every azimuthal angle, φ, significantly above zero, as the deactivation of one mode (at angles 0°, respectively, 90°) in one domain coevally leads to its full excitation in the other domain.

The complete polarization dependence of the epitaxial PFP-films on KCl (100) and NaF (100) spectra is displayed in Figure 5a,b) in false color 3D contour plot. In both cases, the individual modes are found to exhibit distinct intensity variations as the azimuthal direction of the electric field is varied, in accordance with spectra in Figure 4 and the mode polarizations in Table 2. For both substrates, the region from 1390 to 1510 cm^{-1} with narrow-spaced intense modes has been additionally displayed on an enlarged scale.

The residual mode intensity caused by the presence of orthogonally oriented minority domains can be compensated effectively by calculating difference spectra, for example, by first weighting the third spectrum (PFP/KCl, φ = 135°) in Figure 4a, such that the intense peaks (marked by a dashed line) are of the same intensity as in the second spectrum (PFP/KCl, φ = 45°), and calculating the difference of both spectra yields a (hypothetic) spectrum of one uniformly oriented domain showing only IR modes that are polarized along the **b**-vector of the PFP lattice. Analogously, spectra of pure **L**-polarization are obtained by subtracting the weighted spectrum ii from spectrum iii, whereas subtracting a weighted spectrum v from spectrum vi (PFP/NaF, φ = 90°) yields an IR-spectrum of **c**-polarized modes (see Figure S4, Supporting Information). This azimuthal dependency allows us to determine precisely the

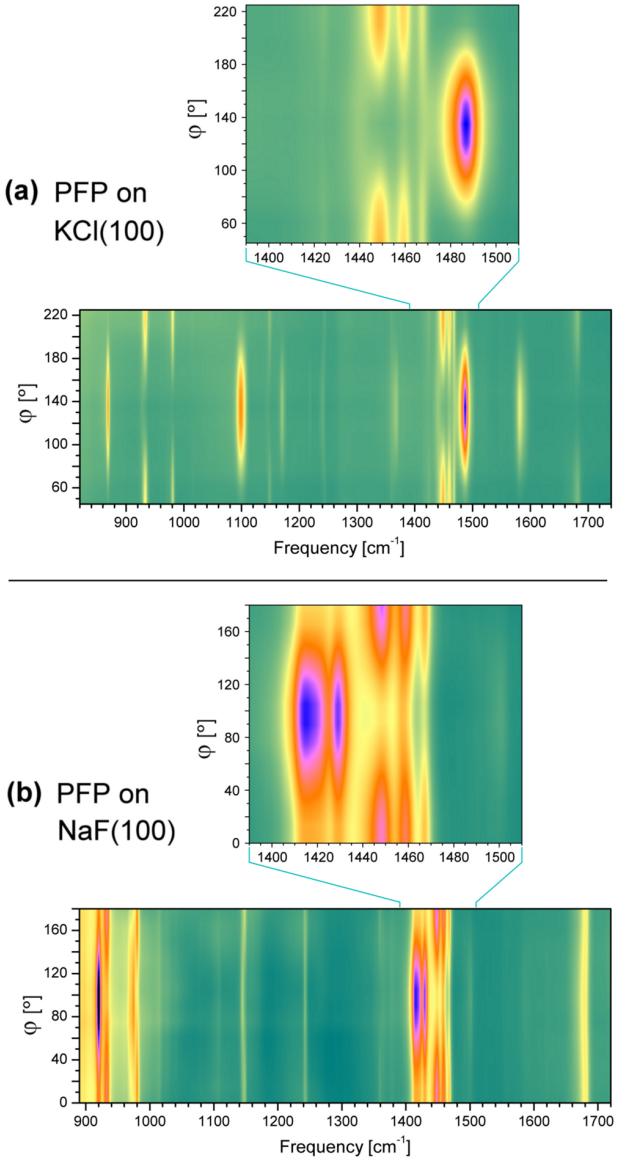

Figure 5. False color 3D plots (color coding: green−yellow−red−blue) of polarization-resolved IR absorption spectra of epitaxial PFP films on (a) KCl(100) and (b) NaF(100) with magnification of frequency range 1390−1510 cm^{-1}. The denoted angle φ represents the angle between the **E**-vector and the substrate ⟨001⟩-direction (cf. Figure 4).

polarization of all experimentally observed IR-active modes, which are summarized in Table 2. The polarization resolved measurements allow, in particular, a separation of modes accumulated in narrow spectral regions (e.g., around 1400−1500 cm^{-1}), whereas this is hardly achieved for the pellet spectrum, where the total intensity results from an incoherent superposition of differently polarized modes.

Considering that both PFP molecules in the unit cell adopt a perpendicular face-on-edge herringbone packing motif in their crystalline bulk phase (Figure 4e), the dynamical dipole moments of the **M**-polarized molecular vibrations are also expected to be orthogonal. Therefore, by simply adding the excitation probabilities of two orthogonal oriented single molecules incoherently, no **bc**-plane polarization dependence

dx.doi.org/10.1021/jp304080g | J. Phys. Chem. C 2012, 116, 14491−14503

Table 2. Frequencies (ν in cm^{-1})[a], Intensities[b] (I, Normalized to the Most Intense Mode at 1486 cm^{-1}), and Polarization (Orientation of Dynamical Dipole Moment $\tilde{\mu}$) of All Experimentally Observed IR-Active Modes in the Crystalline PFP-Films

ν	I	$\tilde{\mu}$
869	0.38	L
919	0.61	c
933	0.40	b
969	0.16	c
974	0.32	c
979	0.32	b
1098	0.51	L
1144	0.07	c
1148	0.10	b
1169	0.12	L
1218	0.03	L
1241	0.06	L
1242	0.11	c
1244	0.04	b
1360	0.11	b
1367	0.15	L
1415	0.47	c
1419	0.63	c
1425	0.08	b
1432	0.85	c
1440	0.13	L
1448	0.60	b
1457	0.20	c
1459	0.46	b
1468	0.44	b
1486	1.00	L
1581	0.25	L
1678	0.14	c
1680	0.17	b

[a]Experimental frequencies were determined in the PFP/KCl and PFP/NaF thin films. [b]Relative intensities were derived from the PFP/KBr pellet spectra.

of the IR modes would be expected. The experiment, however, reveals a distinct in-plane polarization dependence (cf. Figure 4f), thus indicating a coherent coupling of the individual vibrations of the two molecules per unit cell for excitations along and perpendicular to the **b**-axis, respectively. A detailed understanding of this observation is provided by the theoretical analysis given in the next section.

III.4. Vibrational Spectrum Calculated by Ab Initio Methods. To obtain a more detailed understanding of the vibrational spectra, quantum-chemical calculations have been carried out in the single-molecule approximation but also employing the full periodicity of the molecular crystal at the dispersion-corrected density-functional level as outlined in the computational details section. A comparison of the IR spectrum measured for the PFP/KBr pellet with the computed spectra in single-molecule approximation and with the full crystal environment is displayed in Figure 6. Because ab initio harmonic vibrational frequency calculations are known to slightly over- or under-estimate the true mode energies,[46] empirical scaling factors are used. To determine a reliable scaling factor, only those modes were considered that reveal a congruent polarization dependence between experiment and theory (modes 66, 67α, 67β, 69α, 69β, 72α, 74α, 74β, 85β, 90α, 90β, 91α, 91β, 92α, 98β, 101α, 101β). This yields a scaling factor for the calculated modes of 1.015, which reproduces the experimental mode frequencies with a standard deviation of 0.0059 cm^{-1}.

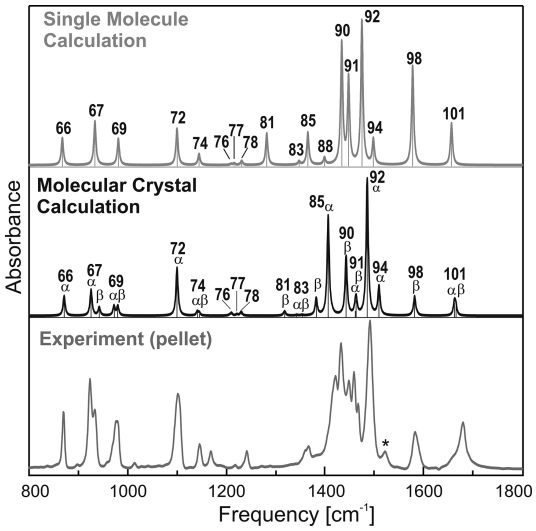

Figure 6. Comparison of experimental (KBr-pellet) and computed IR-spectra for free molecule (PBE-D2) and molecular crystal (PBE-D2$_{PBC}$) of PFP with mode assignments according to Table 3. Davydov splittings are designated with α and β for the respective modes. All calculated mode frequencies have been scaled by a factor of 1.015, and the modes have been convoluted by Lorentzian (fwhm = 5 cm^{-1}) to provide a realistic comparison with the experimental data. An impurity band is designated by *.

Note that such a comparison was only possible in the case of the crystal calculation. Therefore, the same scaling factor was also employed for the analysis of the single-molecule calculation, which is based on the same exchange-correlation functional. We note further that a straightforward approach where simply the most intense modes in experiment and theory are compared yields improper results because of the inability to reproduce all modes. Whereas the separation of valence and deformation vibrations is difficult for cyclic molecules,[47] the ordering according to irreducible representations of the point group of the molecule (D_{2h}) is not valid anymore for the symmetry-reduced molecule in the crystal (C_i). Consequently, we decided to number the vibrational modes consecutively based on mode energies derived in the computations of the single molecule. The mode numbering of the crystal calculation was provided by identifying molecular displacement patterns in the corresponding normal modes of the single-molecule vibrations.

By visual inspection of the spectra, an excellent agreement is found. The major peaks of the experimental spectrum are reproduced by the computed spectra of the isolated molecule (Figure 6), validating this approach usually chosen in the past as a first approximation. A full list of all 102 calculated modes ($3n - 6$) is available in the Supporting Information. Decisive features lacking in the free molecule spectrum are the Davydov splitting of modes. This latter effect can only be reproduced by computations considering the crystal environment (black curve in Figure 6).

Although a rigorous comparison of methods for computing vibrational spectra was not the focus of this investigation, we tested the performance of other functionals (BP86, B3LYP)

dx.doi.org/10.1021/jp304080g | J. Phys. Chem. C 2012, 116, 14491−14503

and ab initio methods (MP2) and checked the influence of adding the D2-correction to the PBE functional for the single-molecule spectrum of PFP (see Figure S5, Supporting Information).

The computed spectra show overall good agreement. Nevertheless, the intensities of individual modes slightly differ for different methods as well as their energies. Therefore, care has to be taken in comparison of single-molecule spectra with experimental results without information about mode polarizations.

Figure 7 shows exemplarily the displacement pattern of the two lowest energy molecular modes obtained in the presently

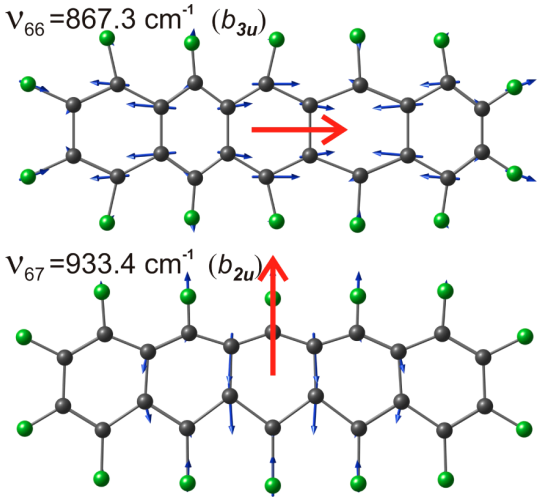

Figure 7. Displacement pattern (blue vectors), dynamical dipole moment $\tilde{\mu}$ (red arrow), and symmetry of the two vibrational modes (ν_{66} and ν_{67}) of the PFP molecule (PBE-D2). Ground-state geometry is displaced along normal modes. Note that the actual displacement vectors are enlarged.

studied spectral range above 750 cm^{-1}, namely, mode 66 (867.3 cm^{-1}) and mode 67 (933.4 cm^{-1}). This illustrates, in particular, that due to the higher mass of the fluorine atoms vibrational motion predominantly comprises the carbon frame, a correlation that also occurs in the other modes. Associated dynamical dipole moments can clearly be identified based on these displacement vectors, and vibrational symmetries can be assigned. A visualization of all modes can be found in the Supporting Information (Figure S6).

Note that we are not limited to a simple comparison of the frequencies of measured and calculated molecular vibrations but can additionally use the polarization information available from the experiment and compare them to the results obtained from the calculations. This enables a detailed matching of vibrational bands, as summarized in Table 3, where all modes with intensities larger than 1% of the most intense band are listed, together with their polarization dependence, as received from experimental and theoretical approaches.

On the basis of the available data, several observations can be made. Besides the magnitude of the calculated Davydov splittings ($\Delta\nu$) that nicely reproduce the experimental findings, the following general behavior was found: all **M**-polarized single-molecule vibrations split into **c**- and **b**-polarized modes in the crystal, whereas **L**-polarized molecular modes exhibit only one counterpart in the crystal, whereas the second mode disappears. In the spectral range between 1380 and 1480 cm^{-1}, however, some deviations between experimental and calculated spectra occur. In particular, additional modes appear in the experimental spectra that have no counterpart in the crystal calculation; these will be discussed in the following section.

IV. DISCUSSION

The present crystal calculations of the vibration spectra provide detailed insight into the mode coupling in molecular crystals. It allows, in particular, to explain the appearance of Davydov splitting for some of the modes in the experimental spectra, whereas other modes exhibit only single peaks. In agreement with the experimental polarization analysis (cf. Table 3), the calculations show that every **L**-polarized mode in the molecule turns into an IR active **L**-mode in the crystal and a second mode that does not exhibit any IR activity. By contrast, molecular modes with **M** polarization give rise to two IR-active modes in the crystal environment with **b** and **c** polarization, respectively. This effect can be traced back to the herringbone packing motif of the molecular PFP planes and the collinear arrangement of the **L**-axes in the crystal structure, yielding different coupling options for the individual molecular vibrations, which will be illustrated at the example of the two modes 66 and 67.

As shown in Figure 7, mode 66 exhibits a dynamical dipole moment along the **L**-axis of the individual molecules. According to the collinear arrangement of the long axes of PFP in the crystal, the individual molecules can either vibrate in-phase, leading to a total dynamical dipole moment $\tilde{\mu}$ oriented along the **L**-direction in the molecular crystal (Figure 8b), or the dynamical dipole moments of both molecules are exactly antiparallel if both molecules vibrate with opposite phase (Figure 8c), leading to only one observable IR mode. On the other hand, mode 67 has a dynamical dipole moment along the **M**-axis in the single molecule (cf. Figure 7). According to the herringbone arrangement of both molecules within the unit cell, the vector-addition of their respective dynamical dipole moments yields total dipole moments $\tilde{\mu}$ oriented either along the **c**-direction (Figure 8d) or the **b**-direction of the PFP crystal (Figure 8e), depending on the exact phase relation. This is completely in line with the experimental mode polarizations and intensities of modes 66 and 67 (cf. Table 3): Whereas only one of both Davydov components of mode 66 shows IR-activity, mode 67 splits into two IR-active modes.

Comparing the results of the theoretical analyses carried out for the single-molecule and crystal approximations illustrates the influence of intermolecular couplings in the molecular solid on the vibrational properties. In addition to the aforementioned Davydov splitting, the mode frequencies are unequally shifted, and also their relative intensities are affected with respect to the single-molecule values.

Table 3 shows that the calculated mode splitting ranges from 0.2 to 36.4 cm^{-1}, which is in close agreement with the experimental findings (2−33 cm^{-1}). Note that the calculations provide, in particular, Davydov splittings $\Delta\nu$ for **L**-polarized modes, whereas they are not accessible in the experiment due to the afore-discussed cancellation. Interestingly, the mode splitting is not simply related to the magnitude of the dynamical dipole moments of the involved modes, as one might anticipate on the basis of a potential energy consideration of one dipole moment in the electrostatic field of another dipole. For example, modes 67 and 90 exhibit distinct molecular dipole moments and a large splitting, whereas mode 91 reveals a large dipole moment for the individual molecule but only a small

dx.doi.org/10.1021/jp304080g | J. Phys. Chem. C 2012, 116, 14491−14503

Table 3. Frequencies (ν in cm^{-1})[a], IR Intensities (I, Normalized to the Most Intense Mode), Dynamical Dipole Moment, $\tilde{\mu}$,[b] and Davydov Splittings ($\Delta\nu$) of the Main Vibrational Modes[c]

single molecule PBE-D2				molecular crystal PBE-D2$_{PBC}$					experiment[d]			
no.	ν	I	$\tilde{\mu}$	no.	ν	I	$\tilde{\mu}$	$\Delta\nu$	ν	I	$\tilde{\mu}$	$\Delta\nu$
66	867.3	0.19	**L** (b_{3u})	**66*α***	871.3	0.14	**L**	0.2	869	0.38	**L**	-
				66*β*	871.5	<0.01						
67	933.4	0.31	**M** (b_{2u})	**67*α***	925.7	0.19	**c**	16.4	919	0.61	**c**⎤	14.0
				67*β*	942.1	0.06	**b**		933	0.40	**b**⎦	
#									969	0.16	**c**	-
69	980.9	0.18	**M** (b_{2u})	**69*α***	972.0	0.07	**c**	7.8	974	0.32	**c**⎤	5.0
				69*β*	979.8	0.07	**b**		979	0.32	**b**⎦	
72	1099.8	0.25	**L** (b_{3u})	**72*α***	1099.5	0.35	**L**	3.5	1098	0.51	**L**	-
				72*β*	1103.0	<0.01						
74	1144.4	0.08	**M** (b_{2u})	**74*α***	1140.5	0.03	**c**	4.0	1144	0.07	**c**⎤	4.0
				74*β*	1144.5	0.02	**b**		1148	0.10	**b**⎦	
#									1169	0.12	**L**	-
76	1209.4	0.01	**L** (b_{3u})	**76*α***	1205.5	<0.01		3.9				
				76*β*	1209.4	0.02	**L**		1218	0.03	**L**	-
77	1215.6	0.01	**L** (b_{3u})	**77*α***	1220.7	<0.01		0.4				
				77*β*	1221.1	<0.01	**L**		--	--		
#									1241	0.06	**L**	-
78	1231.0	0.03	**M** (b_{2u})	**78*α***	1228.7	0.01	**b**	1.0	1242	0.11	**c**⎤	2.0
				78*β*	1229.7	0.02	**c**		1244	0.04	**b**⎦	
81	1281.8	0.22	**L** (b_{3u})	**81*α***	1314.8	<0.01		2.4				
				81*β*	1317.2	0.03	**L**		--	--		
83	1347.5	0.02	**M** (b_{2u})	**83*α***	1341.8	<0.01	**c**	10.4				
				83*β*	1352.2	<0.01	**b**		1360	0.11	**b**	
85	1365.2	0.23	**L** (b_{3u})	**85*α***	1380.4	<0.01		0.6				
				85*β*	1381.0	0.12	**L**		1367	0.15	**L**	
88	1398.9	0.05	**L** (b_{3u})	**88*α***	1410.7	<0.01		2.1				
				88*β*	1412.8	0.01	**L**		--	--		
90	1433.9	0.84	**M** (b_{2u})	**90*α***	1405.1	0.73	**c**	36.4	1415	0.47	**c**⎤	33
				90*β*	1441.5	0.43	**b**		1448	0.60	**b**⎦	
#									1419	0.63	**c**	
#									1425	0.08	**b**	
#									1432	0.85	**c**	
#									1440	0.13	**L**	
91	1447.7	0.60	**M** (b_{2u})	**91*α***	1459.9	0.04	**c**	2.0	1457	0.20	**c**⎤	2
				91*β*	1461.9	0.11	**b**		1459	0.46	**b**⎦	
#									1468	0.44	**b**	
92	1474.8	1.00	**L** (b_{3u})	**92*α***	1484.1	1.00	**L**	5.0	1486	1.00	**L**	-
				92*β*	1489.1	<0.01						
94	1498.0	0.19	**L** (b_{3u})	**94*α***	1507.9	0.21	**L**	2.5				
				94*β*	1510.4	<0.01						
98	1577.7	0.69	**L** (b_{3u})	**98*α***	1574.9	<0.01		5.1				
				98*β*	1580.0	0.14	**L**		1581	0.25	**L**	-
101	1656.5	0.29	**M** (b_{2u})	**101*α***	1660.5	0.09	**c**	2.8	1678	0.14	**c**⎤	
				101*β*	1663.3	0.07	**b**		1680	0.17	**b**⎦	2

[a]Calculated frequencies are scaled by a factor of 1.015. [b]Dynamical dipole moments correspond to the axes denotation in Figure 1. [c]Rows marked by # in Table 3 indicate modes with deviation between experiment and theory, which are assigned to combination bands. (See the text.) [d]Experimental frequencies were determined in the PFP/KCl and PFP/NaF thin films, whereas the intensities were derived from the PFP/KBr pellet spectra.

splitting in the crystal. Mode 83 shows a distinct splitting, although the molecular dipole is rather small. This result shows that although a pairwise summation of both molecular dynamical dipole moments within the unit cell well explains the mode polarization and the IR inactivity of one Davydov component, it does not allow us to estimate the extent of mode splitting. Instead, one has to calculate all dipole interactions to neighboring cells (Madelung summation), like it is implemented in the crystal calculation where the dipole moments are stacked in line as well as side-by-side.

Despite an overall close resemblance of the experimental and theoretical spectra, some of the measured bands (marked by # in Table 3) have no counterparts in the calculations. Most prominent, these additional and partially rather intense modes (85% of the most intense mode) occur in the frequency range between 1400 and 1470 cm^{-1} but also less intensive at 969, 1169, and 1241 cm^{-1}. Various reasons account for the

dx.doi.org/10.1021/jp304080g | J. Phys. Chem. C 2012, 116, 14491−14503

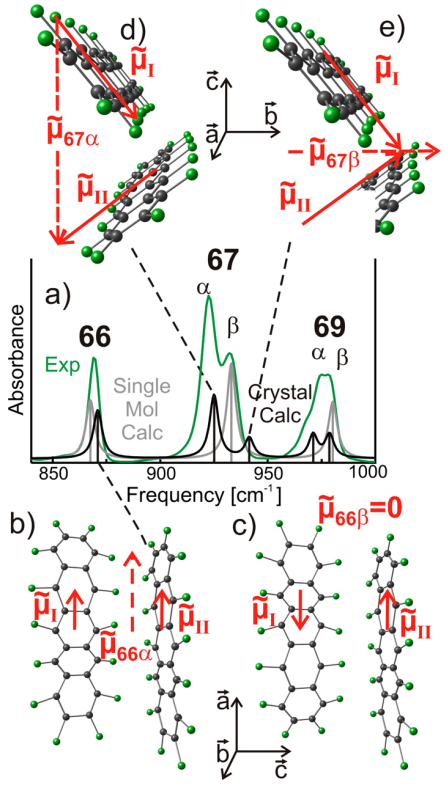

Figure 8. (a) Magnification of experimental (KBr pellet) and computed IR spectra for a single PFP molecule (PBE-D2) and the PFP molecular crystal (PBE-D2$_{PBC}$) with mode assignments according to Table 3. (b–d) Calculated displacement patterns and dynamical dipole moments of both molecules in the unit cell for the IR active mode 66α (b) and the IR-inactive mode 66β (c) as well as the modes 67α (d) and 67β (e), both of them dipole active but with orthogonal polarizations.

appearance of additional IR modes, including a break of symmetry (either of the molecule or the crystalline lattice due to defects or interfaces), overtone-bands, or side-bands due to combination modes. Regarding the molecular symmetry of PFP, we note that our theoretical geometry optimization well-reproduces the experimental finding of a symmetry reduction when going from a single-molecule (D_{2h} point-group symmetry) to the crystalline phase of PFP, which yields C_i symmetry due to site symmetry constraints. Hence the symmetry reduction is fully taken into account in the vibrational calculation of the crystal. A comparison of the calculated spectra of the free molecule and the PFP crystal (cf. Figure 6 and Table 3) reveals only minor differences, such as small intensity variations besides the Davydov splitting due to the doubling of molecules within the unit cell and thus cannot explain the presence of new modes.

Also, defect-related vibrational modes appear to be rather unlikely because the additional modes have been observed for the polycrystalline pellet sample as well as for highly ordered crystalline PFP films. Moreover, they are partially rather intense (85% of the most intense mode) and in addition reveal a distinct polarization like the other PFP crystal modes. By contrast, for disordered molecules at structural defects or impurities a different symmetry than that of the crystal lattice or further modes would be expected and thus can be ruled out. Furthermore, the constant intensity of these modes independent of the actual transmission setup (aperture settings, sample positioning) exclude such a local defect-related effect. Finally, the weak chemical interaction between PFP and the alkali halide substrates or pellet matrix also excludes additional modes due to differently bound molecules, as observed, for example, in the first monolayer chemisorbed on metal substrates.[48]

Overtone bands are expected to appear at about twice the frequency of the corresponding fundamental vibrations because only for higher overtones do notable frequency shifts due to anharmonic effects occur. For all presently observed additional modes, however, no corresponding modes at half frequencies have been found neither in the experimental nor in the calculated spectra.

We note further that also a direct connection of such additional vibrational modes with electronic excitations in PFP (either HOMO–LUMO transitions or excitons) can be safely ruled out as the lowest energetic excitation in crystalline PFP occurs at 1.6 eV.[49] However, the opposite case that electronic excitations are coupled to vibrational modes is rather common and leads to an appearance of characteristic vibrational progressions in the optical excitation spectra (as discussed below).

Therefore, the most reasonable explanation for the appearance of the additional modes is an excitation of combination bands. In fact, coupled excitations of various molecular vibrations or with phonon modes have been suggested to explain additional features observed in IR or electron energy loss (EEL) spectra of molecular films[48b,50] or in optical absorption spectra of aromatic molecular crystals.[51] The question of which combinations are dipole-active requires an analysis involving group theory and evaluation of the direct product of the contributing modes. A prominent class of such simultaneously excited modes is the combination of IR-active and totally symmetric modes (a_g symmetry). In case such a (usually weak) band is located close to a (strong) fundamental mode with the same symmetry, mixing of the respective wave functions may occur, leading to substantial intensity enhancement of the former.

All additional modes (marked by # in Table 3) exhibit a distinct mode polarization and can be reasonably described by combining in each case an IR-active fundamental mode of the same polarization with a totally symmetric mode, as listed in Table 4. Interestingly, the displacement patterns of each mode of the combination bands exhibit a notable correlation. Although belonging to different symmetry classes (IR-active vs symmetric), all mode pairs reveal a similar ring deformation

Table 4. Suggested Band Combinations of Fundamental IR-Active and Totally Symmetric Modes Derived from the Crystal Calculations. All frequencies are given in cm^{-1}.

ν_{exp}	$\tilde{\mu}_{exp}$	ν_{fundIR}	$\tilde{\mu}_{fundIR}$	ν_{sym}	ν_{IR+sym}	$\Delta\nu$
969	c	524.5[a]	c	453.4	977.9	8.9
1169	L	869	L	276.1	1145.1	23.9
1241	L	542.3[a]	L	701.0	1243.3	2.3
1419	c	919	c	496.4	1415.4	3.6
1425	b	979	b	453.4	1432.7	7.7
1432	c	974	c	453.4	1427.7	4.3
1440	L	1098	L	345.3	1443.4	3.4
1468	b	979	b	496.4	1475.4	7.4

[a]Frequency of fundamental mode is below the experimental energy window and was taken from crystal calculation.

dx.doi.org/10.1021/jp304080g | J. Phys. Chem. C 2012, 116, 14491–14503

pattern (cf. Figure S7, Supporting Information), which suggests an effective coupling mechanism. According to the multiplicity of modes in the crystalline lattice (factor-group splitting), also the totally symmetric modes appear twice, whereas their energetic splitting is typically less than 2 to 3 cm^{-1}, thus reflecting an absence of electrostatic (i.e., dipole) coupling, and their multiplicity provides a larger vibrational density of states that can couple to the fundamental IR mode. We note further that for six of the eight observed combination bands the frequencies of the fundamental IR mode and the symmetrically mode exhibit an almost integer factor (better than 10%), hence suggesting efficient dynamical coupling.

Our analysis provides detailed insight into the nature of combination bands beyond pure energetic arguments and may help to understand why the intensity of such combination bands can become almost as large as the most intense IR-active modes. We note that the present calculations provide the one-phonon vibrational spectrum of the PFP crystal so that multiphonon excitations that apparently occur in the experiment are not taken into account.

Our analysis demonstrates, in particular, the importance of a detailed polarization analysis when comparing the measured and computed spectra. On the basis of a matching of the various mode polarizations, we were able to deduce reliably a scaling factor for the PBE functional (including D2-dispersion correction) of 1.015 for these spectra. By contrast, attempts to fit the calculated mode frequencies to the measured spectrum without a precise polarization analysis, and the identification of combination bands would lead to a different scaling factor and an incomplete mode assignment. A scaling factor deduced from one system only, of course, cannot be generalized, and it will be interesting to see if future investigations back the current results.

A precise description of molecular vibrations in crystalline solids is of vital interest for a detailed understanding of charge carrier transport mechanism in organic semiconductors. In the case of hopping transport, the coupling of electronic excitations to vibronic degrees of freedom either to phonons (Peierls coupling) or molecular vibrations (Holstein coupling) is a decisive characteristic.[23c,d] In view of the significant attention on the new class of n-type organic semiconductors, which has been generated by the recent synthesis of perfluorinated acenes,[26] the present vibrational analysis of PFP might be useful to improve the previous description of such materials[52] by considering the complete vibrational spectrum derived from van der Waals corrected DFT calculations. It shows, in particular, that perfluorination of acenes not only affects their electronic structure, yielding for example an inversion of their quadrupolar moments and change of the polarity of the charge carriers,[53] but also affects the vibrational density of states compared with that of the corresponding nonfluorinated acenes (cf. Figure 2).

V. CONCLUSIONS

In this study, we have utilized the specific epitaxial growth relation of PFP films on KCl(100) and NaF(100) substrates (standing vs lying) that allows us to perform directional- and azimuthal-resolved polarized IR measurements on single-crystalline domains, which affords a unique experimental determination of all IR-mode polarizations in the analyzed energy range above 700 cm^{-1}. Accompanied theoretical analyses carried out in the framework of DFT using the PBE functional including dispersion correction (PBE-D2) show that calculations considering the crystalline environment are required to fully explain and reproduce quantitatively the characteristic mode coupling of the individual molecules within the unit cell. The analysis elucidates, in particular, the observed cancellation of one **L**-polarized Davydov component as well as the splitting of **M**-polarized IR-modes into **b**- and **c**-polarized modes. The existence of all Davydov components in the IR-spectrum of corresponding KBr-pellet spectra demonstrates the polycrystalline nature of such powders, which already carry the complete crystalline signature and cannot be described adequately by a single-molecule calculation. Moreover, additional modes not covered by the calculations have been identified and attributed to combination bands consisting of IR-active fundamental modes coupling to totally symmetric modes. Surprisingly, these bands are as intense as the most intense IR-modes and thus emphasize the importance of a complete assignment of all vibrational modes when analyzing coupling phenomena in crystalline organic semiconductors or employing vibrational spectroscopy to characterize multinary molecular crystals consisting of different molecular species.

The presently achieved polarization analysis of all measured IR-active modes may serve as a comprehensive benchmark case to test computational approaches in the future. Moreover, it is an important prerequisite to study also the influence of intermolecular coupling on the vibrational properties of organic heterostructures such as PEN/PFP.

■ ASSOCIATED CONTENT

Supporting Information

Additional experimental and theoretical results, complete list of vibrational modes, characteristic displacement patterns (images and animated GIFs), output files of computational calculations, and full references. This material is available free of charge via the Internet at http://pubs.acs.org.

■ AUTHOR INFORMATION

Notes

The authors declare no competing financial interest.

■ ACKNOWLEDGMENTS

We thank Gernot Frenking (Marburg) and David Karhanek (Tarragona, Spain) for valuable discussions. R.T. thanks the Philipps-Universität Marburg for support via a research advancement grant. T.B. thanks the Friedrich-Ebert-Stiftung for financial support. We thank the HLR Stuttgart, the CSC Frankfurt, the HHLR Darmstadt, and the Hochschulrechenzentrum Marburg for providing computational resources.

■ REFERENCES

(1) (a) Larkin, P. *Infrared and Raman Spectroscopy; Principles and Spectral Interpretation*; Elsevier: Amsterdam, 2011. (b) *Infrared and Raman Spectroscopy: Methods and Applications*; Schrader, B., Ed.; VCH: Weinheim, Germany, 1995.
(2) Gunia, M.; Jakob, P.; Sander, W.; Wöll, C. *J. Phys. Chem. B* **2004**, *108*, 14025−14031.
(3) (a) Hadjiivanov, K. *Catal. Rev.: Sci. Eng.* **2000**, *42*, 71−144. (b) Ryczkowski, J. *Catal. Today* **2001**, *68*, 263−381.
(4) Parikh, A. N.; Allara, D. L. *J. Chem. Phys.* **1992**, *96*, 927−945.
(5) Choi, H.; Kertesz, M. *J. Phys. Chem. A* **1997**, *101*, 3823−3831.
(6) Buergi, T.; Baiker, A. *Adv. Catal.* **2006**, *50*, 227−283.
(7) See, for example: www.ir-spectra.com accessed April 20, 2012).
(8) Dronskowski, R. *Computational Chemistry of Solid State Materials: A Guide for Material Scientists, Chemists, Physicists and Others*; Wiley-VCH: Weinheim, Germany, 2005.

(9) (a) Dovesi, R.; Pascale, F.; Zicovich-Wilson, C. M.; Gejo, F. L.; Civalleri, B.; Orlando, R. *J. Comput. Chem.* **2004**, *25*, 888−897. (b) De La Pierre, M.; Orlando, R.; Maschio, L.; Doll, K.; Ugliengo, P.; Dovesi, R. *J. Comput. Chem.* **2011**, *32*, 1775−1784. (c) Schmuttenmaer, C. A.; Williams, M. R. C.; True, A. B.; Izmaylov, A. F.; French, T. A.; Schroeck, K. *Phys. Chem. Chem. Phys.* **2011**, *13*, 11719−11730.
(10) Grimme, S. *J. Comput. Chem.* **2004**, *25*, 1463−1473.
(11) Grimme, S.; Heitmann, D.; Pape, T.; Hepp, A.; Mück-Lichtenfeld, C.; Hahn, F. E. *J. Am. Chem. Soc.* **2011**, *133*, 11118−11120.
(12) (a) Grimme, S. *Wiley Interdiscip. Rev.: Comput. Mol. Sci.* **2011**, *1*, 211−228. (b) Tkatchenko, A.; Romaner, L.; Hofmann, O. T.; Zojer, E.; Ambrosch-Draxl, C.; Scheffler, M. *MRS Bull.* **2010**, *35*, 435−442. (c) Grafenstein, J.; Cremer, D. *J. Chem. Phys.* **2009**, *130*, 124105. (d) Johnson, E. R.; Mackie, I. D.; DiLabio, G. A. *J. Phys. Org. Chem.* **2009**, *22*, 1127−1135. (e) Sato, T.; Nakai, H. *J. Chem. Phys.* **2009**, *131*, 224104.
(13) Grimme, S. *J. Comput. Chem.* **2006**, *27*, 1787−1799.
(14) (a) Reckien, W.; Bredow, T. *Chem. Phys. Lett.* **2011**, *508*, 54−58. (b) Moellmann, J.; Grimme, S. *Phys. Chem. Chem. Phys.* **2010**, *12*, 8500−8504. (c) Bučko, T.; Hafner, J.; Lebegue, S.; Angyán, J. G. *J. Phys. Chem. A* **2010**, *114*, 11814−11824.
(15) Maschio, L.; Civalleri, B.; Ugliengo, P.; Gavezzotti, A. *J. Phys. Chem. A* **2011**, *115*, 11179−11186.
(16) Todorova, T.; Delley, B. *J. Phys. Chem. C* **2010**, *114*, 20523−20530.
(17) (a) Verhoeven, J. W. *Pure Appl. Chem.* **1996**, *68*, 2223−2286. (b) Davydov, A. S. *J. Exp. Theor. Phys.* **1948**, *18*, 210−218.
(18) (a) Kramer, M.; Hoffman, V. *Opt. Mater.* **1998**, *9*, 65−69. (b) Schwoerer, M.; Wolf, H. C. *Organic Molecular Solids*; Wiley-VCH: Weinheim, Germany, 2007; (c) Degli Esposi, A.; Fanti, M.; Muccini, M.; Taliani, C.; Giampiero, R. *J. Chem. Phys.* **2000**, *112*, 5957−5969. (d) Tenne, D. A.; Park, S.; Kampen, T. U.; Das, A.; Scholz, R.; Zahn, D. R. T. *Phys. Rev. B* **2000**, *61*, 14564−14569.
(19) (a) Halford, R. *J. Chem. Phys.* **1946**, *14*, 8−15. (b) Califano, S. *Mol. Phys.* **1962**, *5*, 601−604. (c) Schrader, B. Raman and Infrared Spectroscopy of Molecular Crystals. In *Molecular Spectroscopy*; Barrow, R. F., Long, D. A., Sheridan, J., Eds.; Chemical Society: London, 1978; Vol. *5*, pp 235−270. (d) Decius, J. C.; Hexter, R. M. *Molecular Vibrations in Crystals*; McGraw-Hill: New York, 1977. (e) Turrell, G. *Infrared and Raman Spectra of Crystals*; Academic Press: London, 1972.
(20) (a) Allis, D. G.; Kosmowski, M. E.; Hudson, B. S. *J. Am. Chem. Soc.* **2004**, *126*, 7756−7757. (b) Hudson, B. S. *J. Phys. Chem. A* **2001**, *105*, 3949−3960. (c) Hudson, B. S. *Vib. Spectrosc.* **2006**, *42*, 25−32. (d) Hudson, B. S.; Braden, D. A.; Parker, S. F.; Prinzbach, H. *Angew. Chem., Int. Ed.*. **2000**, *39*, 514−516. (e) Hudson, B. S.; Verdal, N. *Physica B* **2006**, *385*, 212−215. (f) Hudson, M. R.; Allis, D. G.; Hudson, B. S. *Chem. Phys. Lett.* **2009**, *473*, 81−87. (g) Hudson, M. R.; Allis, D. G.; Hudson, B. S. *J. Phys. Chem. A* **2010**, *114*, 3630−3641. (h) Danchuk, V.; Kravchuk, A.; Puchkovska, G.; Yakubov, A. *Mol. Cryst. Liq. Cryst.* **2008**, *495*, 611−617. (i) Puchkovska, G.; Bezrodna, T.; Styopkin, V.; Baran, J. *Thin Solid Films* **2009**, *517*, 1759−1764. (j) Puchkovska, G. O.; Makarenko, S. P.; Danchuk, V. D.; Kravchuk, A. P.; Baran, J.; Kotelnikova, E. N.; Filatov, S. K. *J. Mol. Struct.* **2002**, *614*, 159−166. (k) Ouillon, R.; Pinan-Lucarre, J. P.; Ranson, P.; Baranovic, G. *J. Chem. Phys.* **2002**, *116*, 4611−4625. (l) Ranson, P.; Ouillon, R.; Perrin, B.; Lemaistre, J. P. *J. Chem. Phys.* **1992**, *96*, 6348−6357. (m) Koleva, B.; Spiteller, M.; Kolev, T. *Amino Acids* **2010**, *38*, 295−304. (n) Parker, S. F.; Jeans, R.; Devonshire, R. *Vib. Spectrosc.* **2004**, *35*, 173−177.
(21) (a) Langhoff, S. R. *J. Phys. Chem.* **1996**, *100*, 2819−2841. (b) Tielens, A. G. G. M. *Annu. Rev. Astron. Astrophys.* **2008**, *46*, 289−337.
(22) Mas-Torrent, M.; Rovira, C. *Chem Rev* **2011**, *111*, 4833−4856.
(23) (a) Kera, S.; Yamane, H.; Ueno, N. *Prog. Surf. Sci.* **2009**, *84*, 135−154. (b) Sanchez-Carrera, R. S.; Paramonov, P.; Day, G. M.; Coropceanu, V.; Bredas, J.-L. *J. Am. Chem. Soc.* **2010**, *132*, 14437−14446. (c) Elliott, A. B. S.; Horvath, R.; Gordon, K. C. *Chem. Soc. Rev.* **2012**, *41*, 1929−1946. (d) Girlando, A.; Grisanti, L.; Masino, M.; Brillante, A.; Della Valle, R. G.; Venuti, E. *J. Chem. Phys.* **2011**, *135*, 084701.
(24) (a) Lunelli, B.; Pecile, C. *J. Chem. Phys.* **1970**, *52*, 2375−2384. (b) Basova, T. V.; Kiselev, V. G.; Schuster, B.-E.; Peisert, H.; Chassé, T. *J. Raman Spectrosc.* **2009**, *40*, 2080−2087.
(25) de Boer, R. W. I.; Gershenson, M. E.; Morpurgo, A. F.; Podzorov, V. *Phys. Status Solidi A* **2004**, *201*, 1302−1331.
(26) Sakamoto, Y.; Suzuki, T.; Kobayashi, M.; Gao, Y.; Fukai, Y.; Inoue, Y.; Sato, F.; Tokito, S. *J. Am. Chem. Soc.* **2004**, *126*, 8138−8140.
(27) (a) Salzmann, I.; Duhm, S.; Heimel, G.; Oehzelt, M.; Kniprath, R.; Johnson, R. L.; Rabe, J. P.; Koch, N. *J. Am. Chem. Soc.* **2008**, *130*, 12870−12871. (b) Salzmann, I.; Duhm, S.; Heimel, G.; Rabe, J. P.; Koch, N.; Oehzelt, M.; Sakamoto, Y.; Suzuki, T. *Langmuir* **2008**, *24*, 7294−7298.
(28) Breuer, T.; Witte, G. *Phys. Rev. B* **2011**, *83*, 155428.
(29) Frisch, M. J.; Trucks, G. W.; Schlegel, H. B.; Scuseria, G. E.; Robb, M. A.; Cheeseman, J. R.; Scalmani, G.; Barone, V.; Mennucci, B.; Petersson, G. A.; et al. *Gaussian 09*, revision A.02; Gaussian, Inc.: Wallingford, CT, 2009.
(30) Ahlrichs, R.; Bär, M.; Häser, M.; Horn, H.; Kölmel, C. *Chem. Phys. Lett.* **1989**, *162*, 165−169.
(31) Perdew, J. P.; Burke, K.; Ernzerhof, M. *Phys. Rev. Lett.* **1996**, *77*, 3865−3868.
(32) Weigend, F.; Ahlrichs, R. *Phys. Chem. Chem. Phys.* **2005**, *7*, 3297−3305.
(33) (a) Perdew, J. P. *Phys. Rev. B* **1986**, *33*, 8822−8824. (b) Becke, A. D. *Phys. Rev. A* **1988**, *38*, 3098−3100.
(34) (a) Becke, A. D. *J. Chem. Phys.* **1993**, *98*, 5648−5652. (b) Stephens, P. J.; Devlin, J. F.; Chabalowski, C. F.; Frisch, M. J. *J. Phys. Chem.* **1994**, *98*, 11623−11627.
(35) Deglmann, P.; Furche, F.; Ahlrichs, R. *Chem. Phys. Lett.* **2002**, *362*, 511−518.
(36) (a) Eichkorn, K.; Treutler, O.; Ohm, H.; Häser, M.; Ahlrichs, R. *Chem. Phys. Lett.* **1995**, *240*, 283−289. (b) Weigend, F. *Phys. Chem. Chem. Phys.* **2006**, *8*, 1057−1065.
(37) (a) Hafner, J. *J. Comput. Chem.* **2008**, *29*, 2044−2078. (b) Kresse, G.; Furthmüller, J. *Phys. Rev. B* **1996**, *54*, 11169−11186.
(38) (a) Blöchl, P. E. *Phys. Rev. B* **1994**, *50*, 17953−17979. (b) Kresse, G.; Joubert, D. *Phys. Rev. B* **1999**, *59*, 1758−1775.
(39) Monkhorst, H. J.; Pack, J. D. *Phys. Rev. B* **1976**, *13*, 5188−5192.
(40) (a) Giannozzi, P.; Baroni, S. *J. Chem. Phys.* **1994**, *100*, 8537−8539. (b) Baroni, S.; de Gironcoli, S.; Dal Corso, A.; Giannozzi, P. *Rev. Mod. Phys.* **2001**, *73*, 515−562.
(41) Gajdoš, M.; Hummer, K.; Kresse, G.; Furthmüller, J.; Bechstedt, F. *Phys. Rev. B* **2006**, *73*, 045112.
(42) (a) Karhanek, D.; Bučko, T.; Hafner, J. *J. Phys.: Condens. Matter* **2010**, *22*, 265006. (b) Karhanek, D.; Bučko, T.; Hafner, J. *J. Phys.: Condens. Matter* **2010**, *22*, 265005.
(43) (a) Porezag, D.; Pederson, M. R. *Phys. Rev. B* **1996**, *54*, 7830−7836. (b) Preuss, M.; Bechstedt, F. *Phys. Rev. B* **2006**, *73*, 155413.
(44) Bucko, T.; Tunega, D.; Angyan, J. G.; Hafner, J. *J. Phys. Chem. A* **2011**, *115*, 10097−10105.
(45) (a) Hudgins, D. M.; Sandford, S. A. *J. Phys. Chem. A* **1998**, *102*, 344−352. (b) Hudgins, D. M.; Sandford, S. A. *J. Phys. Chem. A* **1998**, *102*, 329−343.
(46) Scott, A. P.; Radom, L. *J. Phys. Chem.* **1996**, *100*, 16502−16513.
(47) Weidlein, J.; Müller, U.; Dehnicke, K. *Schwingungsspektroskopie: eine Einführung*, 2nd ed.; Thieme: New York, 1988.
(48) (a) Jakob, P.; Menzel, D. *J. Chem. Phys.* **1996**, *105*, 3838−3848. (b) Tautz, F. S.; Sloboshanin, S.; Schaefer, J. A.; Scholz, R.; Shklover, V.; Sokolowski, M.; Umbach, E. *Phys. Rev. B* **2000**, *61*, 16933−16947.
(49) Hinderhofer, A.; Heinemeyer, U.; Gerlach, A.; Kowarik, S.; Jacobs, R. M. J.; Sakamoto, Y.; Suzuki, T.; Schreiber, F. *J. Chem. Phys.* **2007**, *127*, 194705.
(50) (a) Dunn, D. S.; Scanlon, K.; Overend, J. *Spectrochim. Acta, Part A* **1982**, *38*, 841−847. (b) Ryberg, R. *Phys. Rev. B* **1991**, *44*, 13160−13162. (c) del Rosario, A.; Bitschenauer, R.; Dakkouri, M.; Haller, K.; Laane, J. *J. Phys. Chem. A* **1998**, *102*, 10261−10264. (d) Jakob, P.; Persson, B. N. J. *J. Chem. Phys.* **1998**, *109*, 8641−8651.

(51) Lalov, I. J.; Zhelyazkov, I. *Chem. Phys.* **2008**, *352*, 185−196.
(52) Martinelli, N. G.; Olivier, Y.; Athanasopoulos, S.; Delgado, M. C. R.; Pigg, K. R.; da Silva, D. A.; Sanchez-Carrera, R. S.; Venuti, E.; Della Valle, R. G.; Bredas, J. L.; et al. *ChemPhysChem* **2009**, *10*, 2265−2273.
(53) Delgado, M. C. R.; Pigg, K. R.; Filho, D.; Gruhn, N. E.; Sakamoto, Y.; Suzuki, T.; Osuna, R. M.; Casado, J.; Hernandez, V.; Navarrete, J. T. L.; et al. *J. Am. Chem. Soc.* **2009**, *131*, 1502−1512.

Supporting Information

Vibrational Davydov-Splittings and Collective Mode Polarizations in oriented Organic Semiconductor Crystals

Tobias Breuer [a)], Mehmet A. Celik [b)], Peter Jakob [a)], Ralf Tonner* [b)], Gregor Witte* [a)]
[a)] *Department of Physics and* [b)] *Department of Chemistry,*
Philipps-University Marburg, Germany

Figure S1 shows the molecular structure of PFP optimized with periodic and non-periodic approaches in comparison to the experimental structure. It becomes obvious that the experimental structure is well reproduced. This is confirmed by the RMS values for the C-C and C-F bonds shown in Table S1. Values for a triple-zeta basis set (TZVPP) are essentially converged and all methods applied give similar deviations from experiment. The errors in the periodic calculation drop when the crystal environment is taken into account in comparison to the calculation of the free molecule in a periodic box. All together, the chosen methodology provides accurate structures of the molecule and crystal of PFP, enabling the calculation of vibrational spectra. Note that due to mutual interaction in the crystal PFP molecules no longer adopt the D_{2h} symmetry of the free molecule but exhibit a C_i symmetry.

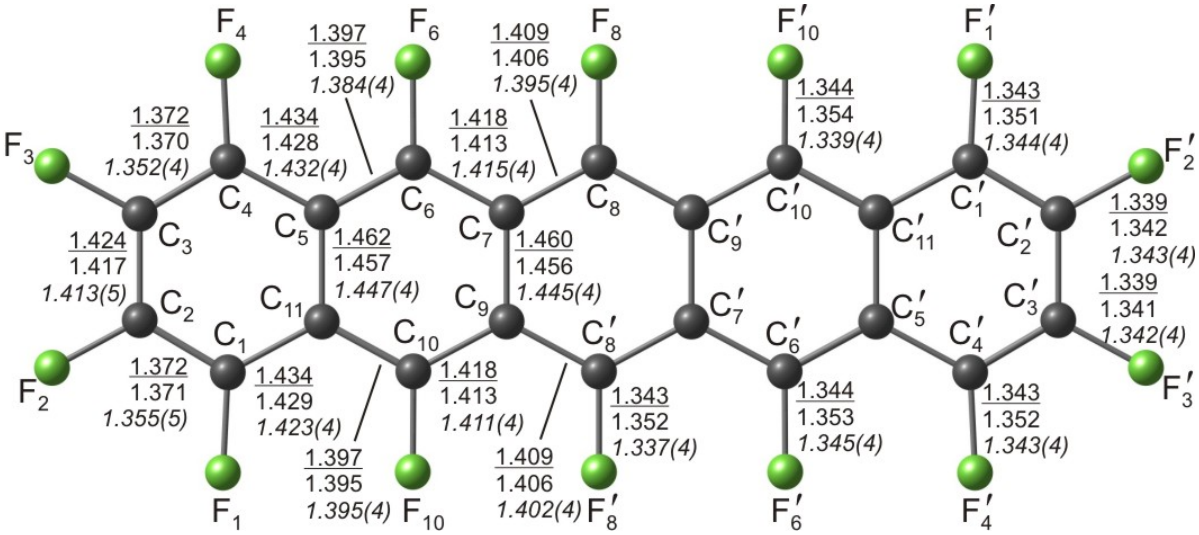

Fig. S1: Molecular structure of Perfluoropentacene with numbering scheme (symmetry-equivalent atoms in the solid state are indicated with a prime) and bond lengths given in Å. The individual values refer to the computed free molecule (PBE-D2, D_{2h} , top), the molecular crystal (PBE-D2$_{PBC}$, C_i *, center*), and experimental reference data[1] (*X-ray*, C_i *, bottom*).

Table S1. Deviation from experimental structure[1] (root mean square in Å) of computed PFP molecule with different methods and basis sets.

Method		**PBE**		**PBE-D2**	**B3LYP**	**MP2**	**PBE-D2$_{PBC}$**	
Basis set	SVP	TZVPP	QZVPP	TZVPP	TZVPP	TZVPP	Molecule[a]	Crystal
All bonds	0.015	0.010	0.010	0.011	0.009	0.011	0.018	0.013
C-C	0.021	0.013	0.013	0.014	0.010	0.011	0.024	0.016
C-F	0.005	0.004	0.004	0.003	0.008	0.012	0.007	0.008

[a] free molecule in a periodic box.

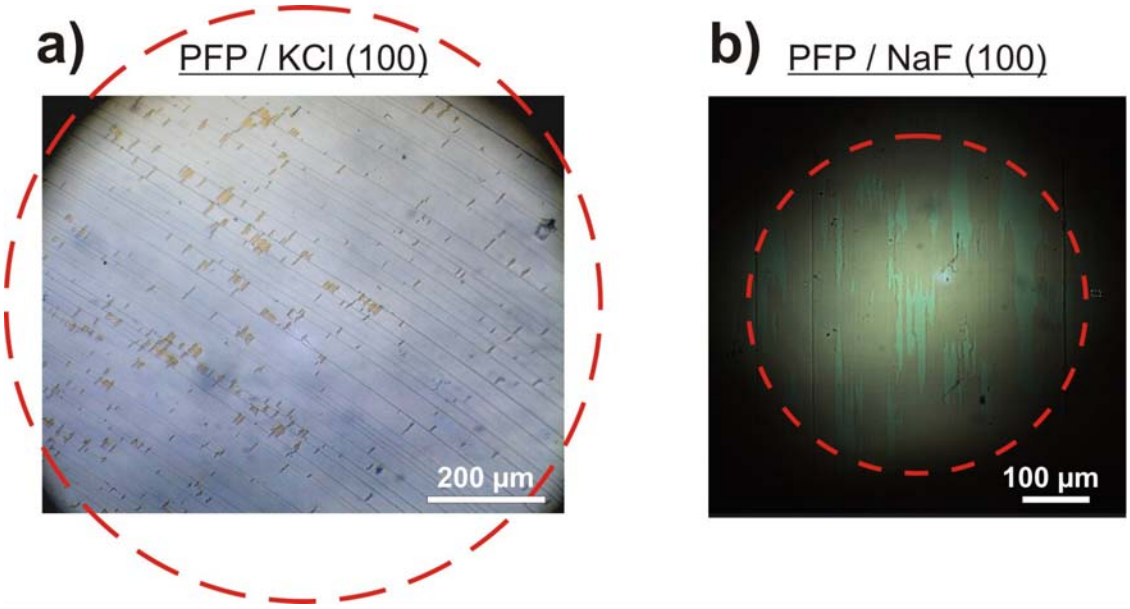

Fig. S2: Microscopic image with polarized light showing the positioning of the apertures relative to the a) PFP / KCl thin film, b) PFP / NaF thin film. Note that more than one exclusive domain is bordered, indicated by the different color appearance of the crystallites within the aperture, representing domains rotated by 90° with respect to each other.

Figure S2 shows the positioning of the PFP samples on the apertures using polarized optical microscopy. As the optical absorption of rotated domains is different[27], the color appearance was used as recognition feature of differently oriented domains. Because of the greater domain size of PFP on KCl(100), clear majorities of one domain were positioned on the aperture (cf. Fig S2a) of 1mm diameter. In the case of PFP thin films on NaF(100), the domain-size is significantly smaller. This complicates the exclusive illumination of one domain. Therefore a smaller aperture (500 µm) was used and the sample was positioned such, that one domain showed a significant excess over the other, but the influence of the residues of the other rotational domain consequently leads to the expected loss of contrast in the spectra (Fig. S2b).

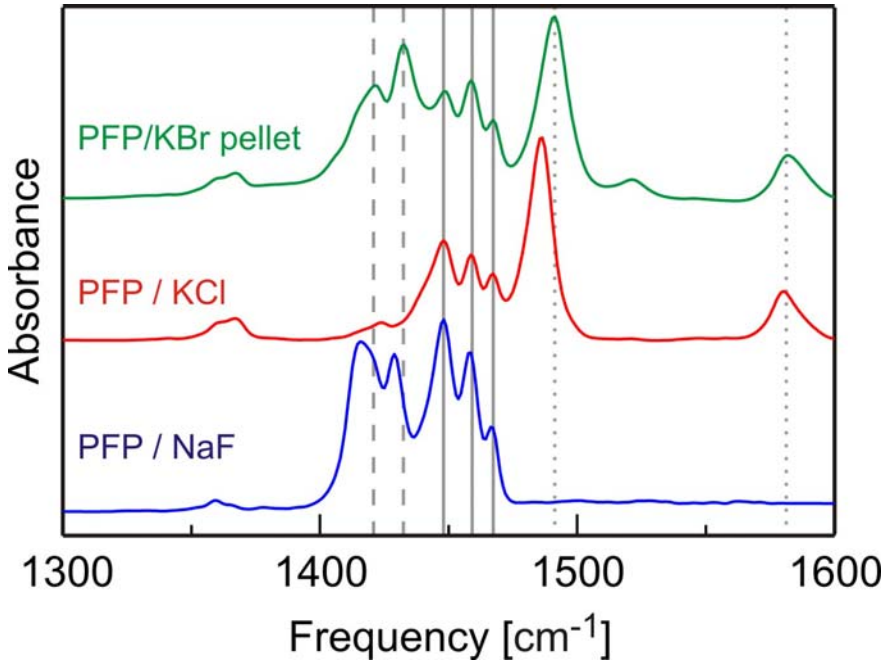

Fig. S3: Magnified region of the IR absorption spectra of isotropically distributed PFP crystallites (top spectrum: PFP/KBr), and of PFP-thin films where molecules adopt a recumbent orientation (central spectrum: PFP/KCl) or an upright orientation (bottom spectrum: PFP/NaF). These thin film spectra have been measured without an aperture and thus are in-plane domain averaged.

As shown in Figure S3 the described procedure to allocate the modes' spectral dependence was also applicable in spectral regions where many modes appear close to each other. The small variations in the mode energies of less than 5 cm^{-1} in the different samples are attributed to slight lattice relaxations due to various degrees of lattice match between the substrate and differently oriented epitaxial PFP-films, respectively the free crystallites in the KBr matrix.

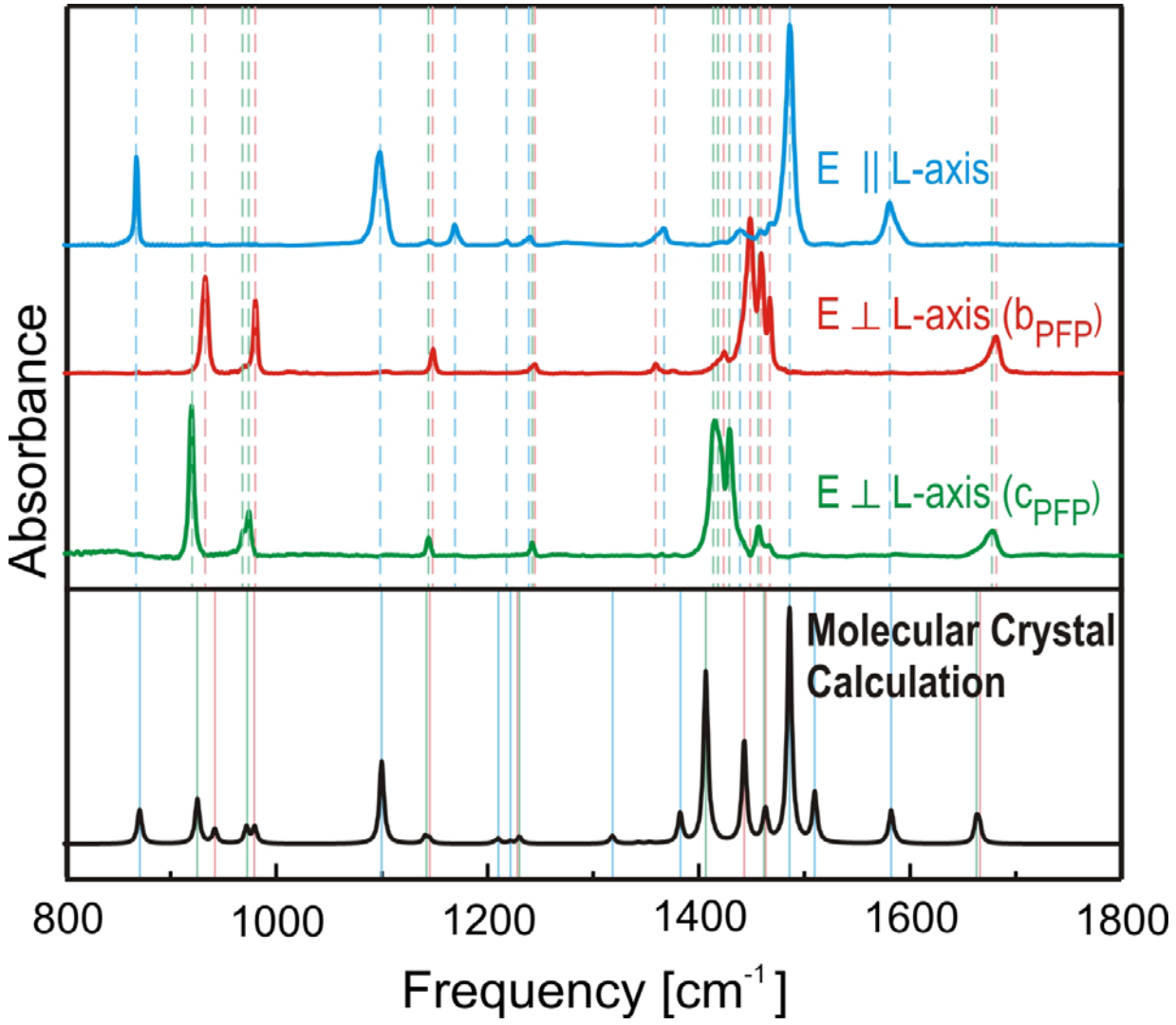

Fig. S4:

Difference spectra of PFP-films with signals from orthogonally oriented minority domains subtracted, showing hypothetic IR-spectra for L-, b- and c-polarization, which are compared to the molecular crystal calculation.

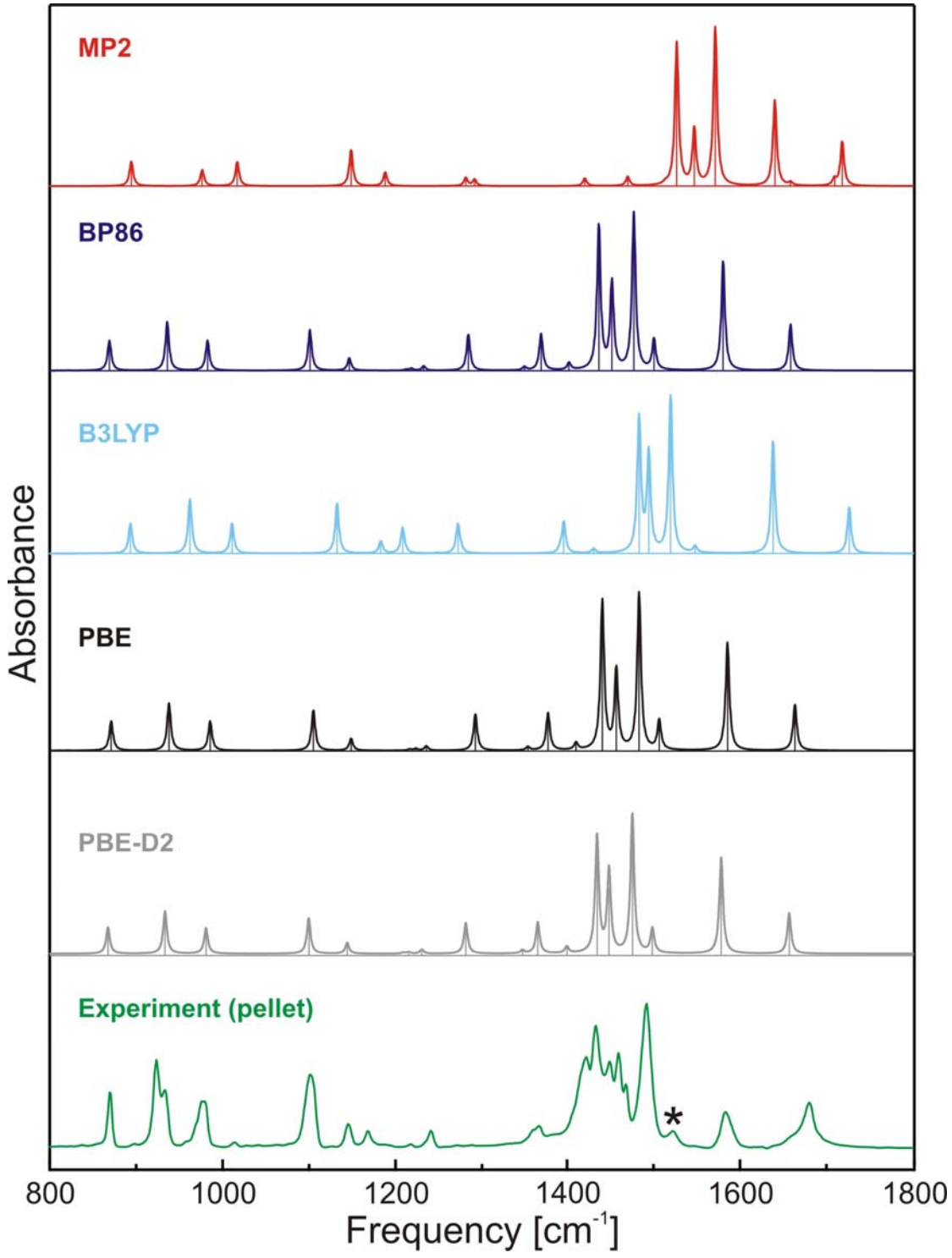

Figure S5. Comparison of PBE-D2, PBE, BP86, B3LYP and MP2 vibrational spectra for the free molecule in comparison to experiment (KBr pellet). All calculated spectra have been scaled by a factor of 1.015 which provides the best agreement of the PBE-D2 calculations with the experimental pellet spectrum and use a def2-TZVPP basis set. The different spectra clearly show that different scaling factors have to be used for the various functionals.

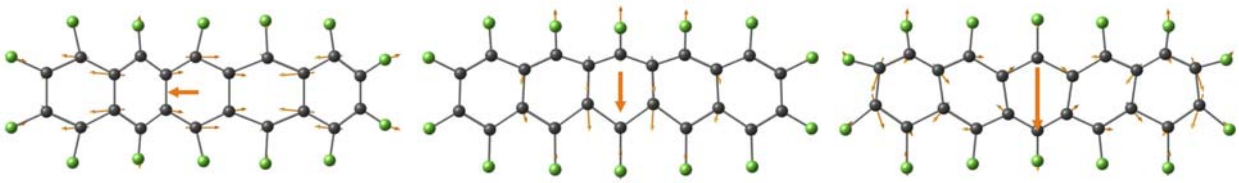

Mode **66**
867.3 cm^{-1} (b_{3u})

Mode **67**
933.4 cm^{-1} (b_{2u})

Mode **69**
980.9 cm^{-1} (b_{2u})

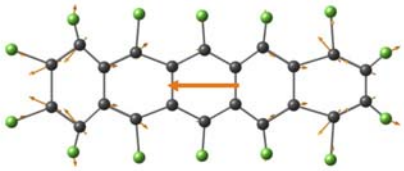

Mode **72**
1099.8 cm^{-1} (b_{3u})

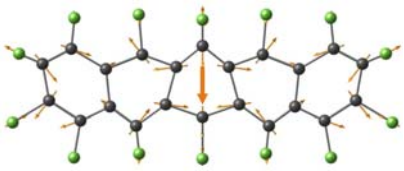

Mode **74**
1144.4 cm^{-1} (b_{2u})

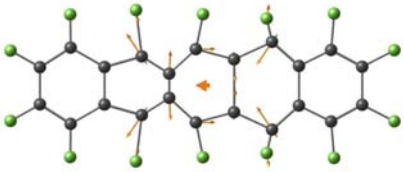

Mode **76**
1209.4 cm^{-1} (b_{3u})

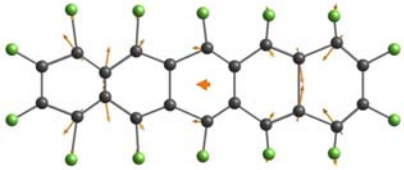

Mode **77**
1215.6 cm^{-1} (b_{3u})

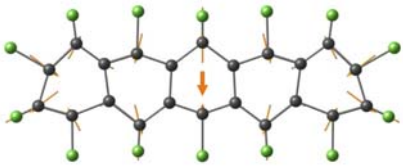

Mode 7**8**
1231.0 cm^{-1} (b_{2u})

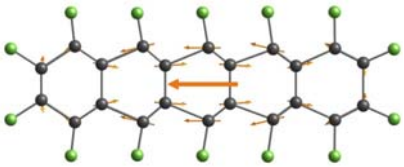

Mode **81**
1281.8 cm^{-1} (b_{3u})

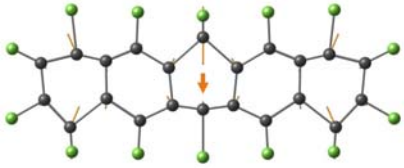

Mode **83**
1347.5 cm^{-1} (b_{2u})

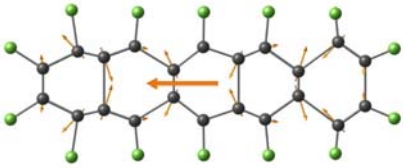

Mode **85**
1365.2 cm^{-1} (b_{3u})

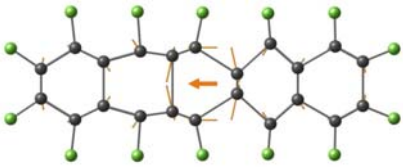

Mode **88**
1398.9 cm^{-1} (b_{3u})

Mode **90**
1433.9 cm^{-1} (b_{2u})

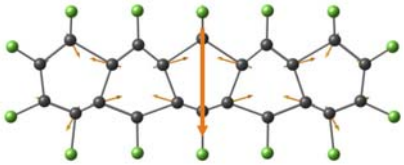

Mode **91**
1447.7 cm^{-1} (b_{2u})

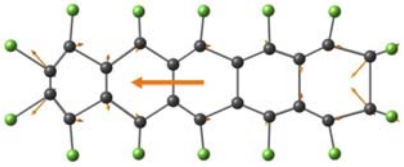

Mode **92**
1474.8 cm^{-1} (b_{3u})

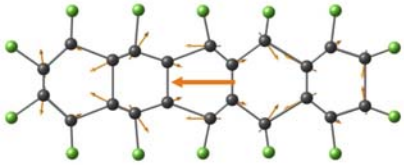

Mode **94**
1498.0 cm^{-1} (b_{3u})

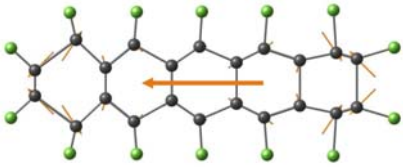

Mode **98**
1577.7 cm^{-1} (b_{3u})

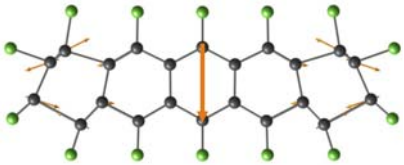

Mode **101**
1656.5 cm^{-1} (b_{2u})

Figure S6. Displacement vectors (blue), transition dipole moments (TDM, orange) and symmetries for most intense modes of the PFP molecule (PBE-D2). Ground-state geometry is displaced along normal modes. Mode numbering is according to Table 3. Note, that the actual displacement vectors are enlarged.

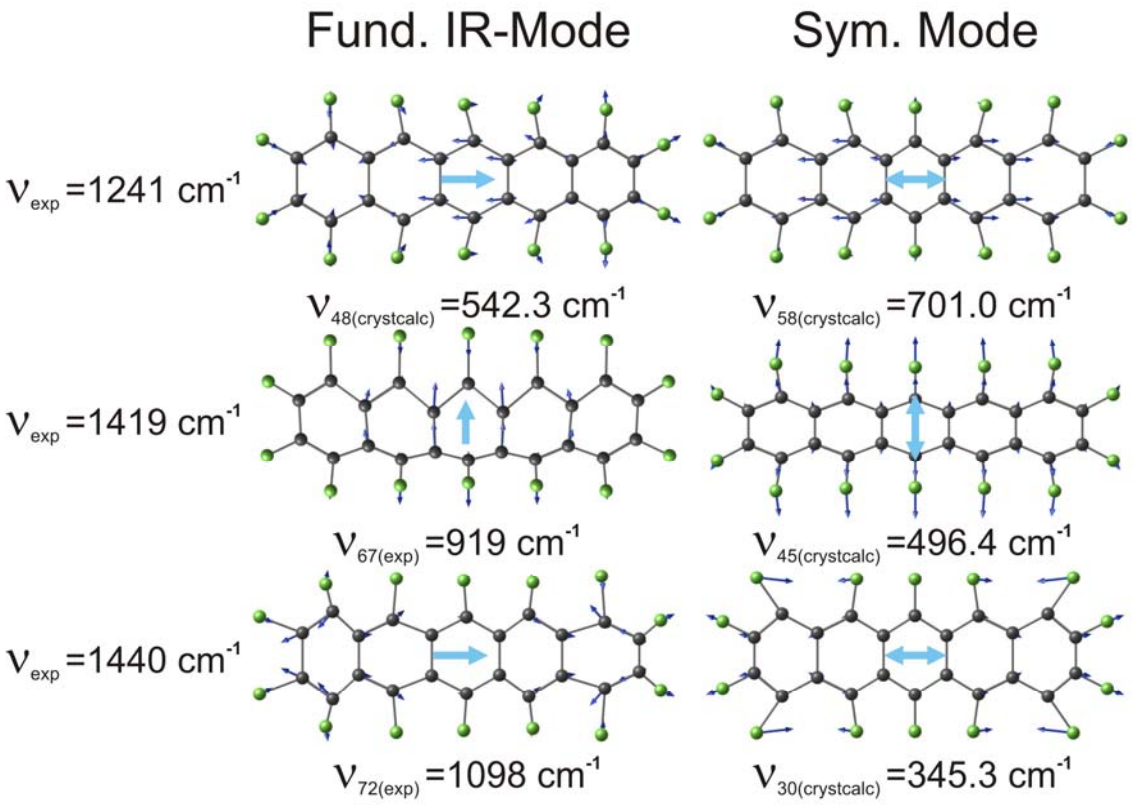

Figure S7. Displacement vectors (blue) of the proposed combination bands

Table S2. All vibrational modes of the PFP single molecule (PBE-D2). All modes with L, M and N-polarisation are IR-active, modes with a_g, b_{1g}, b_{2g} or b_{3g} symmetry are raman-active (grey-shaded). Modes with a_u symmetry are neither IR- nor Raman-active. Intensities were calculated only for IR-active modes. Scaling factor = 1.015 (see main text). Note, that the actual displacement vectors are enlarged.

Nr.	ν [cm^{-1}]	ν_{scaled}[cm^{-1}]	I	symmetry
1	9.8	9.9	0.000	N
2	19.8	20.1	-	a_u
3	47.2	47.9	-	b_{3g}
4	47.6	48.3	-	b_{2g}
5	63.6	64.6	0.000	N
6	65.4	66.4	-	a_u
7	73.5	74.6	0.000	M
8	89.0	90.4	-	b_{2g}
9	89.2	90.5	0.000	N

10	92.5	93.8	-	b_{3g}
11	149.3	151.6	-	b_{3g}
12	149.5	151.7	-	a_u
13	151.0	153.3	-	b_{1g}
14	164.4	166.9	0.003	N
15	166.5	169.0	-	b_{2g}
16	167.0	169.5	-	a_g
17	189.4	192.3	0.001	N
18	231.6	235.0	0.001	M
19	256.4	260.2	-	b_{2g}
20	267.8	271.8	0.000	L
21	271.0	275.1	-	b_{1g}
22	280.7	284.9	-	a_g
23	287.7	292.0	0.000	L
24	289.3	293.7	-	b_{1g}
25	298.2	302.7	0.004	M
26	321.4	326.2	-	b_{1g}
27	329.6	334.5	0.003	L
28	333.7	338.7	-	a_g
29	337.3	342.4	0.002	M
30	341.0	346.1	-	a_g
31	348.4	353.6	0.001	N
32	350.6	355.9	-	a_u
33	351.2	356.5	-	b_{3g}
34	370.0	375.5	-	b_{3g}
35	376.8	382.4	0.000	L
36	395.3	401.2	-	b_{2g}
37	396.9	402.8	-	a_u
38	397.4	403.4	-	b_{1g}
39	431.4	437.9	-	a_g
40	433.2	439.7	0.005	L
41	436.8	443.3	0.000	L
42	441.1	447.7	-	a_g
43	452.5	459.3	0.001	M
44	465.5	472.5	-	b_{3g}
45	478.5	485.6	-	a_g
46	499.2	506.7	-	b_{1g}
47	515.3	523.0	0.006	M
48	528.1	536.1	0.095	L
49	537.1	545.1	0.000	N
50	588.1	596.9	-	b_{2g}

51	594.1	603.0	-	b_{1g}
52	594.8	603.7	-	a_u
53	616.3	625.6	-	b_{3g}
54	630.8	640.3	0.000	N
55	639.6	649.2	-	a_u
56	656.3	666.1	-	b_{3g}
57	666.1	676.1	-	b_{2g}
58	687.8	698.1	-	a_g
59	694.8	705.2	0.002	N
60	700.3	710.8	-	a_u
61	709.7	720.3	0.000	M
62	747.1	758.3	-	b_{3g}
63	785.6	797.4	-	b_{1g}
64	803.6	815.6	-	b_{1g}
65	807.2	819.3	0.001	M
66	854.5	867.3	0.188	L
67	919.6	933.4	0.305	M
68	923.8	937.6	-	b_{1g}
69	966.4	980.9	0.182	M
70	989.7	1004.5	-	a_g
71	1041.7	1057.3	-	b_{1g}
72	1083.6	1099.8	0.253	L
73	1089.0	1105.3	-	a_g
74	1127.5	1144.4	0.077	M
75	1187.6	1205.4	-	a_g
76	1191.6	1209.4	0.008	L
77	1197.7	1215.6	0.011	L
78	1212.8	1231.0	0.029	M
79	1213.6	1231.8	-	b_{1g}
80	1222.4	1240.7	-	a_g
81	1262.9	1281.8	0.220	L
82	1303.6	1323.1	-	b_{1g}
83	1327.5	1347.5	0.023	M
84	1340.9	1361.1	-	a_g
85	1345.0	1365.2	0.225	L
86	1371.3	1391.9	-	b_{1g}
87	1372.8	1393.3	-	a_g
88	1378.2	1398.9	0.047	L
89	1401.5	1422.6	-	a_g
90	1412.7	1433.9	0.844	M
91	1426.4	1447.7	0.598	M

92	1453.0	1474.8	1.000	L
93	1459.3	1481.2	-	a_g
94	1475.9	1498.0	0.176	L
95	1508.7	1531.4	-	a_g
96	1528.9	1551.9	-	b_{1g}
97	1534.6	1557.6	-	b_{1g}
98	1554.4	1577.7	0.689	L
99	1563.1	1586.6	-	a_g
100	1572.4	1596.0	0.000	M
101	1632.0	1656.5	0.290	M
102	1633.9	1658.4	-	b_{1g}

The visualization of the vibration modes of single PFP molecules and the PFP crystals are available and can be visualized using Chemcraft (Shareware) – as done in the Manuscript - or Molden (free to use for academic purpose). Additionally, the modes are available as animated gifs.

References

(1) Sakamoto, Y.; Suzuki, T.; Kobayashi, M.; Gao, Y.; Fukai, Y.; Inoue, Y.; Sato, F.; Tokito, S. *J. Am. Chem. Soc*. **2004**, *126*, 8138.

Full References of main text

(29) Frisch, M. J.; Trucks, G. W.; Schlegel, H. B.; Scuseria, G. E.; Robb, M. A.; Cheeseman, J. R.; Scalmani, G.; Barone, V.; Mennucci, B.; Petersson, G. A.; Nakatsuji, H.; Caricato, M.; Li, X.; Hratchian, H. P.; Izmaylov, A. F.; Bloino, J.; Zheng, G.; Sonnenberg, J. L. H., M.; Ehara, M.; Toyota, K.; Fukuda, R.; Hasegawa, J.; Ishida, M.; Nakajima, T.; Honda, Y.; Kitao, O.; Nakai, H.; Vreven, T.; Montgomery, Jr., J. A.; Peralta, J. E.; Ogliaro, F.; Bearpark, M.; Heyd, J. J.; Brothers, E.; Kudin, K. N.; Staroverov, V. N.; Kobayashi, R.; Normand, J.; Raghavachari, K.; Rendell, A.; Burant, J. C.; Iyengar, S. S.; Tomasi, J.; Cossi, M.; Rega, N.; Millam, N. J.; Klene, M.; Knox, J. E.; Cross, J. B.; Bakken, V.; Adamo, C.; Jaramillo, J.; Gomperts, R.; Stratmann, R. E.; Yazyev, O.; Austin, A. J.; Cammi, R.; Pomelli, C.; Ochterski, J. W.; Martin, R. L.; Morokuma, K.; Zakrzewski, V. G.; Voth, G. A.; Salvador, P.; Dannenberg, J. J.; Dapprich, S.; Daniels, A. D.; Farkas, Ö.; Foresman, J. B.; Ortiz, J. V.; Cioslowski, J.; Fox, D. J. ; Gaussian, Inc.: Gaussian 09, Revision A.02, Wallingford CT, 2009.
(52) Martinelli, N. G.; Olivier, Y.; Athanasopoulos, S.; Delgado, M. C. R.; Pigg, K. R.; da Silva, D. A.; Sanchez-Carrera, R. S.; Venuti, E.; Della Valle, R. G.; Bredas, J. L.; Beljonne, D.; Cornil, J. *ChemPhysChem* **2009**, *10*, 2265-2273.
(53) Delgado, M. C. R.; Pigg, K. R.; Filho, D.; Gruhn, N. E.; Sakamoto, Y.; Suzuki, T.; Osuna, R. M.; Casado, J.; Hernandez, V.; Navarrete, J. T. L.; Martinelli, N. G.; Cornil, J.; Sanchez-Carrera, R. S.; Coropceanu, V.; Bredas, J. L. *J. Am. Chem. Soc.* **2009**, *131*, 1502-1512.

THE JOURNAL OF PHYSICAL CHEMISTRY C

Addition/Correction

pubs.acs.org/JPCC

Correction to "Vibrational Davydov Splittings and Collective Mode Polarizations in Oriented Organic Semiconductor Crystals"

Tobias Breuer, Mehmet A. Celik, Peter Jakob, Ralf Tonner,* and Gregor Witte*

J. Phys. Chem. C **2012**, *116* (27), 14491−14503. DOI: 10.1021/jp304080g

In our paper, the GGA functional for the calculations of the free molecule was BP86-D2 instead of PBE-D2 as stated in the method part. Calculations with PBE-D2 show that the PFP-bond lengths shorten by approximately 0.001 Å and the vibrational frequencies increase uniformly by 3−10 cm^{-1}. The spectra are thus virtually identical (see Figure 1) and the conclusions are not affected by the small numerical differences.

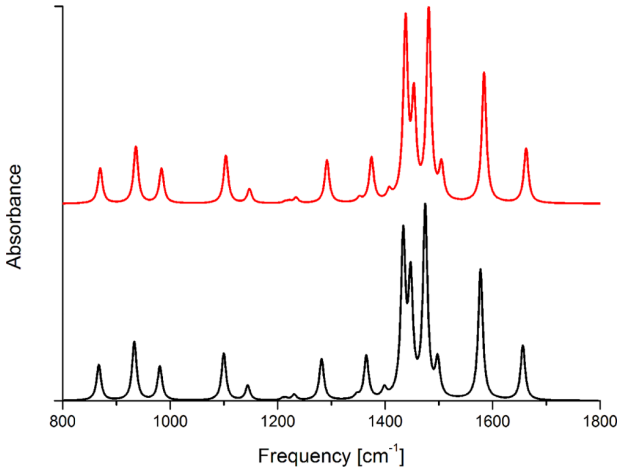

Figure 1. Comparison of simulated spectra for the PFP molecule using BP86-D2 (black) and PBE-D2 (red).

Published: October 10, 2012

5.6 Article VI: Substrate induced thermal decomposition of perfluoro-pentacene thin films on the coinage metals

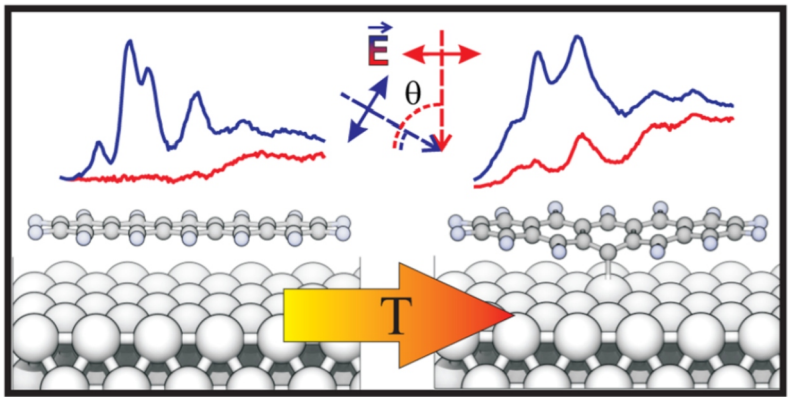

5.6.1 Abstract

The thermal and chemical stability of perfluoropentacene (PFP) thin films grown by organic molecular beam deposition onto the (111)-oriented surfaces of the coinage metals copper, silver, and gold have been studied by means of temperature dependent X-ray photoelectron spectroscopy (XPS) and Near-Edge X-ray absorption fine structure spectroscopy (NEXAFS). Under vacuum conditions, PFP multilayers are completely desorbed at 425 K while molecules in contact with the Au(111) surface remain intact up to 500 K. By contrast, PFP that is in contact with Cu(111) is distinctly distorted and becomes partially defluorinated already upon thermal desorption of multilayers. A pronounced defluorination of PFP also takes place on Ag(111) at temperatures around 440 K, while further heating causes a complete cracking and defluorination. Additional measurements carried out on a regularly stepped silver surface demonstrate that steps are active sites that promote defluorination already at lower temperatures. van der Waals corrected density-functional (DFT-D) calculations show that PFP, though being weakly adsorbed on all three metal surfaces, exhibits a reduced energy barrier for defluorination, in particular on copper and silver, thus reflecting their catalytic activity. The calculations reveal further that defluorinated molecules are covalently bound to the substrate, leading to a notable bending of the molecular backbone. The present study highlights the importance of also considering chemical reactions when theoretically analyzing molecule/metal interactions and indicates that fluorinated aromatic molecules, though offering interesting electronic properties, actually exhibit a limited stability in contact with some electrode surfaces like silver due to catalytic effects.

5.6.2 Methods

Density Functional Theory, Near-Edge X-Ray Absorption Finestructure Spectroscopy, Organic Molecular Beam Deposition, X-Ray Photoelectron Spectroscopy

5.6.3 Own Contribution

I have helped Christian Schmidt to prepare the samples and conduct the NEXAFS and XPS measurements, of which some have been planned and performed exclusively by myself. Furthermore, I have helped to interpret the data and to prepare them for publication as well as to improve the manuscript. Stefan Wippermann and Wolf Gero Schmidt have performed the DFT calculations, Gregor Witte and Wolf Gero Schmidt have also helped to improve the manuscript.

THE JOURNAL OF PHYSICAL CHEMISTRY C

Article

pubs.acs.org/JPCC

Substrate Induced Thermal Decomposition of Perfluoro-Pentacene Thin Films on the Coinage Metals

Christian Schmidt,[†] Tobias Breuer,[†] Stefan Wippermann,[‡] Wolf Gero Schmidt,[§] and Gregor Witte*[,†]

[†]Molekulare Festkörperphysik, Philipps-Universität Marburg, D-35032 Marburg, Germany

[‡]Department of Chemistry, University of California, One Shields Avenue, Davis, California 95616, United States

[§]Lehrstuhl für Theoretische Physik, Universität Paderborn, D-33095 Paderborn, Germany

ABSTRACT: The thermal and chemical stability of perfluoropentacene (PFP) thin films grown by organic molecular beam deposition onto the (111)-oriented surfaces of the coinage metals copper, silver, and gold have been studied by means of temperature dependent X-ray photoelectron spectroscopy (XPS) and Near-Edge X-ray absorption fine structure spectroscopy (NEXAFS). Under vacuum conditions, PFP multilayers are completely desorbed at 425 K while molecules in contact with the Au(111) surface remain intact up to 500 K. By contrast, PFP that is in contact with Cu(111) is distinctly distorted and becomes partially defluorinated already upon thermal desorption of multilayers. A pronounced defluorination of PFP also takes place on Ag(111) at temperatures around 440 K, while further heating causes a complete cracking and defluorination. Additional measurements carried out on a regularly stepped silver surface demonstrate that steps are active sites that promote defluorination already at lower temperatures. van der Waals corrected density-functional (DFT-D) calculations show that PFP, though being weakly adsorbed on all three metal surfaces, exhibits a reduced energy barrier for defluorination, in particular on copper and silver, thus reflecting their catalytic activity. The calculations reveal further that defluorinated molecules are covalently bound to the substrate, leading to a notable bending of the molecular backbone. The present study highlights the importance of also considering chemical reactions when theoretically analyzing molecule/metal interactions and indicates that fluorinated aromatic molecules, though offering interesting electronic properties, actually exhibit a limited stability in contact with some electrode surfaces like silver due to catalytic effects.

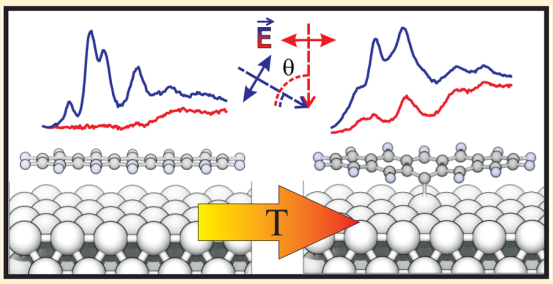

INTRODUCTION

The promising potential of organic electronic applications has triggered considerable research activities aiming at the synthesis of new organic semiconductor (OSC) materials with improved properties.[1,2] In addition to enhanced charge carrier mobility, also improved chemical stability is an important issue since most OSCs exhibit a low threshold for oxidation, leading to a notable degradation under ambient conditions.[3−5] One strategy to avoid such parasitic reactions is based on fluorination of the organic compound, which not only suppresses oxidation but also makes OSC films more hydrophobic, such that additional capping might be redundant.[6] Recently, this approach was also applied to larger acenes such as pentacene (PEN) by the synthesis of perfluoro-pentacene[7] (PFP, Figure 1a). It was further shown that perfluorination also affects the charge carrier polarity, rendering PFP an interesting n-type OSC.

Another aspect of key importance for the successful realization of organic electronic devices is the interaction between OSCs and metals, since it determines the resulting injection barrier of charge carriers at electrodes. Regarding the interaction between PFP and the (111) surfaces of the coinage metals Cu, Ag, and Au, the work function change and adsorption geometry have been studied by means of UPS and XSW.[8−10] In all cases, the vertical adsorption distance between the aromatic plane and the metal surface was found to be about 0.5 Å larger than for the nonfluorinated PEN, while the work function reduction is distinctly smaller than for PEN. These findings have also been obtained in a recent density functional theory study and were attributed to a pronounced Pauli repulsion due to the high electron density of the fluorine atoms.[11] Because of the supposed stability of PFP, only little attention has yet been paid to the thermal and chemical stability of PFP layers adsorbed on metals. Interestingly though, evidence for partial decomposition of PFP on Cu(111) above room temperature was reported,[9,12] while PEN monolayers adsorbed on the more reactive Cu(110) surface can be heated up to 600 K without any noticeable degradation.[13] Similarly surprising was our recent finding that thermal induced decomposition of PFP on Ag(111) occurs already below 450 K.[14] This suggests that on Ag(111) PFP is actually *less* stable than the nonfluorinated analogue which was found to desorb *intactly* at 550 K from Ag(111).[15] Even more surprising is the behavior found for smaller fluoroacenes such as perfluorobenzene. In that case, a decomposition of molecular adlayers is

Received: July 24, 2012
Revised: September 12, 2012
Published: September 20, 2012

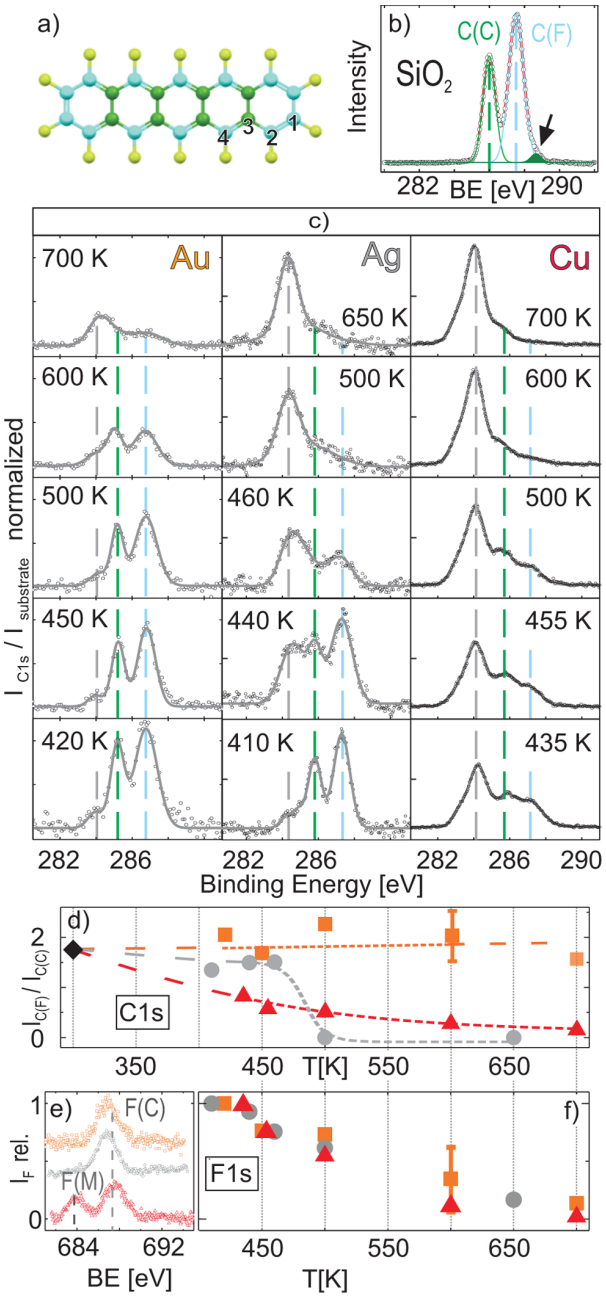

Figure 1. Summary of XPS data obtained for PFP films. Panel b displays the C1s region of a 70 nm PFP film on SiO_2 exhibiting two carbon species, C(C) and C(F), according to their chemical coordination within the molecule as depicted in part a and an additional shake up signal (black arrow, see text). Panel c displays the thermal evolution of XP spectra of PFP monolayer films on the three metal surfaces (Au, orange; Ag, gray; Cu, red) together with (d) the ratio of the carbon species C(F) and C(C). F1s spectra shown in part e revealed only one species on gold and silver, F(C), while on copper also the second species F(M) was found. The thermal evolution of the F(C) intensities is shown in part f.

reported upon heating on polycrystalline silver substrates,[16] while an intact desorption is found for Cu(111).[17] This is counterintuitive, since copper is the more reactive metal, which demonstrates a lack of understanding of the chemical interaction of fluoroacenes and metal surfaces.

As these findings challenge the general concept of fluorinated OSCs, we believe a systematical study to be very important. Therefore, we have studied the thermal stability of PFP adsorbed on the coinage metal surfaces Cu(111), Ag(111), and Au(111) by means of temperature dependent high resolution synchrotron based X-ray photoelectron spectroscopy (XPS) and X-ray absorption spectroscopy (NEXAFS). Particular attention was paid to possible radiation damages as well as to the influence of defects like surface steps. The latter was achieved by additionally examining the stability of PFP films on a vicinal silver Ag(221) surface. To understand the underlying mechanism of the observed decomposition, we performed total-energy calculations based on density-functional theory (DFT). By calculating a potential energy surface for chemical reactions, possible reaction pathways for the decomposition as well as belonging energy barriers were derived.

METHODOLOGY

Experimental Section. All measurements were carried out at the HE-SGM dipole beamline at the synchrotron storage ring facility BESSY II in Berlin (Germany). The X-ray photoemission spectra were recorded at an incident angle of 45° and at normal emission using a hemispherical electron energy analyzer (Scienta R3000) using typical pass energies of 100 eV and photon energies between 500 and 880 eV depending on the substrate and the studied region (C1s or F1s) chosen such that parasitic contributions by, e.g., auger lines were omitted. To provide a precise energy calibration, the XPS binding energies have been referenced to characteristic substrate peaks of the various samples (Au $4f_{7/2}$ 84.0 eV, Ag $3d_{5/2}$ 368.1 eV, Cu $3p_{3/2}$ 75.0 eV)[18] which have been measured simultaneously. The spectra have been corrected by subtracting a Shirley background[19] and dividing by the intensity of the corresponding substrate signals to compensate variations of the photon flux. After that, spectra have been normalized to the maximum intensity of each series to enable comparison. Carbon edge NEXAFS spectra were recorded by measuring the secondary electron yield as a function of photon energy of the linearly polarized (polarization factor 91%) incident synchrotron light. The exit slit of the grating monochromator was chosen such that an energy resolution of about 300 meV was achieved. To enhance surface sensitivity of NEXAFS by essentially detecting auger electrons from surface-near layers and reducing secondary electrons emitted from deeper layers and the surface, a retarding field of −150 eV was applied to the entrance grid of the channel plate detector (*partial electron yield at fixed detector position*).[20] To calibrate the absolute energy scale of the NEXAFS spectra, a simultaneously recorded signal of the photocurrent from a carbon coated gold grid in the incident beam was used which exhibits a sharp resonance at 284.9 eV. All NEXAFS raw data have been normalized with respect to the incident photon flux, and the transmission characteristics of the clean substrates were considered. Different types of metal substrates have been examined in the present experiments. While a Cu(111) and a Ag(221) single crystal were used, the Au(111) and Ag(111) samples consist of 150 nm metal films epitaxially grown on freshly cleaved mica substrates under UHV conditions. All samples were prepared in situ by repeated sputtering and annealing procedures, providing sharp LEED patterns and carbon free XP spectra. All perfluoropentacene (PFP, Kanto Denka Kogoyo, purity >99%) films were deposited onto the various substrates at room temperature from a Knudsen cell at a typical growth rate of 10 Å/min, which

dx.doi.org/10.1021/jp307316r | J. Phys. Chem. C 2012, 116, 24098−24106

was monitored by quartz microbalance. To suppress disturbing signatures from multilayer films and to prepare a nominal monolayer, at first 10 nm of PFP were deposited and subsequently excess multilayers were thermally desorbed by carefully heating the samples to about 410−430 K. Note that this procedure results in a *nominal monolayer*, which does not necessarily equal a *densely packed* layer.[21]

COMPUTATIONAL

The total-energy calculations are performed using the Vienna Ab Initio Simulation Package (VASP)[22] and employing the PW91 functional[23] for the generalized gradient approximation to the electron exchange and correlation (XC) energy. The electron−ion interaction is described by the projector-augmented wave method,[24] which allows for a relatively moderate energy cutoff of 400 eV for the plane-wave basis. The adsystem was modeled by periodically repeated supercells, containing six atomic coinage metal layers arranged in a (7×4) translational symmetry, the adsorbed molecules, and a vacuum region of 15 Å. The calculations were performed using the equilibrium lattice constants that we determined to be 3.63, 4.17, and 4.19 Å for Cu, Ag, and Au, respectively. Brillouin zone integrations are restricted to the Γ point. The smearing of the electronic states is performed with the Methfessel−Paxton scheme of the first order with a width of 0.2 eV.

The accurate modeling of loosely bonded adsorbates is a major challenge for density-functional theory (DFT), because the currently used XC energy functionals do not properly describe the long-range vdW interactions.[25−30] In order to account approximately for dispersion interactions, we use a semiempirical, so-called DFT-D scheme[31,32] based on the London dispersion formula. Reuter and co-workers[28] compared adsorption energies calculated within various DFT-D schemes for the adsorption of benzene on coinage metal (111) surfaces with experimental data and concluded that the approach by Ortmann et al.[31,32]—the one which is used in the following—provides results in the *"right ballpark and could even be semiquantitative"*. Similar conclusions can be drawn from benchmark calculations by Blügel's group[27] for a variety of small, π-conjugated molecules adsorbed on Ag(110). In these calculations, the approximate treatment of dispersion interactions with DFT-D was compared with a more realistic vdW density-functional (vdW-DF) approach.[33] It turned out that—depending on the molecule—the calculated total adsorption energies differ by 50−200 meV. Relative energy differences calculated within either scheme agree within 30−120 meV. It should be borne in mind, however, that vdW-DF is an approximation as well; see, e.g., the results in refs 30 and 34. Altogether, one has to state that the accurate description of dispersion forces for complex systems is not satisfactorily solved yet.[29] Still, since we are primarily interested in energy differences calculated for identical molecules with similar adsorption geometries on different coinage metal (111) surfaces, the present DFT-D scheme is expected to be sufficiently accurate to allow for valid conclusions.

RESULTS

XPS. The thermal stability of PFP monolayer films adsorbed on (111) surfaces of the three coinage metals gold, silver, and copper was at first characterized by means of temperature dependent XPS measurements. This offers a quantitative analysis of the film composition and thus enables monitoring of desorption and chemical alteration processes. To begin with, XP spectra were recorded for a 70 nm PFP film deposited onto SiO_2 to provide bulk-like reference spectra of PFP without any chemical substrate interaction, which are virtually identical to those obtained for multilayer films on gold. As shown in Figure 1b, the C1s signal is split into two peaks according to the different chemical environment of carbon atoms within the molecules.[9,35] The signal at a binding energy of 286.0 eV corresponds to the inner-ring carbon, only bound to neighboring carbon atoms, C(C), while the second, more intense peak at 287.5 eV is due to carbon atoms bound to fluorine, C(F). We note that the two subcomponents exhibit a different peak width (C(C), 0.71 eV; C(F), 0.86 eV), which can be related to slight variations of the chemical shift of C(F) atoms according to different fluorine coordination of their next nearest carbon atoms. As depicted in Figure 1a, this leads to the presence of four different carbon species, [C(C), C(F) surrounded by two C(C), C(F) surrounded by C(C) and C(F), and C(F) surrounded by two C(F)] with a multiplicity ratio of (8:6:4:4). Since the different C(F) species could not be separated in the present data, they were merged and treated as one effective C(F) peak for the analysis of the stoichiometry. The quantitative analysis of the C(C) and C(F) peak areas yields a ratio of 4:7 as expected for PFP. In addition, a rather weak but distinct shoulder appears in the C1s region at a binding energy of 289.2 eV (indicated by the black arrow in Figure 1b), which is attributed to a shakeup satellite. Since it remains unclear whether this signal originates from the C(F) or C(C) peak, the corresponding energy loss amounts to 1.1 or 2.7 eV, respectively. Note that these energies differ from the lowest excitation at 1.75 eV found in optical absorption spectra of PFP films.[36,37] A similar situation has been reported by Rocco et al.[38] for nonfluorinated acenes where the energy loss of shakeup satellites is smaller than the optical HOMO−LUMO band gaps, which might be attributed to the different band gap of the final ionic state formed in the photoemission process.

To examine the thermal stability of PFP monolayer films on the different coinage metals, the samples were in each case heated with a rate of approximately 1 $K\,s^{-1}$ to the denoted temperature before the belonging XP spectra were acquired during cooldown. Figure 1c compares the thermal evolution of the C1s signal. The C1s signals of PFP monolayers on Ag(111) and Au(111) resemble the bulk data, except from a core-hole screening shift due to the underlying metal of about −0.7 eV.[14,35] By contrast, the PFP monolayer on Cu(111) prepared by briefly heating the sample to 435 K exhibits a new, dominating carbon signal around 284 eV (indicated by a dashed gray line). The binding energy of this new peak, which was also observed in a recent study by Glowatzki et al. for heated PFP films adsorbed on Cu(111),[12] indicates the presence of a nonfluorinated carbon species, while the broad peak width hampers a clear distinction between aliphatic or aromatic species which are energetically rather similar. A similar species appears on the Ag(111) surface after heating the PFP adlayer to 440 K where it becomes dominating at 460 K and above. We note that hydrocarbonaceous contributions were observed earlier for PFP films on metals and had been attributed to contaminations or decomposition reactions at surface defects.[9,35] For a quantitative analysis of the temperature dependent XPS measurements, the background-subtracted and normalized areas of the C(C) and C(F) peaks are determined. Figure 1d compares the thermal evolution of the

dx.doi.org/10.1021/jp307316r | J. Phys. Chem. C 2012, 116, 24098−24106

intensity ratios C(F)/C(C) of nominal PFP monolayers on the various metal substrates. The black diamond at 300 K represents the ratio found for the undisturbed bulk reference film (cf. Figure 1b). At temperatures between 400 and 460 K, the C(F)/C(C) signal ratio obtained for PFP films on silver and gold well corresponds to the stoichiometry of PFP within the experimental error. By contrast, the PFP molecules on copper exhibit a distinct reduction of the fluorinated carbon species and the $I_{C(F)}/I_{C(C)}$ ratio decays continuously with increasing temperature. Above 460 K, also the progression of the $I_{C(F)}/I_{C(C)}$ ratio on the noble metals differs. As indicated in our previous study,[14] where a laboratory X-ray source was used, massive decomposition of PFP molecules on Ag(111) occurs already slightly above the multilayer desorption temperature. (This refers to the temperature at which multilayers have desorbed during *our heating protocol*. We note that the process is thermally activated and occurs in a nonequilibrium situation under UHV conditions so that a real *desorption temperature* is not precisely defined.) By contrast, the $I_{C(F)}/I_{C(C)}$ ratio does not significantly change for a PFP monolayer on gold upon heating, though the total carbon intensity decreases which suggests a partial desorption of intact molecules. Only after annealing at 700 K, a small carbonaceous signal of non-fluorinated species arises, which might be attributed to molecular decomposition occurring at defects or to contaminations diffusing from the sample holder. Note that, due to the low intensity caused by thermal desorption, the ratio given in Figure 1d for the last data point is poorly defined. The temperature dependent XPS measurements thus indicate a decomposition of PFP on Cu and Ag, while intact desorption dominates on Au.

In addition, F1s spectra were recorded after every heating step. The quantitative analysis of the peak intensity yields a continuous decrease with increasing temperature for all metals, as shown in Figure 1f. Typical F1s spectra of heated PFP monolayers (450 K) on Au(111) and Ag(111) are shown in Figure 1e, which exhibit only one fluorine species, F(C), as expected from the molecular structure. By contrast, on Cu(111), an additional fluorine species arises upon heating (best visible in the 600 K spectrum shown in Figure 1e), which we assign to copperfluoride, F(M).[18]

NEXAFS. In a next step, temperature dependent carbon edge X-ray absorption measurements were carried out, which allow for determination of the position of unoccupied molecular electronic levels. This information enables a chemical distinction between aromatic and aliphatic units and can be used to complement the XPS data in order to understand the different thermal stability of PFP on the various metals. Moreover, the dichroism of the NEXAFS signatures yields additional information about the orientational ordering of the adsorbed molecules.[20] The top panel of Figure 2 shows a typical normalized C1s NEXAFS spectrum of a PFP multilayer film on SiO_2 that was recorded at an incident angle of $\theta = 55°$ of the field vector $\vec{E}$ relative to the surface normal. On the basis of our previous analysis,[21] the first four peaks (285.3, 286.2, 286.8, and 288.3 eV) can be assigned to excitations of C1s electrons into unoccupied π^* orbitals, while the other resonances appear at energies larger than the continuum step (indicated in the NEXAFS spectrum at 450 K on Au(111) in Figure 2b) and therefore can be attributed to σ^* resonances or Rydberg states. The sharp π^* resonances also appear for PFP monolayers on Au(111) and Ag(111) in the spectra taken at grazing incidence ($\theta = 30°$, blue curves). This indicates the

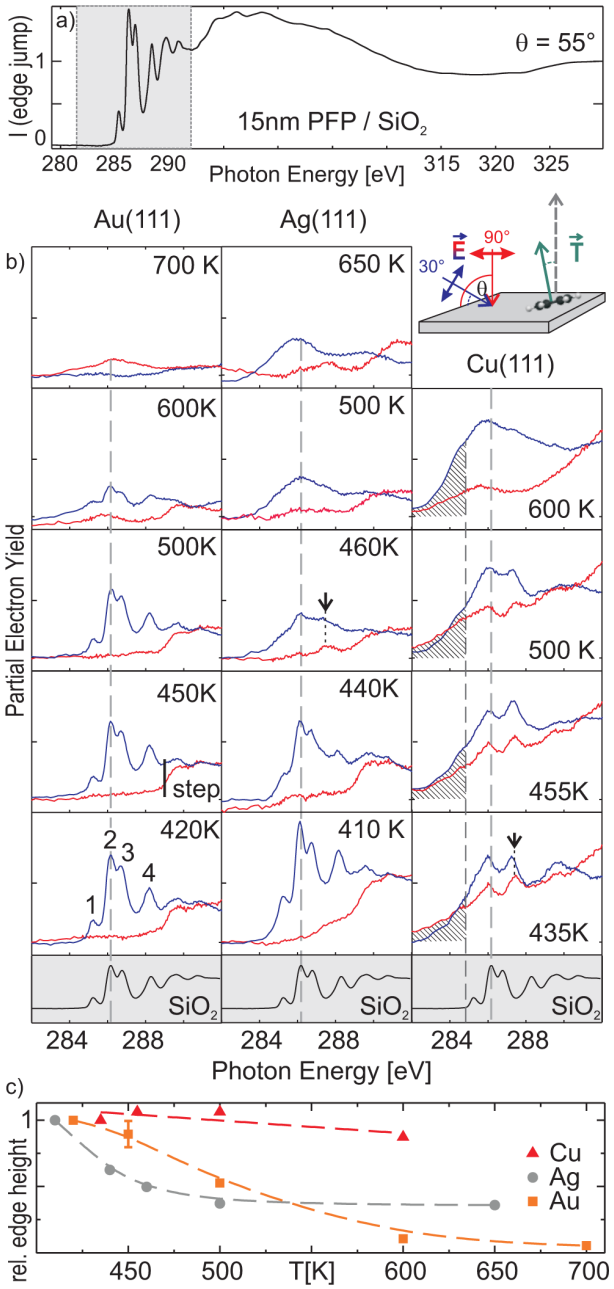

Figure 2. Series of carbon edge NEXAFS spectra of PFP films: (a) full spectrum of a 15 nm thick multilayer on SiO_2 that is used as a reference, together with (b) enlarged spectra of the π^*-region for PFP monolayers on the three metal surfaces recorded after applying different heating steps. For comparison, the relaxation-shift corrected π^*-region of the reference spectrum (a) is also shown in the bottom row. The experimental geometry illustrating the color code and the transition dipole moment of vector type π^* orbitals are depicted in the upper right. Panel c shows the thermal evolution of the height of the carbon edge jump relative to that after the first heating step (i.e., nominal monolayer).

absence of any distinct modification of unoccupied molecular orbitals of PFP due to chemical interaction with the underlying noble metal and suggests an almost van der Waals (vdW) type interaction. For PFP, only a small relaxational shift of about 0.2 eV occurs between NEXAFS data of multi- and monolayer

dx.doi.org/10.1021/jp307316r | J. Phys. Chem. C 2012, 116, 24098−24106

films, due to the underlying metal substrate.[39] NEXAFS spectra of a PFP monolayer on the noble metals taken at normal incidence ($\theta = 90°$, red curves) reveal no π^* resonances, hence showing a pronounced dichroism which reflects a flat lying adsorption geometry (for a quantitative analysis, see Marks et al.[21]). Figure 2 shows further a series of magnified C1s NEXAFS spectra of the π^* region of PFP monolayer films adsorbed on the three metals as a function of the annealing temperature. For each heating step, the NEXAFS spectra were recorded subsequent to the respective XPS measurements. To also provide information about the molecular orientation, the NEXAFS data were taken at normal and grazing incidence. Analyzing the peak area of the individual resonances provides a comparison of the remaining contribution of a species. Moreover, the height of the carbon edge jump (i.e., difference of intensities at 330 and 270 eV) allows for a quantitative monitoring of the overall carbon coverage (see Figure 2c), which corroborates the trend obtained in the temperature dependent XPS measurements (cf. Figure 1d,f).

In contrast to the noble metal substrates, the PFP monolayer on Cu(111) exhibits a distinctly different NEXAFS signature already after thermal desorption of the excessive multilayer (i.e., the first heating step). Instead of four sharp resonances, only one broad resonance around 286 eV remained visible, while the others are smeared out, yielding a broad background signal. In addition, a new peak appears in the NEXAFS spectra at 287.3 eV (indicated by a black arrow), as well as noticeable intensity at energies lower than the first peak of the PFP bulk spectra (hatched area). Since the latter signals appear only for π^* resonances of nonfluorinated carbon species, they indicate the formation of fluorine-free fragments with C−C double bonds which might coke upon further heating. Moreover, the distinct NEXAFS signatures were not only observed at grazing incidence (blue curves) but also seen at normal incidence (red curves), which reveals a changed dichroism. Though this might indicate a change in the molecular orientation, it should also be taken into consideration that the molecular orbitals can be distorted due to chemical interaction with the substrate, such that the transition dipole moment, $\vec{T}$, of the π^* transitions is no longer perpendicular to the aromatic ring plane.[40,41] Therefore, a quantitative analysis of the tilt angle can be misleading[42] and was omitted. A similar situation occurs for pentacene monolayers chemisorbed on Cu(110) where a noticeable dichroism was found in the NEXAFS data[13] although the adsorbed molecules are not tilted.[43] Using standing X-ray waves, it has been demonstrated that PFP molecules adsorbed on Cu(111) also exhibit a distinct geometrical distortion leading to an upright bending of the fluorine atoms.[9]

Upon further annealing, quite different changes appear in the NEXAFS spectra. On Au(111), the distinct signature of the four sharp π^* resonances as well as the pronounced dichroism remain clearly visible up to temperatures of more than 500 K, while the intensity of these resonances and hence the coverage are reduced upon heating above 450 K. This reflects a thermal desorption of entire molecules without noticeable decomposition, which is in agreement with the findings of the temperature dependent XPS measurements (cf. Figure 1). Only for temperatures above 600 K, an additional, broad peak with a reduced dichroism appears around 286 eV, which might be attributed to a thermally induced fragmentation and coking. In view of the rather high temperature of this process, where virtually all molecules are desorbed from the Au(111) surface, the remaining signal is attributed to a minority of molecules that were more firmly bound to defects. In contrast to gold, the thermal evolution of PFP films on Ag(111) is quite different. In the case of the silver sample already after heating to 440 K, a noticeable broadening and intensity reduction of the π^* resonances can be recognized. Briefly heating the film only 20 K higher causes a complete disappearance of the fine structure and the appearance of a new peak at 287.3 eV (indicated by the arrow), as found already in the first annealing step on Cu(111). Further heating causes an additional peak broadening, while the NEXAFS spectra still reveal a distinct signal, even when heating to 650 K. The overall carbon coverage decreases, but in contrast to the case of Au(111), firmly bound species are found up to high temperatures for Ag(111). The thermal evolution of NEXAFS spectra of PFP on Cu(111) very much resembles the situation found for Ag(111) at elevated temperatures. Already after the first heating step, the distinct fine structure has disappeared and only a broad π^* resonance around 286 eV is visible besides the new peak at 287.3 eV. Both features remain visible upon heating up to 500 K and perish in a broad but intense NEXAFS signal, which extends also to lower energies than the first resonance of the PFP bulk spectrum (hatched area) after heating to 600 K. Interestingly, the new spectral feature at 287.3 eV always appears when the nonfluorinated C1s signal (at 284 eV) occurs and simultaneously the C(C) peak (at 286 eV) is still visible in XPS. As shown in Figure 2c, the total carbon coverage remains nearly constant on Cu(111), thus indicating that nearly all molecules are firmly bound after defluorination occurring already during heating at 435 K and do not thermally desorb upon further heating.

Defects. The presented XPS and NEXAFS data clearly demonstrate that the stability of PFP monolayer films depends significantly on the supporting metal substrate. As surface defects such as steps are known to strongly influence catalytic reactions,[44] complementary measurements were carried out for a vicinal silver surface. This material was chosen, as the reactivity of silver was found to be in between that of gold and copper. In particular, a Ag(221) surface was chosen (cf. Figure 3d), as it provides a high density of well-defined monatomic steps. Their lateral separation of 8.7 Å is slightly larger than the molecular width and thus may allow for an aligned adsorption of PFP on the (111) terraces like it was found for PEN on Cu(221).[45] The corresponding NEXAFS spectra of a PFP monolayer that had been prepared by heating a multilayer film to 410 K are displayed in Figure 3a. Like in the case of copper, the π^* resonances found in the bulk spectrum are strongly attenuated and broadened, while a distinct new resonance at about 287.3 eV appears, which developed on the Ag(111) surface only after heating to 460 K. Moreover, in contrast to the PFP film on Ag(111), the dichroism is clearly reduced and the spectral features were also observed at normal incidence (red curve). To discriminate whether this intensity is primarily due to thermal decomposition or due to the different surface geometry of the silver surfaces,[46] additional measurements were carried out for a submonolayer film of PFP by depositing a nominal thickness of less than 2 Å without heating prior to data acquisition. As shown in Figure 3b, the NEXAFS spectra of this preparation again yield four distinct sharp π^* resonances with a pronounced dichroism like on the inert Au(111) surface. This clearly demonstrates that the distinct spectral changes found for the PFP monolayer film on Ag(221) prepared by thermal desorption of excessive multilayers are caused by a thermally

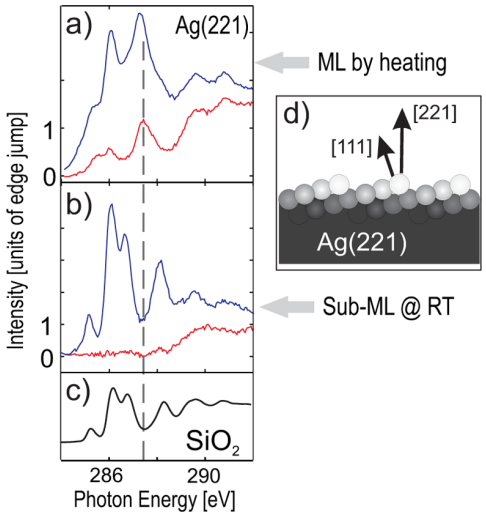

Figure 3. Effect of surface steps on the thermal decomposition of PFP on a stepped Ag(221) surface of which geometry is drawn schematically in part d. Comparison of carbon edge NEXAFS spectra obtained for PFP films on Ag(221), (a) prepared by thermal desorption of excessive multilayers at 410 K and (b) submonolayer film produced by deposition of less than 2 Å at RT. Like in Figure 2, the same color code is used to denote the angles of incidence while a NEXAFS spectrum of PFP on SiO_2 is shown for comparison in part c.

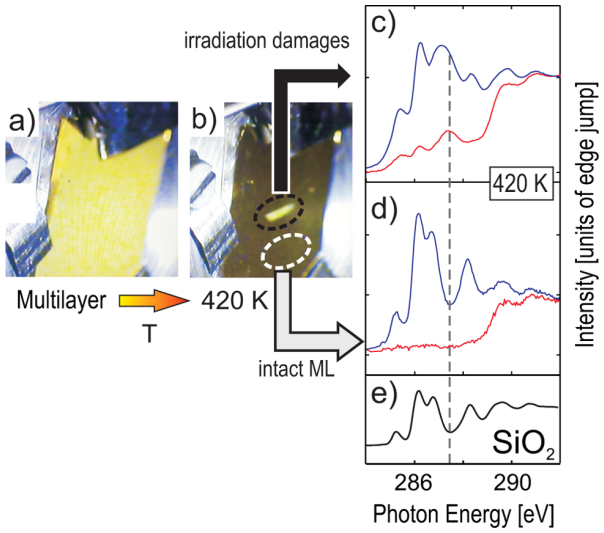

Figure 4. Radiation damage of PFP multilayers. Photographs a and b show an irradiated PFP multilayer on Au(111) before and after heating. While the intact multilayer thermally desorbs, the irradiated layer remains visible (black ellipse). NEXAFS spectra of such beam damaged areas are shown in part c and are compared to areas which had not been irradiated prior to thermal desorption in part d. Like in Figure 2, the same color code is used to denote the angles of incidence, while a NEXAFS spectrum of PFP on SiO_2 is shown for comparison in part e.

activated decomposition which is largely promoted by step edges.

Beam Damages. Though the photon flux at the used dipole beamline is moderate, possible radiation induced damages always have to be considered when analyzing changes in the NEXAFS signature of organic films.[47−50] A striking phenomenon which proves the presence of massive beam damages can be observed when comparing the thermal stability of PFP multilayers with and without former exposure to synchrotron radiation. Figure 4a depicts a photograph of a 22 nm PFP film deposited on Au(111) which appears yellowish due to diffuse scattered light from the rough multilayer film.[14] After XPS and NEXAFS measurements of this film had been carried out, the sample was heated to 420 K in order to prepare a nominal monolayer by desorbing the excessive multilayer. As shown in Figure 4b, the sample color is changed except at the position which had been illuminated by the synchrotron light (marked by the dashed black ellipse). XPS spectra that were recorded at this thoroughly illuminated region after the annealing treatment are virtually indistinguishable from measurements taken at the very beginning. However, the belonging peak intensities are distinctly larger than for a monolayer film, hence proving the presence of remaining multilayers. This finding indicates an enhanced thermal stability of the irradiated PFP film and suggests the appearance of a cross-linking process like it was found previously for aromatic SAMs.[51] On the basis of the XPS data, the stoichiometry of the irradiated films seems to be practically unaffected, thus rendering NEXAFS a much more sensitive tool, as it probes the unoccupied frontier orbitals. In fact, accompanied NEXAFS data that were recorded at this position after the annealing treatment again show the appearance of the additional resonance at about 287.3 eV (see Figure 4c) similar to the case of PFP monolayer films on Cu(111) and on Ag(221). Interestingly, the positions of the monolayer film that have not been illuminated before by synchrotron light do not show this new NEXAFS resonance and instead exhibit an undisturbed NEXAFS spectrum, as depicted in Figure 4d. We note further that this spectrum also does not change even when illuminating this spot for more than 30 min, which indicates an enhanced radiation stability of the monolayer compared to PFP multilayers. Additional experiments that were carried out by irradiating multilayer films with synchrotron light with energies of 300 and 720 eV revealed no noticeable difference. This finding suggests that the occurring damages are not due to resonant excitations or a direct photon induced process within the molecule but rather can be attributed to secondary electrons excited in the metal substrate underneath.

Total-Energy Calculations. A number of plausible starting configurations were probed in order to determine the adsorption geometry of single PFP molecules on the (111) surface of Cu, Ag, and Au. Irrespective of the substrate, PFP is found to only weakly interact with the metal surface. The calculated charge densities do not indicate the formation of covalent bonds or any significant charge transfer between substrate and adsorbate. Rather, the molecules adsorb with a relatively large distance of 3.49, 3.53, and 3.65 Å above the (111) surface of Cu, Ag, and Au. We calculate adsorption energies ΔE_{ads} of −2.84, −1.74, and −1.56 eV for the three substrates corresponding to the reaction

$$PFP_g + M \rightleftharpoons PFP@M \quad \Delta E_{ads}$$

Previous DFT-D calculations by Toyoda et al.[11] resulted in respective equilibrium distances of 2.9, 3.2, and 3.2 Å and adsorption energies of −2.17, −2.40, and −2.68 eV for Cu, Ag, and Au. The difference in the present results may partially be related to numerical differences such as the smaller number of layers used to model the substrate in ref 11, Additionally, according to observations of Reuter's group,[28] the Grimme scheme[52] used by Toyoda et al. results in stronger and shorter

dx.doi.org/10.1021/jp307316r | J. Phys. Chem. C 2012, 116, 24098−24106

adsorbate−substrate bonds than the DFT-D implementation used in the present work.

Next, we consider the partial dissociation of PFP. Since for nonfluorinated acenes the largest reactivity is found for the central ring,[53,54] we model the case that a single fluorine atom dissociates from the central ring of either the surface adsorbed or gas-phase PFP molecule according to

$$\mathrm{PFP@M} \rightleftharpoons \mathrm{C_{22}F_{13}@M} + \mathrm{F^{\bullet}_g} \quad \Delta E_{\mathrm{diss}}$$

$$\mathrm{PFP_g} \rightleftharpoons \mathrm{C_{22}F^{\bullet}_{13g}} + \mathrm{F^{\bullet}_g} \quad \Delta E_{\mathrm{diss}}(\mathrm{gas})$$

The calculated energies ΔE_{diss} are summarized in Table 1. The corresponding value for the gas phase is $\Delta E_{\mathrm{diss}}(\mathrm{gas})$ = 5.4 eV.

Table 1. Adsorption and Dissociation Energies Calculated within DFT-D as Defined in the Text

E (eV)	Cu(111)	Ag(111)	Au(111)
ΔE_{ads}	−2.8	−1.7	−1.6
ΔE_{diss}	3.3	3.8	4.1
$\Delta E_{\mathrm{diss}}(\mathrm{gas}) - E_{\mathrm{diss}}$	2.1	1.6	1.3
$\Delta E^{\bullet}_{\mathrm{ads}}$	−4.0	−2.7	−2.5
$\Delta E^{\bullet}_{\mathrm{ads}} - \Delta E_{\mathrm{ads}}$	−1.2	−1.0	−0.9
$\Delta E_{\mathrm{diss}}(\mathrm{surf})$	−1.9	−0.1	0.4

Obviously, the dissociation of surface adsorbed PFP requires considerably less energy than the corresponding reaction in the gas phase, in particular for Cu and Ag substrates. This is surprising, given the rather weak interaction between PFP and substrate. In order to better understand this phenomenon, we calculated the adsorption energy of the partially defluorinated PFP according to

$$\mathrm{C_{22}F^{\bullet}_{13g}} + \mathrm{M} \rightleftharpoons \mathrm{C_{22}F_{13}@M} \quad \Delta E^{\bullet}_{\mathrm{ads}}$$

Obviously, the energy released upon adsorption of the partially defluorinated PFP, $\Delta E^{\bullet}_{\mathrm{ads}}$, is of the order of 1 eV larger than ΔE_{ads} (see Table 1). This increase in adsorption energy is accompanied by a change in adsorption characteristics. As shown in Figure 5, upon F dissociation, the formerly weakly physisorbed PFP forms a strong C−M bond, which is accompanied by a considerable distortion of the molecular adsorption geometry, leading to a bending of the aromatic backbone. This is consistent with our NEXAFS findings, which showed a notable change in dichroism. If one compares the energy difference $\Delta E^{\bullet}_{\mathrm{ads}} - \Delta E_{\mathrm{ads}}$ with the substrate-induced change in the dissociation energy ΔE_{diss}, one finds the same trend: The less noble the substrate, the stronger the increase in adsorption energy and the stronger the decrease in dissociation energy. The above results show that the possibility of broken-bond healing provided by the coinage-metal substrate is largely responsible for the catalytic action observed experimentally. We mention that a similar effect has recently been found to catalyze the polymerization of tetraazaperopyrene on Cu(111).[55]

While the calculations so far allow for understanding the chemical trend, they certainly do not model the majority of dissociation events. It can be expected that the F dissociation followed by lateral diffusion has a lower activation energy than the immediate F desorption into the gas phase. In order to elucidate the initial stages of this process, we consider the reaction

$$\mathrm{PFP@M} \rightleftharpoons \mathrm{C_{22}F_{13}@M} + \mathrm{F@M} \quad \Delta E_{\mathrm{diss}}(\mathrm{surf})$$

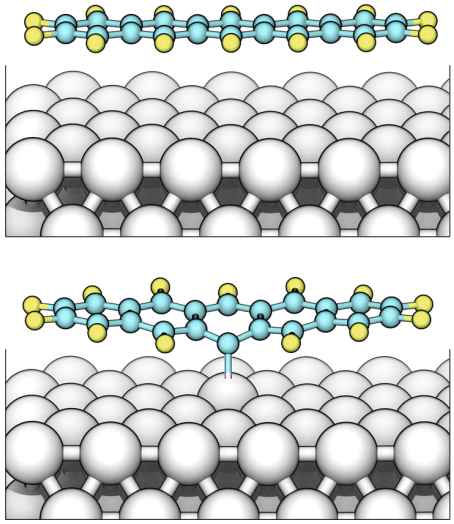

Figure 5. Calculated geometry of intact (top, $C_{22}F_{14}$) and partly defluorinated (bottom, $C_{22}F_{13}$) PFP adsorbed on the Ag(111) surface.

for the case of the Ag(111) surface. In Figure 6, we show the calculated energy landscape $\Delta E_{\mathrm{diss}}(\mathrm{surf})$ seen by a dissociated fluorine atom moving laterally away from the PFP molecule. The potential energy surface has been calculated by fixing the lateral position of the dissociated F atom as well as the two carbon positions farthest away from this fluorine, while all remaining degrees of freedom were allowed to relax. As expected, we find the energy barrier for dissociating the F laterally considerably smaller than that for a vertical reaction path; it amounts to 2.1 eV. Once this barrier is overcome, the originally PFP dissociated F atom adsorbs most favorably in 3-fold coordinated bridge position. Finally, an energy gain of 0.1 eV is realized for dissociation on the Ag(111) surface. It is considerably larger on Cu (1.9 eV, cf. Table 1), whereas energy is required (0.4 eV, cf. Table 1) to dissociate PFP on Au. This explains why the majority of PFP molecules on gold will desorb intactly upon heating, in contrast to Ag and Cu, where dissociation is thermodynamically more favored.

Once partially dissociated PFP molecules are covalently bond to the Cu or Ag substrate, additional cleavage of fluorine will occur, eventually leading to an almost complete defluorination. Regarding the separated fluorine atoms, several reaction paths are conceivable. Comparing the corresponding standard enthalpy of formation of the various metal fluorides ($\Delta_f H^0_s$(CuF) = −2.91 eV,[56] $\Delta_f H^0_s$(AgF) = −2.12 eV,[57] AuF not stable) indicates that they can be formed only on silver or copper. Alternatively, the desorbing F radical can further react with hydrogen (i.e., from covered walls of the vacuum vessel), leading to the formation of the stable HF ($\Delta_f H^0_g$(HF) = −2.83 eV[56]) which could be detected in previous thermal desorption spectra of PFP films adsorbed on Ag(111).[14] The fact that metal fluoride species were only observed in our XPS data for copper but not for silver (cf. Figure 1e) is consistent with these values because only CuF is more stable than the most likely path of fluorine desorption upon heating.

DISCUSSION

The present measurements show distinct differences in the chemical stability of PFP films on the various coinage metal surfaces. Though PFP is only weakly adsorbed on Au(111), this

dx.doi.org/10.1021/jp307316r | J. Phys. Chem. C 2012, 116, 24098−24106

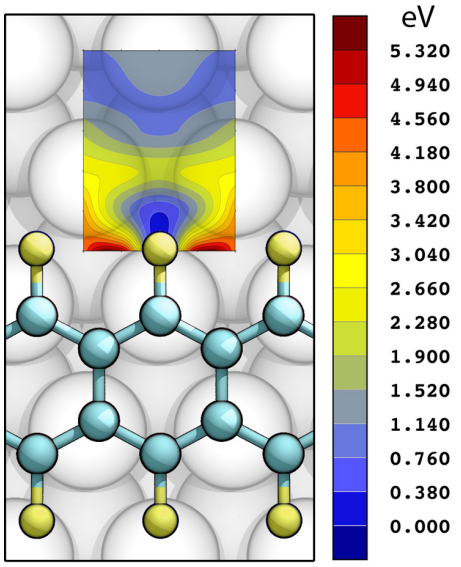

Figure 6. Calculated potential energy surface of the lateral F dissociation from PFP on Ag(111); see text.

interaction exceeds the intermolecular cohesion and allows for a controlled thermal desorption of multilayers. The remaining nominal monolayer reveals neither any broadening of the π^* resonances in the C1s NEXAFS spectra as compared to the bulk data nor a change in the stoichiometry upon heating to temperatures of more than 500 K. Only a continuous decrease of the PFP related intensity occurs for temperatures above 450 K which is indicative for desorption of intact molecules. This physisorption of PFP on Au(111) and Ag(111) at room temperature is in pronounced difference to the adsorption of the nonfluorinated pentacene, where a substantial broadening of the π^* resonances was found for monolayer films on both substrates.[15,58] By contrast, on Cu(111), a significant defluorination takes place already during thermal desorption of multilayer films at about 430 K, which is accompanied by a reduced dichroism of the carbon edge NEXAFS signatures. A temperature induced surface reaction of PFP films on Cu(111) has also been reported previously by Glowatzki et al.[12] In that study, it was further found that after extensive heating of submonolayer films (135 min at 425 K) the adsorbed molecules were fixated so that they could be imaged by means of scanning tunneling microscopy at room temperature while nonheated films appear to be quite mobile. The presently identified decomposition of PFP on Cu(111) continues upon further heating until the layer is almost completely defluorinated at 600 K, leaving a fluorine-free carbon film behind. For comparison, a monolayer of the nonfluorinated pentacene adsorbed on Cu(110) can sustain heating to these temperatures without any degradation.[13] Interestingly, a noticeable degradation was also observed for PFP films on Ag(111) when heating above 440 K. As one would expect, this indicates that the reactivity of silver is in between that of Au and Cu, being strongest for copper. The appearance of a temperature-induced decomposition of PFP molecules on Ag(111) in spite of their physisorption at room temperature indicates a metastable equilibrium of the intact layer. This observation is at variance with the findings of a previous DFT-based analysis of PFP monolayers adsorbed on the (111)-oriented surfaces of these three coinage metals,[11] where the largest adsorption energy was found for gold and the smallest one for copper. On the contrary, the trend found in the experimental data is well reproduced by the DFT-D calculations of the present study. By also considering chemical recations at the molecule−metal interface, it was possible to unravel the observed defluorination mechanism in our theoretical analysis. Though fluorine separation is a thermally activated process, the system benefits from an overall energy gain upon covalent C−M bonding of partially dissociated PFP molecules to the metal surface as well as the formation of metal fluorides in the case of Cu and Ag substrates. Interestingly, in contrast to CuF, no AgF related signal could be detected in the XPS data which suggests that fluorine is only weakly bound at the Ag(111) surface and may thermally desorb at temperatures where PFP becomes defluorinated. Additional measurements on PFP adsorbed on the stepped Ag(221) surface showed a reduced barrier for defluorination which occurs already at lower temperatures, thus demonstrating the catalytic effect of steps. The latter result is of particular relevance for device applications, since electrodes in electronic devices are polycrystalline and exhibit numerous defects so that defluorination is expected to occur already at lower temperatures slightly above room temperature. In this respect, the barriers of decomposition obtained from theoretical analysis of the interaction of PFP with ideal, defect-free (111) surfaces should only be considered as an upper limit, whereas real surfaces always exhibit defects which lower this barrier.

■ CONCLUSIONS

Large differences in the thermal and chemical stability of PFP thin films adsorbed on the coinage metal surfaces of Cu, Ag, and Au were observed. Only on gold PFP desorbs without any noticeable decomposition, while Ag and Cu catalyze a partial defluorination, leading to a distortion of the adsorption geometry. Our DFT-D calculations showed that, even on the noble metal silver, defluorination and subsequent covalent binding of PFP to the metal are energetically favored against desorption. The present study indicates that fluorinated aromatic hydrocarbons, though exhibiting interesting electronic properties such as n-type conduction and robustness against oxidation, might actually be less stable in contact with metal surfaces than their nonfluorinated analogues. It thus emphasizes the importance of not only characterizing possible energy level alignment with respect to the Fermi level of metal substrates but also analyzing the chemical stability to validate their use for organic electronic device applications.

■ AUTHOR INFORMATION

Corresponding Author

*E-mail: gregor.witte@physik.uni-marburg.de.

Notes

The authors declare no competing financial interest.

■ ACKNOWLEDGMENTS

We acknowledge the Helmholtz-Zentrum Berlin - Electron storage ring BESSY II for provision of synchrotron radiation at beamline HE-SGM and travel support as well as the HLRS Stuttgart and the Paderborn PC^2 for providing supercomputer time. We gratefully acknowledge financial support by the Friedrich-Ebert-Stiftung (T.B.) as well as by the Deutsche Forschungsgemeinschaft (S.W. and W.G.S.).

REFERENCES

(1) Anthony, J. E.; Facchetti, A.; Heeney, M.; Marder, S. R.; Zhan, X. W. *Adv. Mater.* **2010**, *22*, 3876−3892.
(2) Jung, B. J.; Tremblay, N. J.; Yeh, M. L.; Katz, H. E. *Chem. Mater.* **2011**, *23*, 568−582.
(3) Kagan, C. R.; Afzali, A.; Graham, T. O. *Appl. Phys. Lett.* **2005**, *86*, 193505.
(4) Sirringhaus, H. *Adv. Mater.* **2009**, *21*, 3859−3873.
(5) Angelis, F. D.; Gaspari, M.; Procopio, A.; Cuda, G.; Fabrizio, E. D. *Chem. Phys. Lett.* **2009**, *468*, 193−196.
(6) Delgado, M. C. R.; Pigg, K. R.; Filho, D. A. d. S.; Gruhn, N. E.; Sakamoto, Y.; Suzuki, T.; Malave Osuna, R.; Casado, J.; Hernandez, V.; Lopez Navarrete, J. T.; Martinelli, N. G.; Cornil, J.; Sanchez-Carrera, R. S.; Coropceanu, V.; Bredas, J.-L. *J. Am. Chem. Soc.* **2009**, *131*, 1502−1512.
(7) Sakamoto, Y.; Suzuki, T.; Kobayashi, M.; Gao, Y.; Fukai, Y.; Inoue, Y.; Sato, F.; Tokito, S. *J. Am. Chem. Soc.* **2004**, *126*, 8138.
(8) Koch, N.; Vollmer, A.; Duhm, S.; Sakamoto, Y.; Suzuki, T. *Adv. Mater.* **2007**, *19*, 112.
(9) Koch, N.; Gerlach, A.; Duhm, S.; Glowatzki, H.; Heimel, G.; Vollmer, A.; Sakamoto, Y.; Suzuki, T.; Zegenhagen, J.; Rabe, J. P.; Schreiber, F. *J. Am. Chem. Soc.* **2008**, *130*, 7300.
(10) Duhm, S.; Hosoumi, S.; Salzmann, I.; Gerlach, A.; Oehzelt, M.; Wedl, B.; Lee, T.-L.; Schreiber, F.; Koch, N.; Ueno, N.; Kera, S. *Phys. Rev. B* **2010**, 81.
(11) Toyoda, K.; Hamada, I.; Lee, K.; Yanagisawa, S.; Morikawa, Y. *J. Phys. Chem. C* **2011**, *115*, 5767−5772.
(12) Glowatzki, H.; Heimel, G.; Vollmer, A.; Wong, S. L.; Huang, H.; Chen, W.; Wee, A. T. S.; Rabe, J. P.; Koch, N. *J. Phys. Chem. C* **2012**, *116*, 7726−7734.
(13) Söhnchen, S.; Lukas, S.; Witte, G. *J. Chem. Phys.* **2004**, *121*, 525−534.
(14) Götzen, J.; Schwalb, C. H.; Schmidt, C.; Mette, G.; Marks, M.; Höfer, U.; Witte, G. *Langmuir* **2011**, *27*, 993−999.
(15) Käfer, D.; Witte, G. *Chem. Phys. Lett.* **2007**, *442*, 376−383.
(16) Dilella, D.; Smardzewski, R.; Guha, S.; Lund, P. *Surf. Sci.* **1985**, *158*, 295−306.
(17) Vijayalakshmi, S.; Fohlisch, A.; Kirchmann, P. S.; Hennies, F.; Pietzsch, A.; Nagasono, M.; Wurth, W. *Surf. Sci.* **2006**, *600*, 4972−4977.
(18) National Institute of Standards and Technology, *NIST X-ray Photoelectron Spectroscopy Database* 2003.
(19) Shirley, D. A. *Phys. Rev. B* **1972**, *5*, 4709−4714.
(20) Stöhr, J. In *NEXAFS Spectroscopy*; Gomer, R., Ed.; Springer: Berlin, Germany, 1992.
(21) Marks, M.; Schmidt, C.; Schwalb, C. H.; Breuer, T.; Witte, G.; Höfer, U. *J. Phys. Chem. C* **2012**, *116*, 1904−1911.
(22) Kresse, G.; Furthmüller, J. *Comput. Mater. Sci.* **1996**, *6*, 15.
(23) Perdew, J. P.; Chevary, J. A.; Vosko, S. H.; Jackson, K. A.; Pederson, M. R.; Singh, D. J.; Fiolhais, C. *Phys. Rev. B* **1992**, *46*, 6671.
(24) Kresse, G.; Joubert, D. *Phys. Rev. B* **1999**, *59*, 1758.
(25) Schmidt, W. G.; Seino, K.; Preuss, M.; Hermann, A.; Ortmann, F.; Bechstedt, F. *Appl. Phys. A: Mater. Sci. Process.* **2006**, *85*, 387.
(26) Rohlfing, M.; Bredow, T. *Phys. Rev. Lett.* **2008**, *101*, 266106.
(27) Atodiresei, N.; Caciuc, V.; Lazić, P.; Blügel, S. *Phys. Rev. Lett.* **2009**, *102*, 136809.
(28) Mcnellis, E. R.; Meyer, J.; Reuter, K. *Phys. Rev. B* **2009**, *80*, 205414.
(29) Mercurio, G.; McNellis, E. R.; Martin, I.; Hagen, S.; Leyssner, F.; Soubatch, S.; Meyer, J.; Wolf, M.; Tegeder, P.; Tautz, F. S.; Reuter, K. *Phys. Rev. Lett.* **2010**, *104*, 036102.
(30) Thierfelder, C.; Witte, M.; Blankenburg, S.; Rauls, E.; Schmidt, W. G. *Surf. Sci.* **2011**, *605*, 746.
(31) Ortmann, F.; Schmidt, W. G.; Bechstedt, F. *Phys. Rev. Lett.* **2005**, *95*, 186101.
(32) Ortmann, F.; Bechstedt, F.; Schmidt, W. G. *Phys. Rev. B* **2006**, *73*, 205101.
(33) Dion, M.; Rydberg, H.; Schröder, E.; Langreth, D. C.; Lundqvist, B. I. *Phys. Rev. Lett.* **2004**, *92*, 246401.
(34) Lazić, P.; Atodiresei, N.; Alaei, M.; Caciuc, V.; Blügel, S.; Brako, R. *Comput. Phys. Commun.* **2010**, *181*, 371.
(35) de Oteyza, D. G.; Wakayama, Y.; Liu, X.; Yang, W.; Cook, P. L.; Himpsel, F. J.; Ortega, J. E. *Chem. Phys. Lett.* **2010**, *490*, 54−57.
(36) Hinderhofer, A.; Heinemeyer, U.; Gerlach, A.; Kowarik, S.; Jacobs, R. M. J.; Sakamoto, Y.; Suzuki, T.; Schreiber, F. *J. Chem. Phys.* **2007**, *127*, 194705.
(37) Breuer, T.; Witte, G. *Phys. Rev. B* **2011**, *83*, 155428.
(38) Rocco, M. L. M.; Haeming, M.; Batchelor, D. R.; Fink, R.; Schöll, A.; Umbach, E. *J. Chem. Phys.* **2008**, *129*, 074702.
(39) Note, that this small final state effect differs from the larger core-hole screening effect found in XPS (0.7−1.15 eV).[35]
(40) Mainka, C.; Bagus, P. S.; Schertel, A.; Strunskus, T.; Grunze, M.; Wöll, C. *Surf. Sci.* **1995**, *341*, L1055−L1060.
(41) Weiss, K.; Gebert, S.; Wuhn, M.; Wadepohl, H.; Wöll, C. *J. Vac. Sci. Technol., A* **1998**, *16*, 1017−1022.
(42) Liu, A. C.; Stöhr, J.; Friend, C. M.; Madix, R. J. *Surf. Sci.* **1990**, *235*, 107−115.
(43) Chen, Q.; McDowall, A.; Richardson, N. *Langmuir* **2003**, *19*, 10164−10171.
(44) Blakely, D. W.; Somorjai, G. A. *J. Catal.* **1976**, *42*, 181−196.
(45) Götzen, J.; Lukas, S.; Birkner, A.; Witte, G. *Surf. Sci.* **2011**, *605*, 577−581.
(46) The silver (221) surface consists of (111) terraces with an inclination of 15.8° with respect to the macroscopic (221) surface plane. Therefore, molecules which lie flat on the (111) terraces are expected to exhibit a molecular orientation of 15.8° relative to the (221) surface determined by NEXAFS.
(47) Zharnikov, M.; Grunze, M. *J. Vac. Sci. Technol., B* **2002**, *20*, 1793−1807.
(48) Zubavichus, Y.; Zharnikov, M.; Shaporenko, A.; Fuchs, O.; Weinhardt, L.; Heske, C.; Umbach, E.; Denlinger, J. D.; Grunze, M. *J. Phys. Chem. A* **2004**, *108*, 4557−4565.
(49) Feulner, P.; Niedermayer, T.; Eberle, K.; Schneider, R.; Menzel, D.; Baumer, A.; Schmich, E.; Shaporenko, A.; Tai, Y.; Zharnikov, M. *Phys. Rev. Lett.* **2004**, *93*, 178302.
(50) Zubavichus, Y.; Fuchs, O.; Weinhardt, L.; Heske, C.; Umbach, E.; Denlinger, J. D.; Grunze, M. *Radiat. Res.* **2004**, *161*, 346−358.
(51) Turchanin, A.; Käfer, D.; El-Desawy, M.; Wöll, C.; Witte, G.; Gölzhauser, A. *Langmuir* **2009**, *25*, 7342−7352.
(52) Grimme, S. *J. Comput. Chem.* **2006**, *27*, 1787.
(53) Zander, M. *Polycyclic Hydrocarbons*; Academic Press: London, UK, 1964.
(54) Schleyer, P. V.; Manoharan, M.; Jiao, H. J.; Stahl, F. *Org. Lett.* **2001**, *3*, 3643−3646.
(55) Blankenburg, S.; Rauls, E.; Schmidt, W. G. *J. Phys. Chem. Lett.* **2010**, *1*, 3266.
(56) Chase, M. *NIST-JANAF Thermochemical Tables 2 Volume-Set (Journal of Physical and Chemical Reference Data Monographs)*; American Institute of Physics: Woodbury, N.Y., USA, 1998.
(57) Lide, D. R., Ed. *CRC Handbook of Chemistry and Physics*, 89th ed.; CRC Press: Boca Raton, FL, USA, 2008−2009.
(58) Käfer, D.; Ruppel, L.; Witte, G. *Phys. Rev. B* **2007**, *75*, 085309.

5.7 Article VII: Epitaxial Growth of π-Stacked Perfluoropentacene on Graphene-Coated Quartz

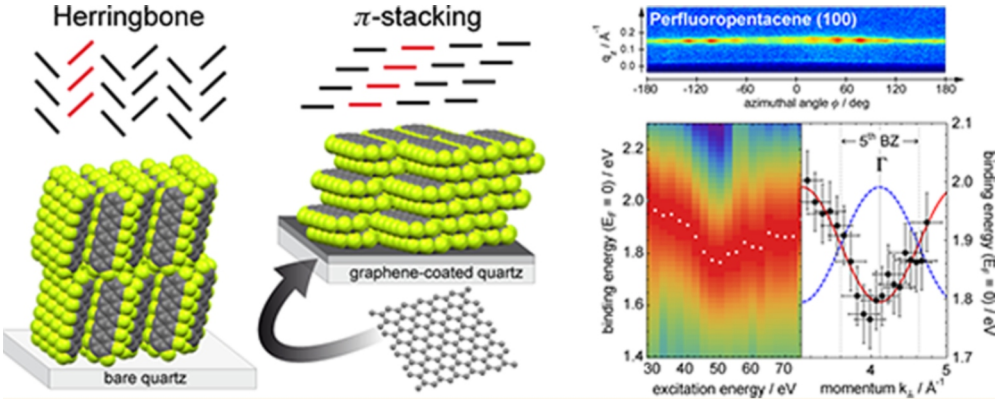

5.7.1 Abstract

Chemical-vapor-deposited large-area graphene is employed as the coating of transparent substrates for the growth of the prototypical organic n-type semiconductor perfluoropentacene (PFP). The graphene coating is found to cause face-on growth of PFP in a yet unknown substrate-mediated polymorph, which is solved by combining grazing-incidence X-ray diffraction with theoretical structure modeling. In contrast to the otherwise common herringbone arrangement of PFP in single crystals and "standing" films, we report a π-stacked arrangement of coplanar molecules in "flat-lying" films, which exhibit an exceedingly low π-stacking distance of only 3.07 Å, giving rise to significant electronic band dispersion along the π-stacking direction, as evidenced by ultraviolet photoelectron spectroscopy. Our study underlines the high potential of graphene for use as a transparent electrode in (opto-)electronic applications, where optimized vertical transport through flat-lying conjugated organic molecules is desired.

5.7.2 Methods

Density Functional Theory, Organic Molecular Beam Deposition, Near-Edge X-Ray Absorption Finestructure Spectroscopy, Raman Spectroscopy, Ultraviolet Photoelectron Spectroscopy, X-Ray Diffraction

5.7.3 Own contribution

I have planned, performed and evaluated the NEXAFS measurements and prepared the corresponding samples. Furthermore, I have prepared this data for publication and helped to improve the manuscript.

Epitaxial Growth of π-Stacked Perfluoropentacene on Graphene-Coated Quartz

Ingo Salzmann,[†,*] Armin Moser,[‡] Martin Oehzelt,[†,§] Tobias Breuer,[⊥] Xinliang Feng,[∥] Zhen-Yu Juang,[∥] Dmitrii Nabok,[¶,▼] Raffaele G. Della Valle,[#] Steffen Duhm,[△] Georg Heimel,[†] Aldo Brillante,[#] Elisabetta Venuti,[#] Ivano Bilotti,[#] Christos Christodoulou,[†] Johannes Frisch,[†] Peter Puschnig,[¶,▲] Claudia Draxl,[¶,▼] Gregor Witte,[⊥] Klaus Müllen,[∥] and Norbert Koch[†,§]

[†]Institut für Physik, Humboldt-Universität zu Berlin, Berlin, Germany, [‡]Institute of Solid State Physics, Graz University of Technology, Graz, Austria, [§]Helmholtz Zentrum Berlin für Materialien und Energie, BESSY II, Berlin, Germany, [⊥]Fachbereich Physik, Molekulare Festkörperphysik, Philipps-Universität Marburg, Marburg, Germany, [∥]Max Planck Institute for Polymer Research, Mainz, Germany, [¶]Department Materials Physics, University of Leoben, Leoben, Austria, [#]Dipartimento di Chimica Fisica e Inorganica and INSTM-UdR, Università di Bologna, Bologna, Italy, and [△]Institute of Functional Nano & Soft Materials (FUNSOM), Soochow University, Suzhou, China

ABSTRACT Chemical-vapor-deposited large-area graphene is employed as the coating of transparent substrates for the growth of the prototypical organic n-type semiconductor perfluoropentacene (PFP). The graphene coating is found to cause face-on growth of PFP in a yet unknown substrate-mediated polymorph, which is solved by combining grazing-incidence X-ray diffraction with theoretical structure modeling. In contrast to the otherwise common herringbone arrangement of PFP in single crystals and "standing" films, we report a π-stacked arrangement of coplanar molecules in "flat-lying" films, which exhibit an exceedingly low π-stacking distance of only 3.07 Å, giving rise to significant electronic band dispersion along the π-stacking direction, as evidenced by ultraviolet photoelectron spectroscopy. Our study underlines the high potential of graphene for use as a transparent electrode in (opto-)electronic applications, where optimized vertical transport through flat-lying conjugated organic molecules is desired.

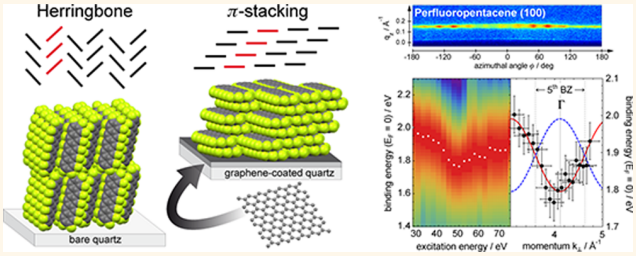

KEYWORDS: graphene · organic electronics · structure solution · pentacene · perfluoropentacene · band dispersion · grazing-incidence X-ray diffraction

Graphene, the two-dimensional hexagonal arrangement of sp^2-hybridized carbon, attracted unprecedented global research interest during the past decade.[1−4] This is due to its outstanding mechanical[1−3] and electronic[4] properties, which may be exploited in a broad range of applications, including field-effect transistors,[5] gas sensors,[6] optical modulators,[7] or organic electronics.[8,9] In particular, its high optical transparency together with its large charge-carrier mobility and low sheet resistance[10−12] renders graphene an ideal electrode material for (opto-)electronic applications[9] with the potential to replace high-cost tin-doped indium oxide (ITO) as standard transparent cathode.[12,13]

For organic electronics, in particular, one key charge-transport parameter is the transfer integral t expressing the ease of charge transfer between adjacent molecules, which depends on intermolecular distance and mutual orientation.[14−16] As molecular organic semiconductors (OSCs) are generally anisotropic—exhibiting a layered bulk crystal structure with a typical edge-to-face herringbone (HB) arrangement[17,18] of molecules within one layer—also t and the charge transport are highly anisotropic:[19] the mobilities are generally higher within the HB layers. In order to increase t in that direction, considerable research efforts have been put toward modifying the molecular packing of OSCs from HB to a parallel arrangement of the molecular planes, referred to as π-stacking.[20] Indeed, such stacking can be favored over HB by the attachment of functional side groups,[20] as shown for bis(triisopropylsilylethynyl)pentacene

* Address correspondence to ingo.salzmann@physik.hu-berlin.de.

Received for review September 15, 2012 and accepted November 15, 2012.

Published online November 15, 2012
10.1021/nn3042607

(TIPS-PEN).[21,22] Furthermore, it was recently demonstrated that, in such π-stacked films, reducing the intermolecular stacking distance from 3.33 to 3.08 Å and, hence, increasing t, increases hole mobilities in transistors from 0.8 to 4.6 $cm^2 V^{-1} s^{-1}$.[23] However, on common substrates like oxides (*e.g.*, ITO), the π-stacking direction lies parallel to the substrate plane,[23,24] while out-of plane π-stacking is actually desired for (opto-)electronic applications, where current flows through the device vertically.

In contrast to ITO, typical OSCs adopt a face-on orientation on residue-free graphene, as evidenced in several studies for the monolayer regime.[25−29] In thicker films, however, where the intermolecular interaction predominates over the molecule−substrate interaction, a transition to the OSC bulk crystal structure, that is, the typical HB arrangement, is generally observed,[29−31] thereby limiting the vertical charge-carrier mobility, which is detrimental for (opto-)electronic applications, such as *vertical* organic field-effect transistors (v-OFETs).[32−34] In standard OFETs, the channel typically lies parallel to the dielectric substrate and, therefore, within the high-mobility directions of prototypical p- and n-type transistor materials like pentacene (PEN)[35] or perfluoropentacene (PFP),[36] respectively, which adopt a standing molecular orientation in such devices. For v-OFET, in contrast, enhanced vertical transport through both a molecular arrangement parallel to the substrate and optimized intermolecular orientation is sought.

In this study, we report on vertically π-stacked growth of PFP in films of application-relevant thickness with an exceedingly small π-stacking distance, which is induced by coating quartz substrates with graphene. This packing motif is in contrast to all reports so far, where a HB arrangement of PFP with an edge-to-face herringbone angle of almost 90° both in the single-crystal polymorph[36] and in a thin-film phase (TFP)—present on oxide substrates—prevails.[37,38] We carried out a full structure solution of this π-stacked polymorph (PSP) on graphene (and of the TFP on SiO_x; see Supporting Information) by combining X-ray diffraction (XRD) methods with theoretical structure modeling. We provide evidence for the long-range epitaxial growth of this polymorph on graphene, that is, orientational registry of the molecules in the film with the underlying graphene layer. Furthermore, all of our experiments are corroborated by measurements on highly oriented pyrolytic graphite (HOPG) as reference, where an identical growth is evidenced by complementary experimental techniques. Finally, by employing ultraviolet photoelectron spectroscopy (UPS), we report electronic band dispersion of the highest occupied molecular orbital (HOMO) derived band in the π-stacking direction, which allows determining the value of the transfer integral t and, finally, estimating the hole mobility μ_h.[39]

RESULTS AND DISCUSSION

Graphene used throughout this work was synthesized through chemical vapor deposition (CVD) of methane on copper foil at 1020 °C substrate temperature with an ensuing wet transfer procedure to supporting quartz glass.[41] A representative Raman spectrum of the sample is depicted in Figure 1a, which shows a symmetric 2D band at 2686 cm^{-1} with an intensity ratio to the G peak of 3.4:1. It can be fitted by a single Lorentzian (full width at half-maximum = 39 cm^{-1}), thus evidencing the sample to be predominantly single-layer graphene. The D band contribution at 1355 cm^{-1} is related to crystal size effects[42] due to defects and grain boundaries from the CVD growth process.[43,44] This graphene-coated quartz sample served as the substrate for a vacuum-deposited PFP film with 30 nm nominal film thickness, as measured by a quartz crystal microbalance.

Figure 1b shows a specular XRD scan of the film compared to that of a PFP/HOPG reference. (For an explicit comparison between specular X-ray diffraction on graphene-coated and noncoated quartz, see the Supporting Information.) Both films show a strong diffraction feature at q_z = 2.06 $Å^{-1}$, which cannot be explained by either of the two known HB polymorphs of PFP, that is, the single-crystal polymorph[36] as well as the TFP (see Supporting Information), evidencing the presence of the yet unknown PSP. Note that in a recent study for PFP on Ag(111), the same reflection was observed;[45] however, the structure was not solved by grazing-incidence X-ray diffraction. This finding is corroborated by supporting confocal Raman microscopy, which points toward the presence of a PFP phase significantly different to the single-crystal polymorph (see Supporting Information). To determine its unit cell parameters, we performed grazing-incidence X-ray diffraction (GIXRD); the corresponding reciprocal space map (RSM) is depicted in Figure 1c (top). The map can be indexed with the triclinic unit cell parameters of a = 15.13 Å, b = 8.94 Å, c = 6.51 Å, α = 78.56°, β = 108.14°, and γ = 92.44°, yielding a cell volume of 820 $Å^3$, which is essentially identical to that of the (monoclinic) TFP (816 $Å^3$). This similarly suggests the presence of two molecules per unit cell (Z = 2) also for the PSP; for the PFP/HOPG reference, identical growth was found *via* GIXRD-RSM (see Supporting Information). Coming back to Figure 1b, the unit cell parameters allow assignment of the specular peak to the PSP(002) reflection.

While the peak positions in GIXRD investigations (Figure 1c) allow precise determination of the unit cell dimensions, the peak intensities provide information on the molecular orientation within the unit cell. One has to bear in mind, however, that taking the experimental intensities from GIXRD as a measure for the structure factors of the PSP requires a perfectly fiber-textured film. This makes the straightforward approach

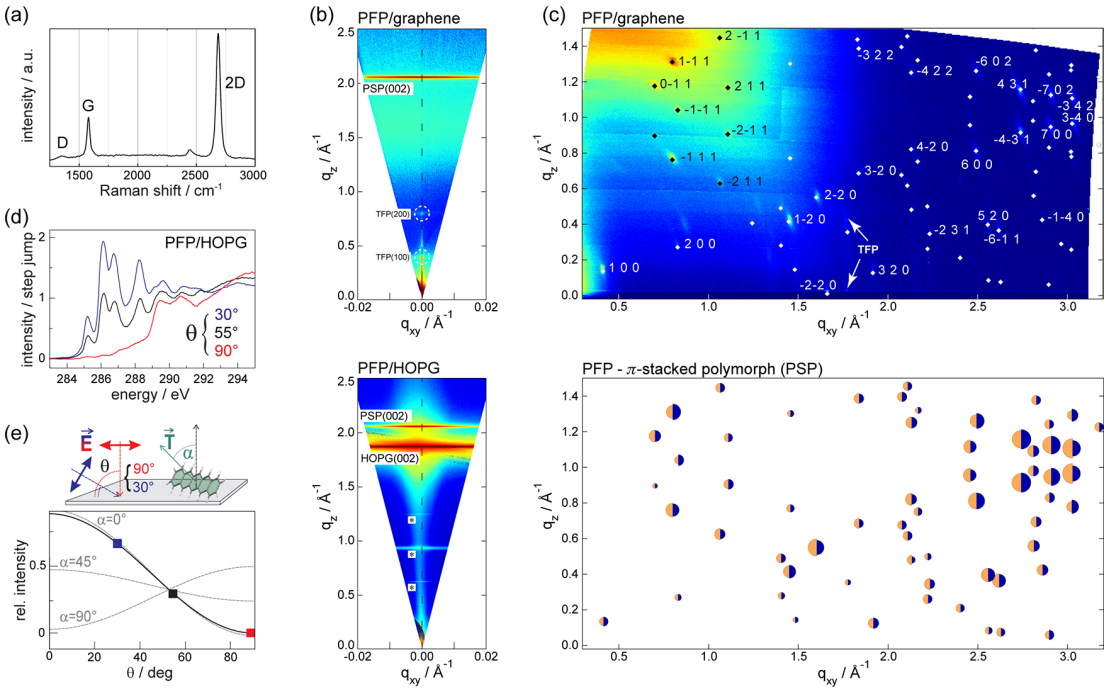

Figure 1. (a) Representative Raman spectrum of the graphene/quartz substrate. (b) Specular XRD scans of PFP/graphene (top) and PFP/HOPG as reference (bottom) both showing the PSP(002) reflection. For PFP/HOPG, the HOPG(002) reflection dominates the spectrum (higher harmonics of the substrate marked by stars), while no such diffraction is observed for PFP/graphene; there, minor contributions of standing PFP grown in the TFP, likely related to nucleation on substrate defects,[40] are found. (c) Top: GIXRD-RSM of PFP/graphene yielding the PSP unit cell dimensions. Bottom: Results of the full structure solution of the PSP; blue and orange half-circle areas compare the calculated to experimental structure factors deduced from the RSM of the PFP/HOPG reference (Supporting Information); values normalized to the (600) peak. (d) Supporting NEXAFS spectra of PFP/HOPG recorded at different incidence angles θ of the beam indicate a strong dichroism of PFP; spectra were corrected by a subtraction of weighted HOPG substrate contributions. (e) Quantitative evaluation of the dichroism indicates an essentially lying molecular conformation; $\vec{E}$ denotes the electric field vector of the beam, and α the angle between the transition dipole moment $\vec{T}$ and the sample normal.

of fitting the molecular orientation against the experimental intensities[24] problematic on graphene, where neighboring grains might exhibit a nonrandom angular relation. Recently, we presented a method to model the molecular orientation of a similar rod-like OSC by force-field calculations, where the only experimental input was the unit cell dimensions deduced from GIXRD.[46] Following the same approach for rigid PFP molecules confined in the PSP unit cell, we derive a full structure solution for the PSP, which is characterized by almost *parallel molecular axes and planes* (deviations below 4°), as illustrated in Figure 2b. To further validate this surprising result, we followed three independent approaches: (i) We employed crystal structure prediction methods[47] constrained to the experimental PSP unit cell with an ensuing comparison to the experimental peak intensities determined for the PFP/HOPG reference, which is fiber-textured; subsequently lifting the constraints corroborates the PSP being a local minimum crystal structure. (ii) We carried out a direct fit of the molecular orientation against the experimental intensities using the software package FOX,[48] which became feasible owing to the large number of reflections in the corresponding map on the (fiber-textured) PFP/HOPG reference. Both approaches led to essentially identical results and fully confirm our structure solution (see Supporting Information for further details). Note that our structure solution fully covers the absence of the PSP(001) reflection in Figure 1b despite the triclinic crystal class of the PSP, where no systematic extinctions occur. The calculated intensity ratio of the PSP(001) to the PSP(002) reflection is 1:10 000, which cannot be experimentally observed. Furthermore, the high intensity of the (113−1) in-plane reflection (Figure 3b) corresponding to planes perpendicular to the long molecular axis is covered by our solution. (iii) Entirely independent from X-ray diffraction, we performed near-edge X-ray absorption fine structure spectroscopy (NEXAFS). Because identical growth on both graphene and HOPG is evidenced by XRD, we carried out NEXAFS on the PFP/HOPG reference to avoid known issues of NEXAFS on (large-area) epitaxial, azimuthally anisotropic organic films,[49,50] hence exploiting the fiber texture of the HOPG substrate (Supporting Information). The spectra in Figure 1d show a strong dichroism indicating a preferential molecular orientation in the film. Because the lower-energy peaks correspond to excitations of C1s electrons into unoccupied π^* orbitals (π^* resonances) and the corresponding transition dipole moments in PFP (denoted as *T* in Figure 1e) are

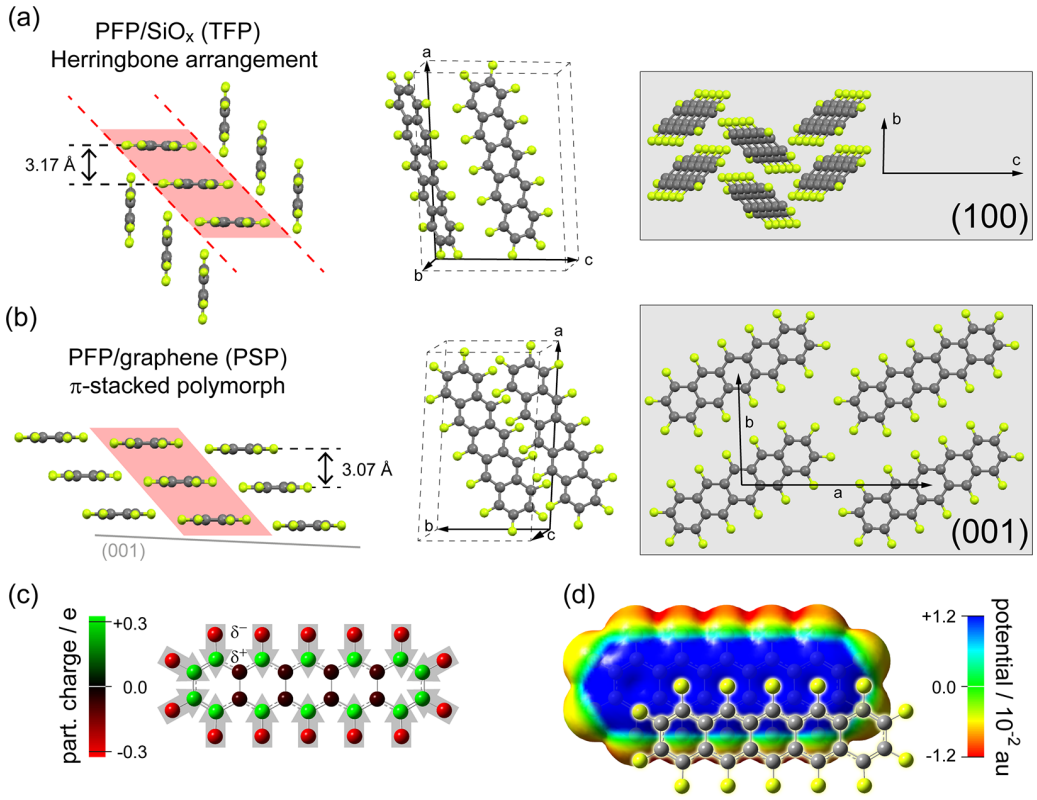

Figure 2. Comparison of the molecular arrangement in the two polymorphs of PFP determined in this work. (a) Herringbone arrangement of the TFP on SiO_x viewed along the long molecular axes (left), illustrated within the unit cell (middle), and as a top view on the (100) texture plane[37,38] (*i.e.*, along the *a axis) (right). (b) π-Stacked arrangement of the PSP viewed along the long molecular axes (left), within the unit cell (middle), and as a top view on the (001) texture plane parallel to graphene (*i.e.*, along the *c** axis) (right). Similar π-stacked motifs are shaded in red; π-stacking distances are indicated. (c) Calculated atomic charges on the constituting atoms of a PFP molecule. (d) Calculated molecular electrostatic potential map (in atomic units) of an individual PFP molecule with an adjacent molecule within the parallel-displaced stacked motif of the PSP.**

oriented perpendicular to the molecular plane,[51] their gradual intensity change from grazing (30°) to normal incidence of the primary beam confirms essentially *flat-lying molecules* in the PSP. This is clearly seen by a comparison of the experimental angle dependence of the π* resonance intensity to calculated values, as shown in Figure 1e.

Although exceedingly different from both the TFP and the single-crystal polymorph, where a HB arrangement with a HB angle of almost 90° is found (Figure 2a), the severe change in molecular arrangement appears counterintuitive only at first glance. Noncovalently bound molecular assemblies, be it of HB or π-stacked type, result from a competition of electrostatic and dispersion interactions. It is understood that a parallel-displaced stacking motif of π-conjugated molecules is due to an interplay between a favorable dispersion component through the π-electron system (frequently termed $\pi-\pi$ interaction) and unfavorable electrostatic effects, which are minimized by lateral displacement.[52] PFP exhibits strong intramolecular polar bonds (IPBs) between the highly electronegative fluorine atoms carrying a negative partial charge F[δ^-] and the backbone carbon atoms C[δ^+], which translates into local dipole moments pointing symmetrically toward the molecular core,[53−55] as sketched in Figure 2c. In addition to dispersion forces, such local dipoles/multipoles impact the intermolecular arrangement,[56−59] and in the present case, attractive dipole−dipole interactions between adjacent PFP molecules further stabilize the parallel-displaced π-stacked arrangement of PFP, as illustrated by the electrostatic potential map in Figure 2d. Note that this is in stark contrast to (nonfluorinated) PEN, where such strong IPBs do not exist and HB arrangement is found in *all* polymorphs with mutually inclined molecular planes; for GIXRD of PEN/HOPG and a discussion of growth (dis-)similarities between PFP and PEN, see the Supporting Information. A closer inspection of the PFP polymorphs reveals that a similarly stacked motif is, in fact, present in both the HB and the π-stacked arrangement, as highlighted in red in Figure 2a,b. On graphene, the molecules are laterally shifted such that four fluorine atoms of one molecule lie exactly in the ring center of the other while being translated by one ring along the long molecular axis, which optimizes the mutual orientation of the local dipole moments associated with the IPBs (Figure 2d). The remaining major difference between the two

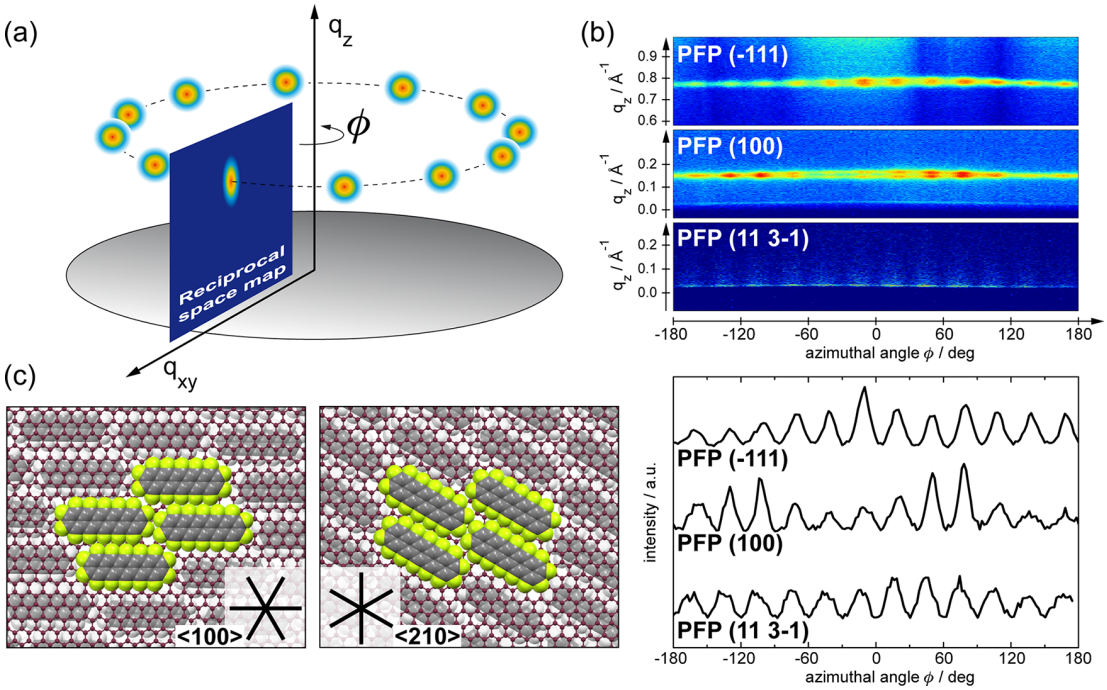

Figure 3. (a) Cartoon of the principle of GIXRD texture analysis. For epitaxially ordered films, discrete peaks are observed, which degenerate to circles for fiber-textured films. (b) Scans around the azimuthal angle φ for the three strong reflections (-111), (100), and (11 3$-$1) of the PSP, each showing 12 maxima (top). Integration of the data along the out-of plane component of the scattering vector (q_z) yields line scans (bottom); φ axes were transformed from the experimental 2 + 2 geometry[66] to common pole figure geometry (Supporting Information). (c) Cartoon of the two suggested alignments of PFP in multilayer films (top view on the PSP(001) plane) with the graphene lattice along its two high-symmetry directions ⟨100⟩ and ⟨210⟩. As these directions are crystallographically and energetically highly different but the observed intensities (b) do not alternate, an alignment with ⟨210⟩ appears improbable (see text).

polymorphs is merely the ∼90° HB angle in the TFP, which can, in principle, be thought of as being constructed by mirroring the stack at the dotted lines in Figure 2. Importantly, the π-stacking distance is significantly reduced from the HB structures (single-crystal phase, 3.26 Å; TFP, 3.17 Å) to 3.07 Å in the π-stacked PSP on graphene, which is among the lowest π-stacking distances ever reported for organic semiconductor crystal lattices.[23]

Clearly, since identical preparation parameters on SiO_x and graphene lead to the growth of stable films in two highly different crystal structures, the nature of the substrate emerges as the decisive factor for the selection of the respective polymorph during growth.[60,61] Recently, the surface unit cell of the closely packed PFP monolayer on HOPG[62] and on metallic substrates was determined by both scanning tunneling microscopy[63−65] and electron diffraction[51] to be almost identical to that found here for the molecules on the (001) texture plane of the PSP (17.2 Å × 8.9 Å, ∠61°), as illustrated in Figure 2b. In analogy to metals and HOPG, the formation of a flat-lying PFP monolayer is expected for the graphene substrate and subsequent multilayer growth is kinetically stabilized by the monolayer arrangement[60] in the almost identical 3D packing motif of the PSP. As the PSP crystal structure results also from our crystal structure prediction approach, where the substrate is *not* taken into account (*vide supra*), the PSP is indeed a local energetic minimum that is selected by the substrate. Note that in a previous study[40] the PSP was observed also in significantly thicker films on HOPG without any evidence of a thickness-driven phase transition to HB. This finding demonstrates the importance of control over the initial OSC growth to achieve desired structural properties in functional films.

Graphene as a substrate not only induces growth in the π-stacked polymorph but also further leads to three-dimensional *epitaxial* growth of uniaxially aligned, flat-lying PFP molecules. This is best envisioned employing GIXRD texture analysis[67] *via* sample rotation around the texture axis (sample normal) by $\varphi = 360°$, as illustrated in Figure 3a. There, modulations in peak intensity for given net planes appear in φ scans if the crystallites exhibit a preferential azimuthal orientation around the texture axis instead of a perfect fiber texture ("2D powder") that would occur as homogeneous intensity distribution instead. Clearly, for PFP/graphene, we find a strong intensity modulation with 12 equidistant maxima for three selected strong PFP reflections [(-111), (100), and the strong in-plane reflection (11 3$-$1)], which exhibit an angular relation in φ that perfectly agrees with the PSP unit cell determined above (Figure 3b). Given the active spot size of the X-ray beam in the range of 1 mm^2, this result

implies epitaxial order of the adsorbate in 12 preferential rotational domains at this length scale, which is possible due to the correspondingly large grain size of the copper foil upon thermal annealing (close to the melting temperature of Cu) during CVD graphene, which is reported to be beyond several millimeters.[43,68] Importantly, the finding of 12 reflections instead of 6, as it would be expected from the 6-fold symmetry of the graphene lattice, can have two causes, which, however, cannot be directly discriminated by the present area averaging experiments. First, the CVD-grown graphene substrate itself exhibits 12-fold symmetry caused by its growth on the copper foil, which is predominantly (100)-textured due to thermal treatment prior to graphene formation.[68] Therefore, there are two equivalent ways for the (6-fold symmetric) graphene layer to align with a supporting (4-fold symmetric) copper grain, finally leading to the observed 12-fold symmetry of the graphene layer.[43,44] The epitaxially grown PFP film aligns to graphene in a single-well-defined manner, thus adopting the substrate's foldness. Second, there exist two high-symmetry directions for the 6-fold symmetric graphene itself, the ⟨100⟩ ("zigzag") and the ⟨210⟩ ("armchair") directions.[69] The long molecular axis of PFP might align with either (Figure 3c), yielding a total of 24 orientations, of which only 12 are distinct. However, given that these two directions of graphene must be expected to be both crystallographically and energetically different, while no azimuthal alternation in intensity of the diffraction peaks (Figure 3b) is observed, we prefer explanation one. Note that growth in the (00−1) mirror texture cannot explain the observed 12 reflections, as upon molecular alignment with the high-symmetry directions the reflections of both textures coincide (Supporting Information). We stress that epitaxial growth on graphene observed here for PFP is by far not self-evident, as, for example, the related organic semiconductor perylene-3,4,9,10-tetracarboxylic acid dianhydride (PTCDA) does *not* epitaxially arrange with graphene.[70]

Having established the crystal structure of π-stacked PFP, we finally turn to investigating its impact on the electronic properties, that is, in particular, the transfer integral t crucial for charge transport, as outlined above. To that end, we carried out ultraviolet photoelectron spectroscopy (UPS) on the PSP under variation of the energies ($h\nu$) of the incident photons at normal emission (Figure 4) to observe intermolecular energy-band dispersion along the surface normal. To avoid sample-charging issues due to the insulating quartz substrates coated by graphene, we performed UPS on PFP/HOPG, where growth in the PSP was likewise found by XRD (*vide supra*). For UPS experiments, a lower nominal film thickness of 10 nm was chosen, which is, on the one hand, sufficiently low to avoid sample charging issues and, on the other hand, large enough to avoid an influence of the HOPG substrate on the PFP electronic

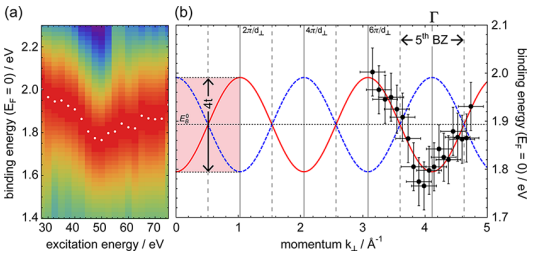

Figure 4. Electron band dispersion of the π-stacked PFP polymorph along the sample normal. (a) Second derivative of the UPS spectra for different excitation energies in the range of the HOMO emission; data represented as photoemission intensity map with fitted peak maxima indicated as white dots (intensity normalized to the respective maxima); binding energy (E_b) given with respect to the Fermi level (E_F). (b) Experimental dispersion of the HOMO band depicted in the extended zone scheme with parameters of $d_\perp$ = 6.11 Å, E_b^0 = 1.89 eV, t = 0.05 eV, and V_0 = −11.7 eV, which compare well to literature values of related systems.[39] The dispersion is illustrated by two tight-binding cosine functions (red and blue curves with $d_\perp/2$) as the PSP unit cell contains two molecules; the derived value of $d_\perp$ equals the (001) lattice spacing of the PSP.

structure. From the UPS data, a value of the ionization energy of 6.0 eV is determined, which is in line with lying PFP[71] (see Supporting Information for raw data). According to the tight-binding model (assuming a parabolic free-electron-like band as the final continuum state), the energy-band dispersion relation is given by[39,72] $E_b(k_\perp) = E_b^0 - 2t\cos(k_\perp d_\perp)$ with $k_\perp = (2m_e^*/\hbar^2)^{1/2}(E_{kin} - V_0)^{1/2}$, where $E_{kin} = h\nu - E_b$ is the kinetic energy of the photoelectron, E_b its binding energy from the vacuum level, $k_\perp$ its wave vector component along the surface normal, E_b^0 the energy of the band center, t the transfer integral, $d_\perp$ the lattice spacing normal to the surface (here, the (001) spacing of the PSP), m_e^* the effective mass of the photoelectron in the final continuum state (approximated by the free electron mass m_0), and V_0 the inner potential. For experimentally assessing t, we varied $h\nu$ from 27.5 to 75 eV (at room temperature) and determined the maxima of the HOMO band by forming the second derivative of the UPS data for each $h\nu$, as depicted in Figure 4a. The HOMO emission maxima shift toward lower binding energy with a minimum around $h\nu$ = 50 eV, where the shift is reversed. These data translate into a dispersion relation $E_b(k_\perp)$, as illustrated in Figure 4b in the extended zone scheme, where the investigated $h\nu$ range corresponds to excitation in the 4th−6th Brillouin zones. For the experimentally observed (001) lattice spacing, the data can be fitted with a cosine function according to the tight-binding model, which yields a value of 0.05 eV for the transfer integral t of the PSP; this value equals that for likewise vertically π-stacked PTCDA analogously determined on HOPG as substrate[73] and is even larger than that recently found for picene single crystals.[74] Finally, in a broad-band model ($W > k_BT$), this allows estimating the hole mobility at room temperature for the PSP in the vertical direction to $\mu_h > 20(m_0/m_h^*) \approx 9.6\ cm^2/(V\cdot s)$, with

the (tight-binding approximated) effective hole mass of $m^*_h = \hbar^2/(2td^2_\perp) \approx 2.08\ m_0$.[39,75]

CONCLUSIONS

We demonstrated that coating transparent quartz substrates with graphene induces lying and coplanar π-stacked growth in thin PFP films. We determined the unit cell parameters of this substrate-mediated PFP polymorph by GIXRD and carried out a full structure solution both by theoretical structure modeling and fitting experimental data. Compared to the herringbone-type polymorphs of PFP, our structure solution reveals a significantly reduced π-stacking distance of 3.07 Å for PFP on graphene, which is among the lowest values reported so far for organic semiconductors, giving rise to distinct electronic band dispersion along the π-stacking direction, as observed by UPS. Finally, we showed that substrate coating with graphene induces large-scale epitaxial growth of the vertically π-stacked molecules, which is expected to maximize the vertical π-orbital overlap being beneficial for the out-of-plane charge-carrier mobility. Our study underlines the versatility of graphene and its high potential as coating for establishing transparent electrodes in future opto-electronic applications, where vertical charge transport is generally disfavored by an edge-on standing molecular orientation on ITO-coated glass as a typical substrate.

METHODS

Materials and Sample Preparation. Perfluoropentacene (PFP) (Kanto Denka Kogyo Co., 99% purity) was deposited *via* evaporation from resistively heated quartz crucibles (deposition rate = 0.5 nm/min monitored with a quartz crystal microbalance, base pressure <5 × 10^{-8} mbar). Graphene-coated quartz pieces (2 × 2 cm^2) served as substrates that were established in analogy to the procedure reported in refs 41 and 42 using a Cu foil (7 × 7 cm^2, 25 μm thickness, 99.8% purity, Alfa Aesar, product no. 13382, annealed for 40 min at 1020 °C) for CVD graphene growth with an ensuing wet transfer to the quartz support. Highly oriented pyrolytic graphite (ZYA-grade, 1 × 1 cm^2) that was *ex situ* cleaved was used as the reference substrate.

Characterizations. Specular and grazing-incidence X-ray diffraction (GIXRD) were performed *ex situ* at beamline W1.1 of the synchrotron radiation source HASYLAB (DESY, Germany; $h\nu$ = 10.5 keV, inert He atmosphere) with an incident beam angle of 0.15° using a MYTHEN 1D detector. Data processing was carried out using the self-implemented software package PyGid,[76] including intensity corrections according to ref 66 and a correction of refraction effects.

NEXAFS was performed at the HE-SGM dipole beamline of the synchrotron storage ring BESSY II in Berlin (Germany) providing linear polarized light (polarization factor = 0.91; energy resolution at the carbon K-edge = 300 meV). All NEXAFS spectra were recorded in partial electron-yield mode using a channel-plate detector with a retarding field of −150 V. For the calibration of the absolute energy scale, the photocurrent from a carbon-coated gold grid in the incident beam (absorption maximum = 284.9 eV) was recorded simultaneously. To determine the average tilt angle of the molecules relative to the sample surface, measurements were carried out at three different angles of incidence (30, 55, and 90°); for further details, see the Supporting Information.

Ultraviolet photoelectron spectroscopy (UPS) experiments were performed under ultrahigh vacuum conditions at the endstation SurICat at the synchrotron light source BESSY II (Helmholtz Zentrum Berlin für Materialien and Energie, Germany) with an energy resolution of 120 meV using excitation photon energies of 27.5−75 eV; the secondary electron cutoff was recorded at −10 V sample bias.

Force-Field Calculations. To determine the molecular orientation within the experimentally determined unit cell of the π-stacked polymorph, we utilize a global total energy minimization scheme employing force fields as described in detail in ref 46. To summarize our approach, we consider the PFP molecules as rigid bodies and search for the molecular orientations, which minimize the total energy. We consider the three spatial coordinates of the molecular center of mass as well as the three Euler angles representing the molecular orientation with respect to the unit cell frame as degrees of freedom. Thus, in total, there are 6Z degrees of freedom, where Z is the number of molecules in the unit cell. To calculate the total energy of the PFP crystal, we use empirical interatomic force fields, in particular, the MM3 force field[77−79] as implemented in the TINKER code,[80] and further checked the influence of the particular choice of force field on the structure solution. To this end, we also utilized the DREIDING force field[81] as implemented in the GULP code,[82] which led to the same structure solutions as already found with MM3. For the global minimum search, we utilize a genetic algorithm (GA) for exploring the configuration space. Details on our implementation of the GA are given in the Appendix of ref 46. In order to ensure that the best crystal structure solution is indeed found, the GA optimization run has been repeated a sufficient amount of times.

Comparing the total energies of the crystal structure solutions, that is, the herringbone (HB)-type thin-film polymorph (TFP) observed on SiO_x and the π-stacked polymorph (PSP) on graphene (and HOPG), the energy per molecule in the PSP is found to be ≈24 meV *higher* than that in the TFP. In fact, this result confirms the observation that, apart from the PSP observed here on graphene coatings, all known PFP polymorphs tend to form a HB arrangement. Otherwise, the strong interaction of the molecules with graphene (or HOPG), which is considered only indirectly in our simulation by using the experimental crystal structure, is responsible for stabilizing the π-stacked packing in the molecular assemblies.

Crystal Structure Prediction. Possible crystal structures are predicted by systematically searching the potential energy hypersurface to identify its local minima. These minima represent the possible configurations of mechanical equilibrium and thus constitute the "natural" or "inherent" structures that the crystalline system can exhibit.[83] About 20 000 initial configurations were generated for PFP films on graphene, evenly distributed among the various possible arrangements consistent with the known structural information, that is, a triclinic unit cell (with the experimental lattice parameters reported in this article) containing two molecules (Z = 2). The triclinic lattice allows only two space groups: $P1$ (no symmetry) and $P\bar{1}$ (inversion symmetry only). In $P\bar{1}$, the molecules have inversion symmetry and are therefore allowed (but not required) to lie on one of the eight possible inversion sites (with coordinates x,y,z equal to 0 or 1/2). The various possibilities thus are $P\bar{1}$ with Z = 2 (1) (a molecule on a generic site "1", plus a second equivalent molecule obtained by inversion), $P\bar{1}$ with Z = 2 ($\bar{1}$,$\bar{1}$) (two independent molecules on inversion sites "$\bar{1}$"), or $P1$ with Z = 2 (1,1) (two independent molecules, one chosen as the origin, the other at generic coordinates).

Starting from each initial configuration, we minimize the potential energy. The molecules are treated as rigid units with the D_{2h} planar geometry determined with Gaussian 03,[84] using the B3LYP/6-31G* combination of density functional and basis set. They interact through a pairwise additive atom−atom

TABLE 1. Experimental[36,37] and Computed Lattice Parameters (axes in Å, angles in degrees)

lattice	structure		*a*	*b*	*c*	α	*β*	*γ*
$P2_1/c$ $Z = 2$ ($\bar{1}$)	single-crystal PFP[36]	expt	15.51	4.49	11.45	90.00	91.57	90.00
	PFP on SiO_x (TFP)[37]	expt	15.76	4.51	11.48	90.00	90.40	90.00
		calcd	15.69	4.53	12.03	90.00	90.15	90.00
$P\bar{1}$ $Z = 2$ ($\bar{1}$,$\bar{1}$)	PFP on graphene (PSP)	expt	15.13	8.94	6.51	78.56	108.14	92.44
		calcd	15.20	9.00	6.87	75.92	108.33	92.16

potential model of the form $V(r) = A_{ij}/r^{12} - B_{ij}/r^6 + q_iq_j/r$, which combines a Lennard-Jones potential model with the DREIDING[81] parameters (A_{ij} and B_{ij}) with a Coulombic contribution described by atomic charges q_i. These parameters are fitted to the electrostatic potential in the isolated molecule.[84] Structural optimization initially proceeded with lattice parameters fixed to the experimental values. Once found all distinct constrained minima [see the Supporting Information (S11) for one in perfect agreement with the experimental intensities], we then continued the energy minimization without constraints, by adjusting also the unit cell axes and angles. We suppose that surface-induced polymorphs, although not necessarily coincident with genuine local minima of the potential energy, cannot be too unstable. Structures which move too far (once removed the constraints on the lattice parameters) or that fail to converge to stable bound states (*i.e.*, to high-density structures with negative potential energy) are unlikely to be correct and are therefore discarded. Bulk crystal structures were also searched, using the methods extensively discussed in previous work[85,86] to obtain information on the global stability of the minima and to validate the potential model. We have, thus, generated and optimized (without constraints) several thousands of additional monoclinic structures in the space group $P2_1/c$ with $Z = 2$ (the structure of both the TFP and the single-crystal phase). The potential model appears quite realistic since these two known structures (single-crystal phase[36] and TFP on SiO_x[37]) both converge to very deep minima (rank 2) and are reproduced extremely well by the calculations (see Table 1).

We suppose that surface-induced forms should closely resemble local minima of the potential energy (inherent structures). The idea is that the interactions with the surface will mostly increase the energetic and/or kinetic stability of minima that already exist, rather than creating brand new minima. This idea is almost certainly correct for weakly interacting surfaces such as SiO_x, where the known structure (TFP)[37] is closely related to the single-crystal structure.[36] The idea is probably also correct also for PFP on graphene, where a flat-lying monolayer is expected and subsequent multilayer growth is kinetically stabilized by the monolayer arrangement in the almost identical 3D packing motif of the π-stacked polymorph determined in this work (with significant initial theoretical input but fully confirmed by the X-ray diffraction experiments). In fact, it converges to a very deep minimum (rank 3), and again, the computed lattice parameters are in good agreement with the experiments (see Table 1).

Calculation of Atomic Charges. Density functional theory (DFT) calculations of the atomic charges on the atoms forming a PFP molecule and of the molecular electrostatic potential map (Figure 2c,d) relied on the hybrid exchange-correlation functional PBE0[87] and a 6-31G** contracted Gaussian basis set.[88,89] Atomic charges reported in Figure 2 were obtained through a Mulliken analysis;[90] calculations were performed with the Gaussian 09 quantum chemistry suite.[91]

Conflict of Interest: The authors declare no competing financial interest. ▼Present address: Humboldt-Universität zu Berlin, Institut für Physik, Berlin, Germany. ▲Present address: Karl-Franzens-Universität Graz, Institut für Physik, Graz, Austria.

Acknowledgment. We thank Wolfgang Caliebe (DESY-HASYLAB) for experimental support and granting access to the very last photons from storage ring DORIS before its final shutdown on October 22, 2012 [for the last spectrum (PFP/quartz) recorded at beamline W1.1, see the Supporting Information]. We further acknowledge Ruslan Ovsyannikov [Helmholtz-Zentrum Berlin (HZB), BESSY II] for experimental support, Roland Resel (TU Graz, Austria) for support in unit cell determination, and the HZB for granting access to beamline HE-SGM and to the optics beamline (SurICat), as well as the HZB and DESY for travel support. T.B. gratefully acknowledges the Friedrich-Ebert-Stiftung (Germany) for financial support. Financing through the DFG (Germany) and the Austrian Science Fund (FWF): [P21094] and [S9714] is gratefully acknowledged.

Supporting Information Available: Crystallographic information files (CIFs), structure solution of the PFP/SiO_x thin-film phase (TFP), UPS data, GIXRD on PFP/HOPG, XRD comparison between PFP on graphene-coated and pristine quartz, XRD rocking curve of PFP/graphene, quantitative NEXAFS analysis, and Raman spectroscopy of PFP/HOPG; methodological remarks on XRD geometries, GIXRD texture analysis in 2 + 2 geometry, relation between the PSP (001) and (00−1) textures; a comparison of the results of the three independent approaches to structure solution. This material is available free of charge *via* the Internet at http://pubs.acs.org.

REFERENCES AND NOTES

1. Geim, A. K. Graphene: Status and Prospects. *Science* **2009**, *324*, 1530–1534.
2. Geim, A. K.; Novoselov, K. S. The Rise of Graphene. *Nat. Mater.* **2007**, *6*, 183–191.
3. Lee, C.; Wei, X. D.; Kysar, J. W.; Hone, J. Measurement of the Elastic Properties and Intrinsic Strength of Monolayer Graphene. *Science* **2008**, *321*, 385–388.
4. Castro Neto, A. H.; Guinea, F.; Peres, N. M. R.; Novoselov, K. S.; Geim, A. K. The Electronic Properties of Graphene. *Rev. Mod. Phys.* **2009**, *81*, 109–162.
5. Lin, Y. M.; Dimitrakopoulos, C.; Jenkins, K. A.; Farmer, D. B.; Chiu, H. Y.; Grill, A.; Avouris, P. 100-GHz Transistors from Wafer-Scale Epitaxial Graphene. *Science* **2010**, *327*, 662–662.
6. Schedin, F.; Geim, A. K.; Morozov, S. V.; Hill, E. W.; Blake, P.; Katsnelson, M. I.; Novoselov, K. S. Detection of Individual Gas Molecules Adsorbed on Graphene. *Nat. Mater.* **2007**, *6*, 652–655.
7. Liu, M.; Yin, X. B.; Ulin-Avila, E.; Geng, B. S.; Zentgraf, T.; Ju, L.; Wang, F.; Zhang, X. A Graphene-Based Broadband Optical Modulator. *Nature* **2011**, *474*, 64–67.
8. Pang, S. P.; Hernandez, Y.; Feng, X. L.; Müllen, K. Graphene as Transparent Electrode Material for Organic Electronics. *Adv. Mater.* **2011**, *23*, 2779–2795.
9. Wan, X. J.; Long, G. K.; Huang, L.; Chen, Y. S. Graphene—A Promising Material for Organic Photovoltaic Cells. *Adv. Mater.* **2011**, *23*, 5342–5358.
10. Nair, R. R.; Blake, P.; Grigorenko, A. N.; Novoselov, K. S.; Booth, T. J.; Stauber, T.; Peres, N. M. R.; Geim, A. K. Fine Structure Constant Defines Visual Transparency of Graphene. *Science* **2008**, *320*, 1308–1308.
11. Chen, J. H.; Jang, C.; Xiao, S. D.; Ishigami, M.; Fuhrer, M. S. Intrinsic and Extrinsic Performance Limits of Graphene Devices on SiO_2. *Nat. Nanotechnol.* **2008**, *3*, 206–209.
12. Bae, S.; Kim, H.; Lee, Y.; Xu, X. F.; Park, J. S.; Zheng, Y.; Balakrishnan, J.; Lei, T.; Kim, H. R.; Song, Y. I.; *et al.* Roll-to-Roll Production of 30-Inch Graphene Films for Transparent Electrodes. *Nat. Nanotechnol.* **2010**, *5*, 574–578.
13. Kim, K. S.; Zhao, Y.; Jang, H.; Lee, S. Y.; Kim, J. M.; Kim, K. S.; Ahn, J. H.; Kim, P.; Choi, J. Y.; Hong, B. H. Large-Scale Pattern Growth of Graphene Films for Stretchable Transparent Electrodes. *Nature* **2009**, *457*, 706–710.
14. Brédas, J. L.; Calbert, J. P.; da Silva Filho, D. A.; Cornil, J. Organic Semiconductors: A Theoretical Characterization of the Basic Parameters Governing Charge Transport. *Proc. Natl. Acad. Sci. U.S.A.* **2002**, *99*, 5804–5809.

15. Coropceanu, V.; Cornil, J.; da Silva Filho, D. A.; Olivier, Y.; Silbey, R.; Brédas, J. L. Charge Transport in Organic Semiconductors. *Chem. Rev.* **2007**, *107*, 926–952.
16. Kera, S.; Yamane, H.; Ueno, N. First-Principles Measurements of Charge Mobility in Organic Semiconductors: Valence Hole-Vibration Coupling in Organic Ultrathin Films. *Prog. Surf. Sci.* **2009**, *84*, 135–154.
17. Anthony, J. E. Functionalized Acenes and Heteroacenes for Organic Electronics. *Chem. Rev.* **2006**, *106*, 5028–5048.
18. Desiraju, G. R.; Gavezzotti, A. Crystal-Structures of Polynuclear Aromatic-Hydrocarbons—Classification, Rationalization and Prediction from Molecular-Structure. *Acta Crystallogr., B* **1989**, *45*, 473–482.
19. Lee, J. Y.; Roth, S.; Park, Y. W. Anisotropic Field Effect Mobility in Single Crystal Pentacene. *Appl. Phys. Lett.* **2006**, *88*, 252106.
20. Hoeben, F. J. M.; Jonkheijm, P.; Meijer, E. W.; Schenning, A. P. H. J. About Supramolecular Assemblies of π-Conjugated Systems. *Chem. Rev.* **2005**, *105*, 1491–1546.
21. Anthony, J. E.; Brooks, J. S.; Eaton, D. L.; Parkin, S. R. Functionalized Pentacene: Improved Electronic Properties from Control of Solid-State Order. *J. Am. Chem. Soc.* **2001**, *123*, 9482–9483.
22. Sheraw, C. D.; Jackson, T. N.; Eaton, D. L.; Anthony, J. E. Functionalized Pentacene Active Layer Organic Thin-Film Transistors. *Adv. Mater.* **2003**, *15*, 2009–2011.
23. Giri, G.; Verploegen, E.; Mannsfeld, S. C. B.; Atahan-Evrenk, S.; Kim, D. H.; Lee, S. Y.; Becerril, H. A.; Aspuru-Guzik, A.; Toney, M. F.; Bao, Z. A. Tuning Charge Transport in Solution-Sheared Organic Semiconductors Using Lattice Strain. *Nature* **2011**, *480*, 504–509.
24. Mannsfeld, S. C.; Tang, M. L.; Bao, Z. Thin Film Structure of Triisopropylsilylethynyl-Functionalized Pentacene and Tetraceno[2,3-*b*]thiophene from Grazing Incidence X-ray Diffraction. *Adv. Mater.* **2011**, *23*, 127–131.
25. Huang, H.; Chen, S.; Gao, X. Y.; Chen, W.; Wee, A. T. S. Structural and Electronic Properties of PTCDA Thin Films on Epitaxial Graphene. *ACS Nano* **2009**, *3*, 3431–3436.
26. Ren, J.; Meng, S.; Wang, Y. L.; Ma, X. C.; Xue, Q. K.; Kaxiras, E. Properties of Copper (Fluoro-)Phthalocyanine Layers Deposited on Epitaxial Graphene. *J. Chem. Phys.* **2011**, *134*, 194706.
27. Emery, J. D.; Wang, Q. H.; Zarrouati, M.; Fenter, P.; Hersam, M. C.; Bedzyk, M. J. Structural Analysis of PTCDA Monolayers on Epitaxial Graphene with Ultra-high Vacuum Scanning Tunneling Microscopy and High-Resolution X-ray Reflectivity. *Surf. Sci.* **2011**, *605*, 1685–1693.
28. Zhou, H. T.; Mao, J. H.; Li, G.; Wang, Y. L.; Feng, X. L.; Du, S. X.; Müllen, K.; Gao, H. J. Direct Imaging of Intrinsic Molecular Orbitals Using Two-Dimensional, Epitaxially-Grown, Nanostructured Graphene for Study of Single Molecule and Interactions. *Appl. Phys. Lett.* **2011**, *99*, 153101.
29. Lee, W. H.; Park, J.; Sim, S. H.; Lim, S.; Kim, K. S.; Hong, B. H.; Cho, K. Surface-Directed Molecular Assembly of Pentacene on Monolayer Graphene for High-Performance Organic Transistors. *J. Am. Chem. Soc.* **2011**, *133*, 4447–4454.
30. Hlawacek, G.; Khokhar, F. S.; van Gastel, R.; Poelsema, B.; Teichert, C. Smooth Growth of Organic Semiconductor Films on Graphene for High-Efficiency Electronics. *Nano Lett.* **2011**, *11*, 333–337.
31. Scardamaglia, M.; Forte, G.; Lizzit, S.; Baraldi, A.; Lacovig, P.; Larciprete, R.; Mariani, C.; Betti, M. G. Metal-Phthalocyanine Array on the Moiré Pattern of a Graphene Sheet. *J. Nanopart. Res.* **2011**, *13*, 6013–6020.
32. Rossi, L.; Seidel, K. F.; Machado, W. S.; Hummelgen, I. A. Low Voltage Vertical Organic Field-Effect Transistor with Polyvinyl Alcohol as Gate Insulator. *J. Appl. Phys.* **2011**, *110*, 094508.
33. Ma, L. P.; Yang, Y. Unique Architecture and Concept for High-Performance Organic Transistors. *Appl. Phys. Lett.* **2004**, *85*, 5084–5086.
34. Watanabe, Y.; Kudo, K. Flexible Organic Static Induction Transistors Using Pentacene Thin Films. *Appl. Phys. Lett.* **2005**, *87*, 223505.
35. Dimitrakopoulos, C. D.; Malenfant, P. R. L. Organic Thin Film Transistors for Large Area Electronics. *Adv. Mater.* **2002**, *14*, 99–117.
36. Sakamoto, Y.; Suzuki, T.; Kobayashi, M.; Gao, Y.; Fukai, Y.; Inoue, Y.; Sato, F.; Tokito, S. Perfluoropentacene: High-Performance p-n Junctions and Complementary Circuits with Pentacene. *J. Am. Chem. Soc.* **2004**, *126*, 8138–8140.
37. Salzmann, I.; Duhm, S.; Heimel, G.; Rabe, J. P.; Koch, N.; Oehzelt, M.; Sakamoto, Y.; Suzuki, T. Structural Order in Perfluoropentacene Thin Films and Heterostructures with Pentacene. *Langmuir* **2008**, *24*, 7294–7298.
38. Kowarik, S.; Gerlach, A.; Hinderhofer, A.; Milita, S.; Borgatti, F.; Zontone, F.; Suzuki, T.; Biscarini, F.; Schreiber, F. Structure, Morphology, and Growth Dynamics of Perfluoropentacene Thin Films. *Phys. Status Solidi Rapid Res. Lett.* **2008**, *2*, 120–122.
39. Ueno, N.; Kera, S. Electron Spectroscopy of Functional Organic Thin Films: Deep Insights into Valence Electronic Structure in Relation to Charge Transport Property. *Prog. Surf. Sci.* **2008**, *83*, 490–557.
40. Breuer, T.; Salzmann, I.; Götzen, J.; Oehzelt, M.; Morherr, A.; Koch, N.; Witte, G. Interrelation between Substrate Roughness and Thin-Film Structure of Functionalized Acenes on Graphite. *Cryst. Growth Des.* **2011**, *11*, 4996–5001.
41. Li, X. S.; Cai, W. W.; An, J. H.; Kim, S.; Nah, J.; Yang, D. X.; Piner, R.; Velamakanni, A.; Jung, I.; Tutuc, E.; *et al.* Large-Area Synthesis of High-Quality and Uniform Graphene Films on Copper Foils. *Science* **2009**, *324*, 1312–1314.
42. Ferrari, A. C.; Meyer, J. C.; Scardaci, V.; Casiraghi, C.; Lazzeri, M.; Mauri, F.; Piscanec, S.; Jiang, D.; Novoselov, K. S.; Roth, S.; *et al.* Raman Spectrum of Graphene and Graphene Layers. *Phys. Rev. Lett.* **2006**, *97*, 187401.
43. Huang, P. Y.; Ruiz-Vargas, C. S.; van der Zande, A. M.; Whitney, W. S.; Levendorf, M. P.; Kevek, J. W.; Garg, S.; Alden, J. S.; Hustedt, C. J.; Zhu, Y.; *et al.* Grains and Grain Boundaries in Single-Layer Graphene Atomic Patchwork Quilts. *Nature* **2011**, *469*, 389–393.
44. Wofford, J. M.; Nie, S.; McCarty, K. F.; Bartelt, N. C.; Dubon, O. D. Graphene Islands on Cu Foils: The Interplay between Shape, Orientation, and Defects. *Nano Lett.* **2010**, *10*, 4890–4896.
45. Duhm, S.; Hosoumi, S.; Salzmann, I.; Gerlach, A.; Oehzelt, M.; Wedl, B.; Lee, T. L.; Schreiber, F.; Koch, N.; Ueno, N.; *et al.* Influence of Intramolecular Polar Bonds on Interface Energetics in Perfluoro-pentacene on Ag(111). *Phys. Rev. B* **2010**, *81*, 045418.
46. Salzmann, I.; Nabok, D.; Oehzelt, M.; Duhm, S.; Moser, A.; Heimel, G.; Puschnig, P.; Ambrosch-Draxl, C.; Rabe, J. P.; Koch, N. Structure Solution of the 6,13-Pentacenequinone Surface-Induced Polymorph by Combining X-ray Diffraction Reciprocal-Space Mapping and Theoretical Structure Modeling. *Cryst. Growth Des.* **2011**, *11*, 600–606.
47. Bardwell, D. A.; Adjiman, C. S.; Arnautova, Y. A.; Bartashevich, E.; Boerrigter, S. X. M.; Braun, D. E.; Cruz-Cabeza, A. J.; Day, G. M.; Della Valle, R. G.; Desiraju, G. R.; *et al.* Towards Crystal Structure Prediction of Complex Organic Compounds—A Report on the Fifth Blind Test. *Acta Crystallogr., B* **2011**, *67*, 535–551.
48. Favre-Nicolin, V.; Cerny, R. FOX, 'Free Objects for Crystallography': A Modular Approach to Ab Initio Structure Determination from Powder Diffraction. *J. Appl. Crystallogr.* **2002**, *35*, 734–743.
49. Oehzelt, M.; Berkebile, S.; Koller, G.; Ivanco, J.; Surnev, S.; Ramsey, M. G. α-Sexithiophene on Cu(110) and Cu(110)-(2 $\times$ 1)O: An STM and NEXAFS Study. *Surf. Sci.* **2009**, *603*, 412–418.
50. Koller, G.; Berkebile, S.; Krenn, J. R.; Netzer, F. P.; Oehzelt, M.; Haber, T.; Resel, R.; Ramsey, M. G. Heteroepitaxy of Organic–Organic Nanostructures. *Nano Lett.* **2006**, *6*, 1207–1212.
51. Marks, M.; Schmidt, C.; Schwalb, C. H.; Breuer, T.; Witte, G.; Höfer, U. Temperature Dependent Structural Phase Transition at the Perfluoropentacene/Ag(111) Interface. *J. Phys. Chem. C* **2012**, *116*, 1904–1911.
52. Grimme, S. Do Special Noncovalent $\pi-\pi$ Stacking Interactions Really Exist? *Angew. Chem., Int. Ed.* **2008**, *47*, 3430–3434.
53. Tang, M. L.; Bao, Z. A. Halogenated Materials as Organic Semiconductors. *Chem. Mater.* **2011**, *23*, 446–455.

54. Heimel, G.; Salzmann, I.; Duhm, S.; Koch, N. Design of Organic Semiconductors from Molecular Electrostatics. *Chem. Mater.* **2011**, *23*, 359–377.
55. Salzmann, I.; Duhm, S.; Heimel, G.; Oehzelt, M.; Kniprath, R.; Johnson, R. L.; Rabe, J. P.; Koch, N. Tuning the Ionization Energy of Organic Semiconductor Films: The Role of Intramolecular Polar Bonds. *J. Am. Chem. Soc.* **2008**, *130*, 12870–12871.
56. Wheeler, S. E. Local Nature of Substituent Effects in Stacking Interactions. *J. Am. Chem. Soc.* **2011**, *133*, 10262–10274.
57. Hunter, C. A.; Lawson, K. R.; Perkins, J.; Urch, C. J. Aromatic Interactions. *J. Chem. Soc., Perkin Trans. 2* **2001**, 651–669.
58. Williams, J. H. The Molecular Electric Quadrupole-Moment and Solid-State Architecture. *Acc. Chem. Res.* **1993**, *26*, 593–598.
59. Käfer, D.; El Helou, M.; Gemel, C.; Witte, G. Packing of Planar Organic Molecules: Interplay of van der Waals and Electrostatic Interaction. *Cryst. Growth Des.* **2008**, *8*, 3053–3057.
60. Djuric, T.; Ules, T.; Flesch, H. G.; Plank, H.; Shen, Q. A.; Teichert, C.; Resel, R.; Ramsey, M. G. Epitaxially Grown Films of Standing and Lying Pentacene Molecules on Cu(110) Surfaces. *Cryst. Growth Des.* **2011**, *11*, 1015–1020.
61. Djuric, T.; Ules, T.; Gusenleitner, S.; Kayunkid, N.; Plank, H.; Hlawacek, G.; Teichert, C.; Brinkmann, M.; Ramsey, M.; Resel, R. Substrate Selected Polymorphism of Epitaxially Aligned Tetraphenyl-Porphyrin Thin Films. *Phys. Chem. Chem. Phys.* **2012**, *14*, 262–272.
62. Glowatzki, H.; Heimel, G.; Vollmer, A.; Wong, S. L.; Huang, H.; Chen, W.; Wee, A. T. S.; Rabe, J. P.; Koch, N. Impact of Fluorination on Initial Growth and Stability of Pentacene on Cu(111). *J. Phys. Chem. C* **2012**, *116*, 7726–7734.
63. Wong, S. L.; Huang, H.; Huang, Y. L.; Wang, Y. Z.; Gao, X. Y.; Suzuki, T.; Chen, W.; Wee, A. T. S. Effect of Fluorination on the Molecular Packing of Perfluoropentacene and Pentacene Ultrathin Films on Ag(111). *J. Phys. Chem. C* **2010**, *114*, 9356–9361.
64. Götzen, J.; Schwalb, C. H.; Schmidt, C.; Mette, G.; Marks, M.; Höfer, U.; Witte, G. Structural Evolution of Perfluoro-pentacene Films on Ag(111): Transition from 2D to 3D Growth. *Langmuir* **2011**, *27*, 993–999.
65. de Oteyza, D. G.; Wakayama, Y.; Liu, X.; Yang, W.; Cook, P. L.; Himpsel, F. J.; Ortega, J. E. Effect of Fluorination on the Molecule−Substrate Interactions of Pentacene/Cu(100) Interfaces. *Chem. Phys. Lett.* **2010**, *490*, 54–57.
66. Smilgies, D. M. Geometry-Independent Intensity Correction Factors for Grazing-Incidence Diffraction. *Rev. Sci. Instrum.* **2002**, *73*, 1706–1710.
67. Oehzelt, M.; Koller, G.; Ivanco, J.; Berkebile, S.; Haber, T.; Resel, R.; Netzer, F. P.; Ramsey, M. G. Organic Heteroepitaxy: *p*-Sexiphenyl on Uniaxially Oriented α-Sexithiophene. *Adv. Mater.* **2006**, *18*, 2466–2470.
68. Robinson, Z. R.; Tyagi, P.; Murray, T. M.; Ventrice, C. A.; Chen, S. S.; Munson, A.; Magnuson, C. W.; Ruoff, R. S. Substrate Grain Size and Orientation of Cu and Cu-Ni Foils Used for the Growth of Graphene Films. *J. Vac. Sci. Technol., A* **2012**, *30*, 011401.
69. Batzill, M. The Surface Science of Graphene: Metal Interfaces, CVD Synthesis, Nanoribbons, Chemical Modifications, and Defects. *Surf. Sci. Rep.* **2012**, *67*, 83–115.
70. Wang, Q. H.; Hersam, M. C. Room-Temperature Molecular-Resolution Characterization of Self-Assembled Organic Monolayers on Epitaxial Graphene. *Nat. Chem.* **2009**, *1*, 206–211.
71. Koch, N.; Vollmer, A.; Duhm, S.; Sakamoto, Y.; Suzuki, T. The Effect of Fluorination on Pentacene/Gold Interface Energetics and Charge Reorganization Energy. *Adv. Mater.* **2007**, *19*, 112–116.
72. Seki, K.; Ueno, N.; Karlsson, U. O.; Engelhardt, R.; Koch, E. E. Valence Bands of Oriented Finite Linear-Chain Molecular-Solids as Model Compounds of Polyethylene Studied by Angle-Resolved Photoemission. *Chem. Phys.* **1986**, *105*, 247–265.
73. Yamane, H.; Kera, S.; Okudaira, K. K.; Yoshimura, D.; Seki, K.; Ueno, N. Intermolecular Energy-Band Dispersion in PTCDA Multilayers. *Phys. Rev. B* **2003**, *68*, 033102.
74. Xin, Q.; Duhm, S.; Bussolotti, F.; Akaike, K.; Kubozono, Y.; Aoki, H.; Kosugi, T.; Kera, S.; Ueno, N. Accessing Surface Brillouin Zone and Band Structure of Picene Single Crystals. *Phys. Rev. Lett.* **2012**, *108*, 226401.
75. Fröhlich, H.; Sewell, G. L. Electric Conduction in Semiconductors. *Proc. Phys. Soc., London* **1959**, *74*, 643–647.
76. Moser, A.; Werzer, O.; Flesch, H. G.; Koini, M.; Smilgies, D. M.; Nabok, D.; Puschnig, P.; Ambrosch-Draxl, C.; Schiek, M.; Rubahn, H. G.; *et al.* Crystal Structure Determination from Two-Dimensional Powders: A Combined Experimental and Theoretical Approach. *Eur. Phys. J.* **2009**, *167*, 59–65.
77. Allinger, N. L.; Yuh, Y. H.; Lii, J. H. Molecular Mechanics: The MM3 Force-Field for Hydrocarbons 0.1. *J. Am. Chem. Soc.* **1989**, *111*, 8551–8566.
78. Lii, J. H.; Allinger, N. L. Molecular Mechanics: The MM3 Force-Field for Hydrocarbons. 2. Vibrational Frequencies and Thermodynamics. *J. Am. Chem. Soc.* **1989**, *111*, 8566–8575.
79. Lii, J. H.; Allinger, N. L. Molecular Mechanics: The MM3 Force-Field for Hydrocarbons. 3. The Vanderwaals Potentials and Crystal Data for Aliphatic and Aromatic-Hydrocarbons. *J. Am. Chem. Soc.* **1989**, *111*, 8576–8582.
80. Ponder, J. W. *TINKER: Software Tools for Molecular Design*, 5th ed.; Washington University School of Medicine: Saint Louis, MO, 2010.
81. Mayo, S. L.; Olafson, B. D.; Goddard, W. A. DREIDING: A Generic Force-Field for Molecular Simulations. *J. Phys. Chem.* **1990**, *94*, 8897–8909.
82. Gale, J. D. GULP: A Computer Program for the Symmetry-Adapted Simulation of Solids. *J. Chem. Soc., Faraday Trans.* **1997**, *93*, 629–637.
83. Stillinger, F. H.; Weber, T. A. Hidden Structure in Liquids. *Phys. Rev. A* **1982**, *25*, 978–989.
84. Frisch, M. J.; Trucks, G. W.; Schlegel, H. B.; Scuseria, G. E.; Robb, M. A.; Cheeseman, J. R.; Montgomery, J. A., Jr.; Vreven, T.; Kudin, K. N.; Burant, J. C.; *et al. Gaussian 03*, revision D.02; Gaussian, Inc.: Wallingford, CT, 2004.
85. Della Valle, R. G.; Venuti, E.; Brillante, A.; Girlando, A. Inherent Structures of Crystalline Pentacene. *J. Chem. Phys.* **2003**, *118*, 807–815.
86. Della Valle, R. G.; Venuti, E.; Brillante, A.; Girlando, A. Are Crystal Polymorphs Predictable? The Case of Sexithiophene. *J. Phys. Chem. A* **2008**, *112*, 6715–6722.
87. Adamo, C.; Barone, V. Toward Reliable Density Functional Methods without Adjustable Parameters: The PBE0 Model. *J. Chem. Phys.* **1999**, *110*, 6158–6170.
88. Hehre, W. J.; Ditchfield, R.; Pople, J. A. Self-Consistent Molecular-Orbital Methods. XII. Further Extensions of Gaussian-Type Basis Sets for Use in Molecular-Orbital Studies of Organic-Molecules. *J. Chem. Phys.* **1972**, *56*, 2257–2261.
89. Hariharan, P. C.; Pople, J. A. Influence of Polarization Functions on Molecular-Orbital Hydrogenation Energies. *Theor. Chem. Acc.* **1973**, *28*, 213–222.
90. Mulliken, R. S. Electronic Population Analysis on LCAO-MO Molecular Wave Functions 1. *J. Chem. Phys.* **1955**, *23*, 1833–1840.
91. Frisch, M. J.; Trucks, G. W.; Schlegel, H. B.; Scuseria, G. E.; Robb, M. A.; Cheeseman, J. R.; Scalmani, G.; Barone, V.; Mennucci, B.; Petersson, G. A.; *et al. Gaussian 09*, revision A.02; Gaussian Inc.: Wallingford CT, 2009.

Supporting Information

Epitaxial Growth of π-Stacked perfluoropentacene on Graphene-Coated Quartz

Ingo Salzmann,[*,1] Armin Moser,[2] Martin Oehzelt,[3,1] Tobias Breuer,[4] Xinliang Feng,[5] Zhen-Yu Juang,[5] Dmitrii Nabok,[6] Raffaele G. Della Valle,[7] Steffen Duhm,[8] Georg Heimel,[1] Aldo Brillante,[7] Elisabetta Venuti,[7] Ivano Bilotti,[7] Christos Christodoulou,[1] Johannes Frisch,[1] Peter Puschnig,[6] Claudia Draxl,[6] Gregor Witte,[4] Klaus Müllen,[5] and Norbert Koch[1,3]

[1] *Humboldt-Universität zu Berlin, Institut für Physik, 12489 Berlin, Germany*

[2] *Institute of Solid State Physics, Graz University of Technology, 8010 Graz, Austria*

[3] *Helmholtz Zentrum Berlin für Materialien und Energie - BESSY II, 12489 Berlin, Germany*

[4] *Philipps-Universität Marburg, FB Physik, Molekulare Festkörperphysik, 35032 Marburg, Germany*

[5] *Max Planck Institute for Polymer Research, D-55128 Mainz, Germany*

[6] *University of Leoben, Department Materials Physics, 8700 Leoben, Austria*

[7] *Università di Bologna, Dipartimento di Chimica Fisica e Inorganica, 40136 Bologna, Italy*

[8] *Soochow University, Institute of Functional Nano & Soft Materials (FUNSOM), Suzhou, P. R. China*

[*] Electronic address: `ingo.salzmann@physik.hu-berlin.de`

CONTENTS

I. STRUCTURE SOLUTION OF THE PFP/SIO$_x$ THIN-FILM PHASE (TFP)

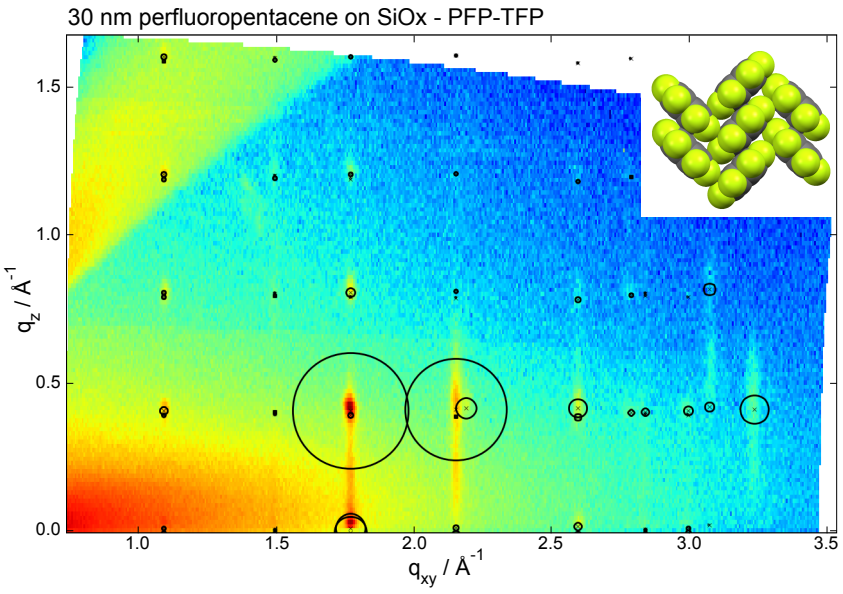

FIG. S1. GIXRD reciprocal space map of a nominally 30 nm thick PFP film grown on native SiO_x indexed with the unit cell reported in Ref. [1]. Circle radii correspond to calculated structure factors of a structure solution derived by following the approach outlined in Ref. [2]; the inset shows a view along the long molecular axis. The data was recorded at beamline W1.1 of the synchrotron radiation source HASYLAB (DESY, Germany) using a LiF point detector. The map consists of 125 horizontal line scans, the incident angle of the primary beam (10.5 keV) was set to $\alpha_i = 0.15°$. Colors correspond to diffraction intensities in logarithmic scale. The Crystallographic Information File (CIF) of the TFP on SiO_x is part of the Supporting Information to this manuscript.

Thin films of nominally 30 nm perfluoropentacene (PFP) on native silicon oxide (SiO_x) substrates grown in a yet unsolved surface-induced thin-film phase (TFP) were investigated by grazing-incidence X-ray diffraction (GIXRD) reciprocal-space mapping, as reported in Ref. [1]. Our study yielded monoclinic ($P2_1/c$) unit-cell parameters of $a = 15.76 \pm 0.02$ Å, $b = 4.51 \pm 0.02$ Å, $c = 11.48 \pm 0.02$ Å, $\beta = 90.4 \pm 0.1°$, which is highly similar to the PFP single-crystal polymorph [3]. A full structure solution was derived following the approach outlined in Ref. [2] yielding a herringbone arrangement of the molecules with almost perpendicularly inclined molecular planes (see Fig. 2a of the main text). The Crystallographic Information File (CIF) of the TFP on SiO_x is part of the Supporting Information to this manuscript.

II. SUPPORTING EXPERIMENTAL DATA

A. Grazing-incidence X-ray diffraction on PFP/HOPG

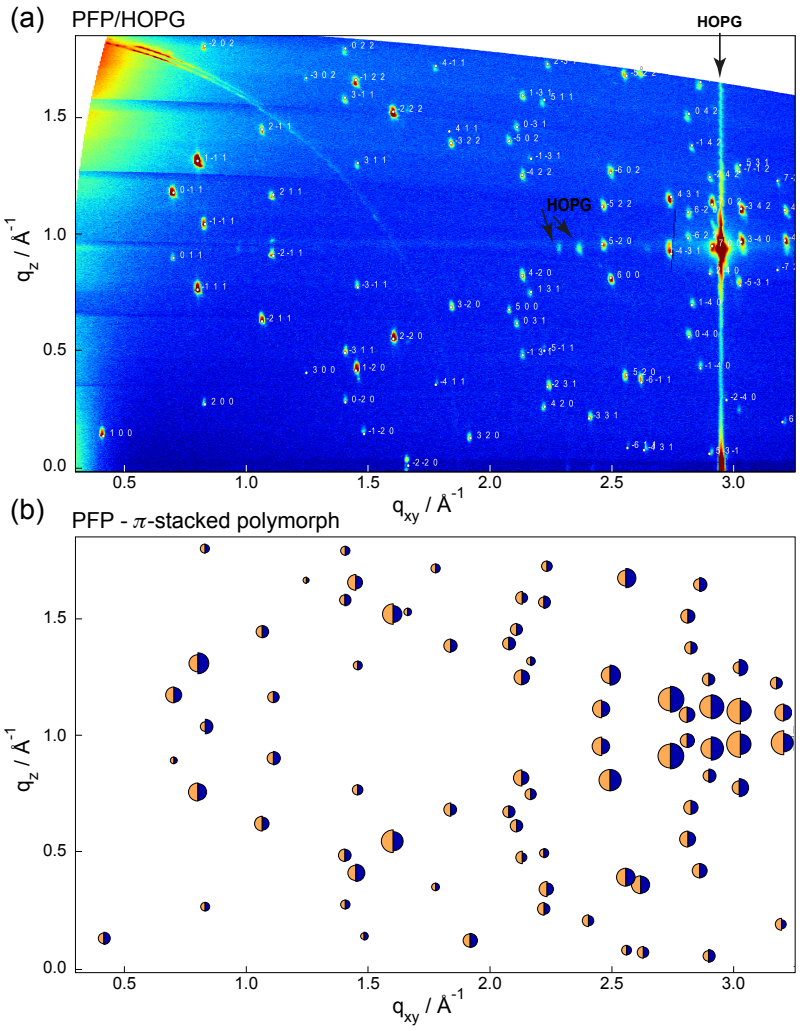

FIG. S2. (a) GIXRD reciprocal space map of the nominally 50 nm thick PFP reference film on HOPG indexed with the π-stacked polymorph (PSP) solved within this work. (b) Comparison of experimental result (orange half-circles) with the full structure solution derived by force-field calculations (blue half-circles) following the approach outlined in Ref. [2]; blue and orange half-circle areas compare the calculated to experimental structure factors; values normalized the (600) peak. In contrast to the result on graphene (Fig. 1c of the main text), strong substrate contributions occur from HOPG. Differences in peak-intensity ratios between this map and that of PFP/graphene (Fig. 1c of the main text), *e.g.*, the (2-10) and (1-10) reflections near the center) reflect the non-local anisotropy of the graphene substrate and point towards epitaxial growth of PFP.

B. X-ray diffraction rocking curve analysis of PFP/graphene

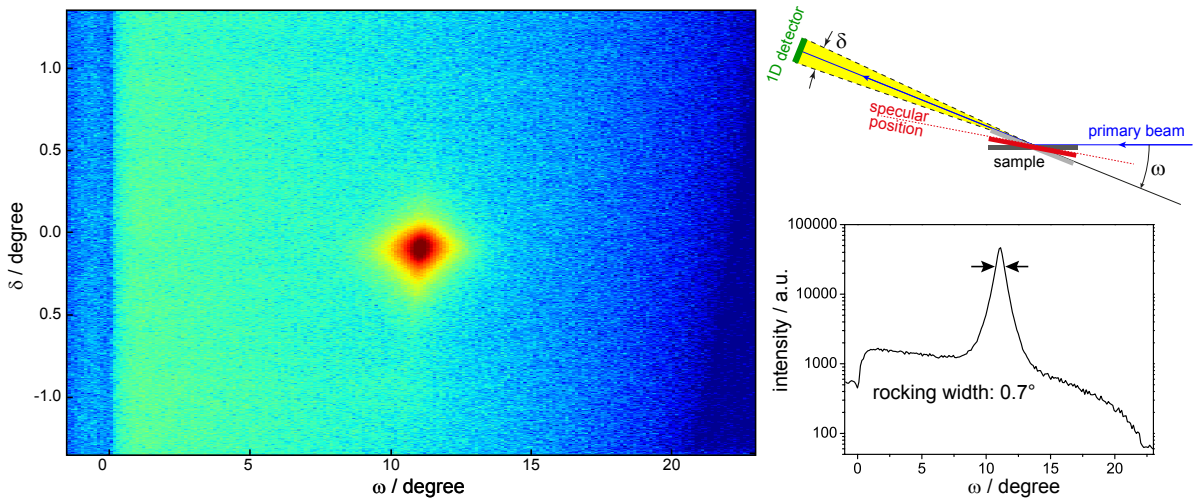

FIG. S3. X-ray diffraction rocking scan on the (002) reflection of the PFP/graphene sample as measured with the 1D detector (left) and as line-scan generated by an integration of 1° along δ around the detector center $\delta = 0°$ (right). The detector position and the primary beam are fixed in space ($q_z = 2.056\,\text{Å}^{-1}$) and the sample is rotated around ω, as illustrated in the sketch of the experimental geometry. From a fit of the line-scan with a Voigt-function the low rocking width of 0.7° is found.

C. Impact of single-layer graphene coating on PFP growth

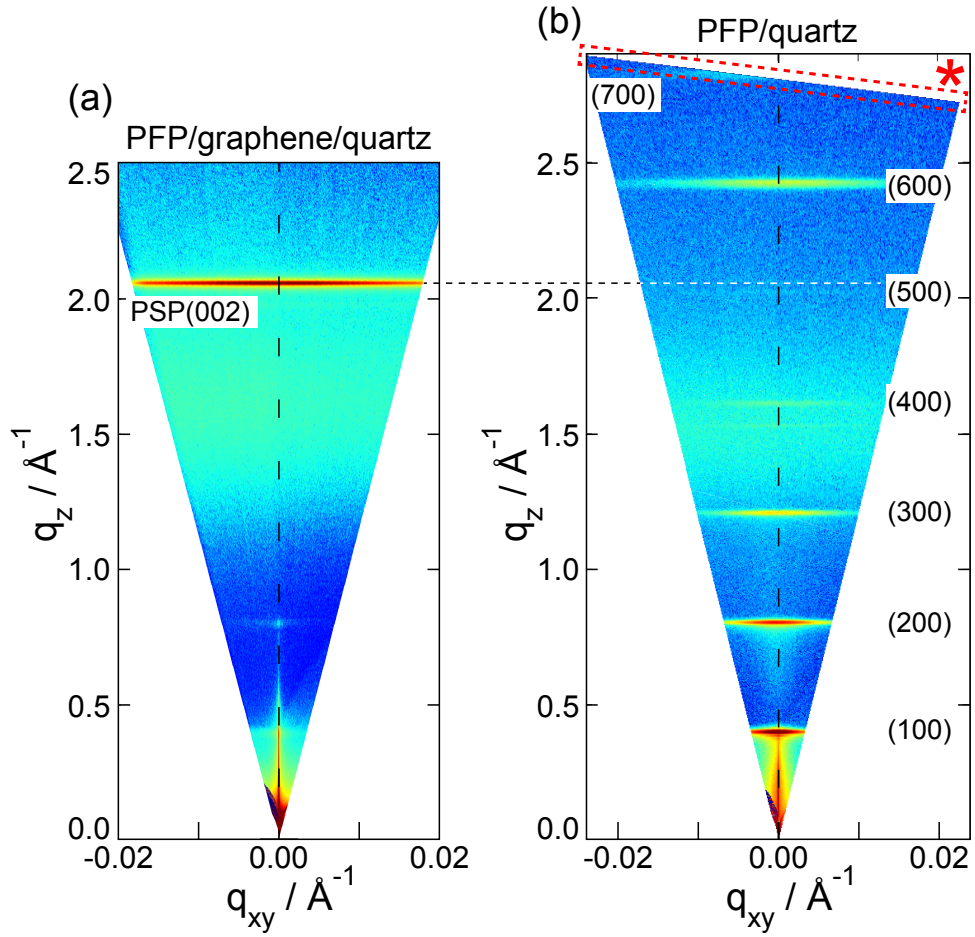

FIG. S4. (a) Specular XRD scan of nominally 30 nm PFP on graphene coated quartz, where lying growth in the π-stacked polymorph (PSP) is found (*cf.* Fig. 1b of the main text), as compared to nominally 30 nm PFP on pristine quartz (b), showing growth of standing PFP in herringbone arrangement. These data demonstrate that even one layer of graphene on quartz drastically changes the stacking of PFP from herringbone to π-stacking. The horizontal dotted line indicates the position on the lying π-stacked PSP(002) reflection dominant on graphene coated quartz (a) and absent on the bare quartz substrate (b). The red star in (b) marks the signature of the last photons diffracted at beamline W1.1 during the final shutdown of the storage ring DORIS on October 22, 2012.

D. Pentacene/HOPG: similarities and dissimilarities of growth

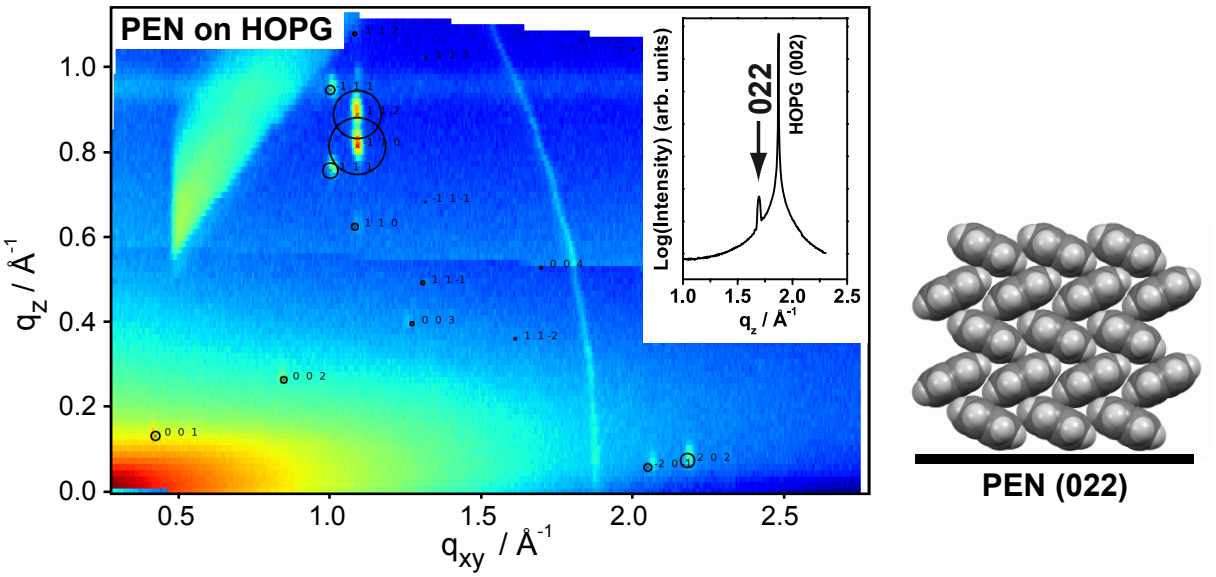

FIG. S5. GIXRD reciprocal space map of a nominally 50 nm thick pentacene (PEN) film on HOPG with the corresponding specular diffraction (inset), where only one single orientation is found (beamline W1.1 HASYLAB, DESY using a beam energy 10.5 keV and a LiF point detector; map is composed of 85 line scans). In analogy to what is found for metal substrates [4–7] and (residue-free) graphene [8, 9], PEN is observed to grow with the long molecular axis parallel to the substrate in a herringbone (HB) polymorph [10] showing a (022) texture, as illustrated in the schematic representation of the respective structure (right). In contrast to PFP, the HB polymorph occurs even though the monolayer on HOPG [11] and metals [5] is clearly formed by flat-lying molecules. For HOPG, it is reported that the flat-lying (physisorbed) PEN monolayer is transformed into the HB-polymorph upon subsequent growth due to a weaker interaction of PEN with the substrate than with neighboring molecules [12] leading to an upward tilting of the molecular planes, which increases the packing density by 1/3 to that of the HB-polymorph. Even if the PEN wetting layer is flat-lying *and* chemisorbed, as it is the case for metallic substrates [5, 6], the transition to HB structure occurs, which is contrary to PFP that retains its initial orientation in further growth, as shown in the main text.

E. Ultraviolet photoelectron spectroscopy (UPS) data

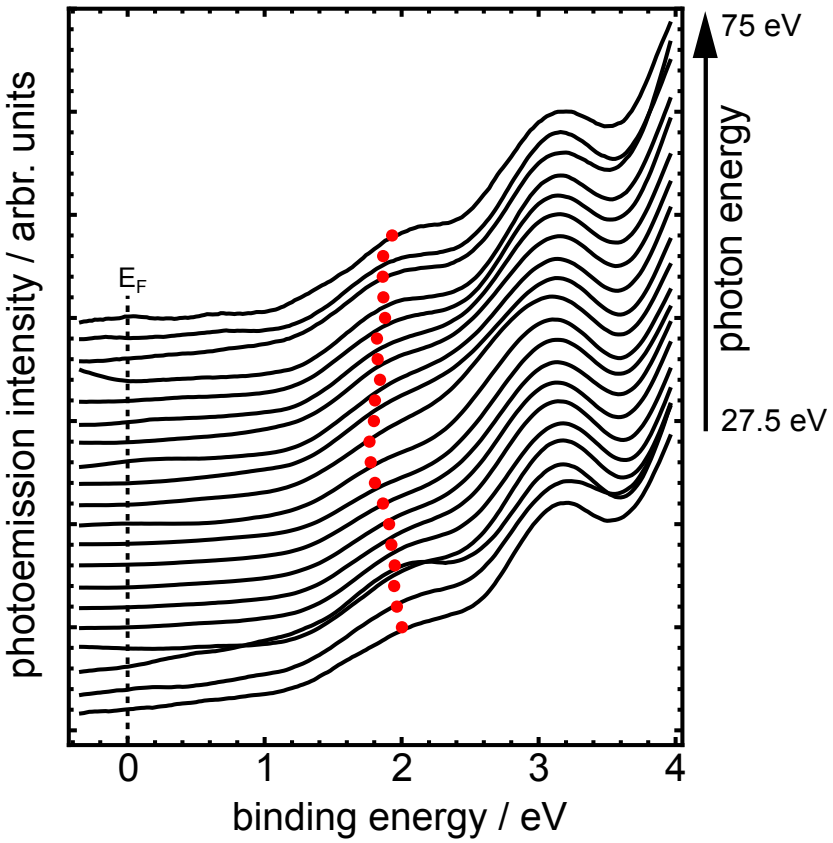

FIG. S6. UPS data in the range of the PFP HOMO recorded at normal emission for a nominally 10 nm thick PFP film on HOPG under a variation of the energies photon energy; data was corrected for synchrotron radiation flux and treated with a 4-th order Savitzky-Golay filter, which was necessary for subsequent numerical differentiation of the data (Fig. 4 of the main text). Dots indicate HOMO peak centers determined from the maxima of the 2^{nd} derivatives of the photoemission data.

F. Quantitative NEXAFS analysis of PFP/HOPG

To assess information on the molecular orientation independent from X-ray diffraction, near edge X-ray absorption fine structure (NEXAFS) spectroscopy was performed on a film of 50 nm PFP on HOPG, as shown in the main text in Figs. 1d - e. Fig. S7 (grey curve) shows a strong π^*-resonance of the HOPG substrate at 285.3 eV, which overlaps with a strong PFP resonance leading to intensity offsets in PFP/HOPG spectra. Therefore, to correct for substrate contributions to the recorded signal, an appropriately weighted spectrum of the clean substrate was subtracted. For that purpose, the relative ratio of the PFP peaks was determined using a PFP/SiO_x reference sample (Fig. S7, black curve), where no substrate contributions exist at the C1s edge. The weighting of the subtracted HOPG signal was chosen such, that the resulting spectrum exhibited the same relative ratio of the PFP peaks as found for the PFP/SiO_x reference. To improve the statistical reliability of the calculated average molecular orientation, three different π^*-resonances were analyzed and the derived angle was averaged.

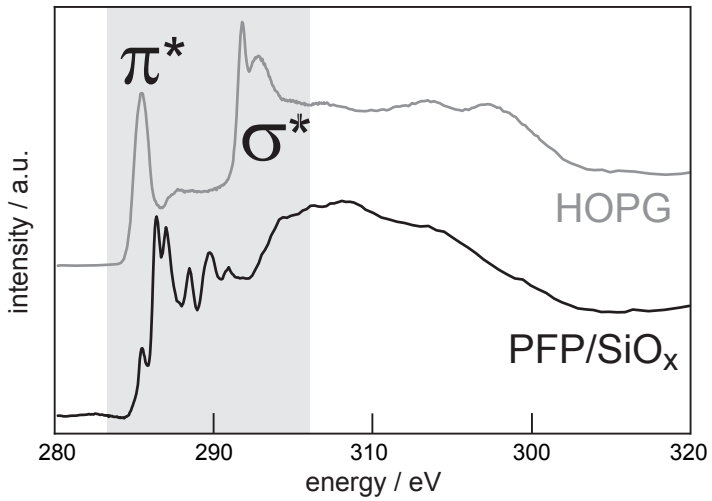

FIG. S7. NEXAFS measurements of the HOPG substrate (grey curve) in the region of strong PFP resonances (black curve), as shown for a nominally 50 nm thick PFP/SiO_x as reference. On SiO_x, no substrate contributions occur at the C1s edge, which allows determining the relative intensity ratio of the PFP peaks for correcting for substrate contributions in our PFP/HOPG measurements (Fig. 1d of the main text). This was done by subtracting an accordingly weighted spectrum of the HOPG substrate such, that the resulting spectra exhibited the characteristic intensity ratio of the PFP/SiO_x reference.

As apparent from Fig. 1d of the main text, the resulting spectra show a strong dichroism, indicating preferred molecular orientation. As the first resonances are known to correspond to excitations of C1s electrons into unoccupied π^* orbitals (π^*-resonances) and the corresponding transition dipole moments are oriented perpendicular to the molecular plane, high intensity of those resonances occurs at grazing incidence (30°) for a preferentially lying configuration, while high intensity at normal incidence (90°) indicates standing molecules [13]. From Fig. 1d of the main text it is therefore clearly seen that the PFP molecules are preferentially oriented with their molecular plane essentially parallel to the substrate in the π-stacked polymorph (PSP) (*flat-lying molecules*). This is clearly seen by a comparison of the experimental angle-dependence of the π^*-resonance intensity to calculated values, as shown in Fig. 1e of the main text.

The intensity of the π^*-resonances depends on the incident angle θ and is given by:

$$I_{\pi^*} \propto P\cos^2\theta\left(\frac{3\cos^2\alpha}{2}-\frac{1}{2}\right)+\frac{\sin^2\alpha}{2}, \tag{1}$$

where P represents the polarization factor of the synchrotron light and α the average orientation of the transition dipole moment relative to the surface normal [14, 15]. The quantitative evaluation of the dichroism (Fig. 1e of the main text) yields an averaged tilt angle of $10^\circ \pm 8^\circ$, which is in good agreement with our structure solution from XRD. We note that in a previous study the molecular orientation of PFP multi- and monolayers on Ag(111) were likewise analyzed [13]. In that case, we found averaged tilt angles of $11^\circ \pm 6^\circ$ (multilayer) and $8^\circ \pm 6^\circ$ (monolayer); the larger error margin in the present study is due to the necessary correction of substrate contributions, as outlined in the main text.

G. Raman spectroscopy on PFP/HOPG

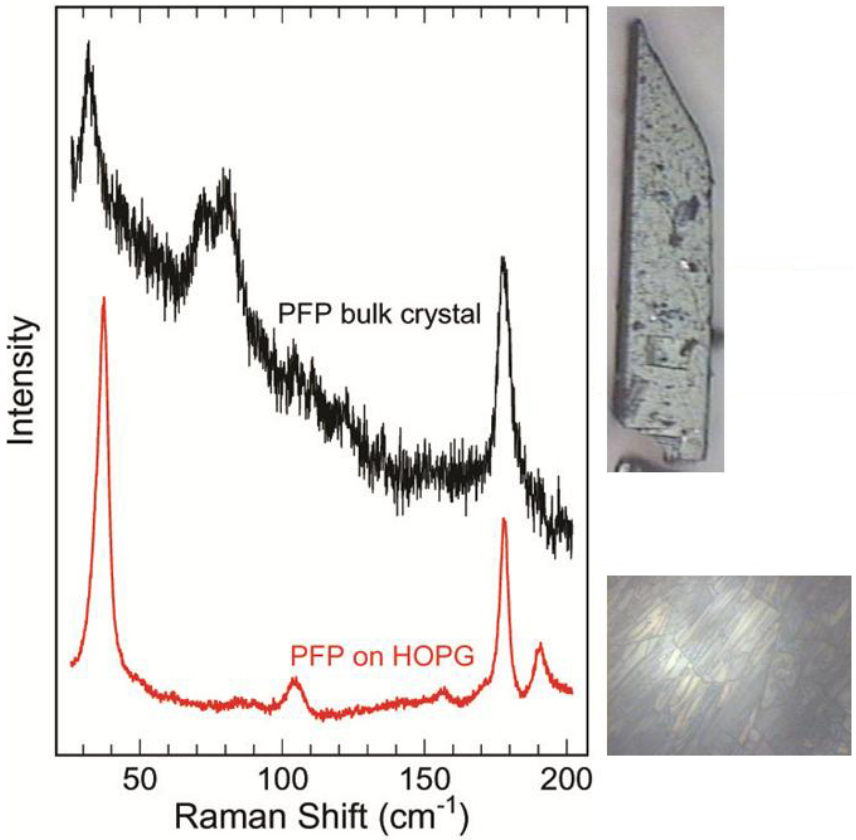

FIG. S8. Typical lattice phonon Raman spectra of a 30 nm PFP film on HOPG (lower trace) compared to that of the PFP single-crystal (upper trace). Optical microscopy images of the respective samples are shown on the right.

Fig. S8 depicts lattice-phonon Raman spectra of a nominally 30 nm thick PFP film and of a (prism-like) single crystal of PFP as reference. Raman spectroscopy directly probes inter-molecular modes, *i.e.*, collective translational or rotational motions of the molecules in the unit cell. Such modes, which produce Raman shifts in the wavenumber range of $\approx 10 - 150$ cm^{-1}, are highly sensitive to changes in the molecular packing.

The central point emerging from our Raman analysis is that we clearly observe two different spectra below 150 cm^{-1}, which indicates two different lattice structures occurring in the thin film on HOPG and in the single crystal. The intense peak at ≈180 cm^{-1}, instead, is persistent in both structures, as it is a molecular vibration and not a lattice mode.

An interesting observation is that the phonon spectrum of single crystalline PFP is significantly weaker than that of the 30 nm film. This is not due to the different laser line used, as under the very same conditions, in fact, pentacene crystals show a much more intense signal. Therefore, the spectrum is *intrinsically* weak, which is especially true for the peak at lowermost wave number, the eigenvector of which describes librations about the axis with the largest moment of inertia (*i.e.* the axis perpendicular to the molecular plane). This mode is the most prominent feature in the spectral profile of the film and is strikingly stronger than its corresponding lattice phonon in the single crystal spectrum. Fully in-line with our findings from XRD and NEXAFS, the flat-lying molecular orientation of the PFP molecules on HOPG explains the large intensity of this mode, which is polarized within the molecular plane.

Experimental details. For Raman spectroscopy on PFP/HOPG, a film of nominally 30 nm PFP and PFP single-crystals as reference (source powder as received from the manufacturer) were investigated with an optical microscope (Olympus BX40) interfaced to a Horiba-Jobin Yvon T64000 Raman spectrometer (50× or 100× objectives), which allowed obtaining a spatial resolution of $\approx$1 μm and a theoretical field depth ranging from $\approx$7 to 25 μm. The laser excitation wavelengths (krypton laser) were 752.5 and 676.4 nm for the single-crystal and the thin film measurements, respectively. The incoming power was reduced with a neutral filter of sufficient optical density to prevent sample damage. For more details on the spectroscopic characterization see Ref. [16].

III. METHODOLOGICAL REMARKS

A. X-ray diffraction geometries

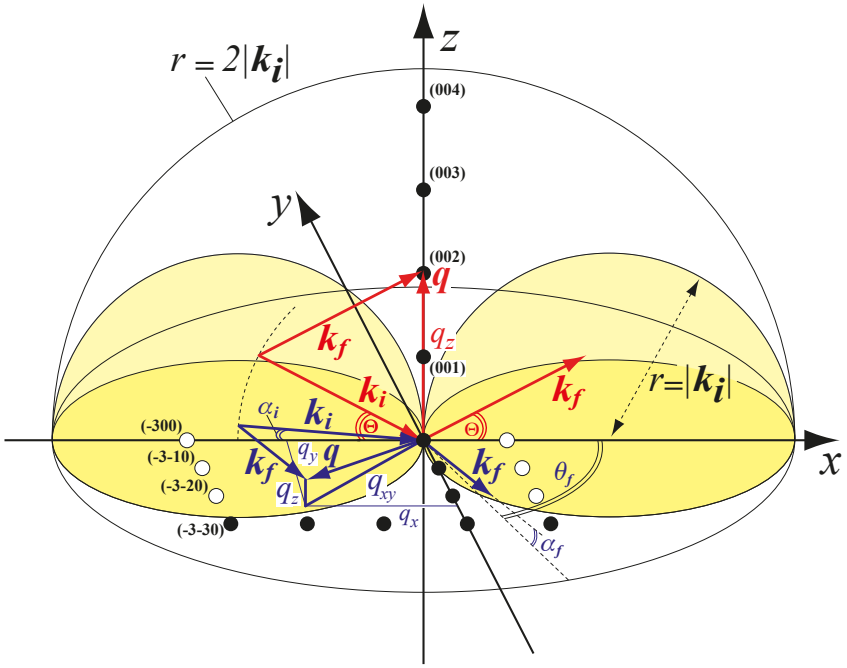

FIG. S9. Illustration of the main experimental geometries for X-ray diffraction (XRD) used in this work; $\mathbf{k_i}$ and $\mathbf{k_f}$ are the wave vectors of the incident and the diffracted beam, respectively. $\mathbf{q}$ denotes the scattering vector, q_{xy} and q_z its parallel and vertical components for *specular XRD* (red vectors) and *grazing-incidence X-ray diffraction* (GIXRD, blue vectors). The uncolored regions of the half-sphere of radius $2k_i$ are experimentally accessible in these geometries, whereas the yellow half-spheres (Laue-zones, radius k_i) are not. Points with indices *hkl* denote reciprocal lattice points of a given crystal structure that are accessible (black) or inaccessible (white) at the given sample orientation. Specular scans (Fig. 1b of the main text) are performed with q_z varying along the z-axis through symmetrically increasing Θ for $\mathbf{k_i}$ and $\mathbf{k_f}$. In contrast, GIXRD-scans are performed at *fixed* incident angle α_i and the diffraction intensity is recorded as function of the detector angles θ_f and α_f, which are transformed into q_{xy} and q_z in the representation of a reciprocal space map (Fig. 1c of the main text). A *GIXRD texture-analysis scan* (Fig. 3 of the main text) is performed at fixed values of q_{xy} and q_z, that is, at fixed detector angles θ_f and α_f, while rotating the sample around the texture axis (e.g., the z-axis). For fiber-textured films (also denoted as *2D-powder*) the reciprocal lattice points degenerate to circles around the fiber axis and a reciprocal space map there contains all accessible information on the crystal structure.

B. GIXRD texture analysis in 2+2 geometry

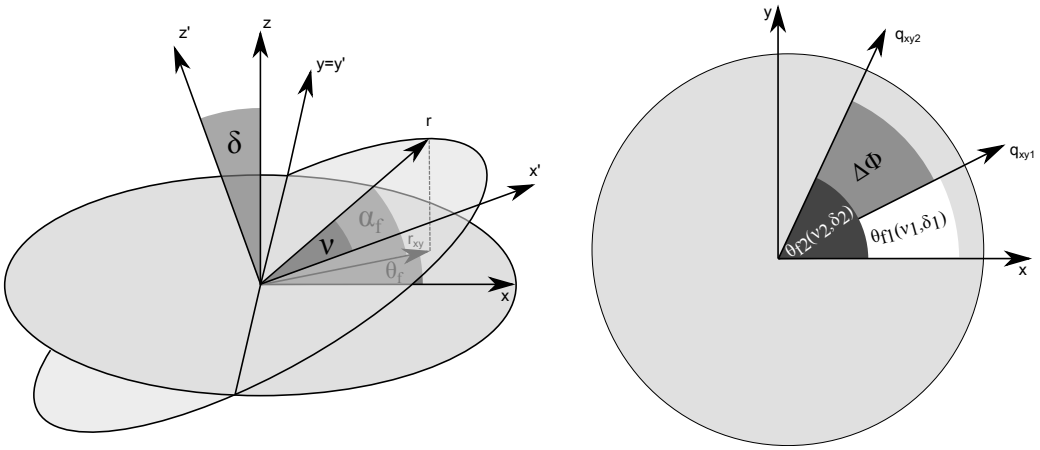

FIG. S10. Left: sketch of the experimental 2+2 geometry used for all X-ray diffraction experiments in this work. The vector $\vec{r}$ points towards the detector at position (δ, ν). The azimuth and elevation angles in the sample coordinate system are θ_f and α_f. Right: projection of two scattering vectors onto the sample surface. To determine the correct azimuthal angle between $\vec{q_1}$ and $\vec{q_2}$, that is, to correctly relate azimuthal scans carried out in GIXRD texture analysis on a 2+2 goniometer [17], ϕ has to be realigned by $\Delta\phi$ (Eq. 3); for further details see Ref. [18].

If azimuthal relationships between two different lattice planes (scattering vectors) are measured in the 2+2 geometry, it must be considered that the projection of the scattering vector onto the sample depends on the position of the detector (Fig. S10, left). Let $\vec{r}$ point towards the detector, which is at position (δ, ν), with its projection $\vec{r_{xy}}$ onto the sample surface; θ_f and α_f are the azimuth and the elevation angles in the sample coordinate system. To measure the correct azimuth the rotation angle around the sample-surface normal (ϕ) has then to be realigned depending on δ and ν.

In the surface-reference frame, $\vec{q}$ is given as

$$\vec{q} = \begin{pmatrix} \cos\nu\cos\delta - \cos\alpha_i \\ \sin\nu \\ \cos\nu\sin\delta + \sin\alpha_i \end{pmatrix} \tag{2}$$

For each scattering vector the azimuthal angle ($\theta_f = \angle(\vec{q}_{xy}, \vec{e}_x)$) in the (x,y)-plane is calculated. The differences $\Delta\phi_n$ relative to θ_f of the first scattering vector then gives the necessary correction (Fig. S10, right), *i.e.* the first experiment defines the zero point of ϕ on the sample.

$$\begin{aligned}
\theta_{f1} &= \arctan\left(\frac{q_{1y}}{q_{1x}}\right) = \arctan\left(\frac{\sin\nu_1}{\cos\nu_1\cos\delta_1 - 1}\right) \\
\theta_{fn} &= \arctan\left(\frac{q_{ny}}{q_{nx}}\right) \arctan\left(\frac{\sin\nu_n}{\cos\nu_n\cos\delta_n - 1}\right) \\
\Delta\phi_n &= \theta_{f1} - \theta_{fn}
\end{aligned} \tag{3}$$

Note that above formulas are only valid for point detectors, or, rather, the zero channel of a one-dimensional detector, as used within this work for the GIXRD texture analysis of PFP on HOPG.

C. Relation between the PSP (001) and (00-1) textures

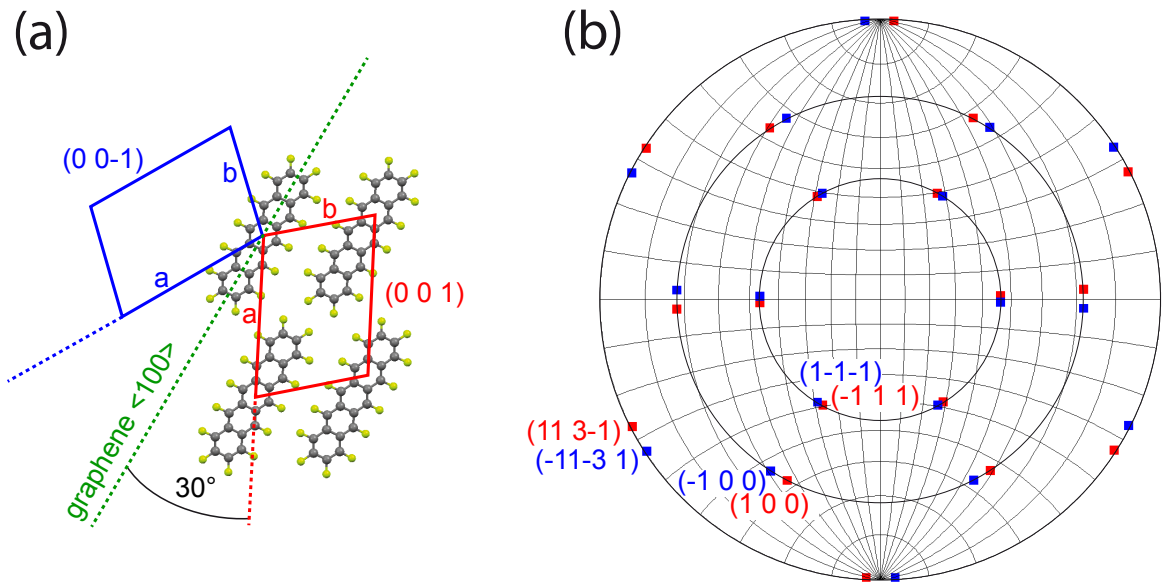

FIG. S11. (a) Suggested alignment of the PFP molecules with the <100>-directions of the graphene substrate in the observed (001)-texture of the PSP, as discussed in the main text (red unit cell). There, the angle between the a-axis and <100> is (almost) exactly 30°. Likewise, growth in the (00-1) mirror-texture in laterally separated domains is expected (blue unit cell), which exhibits, by nature, an identical out-of-plane lattice spacing (i.e., specular diffraction feature). (b) Stereographic projection in Wulff-net representation of the calculated reflections investigated by GIXRD texture analysis (Fig. 3b of the main text); analysis performed with the software STEREOPOLE [19]. Despite the triclinic crystal class of the π-stacked polymorph, the reflections of both textures (almost) coincide and cannot be experimentally resolved at the given peak breadth in azimuthal angle. Therefore, mirror-texture cannot explain the observation of 12 instead of 6 reflections. Note that only if the angle between the a-axes of both unit cells depicted in (a) were 30° (instead of 60°), 12 reflections would occur, which then is, however, identical to a molecular alignment with both the <100> and the <210> directions of graphene, and therefore unlikely, as discussed in the main text.

IV. COMPARISON OF THE THREE APPROACHES TO STRUCTURE SOLUTION

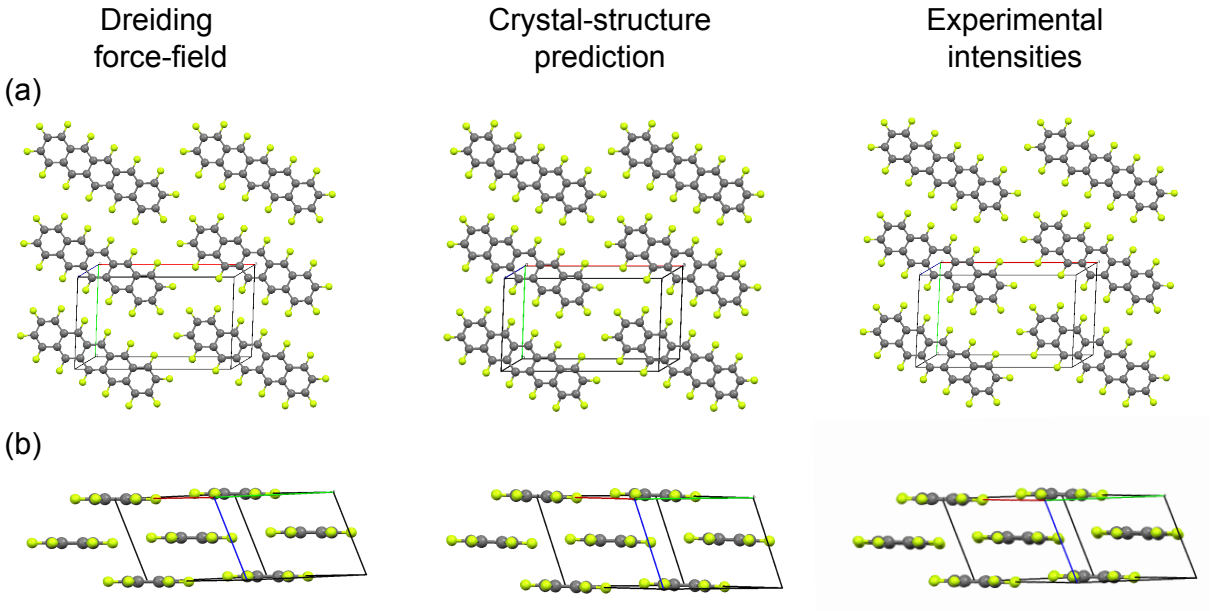

FIG. S12. Comparison of the results of three different approaches to the full structure solution of the PSP. Left: Solution from force-field calculations on rigid molecules confined in the experimentally determined unit cell using the DREIDING force field [20] (following the calculation strategy described in detail in Ref. [2]; see methodology section of the main text). Middle: Low-rank (constrained) solution obtained from crystal-structure prediction methods for the experimentally determined unit cell (see the related methodology section of the main text). Right: Solution from a fit of the molecular orientation against the experimental PFP/HOPG intensities (Fig. S1) using the software package FOX [21]. (a) Top view on the (001)-texture plane. (b) View along the long molecular axes. All three approaches led to essentially identical results.

[1] Salzmann, I.; Duhm, S.; Heimel, G.; Rabe, J. P.; Koch, N.; Oehzelt, M.; Sakamoto, Y.; Suzuki, T. *Langmuir* **2008**, *24*, 7294–7298.

[2] Salzmann, I.; Nabok, D.; Oehzelt, M.; Duhm, S.; Moser, A.; Heimel, G.; Puschnig, P.; Ambrosch-Draxl, C.; Rabe, J. P.; Koch, N. *Cryst. Growth Des.* **2011**, *11*, 600–606.

[3] Sakamoto, Y.; Suzuki, T.; Kobayashi, M.; Gao, Y.; Fukai, Y.; Inoue, Y.; Sato, F.; Tokito, S. *J. Am. Chem. Soc.* **2004**, *126*, 8138–8140.

[4] Lukas, S.; Söhnchen, S.; Witte, G.; Woll, C. *ChemPhysChem* **2004**, *5*, 266–270.

[5] Käfer, D.; Witte, G. *Chem. Phys. Lett.* **2007**, *442*, 376–383.

[6] Käfer, D.; Ruppel, L.; Witte, G. *Phys. Rev. B* **2007**, *75*, 085309.

[7] Koini, M.; Haber, T.; Werzer, O.; Berkebile, S.; Koller, G.; Oehzelt, M.; Ramsey, M. G.; Resel, R. *Thin Solid Films* **2008**, *517*, 483–487.

[8] Lee, W. H.; Park, J.; Sim, S. H.; Lim, S.; Kim, K. S.; Hong, B. H.; Cho, K. *J. Am. Chem. Soc.* **2011**, *133*, 4447–4454.

[9] Berke, K.; Tongay, S.; McCarthy, M. A.; Rinzler, A. G.; Appleton, B. R.; Hebard, A. F. *J. Phys.: Condens. Matter* **2012**, *24*, 255802.

[10] Mattheus, C. C.; Dros, A. B.; Baas, J.; Meetsma, A.; de Boer, J. L.; Palstra, T. T. *Acta Crystallogr C* **2001**, *57*, 939–41.

[11] Chen, W.; Huang, H.; Thye, A.; Wee, S. *Chem. Commun.* **2008**, 4276–4278.

[12] Götzen, J.; Käfer, D.; Wöll, C.; Witte, G. *Phys. Rev. B* **2010**, *81*, 085440.

[13] Marks, M.; Schmidt, C.; Schwalb, C. H.; Breuer, T.; Witte, G.; Höfer, U. *J. Phys. Chem. C* **2012**, *116*, 1904–1911.

[14] Stöhr, J.; Outka, D. A. *Phys. Rev. B* **1987**, *36*, 7891–7905.

[15] Stöhr, J. *NEXAFS Spectroscopy*; Springer: Berlin, 1992.

[16] Brillante, A. et al. *CrystEngComm* **2008**, *10*, 1899–1909.

[17] Smilgies, D. M. *Rev. Sci. Instrum.* **2002**, *73*, 1706–1710.

[18] Moser, A. Ph.D. thesis, Graz University of Technology, 2012.

[19] Salzmann, I.; Resel, R. *J. Appl. Crystallogr.* **2004**, *37*, 1029–1033.

[20] Mayo, S. L.; Olafson, B. D.; Goddard, W. A. *J. Phys. Chem.* **1990**, *94*, 8897–8909.

[21] Favre-Nicolin, V.; Cerny, R. *J. Appl. Crystallogr.* **2002**, *35*, 734–743.

5.8 Article VIII: Thermally activated intermixture in pentaceneperfluoropentacene heterostructures

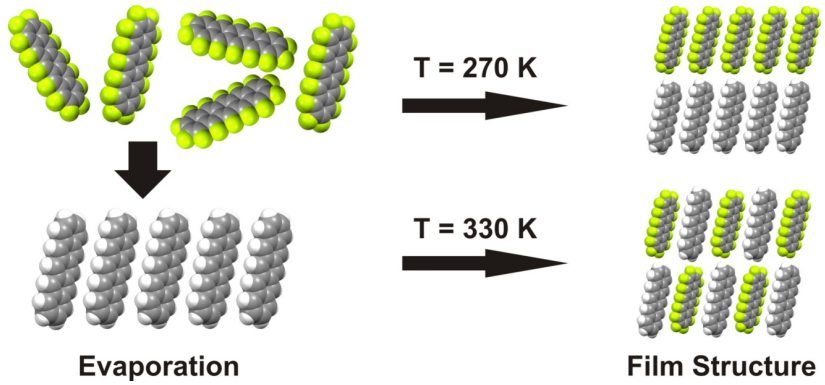

5.8.1 Abstract

Using thermal desorption spectroscopy (TDS) the thermal stability of binary pentacene/perfluoropentacene (PEN/PFP) thin films has been investigated for various preparation protocols. Variation of stoichiometry ratio reveals a significantly enhanced thermal stability in comparison to the single compounds only for films with equimolar stoichiometry. The stabilization also depends on the preparation method and was found for co-deposition as well as for multi-stacks and subsequently grown PEN/PFP-stacks but not for stacks grown in the reversed order. By systemically varying the substrate temperature during deposition, we prove that the resulting intermixture is caused by a thermally activated diffusion during film growth and not due to post-deposition diffusion induced upon heating during TDS measurements. The different extents of thermal stabilization are discussed in the context of the film morphology studied by means of atomic force microscopy (AFM). For complementary information, optical absorption spectra of the heterostructures are analyzed, where the arisal of new absorption bands and the extinction of excitonic bands existing in the pure compounds are identified as decisive criteria to judge the efficiency of intermixture.

5.8.2 Methods

Atomic Force Microscopy, Organic Molecular Beam Deposition, Thermal Desorption Spectroscopy, UV/Vis Spectroscopy, X-Ray Diffraction

5.8.3 Own Contribution

I have prepared all samples and planned and conducted all experiments. I have written the major part of the manuscript, while Gregor Witte has helped to interpret the data as well as to improve the manuscript.

THE JOURNAL OF CHEMICAL PHYSICS **138**, 114901 (2013)

Thermally activated intermixture in pentacene-perfluoropentacene heterostructures

Tobias Breuer and Gregor Witte[a)]
Molekulare Festkörperphysik, Philipps-Universität Marburg, D-35032 Marburg, Germany

(Received 18 December 2012; accepted 26 February 2013; published online 18 March 2013)

Using thermal desorption spectroscopy (TDS) the thermal stability of binary pentacene/perfluoropentacene (PEN/PFP) thin films has been investigated for various preparation protocols. Variation of stoichiometry ratio reveals a significantly enhanced thermal stability in comparison to the single compounds only for films with equimolar stoichiometry. The stabilization also depends on the preparation method and was found for co-deposition as well as for multi-stacks and subsequently grown PEN/PFP-stacks but not for stacks grown in the reversed order. By systemically varying the substrate temperature during deposition, we prove that the resulting intermixture is caused by a thermally activated diffusion during film growth and not due to post-deposition diffusion induced upon heating during TDS measurements. The different extents of thermal stabilization are discussed in the context of the film morphology studied by means of atomic force microscopy (AFM). For complementary information, optical absorption spectra of the heterostructures are analyzed, where the arisal of new absorption bands and the extinction of excitonic bands existing in the pure compounds are identified as decisive criteria to judge the efficiency of intermixture.
 [http://dx.doi.org/10.1063/1.4795004]

I. INTRODUCTION

Cocrystallization of different molecules is an interesting approach to tune physical properties of the target materials. In pharmaceutical industry, for example, cocrystals of active components of drugs allow to improve certain properties such as solubility or ease of formulation without altering the inherent physiological effects of the key ingredients.[1,2] On the other hand, when properties emerge not just from the activity of individual molecules but from their collective arrangement, cocrystallization allows for engineering of materials with new electronic functionalities which is of particular interest for applications in organic electronics.[3] Striking examples are molecular charge transfer salts such as TTF/TCNQ which exhibit strong intermolecular electronic coupling.[4] This causes not only a substantial thermal stabilization of the mixed crystal compared to the respective single compounds but also results in high room temperature conductivity as well as the appearance of Peierls transitions at low temperature.[5] Depending on the chemical structure of the molecular entities the cocrystals are stabilized by various types of interaction ranging from strong Coulomb forces in case of partial ionization, over hydrogen bonds to weak van der Waals forces which in each case reveal characteristic interaction distances.[6] Of particular interest in the field of organic semiconducting materials is a face-to-face stacking of aromatic molecules in order to improve the overlap of π-orbitals and to achieve an efficient charge transport.[7] One successful approach along this direction has been demonstrated by cocrystallization of molecular semiconductors with bifunctional molecules acting as cocrystal former which are stabilized by hydrogen bonds and result in an improved π-stacking.[8]

Another type of interaction occurs between π-conjugated molecules and their perfluorinated analogs since fluorination causes an inversion of the quadrupole moment which in turn favors a coplanar stacking.[9,10] The resulting thermal stabilization has been demonstrated for small acenes, such as benzene and naphthalene, where melting points of equimolar cocrystals with the belonging fluorinated acenes increase by 19 K and 55 K, respectively.[11,12] Comparing the intermolecular distances occurring in naphthalene/octafluoronaphthalene cocrystals with that in pure napthalene crystals[13] suggests that the coplanar stacking in cocrystals is not brought about by hydrogen bonds but is due to quadrupolar coupling. Though being interesting model systems the small acenes are not qualified for device applications because of their large HOMO-LUMO band gap and high vapor pressure which limits their handling to low temperatures. By contrast, the larger pentacene (PEN, $C_{22}H_{14}$) and its perfluorinated sibling perfuoropentacene (PFP, $C_{22}F_{14}$) are well known organic semiconductors exhibiting excellent *p*- and *n*-type charge carrier mobilities, respectively.[14,15] Therefore, a well-directed cocrystallization of both materials appears to be promising for the realization of bipolar organic transistors. This system is additionally favored by the structural compatibility of both almost equally sized molecules which exhibit similar crystal structures and lattice energies in their pure phases.[16–18] Although evidence for local cocrystalline ordering has been observed in XRD data of co-evaporated PEN/PFP films[19,20] and the formation of charge transfer (CT) excitons was found in the optical absorption spectra of the binary films reflecting strong intermolecular electronic coupling,[21,22] a complete structural analysis of the cocrystalline phase has not yet been

a)Electronic mail: gregor.witte@physik.uni-marburg.de

possible. One reason is the very poor solubility of extended acenes which strongly decreases with the number of aromatic rings and thus hampers the cocrystallization from solution like in the case of naphthalene/octafluoronaphthalene.[12,23] Also a crystallization from melting phase is not feasible because of thermal disintegration of such extended acenes at elevated temperatures,[24] and instead requires evaporation of both molecular compounds.

Though this allows the fabrication of binary organic films with preset nominal stoichiometry, an achievement of desired crystalline ordering is even more complex. For example (spatial) inhomogeneities of the relative stoichiometry upon codeposition may lead to phase separation of both molecular components.[3] Even if intermixture is energetically favored according to consideration of the free energy of solid solutions, the formation of molecular cocrystals requires besides a positional ordering also orientational and if applicable conformational ordering.[25] In order to achieve a solid intermixture the ordering process requires a sufficient diffusivity of the molecular entities which is controlled by the substrate temperature. Especially in the case of acenes with distinct shape anisotropy, interdiffusion is a thermally activated process so that the extent of intermixture[26] in binary films is expected to depend sensitively on the growth conditions. On the other hand with increasing substrate temperature the vapor pressure of molecular solids increases and eventually leads to a competing sublimation. Therefore, a precise knowledge of the accessible temperature range for thermally induced ordering of mixed films is of key interest.

In this study we have analyzed the stabilization of binary PEN/PFP films grown on SiO_2. Using thermal desorption spectroscopy (TDS) we were able to identify a mixed phase that is thermally stabilized compared to the respective pure phases. To monitor the thermally activated interdiffusion within the binary films and to distinguish between interdiffusion during film growth and upon subsequent heating (post-deposition diffusion), films were also prepared at different substrate temperatures. Since both molecules grow with upright orientation on SiO_2 and exhibit rather similar interlayer spacings,[27,28] a refined structural characterization by out-of-plane XRD diffraction is hampered. Therefore, optical absorption spectroscopy was utilized to monitor the appearance of the CT-exciton state in order to complementary characterize the degree of intermixture while the resulting morphology was analyzed by means of atomic force microscopy (AFM). Moreover, since previous studies have shown that the morphology and roughness of such binary films depend on the order of evaporation and the stoichiometry ratio of both molecules,[27] systematic measurements were carried out for films prepared differently either by evaporation of alternating stacks, multistacks or co-evaporation.

II. EXPERIMENTAL

All PFP (Kanto Denka Kogoyo Co. LTD, purity ≥ 99%) and PEN (Sigma Aldrich, purity ≥ 99.9%) films were grown under ultrahigh-vacuum (UHV) conditions by organic molecular beam deposition from an aluminum crucible of a resistively heated Knudsen cell at deposition rates of 8 Å/min,[29] monitored by quartz crystal microbalance (QCM). For thermal desorption spectroscopy (TDS) measurements and morphological studies films were grown onto SiO_2 substrates which were prepared by rinsing in ethanol and acetone, followed by heating in UHV to 500 K for 30 min. Additionally, thin films of 30 nm thickness of the single compounds (60 nm in total) were grown onto glass microscope slides in order to perform optical transmission absorption spectroscopy. If not otherwise stated all samples were prepared at a temperature of 330 K to enhance the smoothness and crystalline size of the thin films and simultaneously prevent decreasing sticking coefficients.[30] The thermal stability of the various films was characterized by TDS, using a quadropole mass spectrometer (Balzer QMG 220) with a Feulner cup positioned close to the sample surface. The spectra were acquired by recording the mass signal of the double-charged PFP molecule ion (M^{++}, $m/z = 265$ amu) and the single-charged PEN molecule ion (M^{+}, $m/z = 278$ amu) during a computer-controlled linear increase of the substrate temperature from 300 to 500 K with a heating rate of $\beta = 0.5$ K/s. To provide reliable temperature measurements, a K-type thermocouple was attached directly to the sample surface. Due to the detection of differently charged molecule ions of both molecular materials, the ion signals of PEN and PFP cannot be compared directly. To account for these differences in absolute signal intensity and at the same time allow adequate visualization, the signals were scaled such that PEN films exhibit twice the intensity as PFP films of equivalent thickness, except for the comparison of single compound spectra (Figs. 1(a) and 1(b)), where for both compounds the same intensity scale was applied. The film morphology was characterized by atomic force microscopy (AFM, Agilent SPM 5500) operated in

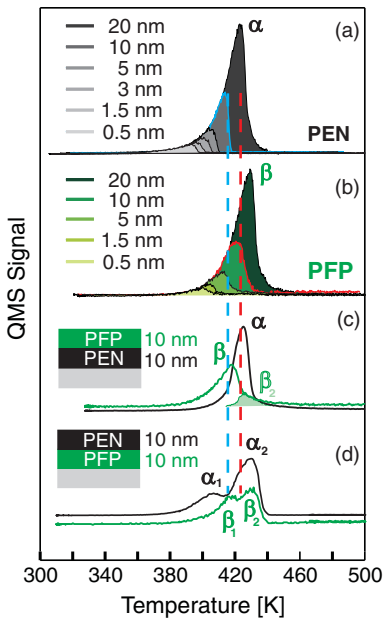

FIG. 1. Series of thermal desorption spectra of unitary and stacked PEN and PFP films grown on SiO_2: (a) pure PEN and (b) pure PFP films of different thickness, stacks of (c) 10 nm PFP grown onto 10 nm PEN and (d) 10 nm PEN grown onto 10 nm PFP. Black and green curves denote the mass signal of the single-charged PEN molecule ion ($m/z = 278$ amu) and double-charged PFP molecule ion ($m/z = 265$ amu), respectively.

tapping mode at ambient conditions. A UV/Vis spectrophotometer (Agilent 8453) was utilized to characterize the optical properties of the films. The crystalline orientation of selected samples was determined from XRD data acquired with a diffractometer (Panalytical XPert Pro) using Cu Kα radiation ($\lambda = 1.54056$ Å) and a PiXcel detector (results presented in the supplementary material[41]).

III. RESULTS

A. Stacked layers

1. Thermal stability

To provide reference data for the thermal stability of PEN and PFP films, at first TD-spectra of the respective pure components were recorded. As depicted in Figs. 1(a) and 1(b), each of these films exhibits one prominent desorption peak of which intensity increases with film thickness, hence reflecting multilayer desorption.[31] Unlike the case of organic films grown on metals no further, monolayer-related desorption signal occurs on the inert SiO_2 surface. According to the zeroth-order kinetics of multilayer desorption the mass signal increases exponentially with temperature and reveals a sudden drop upon completed film desorption. Consequently, the temperature of this *tearing edge* increases with film thickness while the ascending peak flank remains constant. Though sublimation enthalpies can be obtained from a quantitative leading edge analysis of the multilayer desorption signals, this approach is, however, hampered in the presence of overlapping peaks (which have been observed for mixed films as discussed below). Therefore, we have used the temperatures of the tearing edges of films with known thickness to enable a qualitative comparison of the thermal stability of mixed and pure films. To ensure precise temperature measurements and avoid inaccuracies due to poor thermocouple contacts, the TD measurements were carried out on the identical sample and transferring between individual preparations and measurements was obviated as far as possible.[32] Note that this is made possible by a residue-free desorption of multilayers yielding clean SiO_2 surfaces after heating. *Ex situ* AFM measurements employing shadow masks yield an accuracy of the film thickness determination by means of QCM of better than ± 1 nm while the temperature of tearing edges of nominal identical film compositions are reproducible within of ± 2 K in repeated film preparations. Comparing the TD-spectra of pure PEN and PFP films clearly reveals an increase of the position of the tearing edge, T_E, with film thickness but also a somewhat larger thermal stability for PFP (d = 0.5 nm: T_E(PEN) = 394 K and T_E(PFP) = 402 K, d = 20 nm: T_E(PEN) = 424 K and T_E(PFP) = 434 K) which might be attributed to the larger mass of PFP.

Next we have analyzed the TD-spectra of sequentially deposited stacks. Note that these stacks can be produced in a different manner: either by deposition of PFP on top of a PEN layer (PFP/PEN) or vice versa (PEN/PFP). The belonging TD-spectra of such binary stacks consisting in each case of 10 nm layers of both molecular materials are depicted in Figs. 1(c) and 1(d). For the PFP/PEN-stack only one PEN desorption peak (denoted as α) is found. Its tearing edge appears shifted towards higher temperatures by about 10 K compared to a pure PEN film of same thickness (indicated by blue dashed line). This stabilization might be related to a capping effect due to the PFP adlayer which effectively reduces the evaporization of PEN. Such an effect has been reported previously for diindenoperylene films encapsulated by sputtered aluminum oxide layers.[33] By contrast, the peak maximum of the simultaneously measured PFP desorption signal (denoted as β) appears at a distinctly lower temperature than a pure film of same thickness (indicated by red dashed line). A closer inspection reveals, however, an additional weak shoulder (denoted as β_2) at the same temperature as the PEN signal. This indicates the presence of two different desorption channels: One which represents desorption of a pure molecular film that is not influenced by the presence of the different compound and a hetero-peak with enhanced thermal stability, caused by intermixture and mutual interaction between both compounds. The lower desorption temperature of peak β compared to the pure PFP film of 10 nm thickness thus indicates that only a small fraction of PFP molecules is stabilized by an intermixture which effectively reduces the apparent film thickness of the non-stabilized, pure capping layer. Interestingly, this effect is even more pronounced for stacks that are grown in the reverse order, i.e., PEN/PFP. In that case both mass signals exhibit two desorption peaks as depicted in Fig. 1(d). Again we attribute the lower temperature peaks to desorption of non-mixed, single-component regions that appear as films with reduced effective thicknesses, while the dominating higher temperature peaks (α_2 and β_2) occur at the same elevated temperature, hence reflecting a mutual stabilization. This results clearly show that the resulting stabilization depends critically on the order of deposition which can be related to the film morphology presented below. From the intensity ratio of both PEN desorption peaks (α_1 and α_2) and the position of the tearing edge of the first peak, an effective thickness of the non-stabilized fraction of the PEN film of about 2.5 nm can be estimated.

To study the influence of the top-layer thickness on the extension of the stabilization zone, additional TDS measurements were carried out for PEN/PFP stacks with different PEN adlayer thicknesses grown on a 10 nm PFP bottomlayer. Figure 2 compares the corresponding TD-spectra of such stacks with increasing PEN thickness ranging from 5 nm to 20 nm. Clearly, the fraction of the stabilized phase depends on the thickness of the top layer. In case of the 5 nm PEN adlayer only a small fraction of PEN exhibits pure-phase desorption (α_1) while the major part desorbs stabilized (α_2). This finding is reversed in case of a 20 nm adlayer, resulting in a dominating desorption signal of a non-stabilized phase, which exhibits only a shoulder due to desorption of the stabilized phase. A quantitative inspection of Fig. 2(b) yields for the desorption peaks of both PEN phases (α_1 and α_2) a ratio of about 1:3 which suggests an extension of the stabilized PEN zone of about 7 nm. For the 20 nm PEN toplayer the position of the tearing edge of the stabilized PEN phase (α_2) is identical to that of a 10 nm toplayer, suggesting that an equivalent number of layers had intermixed. This is further corroborated by the ratio of the desorption signals of the stabilized and non-stabilized peaks which indicates that about 1/3 of the

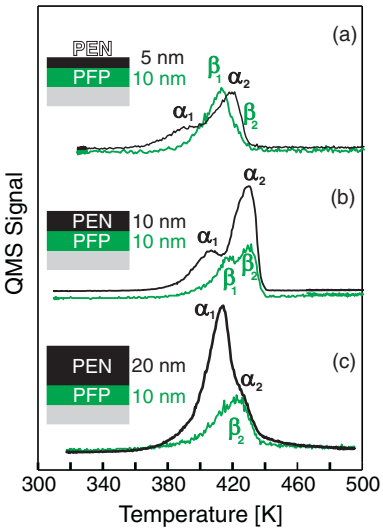

FIG. 2. Series of TD-spectra of PEN/PFP stacks consisting of (a) 5 nm, (b) 10 nm, and (c) 20 nm PEN films deposited onto 10 nm PFP.

PEN toplayer has been stabilized by interdiffusion thus leading to the conclusion that the interdiffusion zone amounts to about 6–7 nm at 330 K.

In a further step, the influence of substrate temperature during deposition on the thermal stabilization of PEN/PFP stacks was studied by preparing equivalent stacks at sample temperatures ranging from 240 K to 330 K. Corresponding TD-spectra that are summarized in Fig. 3 reveal no thermal stabilization for samples prepared at temperatures below 285 K, where only one desorption peak like in the case of pure films was found. At a growth temperature of 285 K, a small shoulder appears in both mass signals, indicating the beginning of the formation of a stabilized mixed phase. With further increasing growth temperature the intensity of this shoulder rises and develops as intense peaks (α_2, β_2), reaching their maximum at a growth temperature of 330 K. Larger substrate temperatures have not been put into practice because the sticking coefficients were found to decrease significantly at elevated temperature which hampers the preparation of films with defined thickness.

Though the results of Fig. 3 indicate that stabilization by interdiffusion is a thermally activated process that occurs during growth and not upon heating during the TDS measurements, one has to consider that films grown at low temperature are also less crystalline (or even amorphous at sufficient low temperatures[34]). Therefore, rather disordered bottom layers might hinder effective interdiffusion of pentacene into the PFP layer. In order to distinguish, whether primarily the reduced molecular ordering of the bottom layer or the low mobility of impinging molecules avoids an efficient interdiffusion, we have expanded our study by two further experiments. In the first one, the PFP bottom-layer was grown at elevated temperature (330 K) to provide long range crystalline ordering, but the subsequent PEN deposition was performed at 270 K. Complementary, an initial PFP layer was deposited at 270 K, yielding a rather disordered layer, while the following PEN deposition was performed at 330 K. As shown

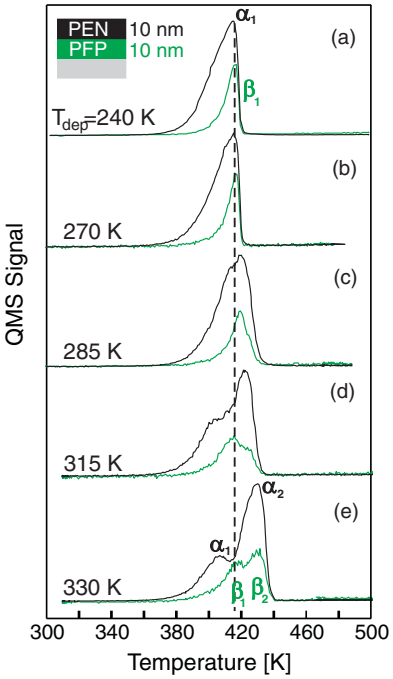

FIG. 3. Series of TD-spectra of PEN/PFP stacks (10 nm PEN on 10 nm PFP) that were grown at different substrate temperatures ranging between (a) 240 K and (e) 330 K.

in Fig. 4, the deposition of PEN at low temperature onto a crystalline PFP-film yields no stabilization and resembles the situation where both layers are grown at low temperature. By contrast, a distinct stabilization is found when the PEN toplayer is grown at elevated temperature onto a disordered PFP

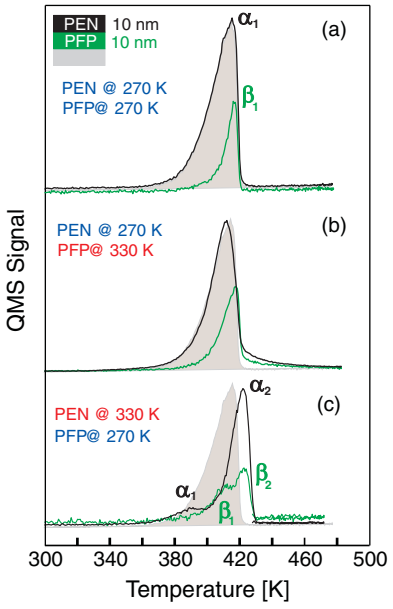

FIG. 4. TD-Spectra of PEN/PFP stacks (10 nm PEN on 10 nm PFP) with individual layers grown at different substrate temperatures: (a) both films deposited at T = 270 K, (b) bottom PFP film deposited at T = 330 K and PEN adlayer grown at T = 270 K, (c) bottom PFP film deposited at T = 270 K and PEN adlayer grown at T = 330 K. The shaded peak superimposed in panels (b) and (c) represents the PEN desorption signal of spectrum (a).

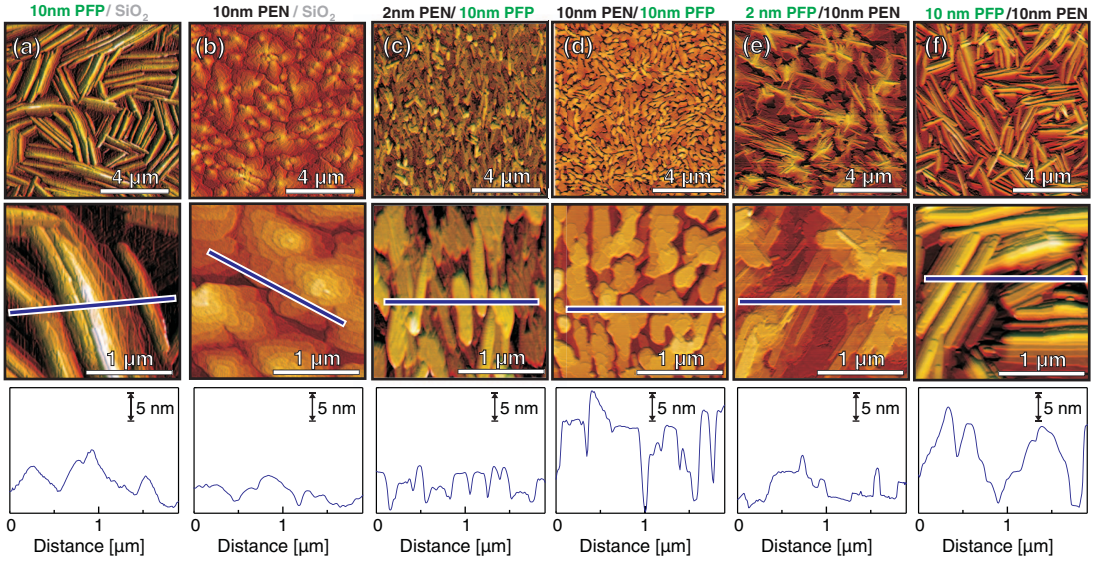

FIG. 5. Summary of AFM micrographs showing the morphology of different molecular films: (a) 10 nm PFP, (b) 10 nm PEN, (c) 2 nm PEN/10 nm PFP, (d) 10 nm PEN/10 nm PFP, (e) 2 nm PFP/10 nm PEN, and (f) 10 nm PFP/10 nm PEN together with corresponding linescans (bottom panels).

film (cf. Fig. 4(c)). Therefore, we conclude that the temperature upon growth of the top layer is the key parameter for efficient intermixture.

2. Morphology

To study the morphology of the different intermixed layers, AFM measurements were employed. Figure 5 presents a comparison of the morphology of pure PFP and PEN films and different subsequent stacks. Pure PFP films with 10 nm thickness consist of isotropically distributed spicular crystallites with typical lengths of several microns. As demonstrated in previous studies,[30,35] the PFP-molecules adopt an upright orientation. This finding is confirmed by height measurements of monomolecular steps, that are determined as 1.5 nm, which is in agreement with the d-spacing of the (100)-plane. Pure pentacene deposited on SiO_2 on the other hand crystallizes in pyramidal islands, again exhibiting molecular steps of 1.5 nm which can be attributed to upright molecular growth.[34]

Figures 5(c) and 5(d) show the morphology of subsequent stacks of 2 nm, respectively 10 nm pentacene deposited on top of 10 nm PFP. Clearly, the deposition of 10 nm PEN on top of PFP yields enhanced individual crystallite size and smoothness compared to the earlier growth stage. The morphology of the thickness-equivalent stack corresponds nicely to the morphology of pure pentacene: Rather pyramidal islands with monomolecular steps that amount to the $d_{(001)}$-spacing of pentacene are found.[36]

By contrast, the stacks with PFP on top (Figs. 5(e) and 5(f)) exhibit spicular islands which also exhibit characteristic monomolecular steps that equal the PFP-$d_{(100)}$-spacing, thus representing upright molecular growth, like in the pure PFP phase. This finding agrees with previous studies where the orientation and structure of subsequent PFP/PEN and PEN/PFP stacks were analyzed by means of X-ray diffraction[28] and our own XRD measurements.[41]

Consequently, the growth of PEN and PFP on each other mostly equals their individual growth, thus no crystallographic or morphological changes are induced in rather thick films of 10 nm during deposition. However, there is one interesting difference between both stacked systems. While PFP exhibits comparably high roughness when grown on PEN, the reverse stack is clearly smoother, as the PEN molecules fill the trenches between the PFP crystallites. This smoothing effect of PEN on PFP has already been observed before by means of X-ray reflectivity measurements and results in reduced PEN roughness compared to individual PEN growth, even in thicker films.[27] Clearly, this smoothing and gap-filling results in an enhanced effective interdiffusion zone of PEN and PFP molecules and might therefore explain the asymmetry of thermal stabilization in the stacks deposited in reverse sequence, where PEN/PFP stacks were found to be strongly thermally stabilized, while PFP/PEN-stacks hardly showed any stabilization (cf. Figs. 1(c) and 1(d)).

B. Intermixed stacks

While in Sec. III A the structural and thermal properties of subsequently grown stacks of PEN and PFP were described, the focus will now be set on heterostructures prepared differently either by multi-stacks, co-evaporation or by selective annealing of subsequent stacks. Multi-stacks are stacks which do not consist of only one layer of each, but are prepared by repeated alternating deposition of thin layers of both compounds. The discussed multi-stacks have been produced by deposition of 1 nm layers of the individual molecules up to a cumulative thickness of 10 nm for each compound (i.e., 20 nm in total). Co-evaporated thin films are produced by setting constant and stoichiometrically equal deposition rates for both Knudsen cells and thus potentially allow interdiffusion at the molecular level immediately during arrival at the sample surface. Our final preparation method for heterostructures

was the annealing of subsequent PEN/PFP stacks of 10 nm thickness for each compound. In this case, a thermally activated interdiffusion of the layers is expected.

1. Thermal stability

As shown in Fig. 6(a) the preparation of the multi-stack leads to a stabilized intermixture of PFP and PEN, resulting in a multilayer-desorption peak with tearing edge at 435 K. A similar situation is found in the case of a co-evaporated PEN/PFP film (Fig. 6(b)). The tearing edge appears again at about 435 K. In this case, however, a small signal ascribed to non-intermixed pentacene desorption (α_1) is observed, which is due to slight deviations from an ideal 1:1 stoichiometry during deposition (from the integrals of both mass signals a pentacene surplus of 10 % can be estimated).

Finally, Fig. 6(e) shows the TD-spectra of an annealed stack. For comparison, Fig. 6(c) (same data as Fig. 1(d)) again shows a TD-spectrum of a 10 nm PEN/10 nm PFP stack prepared at 330 K. Subsequently, an equal layer was prepared, but heated ($\beta = 0.5$ K/s) only to 405 K to selectively desorb the non-intermixed PEN and PFP molecules, leaving only the intermixed phase behind. Figure 6(d) shows the corresponding QMS signal recorded during annealing, where an ascending signal occurred, belonging to the desorption of single PEN/PFP. Note that also during cool-down initially some desorption occurs due to the remaining heat of the sample. To verify the success of this approach to prepare an intermixed-phase only, a complete TDS run was performed after complete cool-down of the sample. As depicted in Fig. 6(e), indeed only the stabilized phase is detected, which shows the success of this approach.

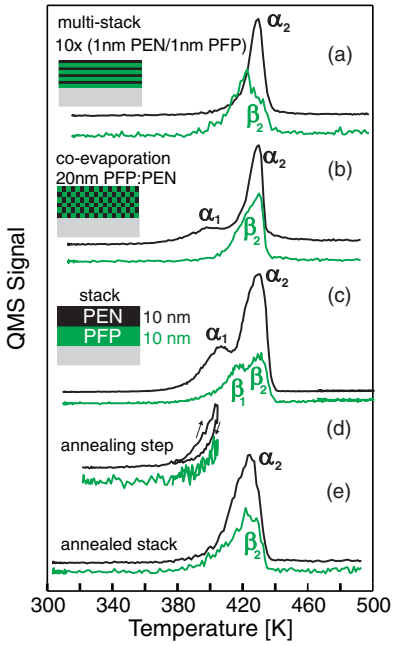

FIG. 6. TD-spectra of differently prepared heterostructures of PEN and PFP. (a) multi-stack of PEN and PFP (10 nm of each, evaporated in 1 nm layers), (b) co-evaporation (20 nm in total with stoichiometrically equivalent amounts of PEN and PFP), and (c)–(e) annealing of 10 nm PEN/10 nm PFP stack (see text).

2. Morphology

To find out possible correlation between thermal stability and morphology of the differently prepared PEN/PFP heterostructures, additional AFM scans were performed for the various mixed films. As shown in Fig. 7(a), the heterostructure prepared by co-evaporation consists of small spicular islands, which is in quite good agreement with the results from previous studies.[19,20] The other preparation methods, the multi-stack, the annealed stack, and—additionally to the TDS measurements—an annealed multi-stack, led to quite comparable results. Comparing the roughness of the individual films, the lowest values (rms 3.7 nm and 3.6 nm, respectively) are found for the coevaporated heterostructure and the non-annealed multi-stack while the observed values for the other preparation methods yield values greater than 6.5 nm. Interestingly, the morphology of the annealed subsequent PEN/PFP stack (Fig. 7(c)) is clearly different from the morphology before annealing (cf. Fig. 5(d)), hence proving film-evolution due to annealing. Heating of the multistack does not change the morphology significantly (Fig. 7(d)), except from increasing the film roughness.

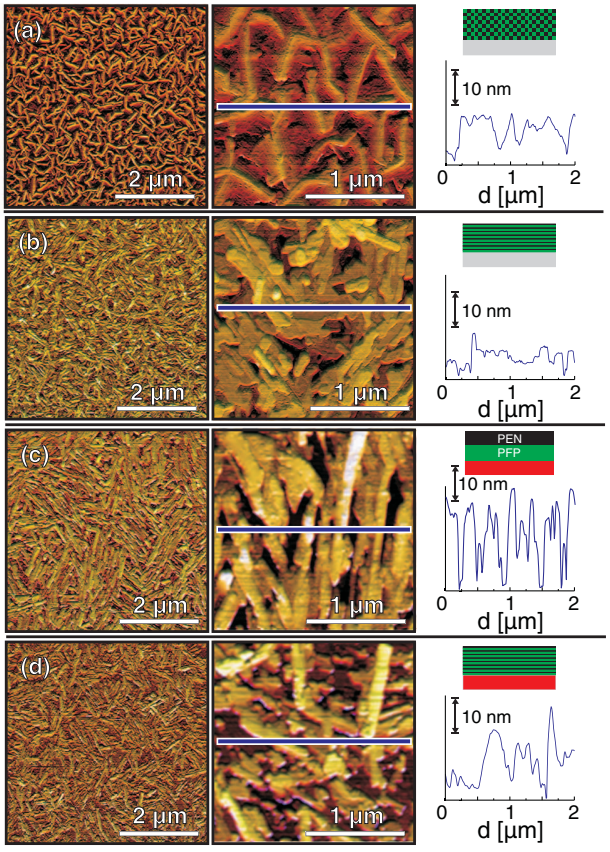

FIG. 7. Summary of AFM micrographs showing the morphology of different molecular films: (a) co-evaporation (20 nm in total with stoichiometrically equivalent amounts of PEN and PFP), (b) 10 nm PEN, 10 nm PFP multi-stack (1 nm per evaporation), (c) annealed 10 nm PEN/10 nm PFP-stack, and (d) annealed multi-stack together with corresponding linescans.

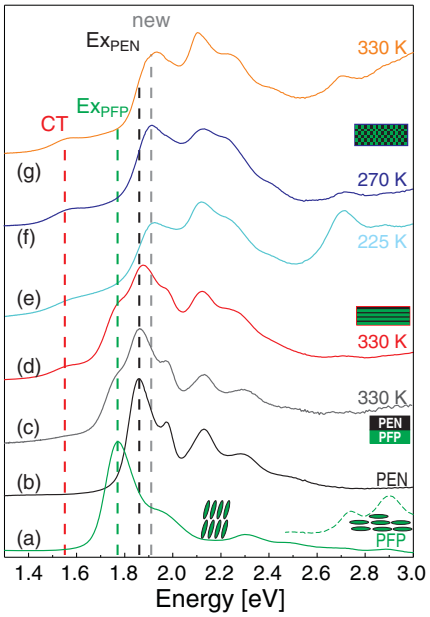

FIG. 8. Optical absorption spectra of differently prepared heterostructures of PEN and PFP with total thicknesses of 60 nm on glass substrates compared to reference spectra of single compounds: (a) pure PFP, (b) pure PEN, (c) PEN deposited on PFP at 330 K, (d) multi-stack deposited at 330 K, and (e)–(g) co-evaporation at 225 K/270 K/330 K. For samples (c)–(g) equivalent amounts of PFP and PEN were deposited.

C. Optical properties

To find about the efficiency of intermixture in the prepared stacks, their optical absorption spectra have been analyzed.[37] In the case of intermixed PEN:PFP layers the resulting optical signature significantly differs from a superposition of the single compound spectra. Especially, in previous studies a new absorption band at lower energies (1.55 eV) was observed, which was attributed to an excitation of a charge-transfer (CT) exciton in intermixed PEN:PFP layers.[21] By contrast, in the case of phase-separation, the optical spectrum of stacked films is expected to be a perfect superposition of the single compound spectra.[28]

Figure 8 compares the optical absorption spectra of pure PFP and PEN films and their heterostructures deposited onto glass substrates. Our XRD measurements show that the differently prepared thin films essentially adopt an upright molecular orientations in all cases, both, on SiO_2 and on glass substrates.[41] We note, however, that the absence of diffraction peaks corresponding to recumbent molecular orientations does not neccessarily exclude small remaining areas with deviant orientation as amorphous regions may exist. The spectra of the pure films are in agreement with previous reports.[38] The resonances at 1.86 eV and 1.97 eV (PEN) and 1.75 eV (PFP) are attributed to excitonic states[39] and exhibit the highest intensity when the molecules are in upright orientation,[40] while the peaks at 2.12 eV (PEN) and 1.98 eV (PFP) correspond to the HOMO-LUMO transitions. Analyzing the spectra of subsequently deposited stacks (PEN/PFP see Fig. 8(c) , PFP/PEN see the supplementary material[41]) shows that the optical signatures of these heterostructures are mainly superpositions of the PEN and PFP spectra. Only the PEN/PFP stack grown at 330 K (Fig. 8(c)) shows a small, but distinct excitation due to the charge transfer exciton at 1.55 eV, thus indicating interaction of both compounds to some extent. By contrast, the preparation of a similar stack at lower temperature (270 K) reveals no excitation of the CT exciton in the optical absorption spectra (see the supplementary material[41]) which suggests that the reduced molecular diffusion hampers intermixture. The optical spectrum of a multi-layered stack exhibits a more pronounced CT-exciton peak than the subsequent stack, but in other respect resembles the superposition of both single compound spectra quite well. This shows that still noticeable amounts of phase-separated molecules remain. Note that phase-separation does not necessarily mean separation of both compounds on a large length scale. Contrary—as very likely in the case of multi-layered stacks—the pure compounds may also form small aggregates of one another which are able to intermix if sufficient thermal energy is provided, as during the TDS measurements.

As presented in Figs. 8(e)–8(g), co-deposition of both compounds in equimolar ratios yields clearly different signatures than subsequent stacks. Independent of deposition temperature, the charge-transfer exciton is observed. Surprisingly, the highest intensity of this related absorption is observed for the co-deposition at 270 K. Furthermore, the exciton peak of PFP at 1.74 eV completely disappears, again independent from deposition temperature. The energetically second-lowest peak is found at 1.92 eV which is slightly different from the first Davydov-component of the PEN-exciton peak (1.86 eV). We note that for all co-depositions a single peak at 2.72 eV is found, which we attribute to molecules in lying configuration, as in pure PFP films (cf. Fig. 9, lower panel). The highest intensity of this peak is observed for the co-evaporation deposited at low temperature (270 K). Note that the co-existence of molecules in standing and lying configuration in PEN:PFP co-deposited films has been reported before.[20] In this case however, a vibrational progression is not observed, representing a distorted vicinity of the PFP molecules and therefore modified vibrational properties.

To study the appearance and absence of the PFP exciton peak in more detail, two further samples with deviant composition were prepared. While the sample with PFP excess (2:1) yields a strong signal of the excitonic excitation, co-depositon with PEN excess (2:1) again does not show the corresponding peak (see the supplementary material[41]). Our data clearly show that the PFP-exciton peak occurs in pure PFP phases only. This means that it only appears if either the stoichiometry is non-equal or the deposition conditions (e.g., non-constant deposition rates, inhomogeneous sample exposure or subsequent deposition) do not allow homogeneous intermixture and therefore provides a decisive criterion. Consequently, one must consider both signals, the appearance of the charge-transfer exciton and the disappearance of the PFP exciton peak, if the efficiency of intermixture shall be judged.

IV. DISCUSSION

The present analysis of differently prepared heterostructures of perfluoropentacene and pentacene on SiO_2 clearly shows a thermal stabilization of well mixed binary films

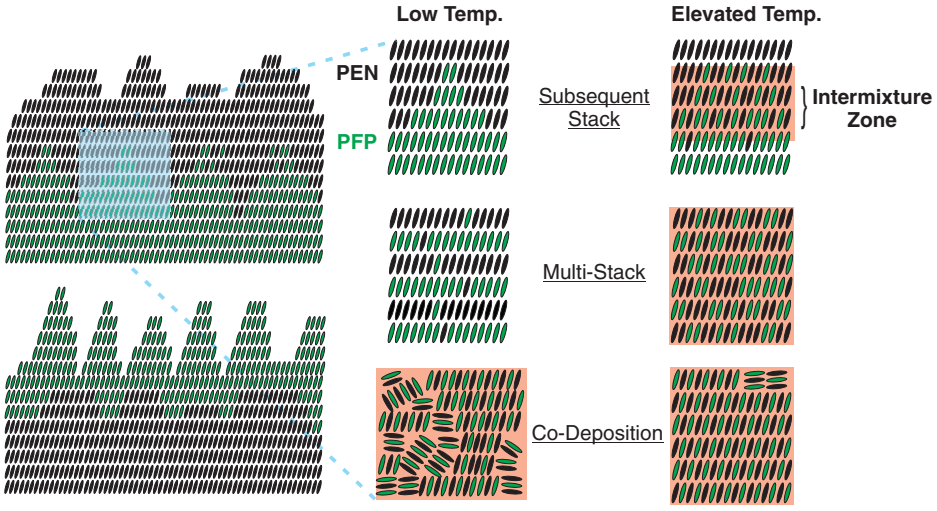

FIG. 9. Simplified schematical representations of different growth scenarios occurring for binary PEN/PFP films at low and elevated temperatures.

yielding an upward shift of the tearing edge in the TD-spectra of about 20 K compared to the pure compounds for a film thickness of 10 nm. Interestingly, this stabilization does not only occur in the case of co-evaporation, but even in subsequently grown stacks, which shows that the interface between both compounds is not rigid, but allows interdiffusion and resulting stabilization. However, the intermixture of both compounds depends on the succession of material deposition and especially is related to the surface roughness of the bottom layer. A stacked layer with perfluoropentacene deposited on top of pentacene hardly exhibits any intermixture, but only delayed desorption of pentacene compared to unitary pentacene films, which results from capping by a perfluoropentacene top-layer. By contrast, the reverse stack exhibits intermixture of both compounds, yielding enhanced thermal stability of the layer. Associated AFM measurements as well as the non-symmetric effect of smoothing in PEN/PFP/SiO_2 stacks indicate, that the rough surface of the PFP bottom layer yields a large contact area of the PEN/PFP interfaces and therefore provides efficient interdiffusion.

The quantitative analysis of the relative intensity of the different desorption channels (α_i and β_i peaks) for different top layer thicknesses allows to compare the fraction of stabilized regions and shows that the intermixture zone is limited to about 6–7 nm layers upon deposition at 330 K. Therefore, the approach of preparing PEN/PFP intermixtures by diffusion of subsequently grown stacks is limited to thin individual layers.

Variation of substrate temperatures during deposition of subsequently grown PEN/PFP stacks showed that efficient interdiffusion requires adequate deposition temperatures, so that no thermal stabilization occurs for stacks prepared below 285 K. The most efficient intermixture is achieved at a temperature of 330 K. Furthermore, analyses of stacks prepared at different substrate temperatures during deposition of both compounds identified the diffusion upon growth of the upper layer as the key parameter. Compared to the heterostructure of naphtalene and perfluoronaphtalene, a higher energetic stabilization is expected in the case of pentacene and perfluoropentacene due to larger expansion of the molecules and therefore enhanced contact area. On the other hand, a larger activation energy is required to achieve order within the heterostructure so that crystalline intermixtures of rather shape anisotropic molecules are more difficult to prepare.

More sophisticated approaches to prepare mixtures of pentacene and perfluoropentacene, like co-evaporation, multi-stacks and annealing of stacks yield spectra which exhibit larger fractions of the stabilized phase compared to the stacked layer systems. Moreover, they prove that the formation of a stabilized phase requires an exact stoichiometry relation of PFP and PEN of 1:1, since possible excess of one compound leads to desorption peaks of the non-stabilized phase (α_1 and β_1). On the other hand, this finding allows promising routes to prepare very defined and exact equimolar heterostructures of perfluoropentacene and pentacene, because difficulties in setting exactly equal deposition rates might hamper the preparation of equimolar heterostructures in other preparation methods, like growth from solution.

The analyses of optical absorption spectra are in good agreement with these findings: While the subsequent stack with PFP deposition onto PEN layers does not give indications for efficient molecular intermixture, the stack deposited in reverse sequence clearly exhibits a signature in the optical spectra which is assigned to the charge-transfer exciton, thus proving intermixture of both compounds. Furthermore, the rather low intensity of this peak corresponds well to the aforementioned limited extension of intermixture zone as derived from TDS measurements. Co-deposition and multi-stacks on the other hand in all cases show distinct signals of the CT-exciton. However, the appearance of this excitation represents no decisive criterion of the efficiency of intermixture. Rather, the PFP pure phase exciton has been shown to disappear in efficient intermixtures. This finding is consistent with the expectation that a changed molecular surrounding is known to influence the exciton binding energy. For example, the excitonic peaks are absent for PFP and PEN molecules dissolved in dichlorobenzene, representing free molecule spectra.[38] We therefore identify the appearance of the CT-related

absorption peak and the simultaneous disappearance of the excitonic peaks of the pure compounds as a credible benchmark to judge the efficiency of intermixture. Note that this effect has not been observed in previous studies. On the contrary, in the study of Broch *et al.*[21] a significant absorption peak due to excitation of the PFP exciton was observed for stoichiometrically equivalent coevaporated films and even in mixed films with PEN excess. We attribute this discrepancy to a non-ideal control of the stoichiometry during film preparation in that work. To ensure the right stoichiometry of films in our study we have taken particular care to precisely control the deposition rates by using QCM on the one hand but also by recording TD-spectra to cross-calibrate the resulting film thickness otherwise. In total more than 100 TD-spectra and about 30 optical spectra of different films have been acquired which assures reproducibility and significance of our data. In that way an optimized intermixture of binary PEN/PFP films was achieved, showing rather sharp absorption peaks which allowed in particular to identify a new optical absorption peak at 1.91 eV that appears only for well mixed binary films.

Summing up, the optical absorption spectra show clear signs for molecular intermixture in case of those heterostructures which also exhibit thermal stabilization in TDS measurements (co-depositions and multi-stacks), limited intermixture for structures with limited interdiffusion zone (PEN/PFP stacks deposited at 330 K) and no intermixture for non-stabilized systems (PFP/PEN, PEN/PFP deposited at 270 K). Furthermore, our results show that due to the observed interplay of diffusivity, roughness evolution, orientation, and molecular intermixture a consideration of kinetic growth effects is required, which hampers the commitment to a unique preparation method. As a consequence, the discussed preparation protocols allow to prepare heterostructures with well-defined characteristics like films with well-defined interfaces without molecular intermixture (subsequent stacks deposited at low temperature), layers with exclusive orientation (subsequent stacks and multi-stacks) and efficient molecular intermixture without phase-separation (co-evaporation). However, a unique preparation method which combines exclusive orientation with efficient molecular intermixture has not yet been found.

V. CONCLUSION

Pursuing the effect of enhanced thermal stability of equimolar mixtures of benzene and hexafluorobenzene[11] as well as napthalene and octafluoronaphtalene,[12] we prove that also the mixture of pentacene and perfluoropentacene yields thermally stabilized heterostructures. Because other studies require exact certainty of the right stoichiometry to dependably isolate the spectroscopic signature of the heterostructure, the approach of thermodynamically controlled preparation of equimolar heterostructures promises further, detailed insight into the coupling of heterostructures of pentacene and perfluoropentacene. As molecular heterostructures are of broad interest and certainly not restricted to the presently studied model system PEN/PFP, we are convinced that the expansion of our approach to other systems may help to gain further insight in this field.

ACKNOWLEDGMENTS

Tobias Breuer gratefully acknowledges financial support by the Friedrich-Ebert-Stiftung.

[1] N. Schultheiss and A. Newman, Cryst. Growth Des. **9**, 2950 (2009).
[2] T. Friscic and W. Jones, J. Pharm. Pharmacol. **62**, 1547 (2010).
[3] A. Hinderhofer and F. Schreiber, ChemPhysChem **13**, 628 (2012).
[4] J. Ferraris, V. Walatka, J. H. Perlstei, and D. O. Cowan, J. Am. Chem. Soc. **95**, 948 (1973).
[5] D. Jerome, Chem. Rev. **104**, 5565 (2004).
[6] A. Nangia, J. Chem. Sci. **122**, 295 (2010).
[7] J. E. Anthony, Chem. Rev. **106**, 5028 (2006).
[8] A. N. Sokolov, T. Friscic, and L. R. MacGillivray, J. Am. Chem. Soc. **128**, 2806 (2006).
[9] J. Vrbancich and G. L. D. Ritchie, J. Chem. Soc., Faraday Trans. 2 **76**, 648 (1980).
[10] J. H. Williams, Acc. Chem. Res. **26**, 593 (1993).
[11] C. R. Patrick and G. S. Prosser, Nature (London) **187**, 1021 (1960).
[12] F. Michaud, P. Negrier, D. Mikailitchenko, A. Marbeuf, Y. Haget, M. Cuevas-Diarte, and H. A. J. Oonk, Mol. Cryst. Liq. Cryst. Sci. Technol., Sect. A **326**, 1 (1999).
[13] C. P. Brock and J. D. Dunitz, Act. Crystallogr. **B38**, 2218 (1982).
[14] D. J. Gundlach, Y. Y. Link, T. N. Jackson, S. F. Nelson, and D. G. Schlom, IEEE Electron Device Lett. **18**, 87 (1997).
[15] Y. Inoue, Y. Sakamoto, T. Suzuki, M. Kobayashi, Y. Gao, and S. Tokito, Jpn. J. Appl. Phys. **44**, 3663 (2005).
[16] R. B. Campbell, J. M. Robertson, and J. Trotter, Acta Crystallogr. **15**, 289 (1962).
[17] T. Siegrist, C. Kloc, J. H. Schön, B. Batlogg, R. C. Haddon, S. Berg, and G. A. Thomas, Angew. Chem., Int. Ed. **40**, 1732 (2001).
[18] Y. Sakamoto, T. Suzuki, M. Kobayashi, Y. Gao, Y. Fukai, Y. Inoue, F. Sato, and S. Tokito, J. Am. Chem. Soc **126**, 8138 (2004).
[19] I. Salzmann, S. Duhm, G. Heimel, J. P. Rabe, N. Koch, M. Oehzelt, Y. Sakamoto, and T. Suzuki, Langmuir **24**, 7294 (2008).
[20] A. Hinderhofer, C. Frank, T. Hosokai, A. Resta, A. Gerlach, and F. Schreiber, J. Chem. Phys. **134**, 104702 (2011).
[21] K. Broch, U. Heinemeyer, A. Hinderhofer, F. Anger, R. Scholz, A. Gerlach, and F. Schreiber, Phys. Rev. B **83**, 245307 (2011).
[22] F. Anger, J. O. Ossó, U. Heinemeyer, K. Broch, R. Scholz, A. Gerlach, and F. Schreiber, J. Chem. Phys. **136**, 054701 (2012).
[23] J. Potenza and D. Mastropaolo, Acta Crystallogr. **B31**, 2527 (1975).
[24] M. Fulem, V. Lastovka, M. Straka, K. Ruzicka, and J. M. Shaw, J. Chem. Eng. Data **53**, 2175 (2008).
[25] A. I. Kitaigorodsky, *Mixed Crystals*, Springer Series in Solid-State Sciences Vol. 33 (Springer-Verlag, Berlin, 1984).
[26] Throughout this paper, the terms *interdiffusion* and *intermixture* are used. While *interdiffusion* is used to describe the microscopic effect of molecules of different compounds that disperse within the sample, changing positions and vicinity, *intermixture* describes the final effect of interdiffusion, the state of being intermixed.
[27] A. Hinderhofer, A. Gerlach, S. Kowarik, F. Zontone, J. Krug, and F. Schreiber, Euro. Phys. Lett. **91**, 56002 (2010).
[28] S. Duhm, I. Salzmann, G. Heimel, M. Oehzelt, A. Haase, R. L. Johnson, J. P. Rabe, and N. Koch, Appl. Phys. Lett. **94**, 033304 (2009).
[29] Note that for stoichiometrically non-equivalent (e.g., co-evaporations with PFP excess or PEN excess for comparison) the individual rates were non-equal.
[30] B. Haas, A. Beyer, W. Witte, T. Breuer, G. Witte, and K. Volz, J. Appl. Phys. **110**, 073514 (2011)
[31] D. Käfer, C. Wöll, and G. Witte, Appl. Phys. A **95**, 273, (2009)
[32] If transfers were inevitable, the absolute temperature scale was cross-verified by calibration measurements before each new series of measurements.
[33] S. Sellner, A. Gerlach, F. Schreiber, M. Kelsch, N. Kasper, H. Dosch, S. Meyer, J. Pflaum, M. Fischer, B. Gompf, and G. Ulbricht, J. Mater. Res. **21**, 455 (2006).
[34] C. D. Dimitrakopoulos, A. R. Brown, and A. J. Pomp, J. Appl. Phys. **80**, 2501 (1996).
[35] S. Kowarik, A. Gerlach, A. Hinderhofer, S. Milita, F. Borgatti, F. Zontone, T. Suzuki, F. Biscarini, and F. Schreiber, Phys. Status Solidi (RRL) **2**, 120 (2008).

[36]Note that due to inconsistencies in lattice definition, in the PEN-lattice the **c**-axis is mostly parallel to the long molecular axes, while in case of PFP the **a**-axis is mostly parallel to the long molecular axes.
[37]To achieve satisfying signals, all films had individual thicknesses of 30 nm of each compound (60 nm total). Comparing XRD measurements show in particular that the thin films deposited on SiO_2 adopt the same crystalline orientation as thicker films grown onto glass substrates.
[38]A. Hinderhofer, U. Heinemeyer, A. Gerlach, S. Kowarik, R. M. J. Jacobs, Y. Sakamoto, T. Suzuki, and F. Schreiber, J. Chem. Phys. **127**, 194705 (2007).
[39]J. Helzel, S. Jankowski, M. El. Helou, G. Witte, and W. Heimbrodt, Appl. Phys. Lett. **99**, 211102 (2011).
[40]T. Breuer and G. Witte, Phys. Rev. B **83**, 155428 (2011).
[41]See supplementary material at http://dx.doi.org/10.1063/1.4795004 for Fig. S01 and Fig. S02 for a presentation and discussion of additional optical spectra and the XRD data, respectively.

SUPPORTING INFORMATION
Thermally Activated Intermixture in Pentacene - Perfluoropentacene Heterostructures

Tobias Breuer and Gregor Witte[1]

[1] *Molekulare Festkörperphysik, Philipps-Universität Marburg, D-35032 Marburg, Germany*

Fig. S1 presents additional UV/Vis absorption spectra of differently prepared thin-films of pentacene-perfluoropentacene heterostructures. As discussed in the main text, the subsequently deposited stack of pentacene on top of PFP shows intensity at the energetic position of the charge-transfer exciton (1.55 eV) only if deposited at a sample temperature of 330 K (Fig. S1 c)), while no absorption occurs when deposited at 270 K (Fig. S1 d)), which is ascribed to non-sufficient molecular interdiffusion. The opponent stack with PFP on top of PEN (Fig. S1 e)) also shows no significant contribution at this position, which is in line with our findings from TDS measurements. Figures S1 f-h) compare the spectra of PEN:PFP co-evaporations with different stoichioemetric ratios. While in the co-deposition with PEN excess (Fig. S1 f)) the PEN exciton is clearly and the PFP excitonic excitation is not observed, the reverse is true for the sample with PFP excess (Fig. S1 g)). Comparing these to the equimolar co-deposition (Fig. S1 h)) shows that both excitonic excitations of the pure compounds are suppressed in this spectrum and a new excitation (additionally to the CT-excitation at 1.55 eV) is found at 1.92 eV.

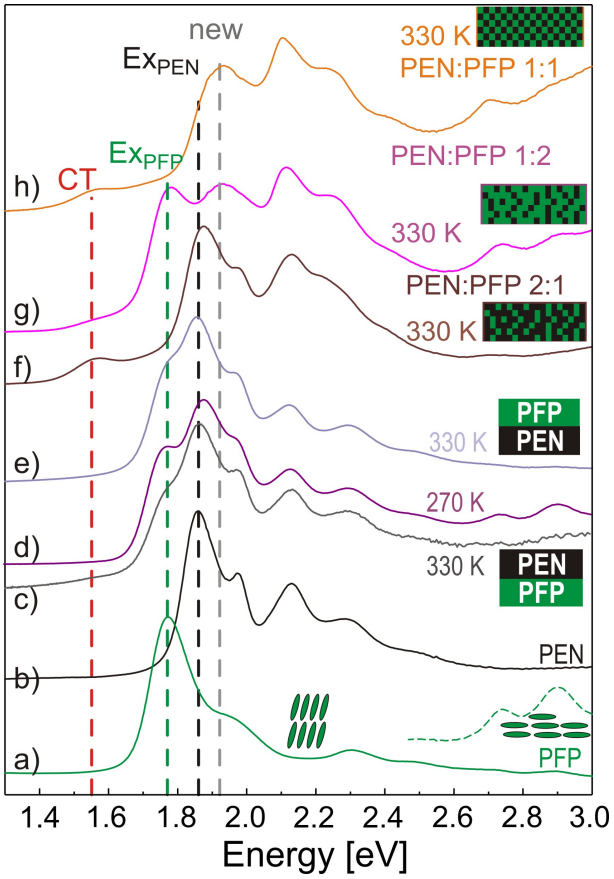

Figure S 1: Optical absorption spectra of differently prepared heterostructures of PEN and PFP on glass substrates compared to reference spectra of single compounds: a) pure PFP, b) pure PEN, c) 30 nm PEN deposited on 30 nm PFP at 330 K, d) at 270 K, e) 30 nm PFP deposited on 30 nm PEN at 330 K, f) co-evaporation at 330 K with 2:1 PEN:PFP ratio, g) 1:2 PEN:PFP ratio, h) 1:1 PEN:PFP ratio

To verify the orientation of the heterostructures, out-of-plane X-Ray diffraction was applied. In Fig. S2 spectra of multi-stacks [a) and d)], co-evaporated films [b) and e)] and subsequently deposited PEN / PFP stacks [c) and f)] on SiO_2 (total film thickness 20 nm) and glass substrates (total film thickness 60 nm), all of which prepared at substrate

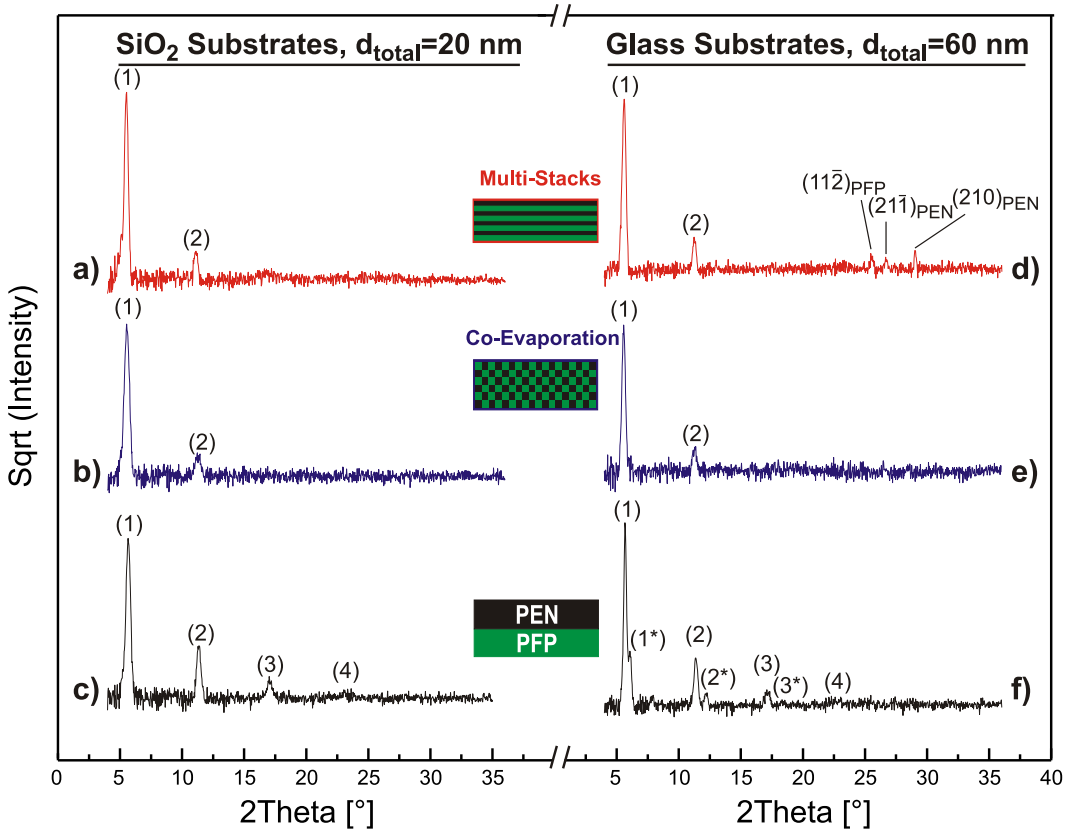

Figure S 2: X-Ray Diffraction spectra of differently prepared heterostructures of PEN and PFP on SiO_2 (total film thickness 20 nm) and glass substrates (total film thickness 60 nm): a),d) Multi-Stacks, b),e) Co-Evaporation, c),f) Subsequent Stacks PEN on PFP. All samples were prepared at temperatures of 330 K

temperatures of 330 K, are compared. In all cases prominent peaks at positions of $2\Theta = 5.6°$ and their higher order replica [labelled (1) to (4)] were found, which reflects an upright molecular orientation in all examined configurations. Due to the low resolving power of the used diffractometer and the high peak width however, the three different crystal structures of PEN ($d_{(001),tf}$ = 5.73Å[1]), PFP ($d_{(100),tf}$ = 5.61 Å[2]) and the PFP:PEN heterostructure ($d_{(100)}$ = 5.54Å[2]) could not be differentiated by means of out-of-plane diffraction. The comparison shows that essentially the same film structure - consisting of uprightly oriented molecules - is observed in binary PEN/PFP films in thin films on SiO_2 as well as in thicker films grown on glass substrates.

We note that, additional to the dominant upright orientation, small contributions of non-standing orientations were found in the case of the multi-stacks prepared on glass substrates (Fig. S2 d)). We note further, that the thick subsequent PEN/PFP stack (Fig. S2 f)) is not only composed of pentacene crystallites in their thin film phase, but exhibits some in the Campbell phase, resulting in a smaller lattice plane distance and therefore peaks at higher angles (first order at 6.1°, labelled with asterisk). The transition of crystallization in the thin film phase to the Campbell phase at elevated temperatures and increasing film thickness is in good congruence with previous findings[3].

[1] S. Schiefer, M. Huth, A. Dobrinevski, B. Nickel, J. Am. Chem. Soc. **129**, 10316 (2007).
[2] I. Salzmann, S. Duhm, G. Heimel, J. P. Rabe, N. Koch, M. Oehzelt, Y. Sakamoto, T. Suzuki, Langmuir **24**, 7294 (2008).
[3] I. P. M. Bouchoms, W. A. Schoonveld, J. Vrijmoeth, T. M. Klapwijk, Synthetic Metals **104**, 175 (1999).

5.9 Article IX: Diffusion-controlled growth of molecular hetero-structures: fabrication of 2D, 1D and 0-Dimensional C60-nanostructures on pentacene substrates

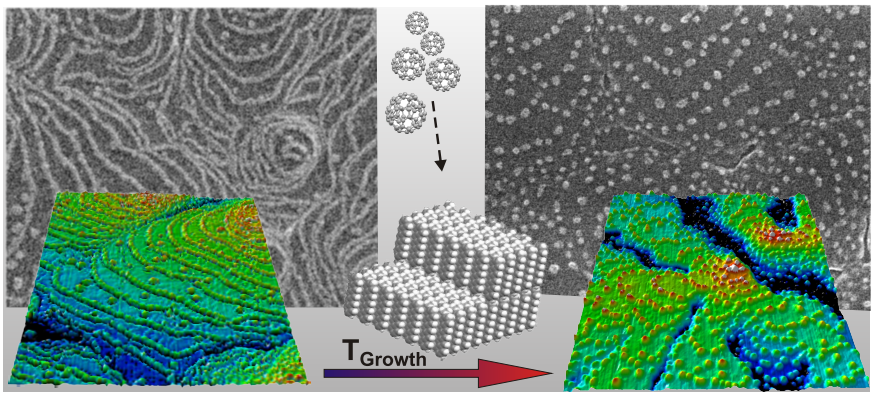

Reproduced with permission from
T. Breuer and G. Witte, Advanced Materials (2013), submitted.

5.9.1 Abstract

A variety of low dimensional C_{60} structures has been grown on supporting pentacene multilayers. By choice of substrate temperature during growth the effective diffusion length of evaporated fullerenes and their nucleation at terraces or step edges can be precisely controlled. AFM and SEM measurements show that this enables the fabrication of either 2D adlayers or solely 1D chains decorating substrate steps, while at elevated growth temperature continuous wetting of step edges is prohibited and instead the formation of separated C_{60} clusters pinned at the pentacene step edges occurs. Remarkably, all structures remain thermally stable at room temperature once they are formed. In addition the various fullerene structures have been overgrown by an additional pentacene capping layer. Utilizing the different probe depth of XRD and NEXAFS we found that no contiguous pentacene film is formed on the 2D C_{60} structure, whereas an encapsulation of the 1D and 0D structures with uniformly upright oriented pentacene is achieved, hence allowing the fabrication of low dimensional buried organic hetero-structures.

5.9.2 Methods

Atomic Force Microscopy, Near-Edge X-Ray Absorption Finestructure Spectroscopy, Organic Molecular Beam Deposition, Scanning Electron Microscopy, X-Ray Diffraction

5.9.3 Own Contribution

I have prepared all samples and planned and conducted all experiments. I have written the major part of the manuscript, while Gregor Witte has helped to interpret the data as well as to improve the manuscript.

Diffusion-controlled growth of molecular hetero-structures: fabrication of 2D, 1D and 0-Dimensional C_{60}-nanostructures on pentacene substrates

Tobias Breuer and Gregor Witte*
Molekulare Festkörperphysik, Philipps-Universität Marburg, D-35032 Marburg, Germany
**E-Mail: gregor.witte@physik.uni-marburg.de*

Low dimensional semiconductor hetero-structures have been the subject of intense research because they enable electron confinement and exhibit new transport properties which are useful for device applications.[1] In contrast to such inorganic semiconductor structures, which can be specifically fabricated by means of molecular beam epitaxy in combination with lithography based structuring methods, hetero-structures consisting of organic semiconductors are studied by far less thoroughly. Present efforts to prepare molecular nanostructures are mostly limited to hybrid systems such as self assembled monolayers,[2] nano-particles coated by ligand shells [3] or block copolymer micelles.[4] A commonly used strategy to fabricate 2D molecular nanostructures is based on the surface science approach where a large variety of structures has been observed for monolayer films chemisorbed at metal substrates [5] that result from supra-molecular association and substrate template effects. Though template controlled growth can be used to prepare long range ordered monolayers with uniaxial molecular orientation,[6] such structural motifs are usually not transferred to multilayer films.[7] This limitation can be rationalized by rather different molecular interactions acting within the film and towards the substrate: while molecules are fixated by chemical bonds at the surface, they experience only weak, essentially van-der-Waals type mutual interactions. As a consequence, multilayer structures generally exhibit a larger degree of imperfection and strongly reduced thermal stability compared to chemisorbed monolayers. In case of molecular hetero-structures the situation is even more complex since unequal interactions between the different molecular entities may cause phase separation upon growth.[8] On the other hand the weak intermolecular interaction favors notable diffusion already at room temperature and can lead to substantial intermixture of sequentially deposited molecular films [9] which might hamper the formation of well separated molecular hetero-layers. To date, only few examples of ordered molecular hetero-structures have been reported, essentially showing orientational control in vertically stacked layers.[10]

The promising potential of organic photovoltaic (OPV) devices based on acceptor-donor hetero-junctions of conjugated polymers and/or oligomers has recently attracted substantial research interest in such interfaces. Aiming to improve the understanding of the microstructure and energetics of molecular hetero-structures, prototypical model interfaces between small molecular weight organic compounds that form crystalline films, such as fullerene (C_{60}) and pentacene (PEN), are of particular interest.[11] Moreover, they have been successfully used to fabricate ambipolar organic field effect transistors.[12] Previous studies have shown that PEN/C_{60} blends prepared by co-evaporation reveal phase separation.[13] In contrast, the formation of well ordered network or pinwheel structures was found upon co-crystallization of monolayers on metal substrates,[14] while deposition of C_{60} onto pentacene films yields clusters pinned at pentacene step edges.[15] The complexity of such structural motifs has also triggered significant theoretical efforts to analyze PEN/C_{60} interfaces.[16–18] In addition, detailed energy calculations indicate that the electronic coupling between PEN and C_{60} depends significantly on their relative molecular orientation which has important implications for electronic devices employing such hetero-junctions.[19, 20]

In this study, we have extensively analyzed the growth of C_{60} layers onto (001)-oriented PEN films by combining atomic force microscopy (AFM), scanning electron microscopy (SEM), X-ray diffraction (XRD) and X-ray absorption spectroscopy (NEXAFS). A systematic variation of the growth conditions shows that at appropriate substrate temperatures rather different C_{60} structures can be fabricated: at cryogenic temperatures homogeneous wetting occurs yielding 2D C_{60} films while with increasing growth temperature the fullerenes diffuse towards step edges of the PEN layer and form 1D chains. By contrast, growth of C_{60} at room temperature or above causes dewetting and formation of separate C_{60}-clusters that nucleate at PEN step edges. In addition we have also addressed the topic whether the various C_{60} structures can be overgrown by PEN films in order to fabricate buried hetero-structures. The different probe depth of XRD and NEXFAS provides detailed information about the orientational ordering of bottom and top PEN layers and shows that fullerene chains and clusters can be well overgrown by a crystalline PEN capping layer that maintains it upright molecular orientation.

To provide well defined pentacene substrates with uniform molecular orientation and to exclude competing interaction of fullerenes with the supporting substrate, which might affect the film structure,[21] all C_{60} films were deposited onto 30 nm PEN bottom layers that had been grown on SiO_2. In accordance with previous works such PEN layers crystallize in the *thin film phase* and form (001)-oriented films.[22] As shown by the AFM micrograph in Fig. 1a) they consist of coalesced single crystalline grains of a width of few microns and exhibit atomically flat terraces extending over 100-200 nm separated by mono-molecular steps yielding an overall RMS roughness of less than 5nm (for additional XRD data see Supp. Inf., Fig. S4). Since previous work revealed severe tip-induced film modifications upon imaging of molecular multilayer films by scanning tunneling microscopy, owing to their low conductivity,[23] we instead used AFM to characterize the morphology of the molecular hetero-structures.

Fig. 1b) displays the interface formed by deposition of small C_{60} amounts (d_{nom}=0.25 nm) at room temperature onto the PEN bottom layer, yielding small C_{60}-clusters that are exclusively pinned at PEN step edges. To accentuate the lateral distribution of these clusters and decouple the superimposed height variation due to PEN substrate terraces, we present amplitude images of the AFM data shown in false colors, while

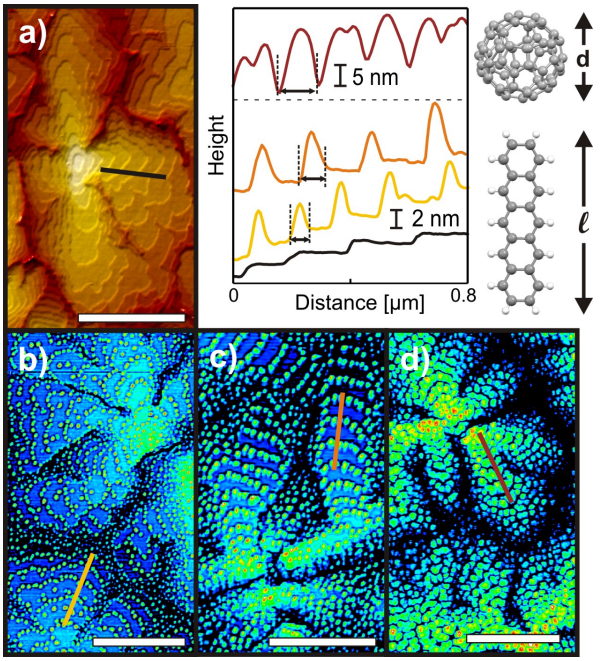

FIG. 1: AFM micrographs showing a) the morphology of the 30 nm PEN bottom layer and the amplitude images after C_{60} deposition of various thickness at room temperature, b) 0.25 nm, c) 0.5 nm and d) 5 nm together with corresponding line scans showing the height profile of the films. All scale bars correspond to 1 μm.

line scans represent the corresponding topography. The observed step decoration reflects enhanced adsorption energy of C_{60} molecules on PEN step edges as compared to terrace sites which is in line with recent force field based MD simulations.[17] As the precise determination of the cluster size might be limited by the resolution of the AFM due to the finite tip apex, additional SEM measurements have been performed at the identical samples (see Supp. Inf. S3). The quantitative analysis, combining the lateral dimensions of the clusters determined by SEM and height information provided by AFM yields cluster diameters of about 25 nm and a height of 4-6 nm. These values are much larger than the van der Waals diameter of fullerenes (0.7 nm) and therefore indicate agglomeration of the fullerenes. Doubling the amount of deposited C_{60} (d_{nom}=0.5 nm) still reveals no nucleation on the terraces and, surprisingly, does not result in continuous decoration of the step edges, but leads to clusters of increased height (8-10 nm) and diameter (40 nm). To monitor the film evolution at a later stage, also explicitly higher amounts of C_{60} (d_{nom}=5 nm) were deposited onto the PEN bottom layer. Even for this coverage (which corresponds to 6 monolayers of (001)-oriented C_{60}) individual C_{60} clusters can be recognized that have further extended in size (up to 15 nm in height, about 80 nm in diameter) and are partially coalesced, resulting in significant film roughness. The formation of individual C_{60} clusters coexistent with notable regions of undecorated step edges indicates that the C_{60} cohesion exceeds the C_{60}-PEN adhesion.

Moreover, it shows that upon RT deposition C_{60} diffusion at terraces and along step edges is activated. Considering further the different adsorption energy of C_{60} on (001)-terraces and step edges of PEN, it appears conceivable to control the diffusion length on terraces and steps separately by the substrate temperature. To test this hypothesis and to better understand the dynamics of step edge decoration, additional C_{60} films (in each case with a fixed nominal thickness of 0.5 nm) were grown on PEN bottom layers at different substrate temperatures ranging from 145 K to 345 K. Interestingly, a continuous evolution of the growth of C_{60} on PEN is found as summarized in Fig. 2. While rather homogeneous coating of the PEN terraces occurs for fullerene deposition at 145 K (which is also found for higher C_{60} thicknesses, cf. Supp. Inf., Fig. S1), at somewhat elevated temperatures coexistence between terrace growth and step edge decoration is present. Further elevation of the subtrate temperature to 240 K yields continuous step edge decoration without observable gaps between the C_{60} clusters along the step edges. The initially mentioned more discrete step edge decoration with enhanced individual cluster heights at room temperature becomes even more pronounced at a temperature of 345 K during C_{60} evaporation. In this case, large regions of the step edges remain uncovered while the higher diffusivity of the C_{60} molecules at elevated substrate temperature supports the formation of clusters of more than 9 nm in height. Measurements at higher substrate temperatures have not been carried out to avoid thermally activated roughening or even desorption of the PEN bottom layer.[24]

Interestingly, the various film morphologies are fully maintained at room temperature where all micrographs have been acquired. We note further that no evidence was found for any morphological changes after deposition by comparing samples which have been quickly transferred out of the vacuum chamber to those that have been prepared at low temperatures and post-annealed to higher temperatures or stored for several days under UHV at RT. This behavior is quite different from the case of PEN where a pronounced *post-deposition dewetting* occurs.[24] It demonstrates that C_{60} layers are thermally rather stable once a certain island size is reached which prevents subsequent diffusion. This observation is well rationalized by a recent computational study of the diffusion of C_{60} on PEN which showed that the diffusion coefficients decrease rapidly when instead of single molecules small fullerene clusters are moving over the PEN surface.[16] Conclusively, our results show that the diffusivity of C_{60} is sufficient to decorate the step edges of PEN even at temperatures as low as 170 K, which is quite surprising regarding the high molecular mass and the high thermal stability of solid C_{60}. By contrast, smooth interfaces with homogenous coverage are found at cryogenic growth temperatures, where even diffusion on the terraces is thermally not activated and fullerenes freeze out upon deposition, while the interface roughness increases with deposition temperature yielding only a small contact area at high temperatures (cf. Fig. 2g). Comparing the different nucleation scenarios, one can assign different dimensionalities to the resulting C_{60} films: low substrate temperatures during C_{60} deposition cause planar covering of the PEN surface and yield quasi 2D-structures, while at temperatures of 240 K essentially only the PEN step edges are covered homogeneously (1D-covering) and at elevated temperatures (345 K) separated 0-dimensional clusters are formed.

In a next step, we were also interested in the consequences of further pentacene deposition onto the various hetero-structures, aiming at the preparation of buried C_{60} structures. For this purpose, a 5 nm PEN capping layer was

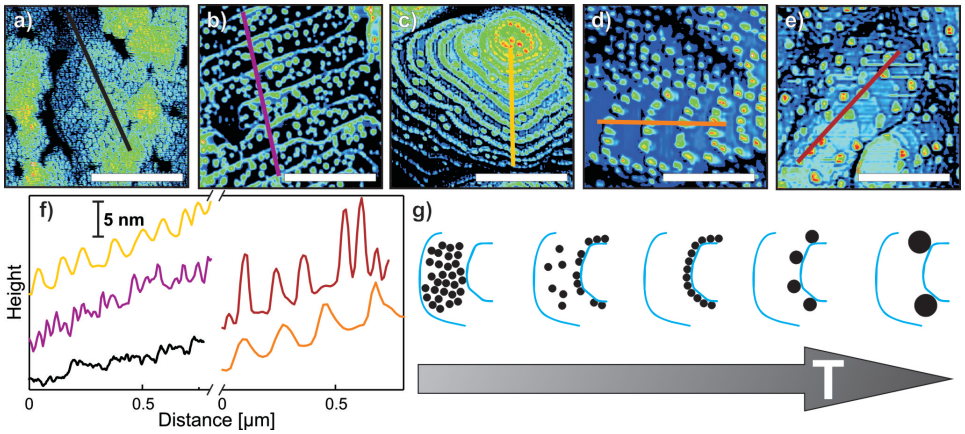

FIG. 2: Summary of AFM micrographs showing the resulting hetero-structures obtained by deposition of 0.5 nm C_{60} onto a 30 nm (001) oriented pentacene bottom layer at different substrate temperatures: a) T=145 K, b) T=170 K, c) T=240 K, d) T=300 K, and e) T=345 K together with f) corresponding line scans of the height profiles and schematic representation of the formed C_{60} structures. All scale bars correspond to 0.5 μm.

deposited at room temperature onto the various C_{60}/PEN hetero-structures (0.5 nm C_{60} on 30 nm PEN), where C_{60} had been deposited at different substrate temperatures of 145 K, 240 K and 300 K, respectively. Fig. 3a-c) summarizes the corresponding AFM micrographs of the resulting structures. On the 2D C_{60} layer rather small but tall PEN islands are formed which reveal elevations of about 10-15 nm relative to the C_{60}/PEN underlayer. Interestingly, some areas between the pentacene islands exist where the uncovered C_{60} film remains visible, hence reflecting incomplete wetting (white arrow in Fig. 3a).

When PEN is deposited on C_{60}-chains, a significantly different morphology is found. The capping layer has clearly reduced roughness and consists of extended islands which exhibit characteristic molecular steps that correspond to upright molecular orientation. In contrast to the morphology of the bare PEN bottom layer (cf. Fig. 1a) the PEN adlayer, however, reveals additional steps and grain boundaries on the terraces of the bottom layer - in some cases even orthogonal to the substrate step edge direction (see Fig. 3b). Their formation might be related to the step decoration which is expected to reduce the diffusion of PEN ad-molecules, hence causing additional nucleation.

Overgrowing the C_{60} clusters by PEN yields a surface morphology which is very similar to the bare PEN film (cf. Fig. 1a). Dendrites of similar morphology are found as well as typical monomolecular steps of 1.5 nm as depicted in Fig. 3c). Due to the large fullerene cluster size of about 8 nm, some of them are not completely buried by the 5 nm PEN cap layer and remain visible (indicated by black arrows in Fig. 3c), but can be completely covered by thicker PEN films (cf. Supp. Inf., Fig. S2).

The different resulting morphologies emphasize in particular the influence of steps on film growth. Once they are covered, the inter-terrace diffusion is largely reduced which in turn causes increased film roughness.

To determine the molecular orientation within the capping layer, the application of x-ray diffraction is only of limited use due its large probe depth and the diffractograms are therefore mostly governed by the crystalline ordering of the supporting bottom layer. However, it allowed to exclude the existence of crystalline PEN islands with recumbent molecular orientation (data presented in Supp. Inf., Fig. S4). To reliably support our finding that the subsequently deposited PEN molcules also adopt an upright orientation, NEXAFS measurements were carried out. Due to the low mean free path of the detected Auger electrons, this technique is inherently surface-sensitive and therefore allows to determine the average molecular orientation in the capping layer by analyzing the dichroism of the NEXAFS signatures due to excitations into the unoccupied π^*-orbitals[25] (see Supp. Inf.).

Except for PEN capping layers that were deposited on the 2D C_{60} layer, average molecular tilt angles of about 85° were obtained. This value is in excellent agreement with the orientation adopted in (001) oriented crystalline films (86°) and reflects high crystalline ordering of the capping layer. The

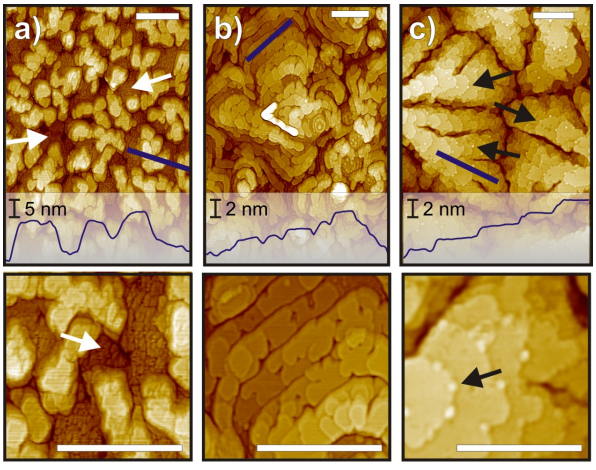

FIG. 3: AFM micrographs showing the morphology of 5 nm PEN capping layers grown on C_{60} nanostructures of different dimensionality: a) 2D, b) 1D, c) 0D C_{60} nanostructures, with corresponding line-scans and magnifications. All scale bars correspond to 0.5 μm

somewhat smaller average tilt angle of 71° found for PEN layers grown on the 2D fullerene film can be understood by considering that the C_{60} layer does not represent a single crystalline film but contains vacancies and other defects which cause pinning of PEN. They reduce the crystalline ordering and create notable film roughness as it was found before for PEN films grown on polycrystalline gold substrates.[25]

Our NEXAFS measurements enable further to characterize the molecular orientation near the surface of the PEN bottom layer upon C_{60} deposition. This allows in particular a detailed comparison with a previous MD growth study, in which it was projected that fullerenes interdiffuse into an uprightly-oriented PEN bottom layer, causing significant structural disorder in the top layers.[18] Our present results do not support this projection, as the molecular orientation of the PEN surface layer remains unchanged (85°) upon deposition of C_{60}. Furthermore, interdiffusion of C_{60} into the PEN layer would cause additional nuclei at the terraces, for which no evidence has been found in the AFM measurements.[26]

In summary, we have demonstrated for the case of C_{60}/PEN hetero-structures that in addition to energetic aspects, such as adhesion and cohesion energies of the individual compounds, which has been considered to rationalize the stability and possible intermixture of hetero-structures,[8] also the dynamics upon deposition are decisive for the resulting film structures. By adjusting the substrate temperature during growth, the effective diffusion length is tuned and a site specific nucleation is achieved which allows or suppresses C_{60} nucleation at step edges, or even activates diffusion along step edges yielding separated but edge-pinned C_{60} clusters. As a result C_{60}-adlayer structures of different dimensionality have been realized ranging from planar films (2D), over step decorated chains (1D) to clusters (0D). It is further demonstrated that such 1D and 0D C_{60}-structures can be overgrown by subsequent PEN deposition, forming a crystalline cover layer of same orientation as the bottom layer, hence enabling the formation of low dimensional buried organic hetero-structures. The present approach of gaining structural control over nanostructures by utilizing the anisotropic interaction between different molecular compounds and tuning the effective diffusion length is not restricted to monolayer films. It thus appears to be a rather versatile route to fabricate well ordered artificial molecular hetero-structures that are neccesary to explore the coupling at organic acceptor/donor interfaces and also serve as benchmark systems for detailed growth simulations.

EXPERIMENTAL

The thin films of pentacene (Sigma Aldrich, purity ≥ 99.9 %) and C_{60} (Sigma Aldrich, purity ≥ 99.5 %) were grown under ultrahigh-vacuum (UHV) conditions by organic molecular beam deposition (OMBD) from alumina crucibles of resistively heated Knudsen cells. By using cell temperatures of 500 K and 650 K for PEN and C_{60}, respectively, typical deposition rates of 6 Å/min (PEN) and 2 Å/min (C_{60}) were achieved that were monitored by quartz crystal microbalance (QCM). The films were grown onto natively oxidized Si(100) substrates which were cleaned by rinsing with ethanol, followed by heating in UHV to 600 K for 30 min.

The film morphology was characterized by atomic force microscopy (AFM, Agilent SPM 5500) operated in tapping mode at ambient conditions and room temperature. AFM tips with resonance frequencies of about 260 kHz, radii of 7 nm and force constants of 26.1 $^{N}/_{m}$ were used. Details on complementary NEXAFS, SEM and XRD measurements are presented in the Supporting Information.

Supporting Information

Supporting Information is available from the Wiley Online Library or from the author.

Acknowledgements

We acknowledge the Helmholtz-Zentrum Berlin - electron storage ring BESSY II - for provision of synchrotron radiation at beamline HE-SGM and M. Hellwig (WZMW Marburg) for his assistance with the SEM measurements. T.B. gratefully acknowledges financial support by the Friedrich-Ebert-Stiftung.

[1] a) A. D. Yoffe, *Adv. Phys.* **2001,** *50(1)*, 1-208. b) Y. Huang, C. M. Lieber, *Pure Appl. Chem.* **2004,** *76(12)*, 2051-2068.
[2] a) F. Schreiber, *Prog. Surf. Sci.* **2000,** *65(5-8)*, 151-256. b) J. C. Love, L. A. Estroff, J. K. Kriebel, R. G. Nuzzo, G. M. Whitesides, *Chem. Rev.* **2005,** *105(4)*, 1109-1169.
[3] a) D. B. Kittelson, *J. Aerosol Sci.* **1998,** *29(5-6)*, 575-588. b) J. Shan, H. Tenhu, *Chem. Comm.* **2007,** *44*, 4580-4598.
[4] G. Gaucher, M. H. Dufresne, V. P. Sant, N. Kang, D. Maysinger, J. C. Leroux, *J. Controll. Rel.* **2005,** *109(1-3)*, 169-188.
[5] a) J. V. Barth, G. Costantini, K. Kern, *Nature* **2005,** *437*, 671. b) M. Treier, R. Fasel, *Chimia* **2009,** *63(3)*, 122. c) S. M. Barlow, R. Raval, *Surf. Sci. Rep.* **2003,** *50(6-8)*, 201-341.
[6] a) S. Lukas, G. Witte, C. Wöll, *Phys. Rev. Lett.* **2001,** *88(2)*, 028301. b) W. Xiao, P. Ruffieux, K. Ait-Mansour, O. Gröning, K. Palotas, W. A. Hofer, P. Gröning; R. Fasel, *J. Phys. Chem. B* **2006,** *111*, 21394-21398. c) J. Wang, I. Kaur, B. Diaconescu, J.-M. Tang, G. P. Miller, K. Pohl, *ACS Nano* **2011,** *5(3)*, 1792-1797.
[7] J. Götzen, S. Lukas, A. Birkner, G. Witte, *Surf. Sci.* **2011,** *605(5-6)*, 577-581.
[8] a) A. Hinderhofer, F. Schreiber, *Chem. Phys. Chem.* **2012,** *13*, 628. b) A. I. Kitaigorodsky, Mixed Crystals. Springer Series in Solid-State Sciences Vol. 33 Springer-Verlag: Berlin, 1984.
[9] T. Breuer, G. Witte, *J. Chem. Phys.* **2013,** *138*, 114901.
[10] a) S. Heutz, R. Cloots, T. S. Jones, *Appl. Phys. Lett.* **2000,** *77(24)*, 3938. b) G. Koller, S. Berkebile, J. R. Krenn, F. P. Netzer, M. Oehzelt, T. Haber, R. Resel, M. G. Ramsey, *Nano Lett.* **2006,** *6(6)*, 1207-1212. c) W. Chen, D. C. Qi, H. Huang, X. Gao, A. T. S. Wee, *Adv. Funct. Mat.* **2011,** *21* 410-424.

[11] a) N. S. Sariciftci, *Quant. Electr.* **1995,** *19(2)*, 131-159. b) S. Yoo, B. Domercq, B. Kippelen, *Appl. Phys. Lett.* **2004,** *85(22)*, 5427-5429.
[12] S. J. Noever, S. Fischer, B. Nickel, *Adv. Mat.* **2013,** *25(15)*, 2147-2151.
[13] a) I. Salzmann, S. Duhm, R. Opitz R. L. Johnson, J. P. Rabe, N. Koch, *J. Appl. Phys.* **2008,** *104(11)*, 114518. b) Y. Zhang, S. K. Pregler, J. D. Myers, J. Ouyang, S.B. Sinnott, J. Xue, *J. Vac. Sci. Technol.* **2009,** *B27(1)*, 169.
[14] a) W. Jin, D. B. Dougherty, W. G. Cullen, S. Robey, J. E. Reutt-Robey, *Langmuir* **2009,** *25(17)*, 9857. b) J. A. Smerdon, R. B. Rankin, J. P. Greeley, N. P. Guisinger, J. R. Guest, *ACS Nano* **2013,** *7(4)*, 3086-94.
[15] B. R. Conrad, J. Tosado, G. Dutton, D. B. Dougherty, W. Jin, T. Bonnen, A. Schuldenfrei, W. G. Cullen, E. D. Williams, J. E. Reutt-Robey, S. W. Robey, *Appl. Phys. Lett.* **2009,** *95*, 213302.
[16] a) R. A. Cantrell, P. A. Clancy, *Surf. Sci.* **2008,** *602*, 3499. b) L. Muccioli, G. D'Avino, C. Zannoni, *Adv. Mater.* **2011,** *23*, 4532.
[17] R. A. Cantrell, C. James, P. Clancy, *Langmuir* **2011,***27*, 9944.
[18] Y. T. Fu, C. Risko, J.-L. Bredas, *Adv. Mater.* **2013**, *25*, 878.
[19] Y. P. Yi, V. Coropceanu, J.-L. Bredas, *J. Am. Chem. Soc.* **2009,** *131(43)*, 15777.
[20] S. Verlaak, D. Beljonne, D. Cheyns, C. Rolin, M. Linares, F. Castet, J. Cornil, P. Heremans, *Adv. Funct. Mater.* **2009**, *19*, 3809.
[21] C. Tao, T. J. Stasevich, W. G. Cullen, T. L. Einstein, E. D. Williams, *Nano Lett.* **2007,** *7(6)*, 1495.
[22] I. P. M. Bouchoms, W. A. Schoonveld, J. Vrijmoeth, T. M. Klapwijk, *Synth. Met.* **1999,** *104*, 175.
[23] G. Witte, K. Hänel, S. Söhnchen, C. Wöll, *Appl. Phys. A* **2006,** *82*, 447-455.
[24] D. Käfer, G. Witte, C. Wöll, *Appl. Phys. A* **2009,** *95*, 273-284.
[25] D. Käfer, K. Ruppel, G. Witte, *Phys. Rev. B* **2007,** *75*, 085309.
[26] Since at elevated temperatures the dynamical motion and molecular displacements are thermally activated, the projected intermixture and nucleation is expected to occur in particular at room temperature or above. As presented in Fig. 2, however no evidence for this behavior has been found.

SUPPORTING INFORMATION

Diffusion-controlled growth of molecular hetero-structures: fabrication of 2D, 1D and 0-Dimensional C_{60}-nanostructures on pentacene substrates

Advanced Materials

Tobias Breuer and Gregor Witte
Molekulare Festkörperphysik, Philipps-Universität Marburg, D-35032 Marburg, Germany

EXPERIMENTAL DETAILS

Scanning electron microscopy (SEM, Jeol JSM-7500F operated at 20 kV acceleration voltage) was applied to obtain additional, complementary information about the lateral ordering of the interface. The crystalline orientation of selected samples was determined from XRD data acquired with a diffractometer (Bruker D8 Discovery) using Cu K_α radiation (λ=1.54056 Å) and a LynxEye detector.

NEXAFS measurements were carried out at the HE-SGM dipole beamline at the synchrotron storage ring facility BESSY II in Berlin (Germany). The spectra were recorded by measuring the secondary electron yield as function of the photon energy of the linearly polarized incident synchrotron light (polarization factor 91%). The exit slit of the grating monochromator was chosen such that an energy resolution of about 300 meV was achieved. To enhance the surface sensitivity, a retarding field of –150 eV was applied to the entrance grid of the channel plate detector (*partial electron yield*). To calibrate the absolute energy scale of the NEXAFS spectra, a simultaneously recorded signal of the photocurrent from a carbon coated gold grid in the incident beam was used which exhibits a sharp resonance at 284.9 eV. All NEXAFS raw data have been normalized with respect to the incident photon flux and considering the energy dependent transmission characteristic of the monochromator grating. Furthermore, the signal contributions from the C_{60} layers have been subtracted prior to the orientation determination of the PEN films. To improve the statistical reliability, all spectra have been acquired twice at four different angles ($\theta = 30°, 55°, 70°, 90°$). The assignment of the peaks to π^*-transitions bases on [1] and [2].

HIGHER AMOUNTS OF C_{60} DEPOSITED ON PEN MULTILAYERS

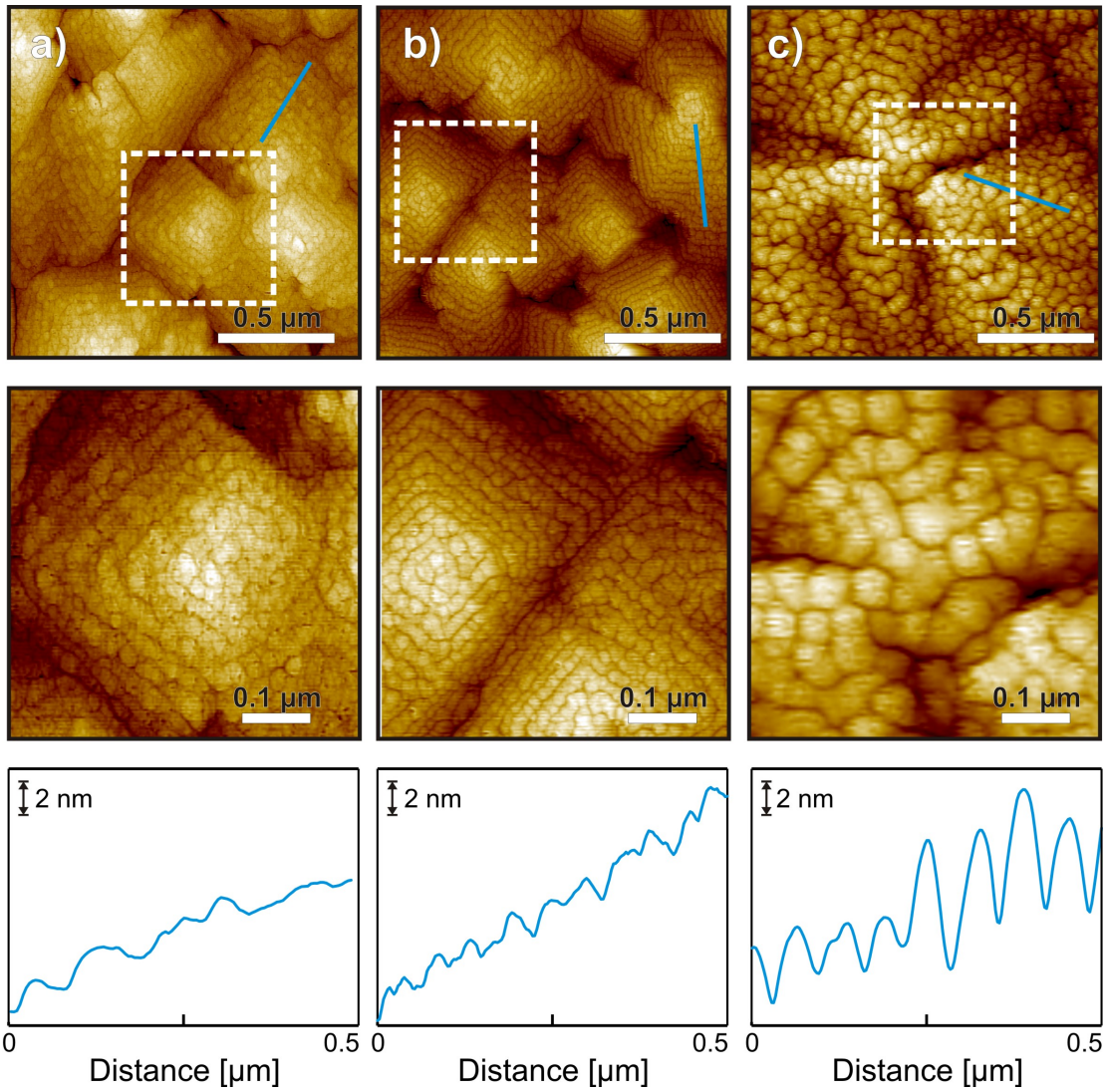

Figure S 1: AFM micrographs of 5 nm C_{60} on 30 nm PEN where the substrate temperature during C_{60} deposition was a) 145 K, b) 200 K, c) 300 K

Additionally to the temperature-dependent series of the C_{60} / PEN interfaces discussed in the main text, where 0.5 nm C_{60} have been deposited at various substrate temperatures, such a series has also been conducted for thicker C_{60} films to find out whether also for comparably high C_{60} amounts (5 nm), the observed effects remain valid. In Fig S 1 the morphologies of such junctions where the sample temperature during C_{60} deposition were 145 K (a), 200 K (b) and 300 K (c) are compared.

Clearly, the morphology of the deposition at 145 K and 200 K are equal such that the interface between the fullerene and PEN is rather smooth and the bottom PEN terrace steps remain visible. The PEN islands are covered quite equally and the C_{60} film exhibits comparably low roughness. The deposition of C_{60} at higher temperature however leads to a significant rougher C_{60} film, where the individual cluster are of increased diameter and exhibit heights of up to 15 nm.

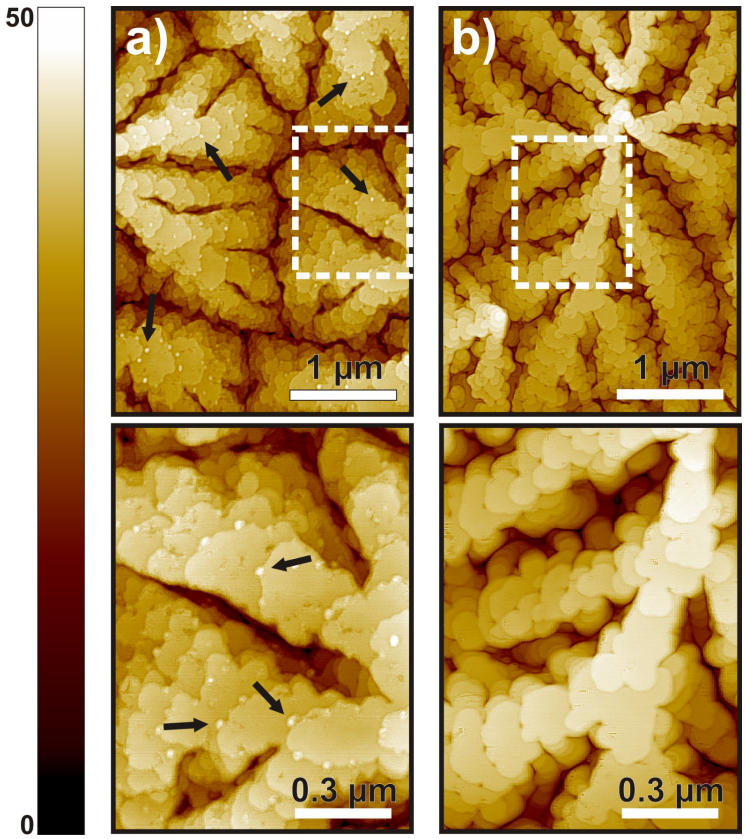

Figure S 2: AFM micrographs of a) 5 nm PEN, b) 10 nm PEN deposited onto 0.5 nm C_{60} on 30 nm PEN, where the sample temperature was 300 K during all deposition processes.

COMPLETE BURIFICATION OF C_{60} CLUSTERS (0D) BY PEN

As discussed in the main text, deposition of 5 nm pentacene onto 0.5 nm C_{60} on 30 nm PEN does not completely bury the C_{60} clusters when all depositions are conducted at 300 K. Thus, some C_{60} clusters remain visible after this deposition process due to their great heights (black arrows in Fig S 2 a)). However, deposition of higher amounts of pentacene (10 nm) results in complete burification of these clusters and a growth mode is observed that corresponds very well to the one of pure pentacene (cf. Fig S 2 b)).

SCANNING ELECTRON MICROSCOPY

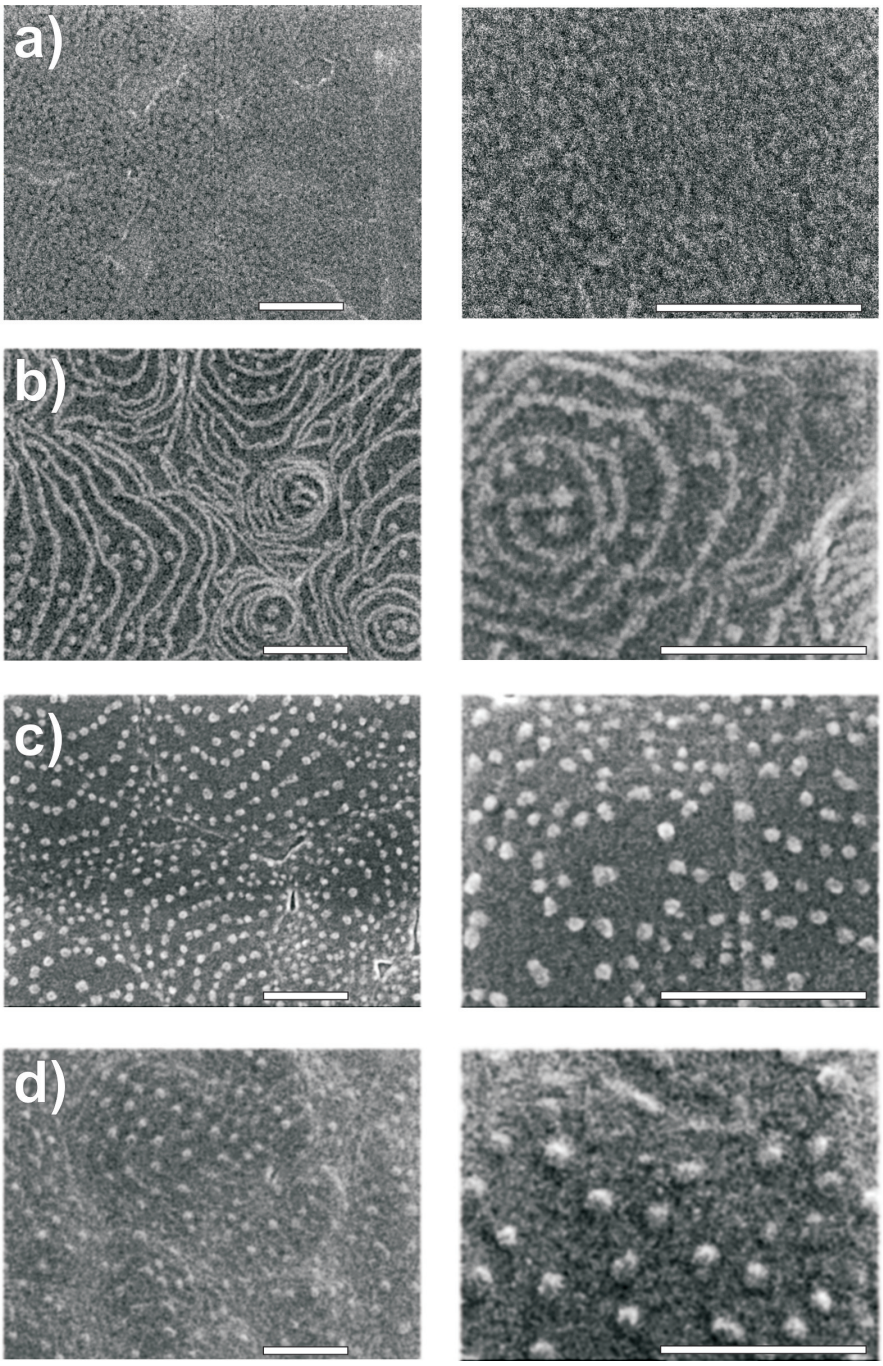

Figure S 3: SEM micrographs of 0.5 nm C_{60} deposited onto 30 nm PEN where the sample temperature during C_{60} deposition was a) 145 K, b) 240 K, c) 300 K, d) 345 K. All scale bars correspond to 200 nm.

Fig. S 3 shows micrographs from scanning electron microscopy. Due to the high lateral resolution of this technique, these images allowed to determine the cluster size of the C_{60} clusters more precisely than by means of atomic force microscopy. Furthermore, these images support the trends discussed within the main paper.

X-RAY DIFFRACTION

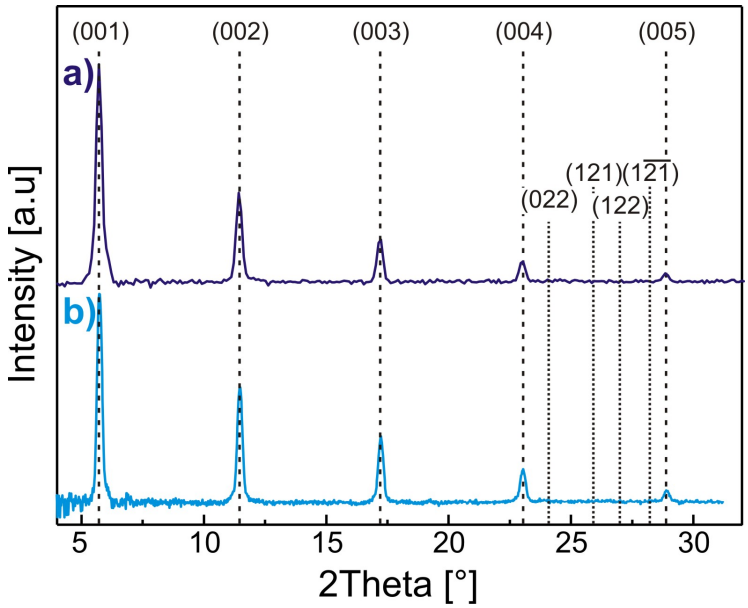

Figure S 4: XRD patterns of a) pure PEN thin film (30 nm), b) 5 nm PEN on 0.5 nm C_{60} on 30 nm PEN, where the sample temperature was 300 K during all deposition processes. Dashed lines correspond to the (00n) peak positions of the PEN thin film phase, while dotted lines correspond to typically observed peaks for recumbent orientations.

Though x-ray diffraction does not allow the exclusive determination of the orientation of PEN capping layers on top of PEN / C_{60} interfaces because of contributions from the bottom multilayer due to the high penetration depth of x-rays, the analysis of those patterns nevertheless allows to draw some conclusions. First, they prove the crystalline, upright (001) orientation of PEN in the multilayers (Fig. S 4 a) and b)) in the PEN thin-film phase, as the (00n)-peaks of the thin film phase at positions of 5.73°, 11.48°, 17.26°, 23.08° and 28.99° are found. Furthermore, the absence of diffraction peaks related to lying configurations of pentacene, as found in the case of pentacene on single-crystalline gold (111) surfaces [1], like the (022), (121), (122) and ($1\bar{2}1$) peaks of the Siegrist-phase (sketched in Fig. S 4 by dotted lines) allows to conclude that no crystalline pentacene islands in lying configurations are formed upon deposition of the pentacene capping layer. The presented data were acquired for capping layers deposited onto the 0D C_{60} clusters. In the case of C_{60} nanostructures of different dimensionality (prepared by different subtrate temperatures during the C_{60} evaporation process), also no evidence was found for lying species. However, this does not mean that all pentacene molecules are in upright configuration, as nevertheless non-crystalline regions with more recumbent molecular orientation may exist, which cannot be determined by means of x-ray diffraction. In turn, this information can be obtained by analysis of the NEXAFS-spectra.

NEXAFS SPECTROSCOPY

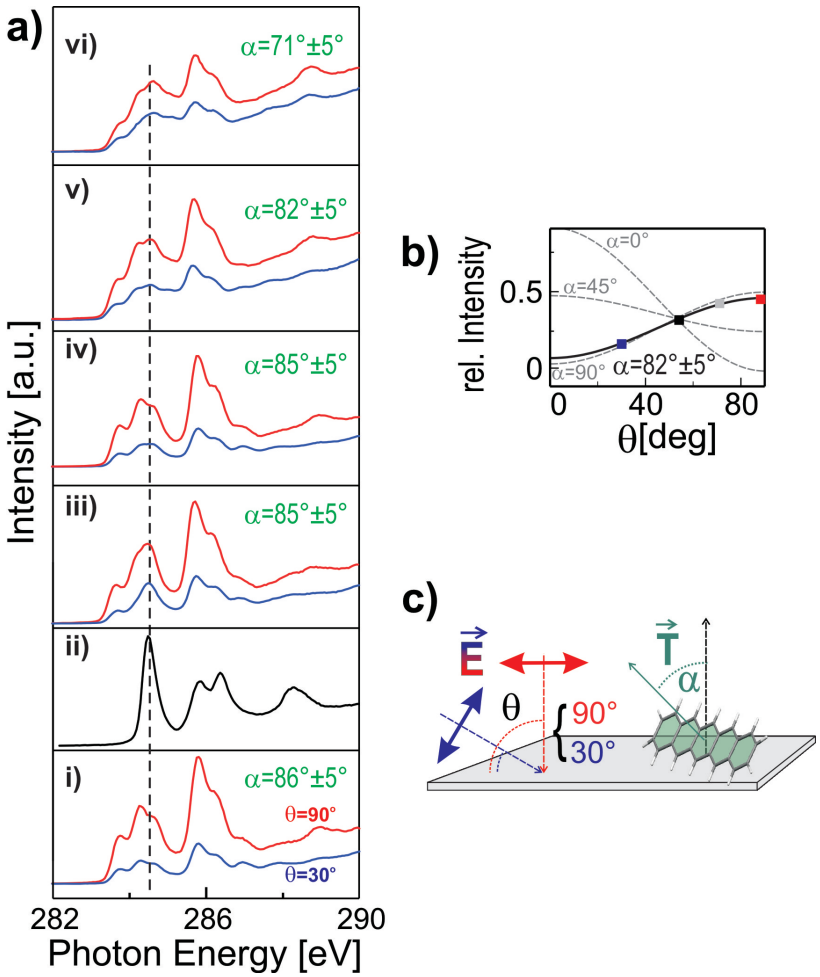

Figure S 5: a) C1s NEXAFS-spectra of i) bare PEN bottom layer on SiO_2, ii) C_{60}[4], iii) 0.5 nm C_{60} on PEN, iv) PEN on 0D C_{60} nanostructure (substrate temperature during C_{60} deposition 300 K), v) PEN on 1D C_{60} nanostructure (substrate temperature during C_{60} deposition 240 K K) vi) PEN on 2D C_{60} nanostructure (substrate temperature during C_{60} deposition 145 K K). b) examplary evaluation of dichroism, c) denotation of angles α and θ.

Utilizing the dichroism of x-ray absorption, NEXAFS spectroscopy allows to determine the average molecular orientation in thin films. The exact intensity dependence for π^*-transitions for substrates of at least threefold-symmetry is given by [3]:

$$I_{\pi*} \propto P\cos^2\theta\left(\frac{3\cos^2\alpha}{2}-\frac{1}{2}\right)+\frac{\sin^2\alpha}{2}, \tag{1}$$

where θ is the relative orientation between the transition dipole moment (TDM) of the excitation and the polarization of the synchrotron light (cf. Fig. S 5 c), P is the polarization factor of the beamline and α is the average molecular orientation. By fitting this formula in α to the experimental values, α can be determined (cf. Fig. S 5 b). Note that α - different from angles derived from x-ray diffraction - is an averaged value and does not represent the exact orientation of all molecules but results from contributions of all - regardless whether crystalline or amorphous - orientations within the sample. In the case of PEN/C_{60} hetero-structures, the isotropic contribution of C_{60} has to be subtracted from the spectra to enable the determination of the PEN molecules.

The average molecular orientations determined for the different PEN/C_{60} interfaces (cf. Fig. S 5) are presented in table S I.

	Average Orientation
bare PEN bottom layer on SiO_2	$86^\circ \pm 5^\circ$
C_{60} on PEN	$85^\circ \pm 5^\circ$
PEN capping layer on 2D-C_{60}	$85^\circ \pm 5^\circ$
PEN capping layer on 1D-C_{60}	$82^\circ \pm 5^\circ$
PEN capping layer on 0D-C_{60}	$71^\circ \pm 5^\circ$

Table S I: Average orientation of pentacene determined form NEXAFS-measurements

[1] Käfer, D.; Ruppel, K.; Witte, G. Growth of pentacene on clean and modified gold surfaces. *Phys. Rev. B* **2007,** *75*, 085309.
[2] Terminello, L. J.; Shuh, D. K.; Himpsel, F. J.; Lapiano-Smith, D. A.; Stöhr, J.; Bethune, D. S.; Meijer, G. Unfilled orbitals of C_{60} and C_{70} from carbon K-shell X-ray absorption fine structure. *Chem. Phys. Lett.* **1991**, *82 (5)*, 491-496.
[3] Stöhr, J. edited by Gomer, R. NEXAFS Spectroscopy. Springer-Verlag: Berlin, 1992.
[4] Due to the its circular shape, C_{60} does not exhibit any dichroism. Therefore we present a spectrum of a polycrystalline C_{60} sample as reference.

5.10 Article X: Polarization resolved absorption in highly ordered organic semiconductors: One dimensional anisotropic response beyond the Davydov splitting

K. Kolata, T. Breuer, J. Kunert, G. Witte and S. Chatterjee, in preparation (2013).

5.10.1 Abstract

We identify distinct excitonic resonances in the optical absorption spectra in highly-ordered crystalline perfluropentacene films. Polarization-resolved measurements on single-crystalline domains grown on NaF and KCl substrates reveal the appearance of a quasi-one-dimensional delocalized exciton band along the crystalline axis with parallel stacking of the π-electron systems. This goes beyond the standard Davydov-splitting of excitons due to unequal molecules in the crystal unit cell. No significant structural of phase changes are found for lattice temperature in the range from 10 to 300 K.

5.10.2 Methods

Optical Absorption Spectroscopy, Organic Molecular Beam Deposition, Polarized Optical Microscopy, X-Ray Diffraction

5.10.3 Own Contribution

The preparation and structural characterization of all samples has been conducted by me. I have performed the XRD measurements and acquired the polarized optical micrographs, written the corresponding paragraph in the manuscript and prepared these data for publication. The optical absorption spectroscopy measurements have been conducted by Kolja Kolata and Jan Kunert under supervision of Sangam Chatterjee. The interpretation of all data has developed from joint discussions of all authors.

Scientific Curriculum Vitae

Wissenschaftlicher Werdegang (Scientific Curriculum Vitae in German)

Bibliography

[1] http://www.heliatek.com/wp-content/uploads/2013/01/130116_PR_Heliatek_achieves_record_cell_effiency_for_OPV.pdf. 19.06.2013

[2] http://www.basf.com/group/corporate/chemistryworldtour/en/innovationen/organic-solar-cells. 19.06.2013

[3] http://news.merck.de/N/0/6990D73E2AFB0148C1257B8500464361/$File/LC20130610en.pdf. 19.06.2013

[4] Dimitrakopoulos, C. D. ; Mascaro, D. J.: Organic thin-film transistors: A review of recent advances. In: *IBM Journal of Research and Development* 45 (2001), Nr. 1, 11-27. http://dx.doi.org/10.1147/rd.451.0011. – DOI 10.1147/rd.451.0011

[5] http://www.ge.com/audio_video/ge/innovation/ge_oleds_the_future_of_lighting.html. 19.06.2013

[6] http://techon.nikkeibp.co.jp/english/NEWS_EN/20110217/189647/. 19.06.2013

[7] http://www.oled-info.com/lg-start-shipping-their-curved-oled-tv-korea-few-days. 19.06.2013

[8] http://www.printedelectronicsnow.com/whitepapers/download/7/NMOEMaterials_032408.pdf. 19.06.2013

[9] http://www.strategyr.com/Organic_Electronics_Market_Report.asp. 19.06.2013

[10] http://www.icis.com/Articles/2008/07/14/9139393/market-for-organic-electronics-materials-is-growing.html. 19.06.2013

[11] http://www.oled-info.com/idtechex-sees-13-billion-oled-lighting-market-2013. 19.06.2013

[12] Vollmer, A. ; Weiss, H. ; Rentenberger, S. ; Salzmann, I. ; Rabe, J.P. ; Koch, N.: The interaction of oxygen and ozone with pentacene. In: *Surface Science* 600 (2006), Nr. 18, 4004 - 4007. http://dx.doi.org/10.1016/j.susc.2005.11.067. – DOI 10.1016/j.susc.2005.11.067

[13] Yang, H. ; Yang, L. ; Ling, M.-M. ; Lastella, S. ; Gandhi, D. D. ; Ramanath, G. ; Bao, Z. ; Ryu, C. Y.: Aging Susceptibility of Terrace-Like Pentacene Films. In: *The Journal of Physical Chemistry C* 112 (2008), Nr. 42, 16161-16165. http://dx.doi.org/10.1021/jp8055224. – DOI 10.1021/jp8055224

[14] Zhu, Z.-T. ; Mason, J.T. ; Dieckmann, R. ; Malliaras, G. G.: Humidity sensors based on pentacene thin-film transistors. In: *Applied Physics Letters* 81 (2002), Nr. 24, 4643-4645. http://dx.doi.org/10.1063/1.1527233. – DOI 10.1063/1.1527233

[15] Li, D. ; Borkent, E.-J. ; Nortrup, R. ; Moon, H. ; Katz, H. ; Bao, Z.: Humidity effect on electrical performance of organic thin-film transistors. In: *Applied Physics Letters* 86 (2005), Nr. 4, 042105. http://dx.doi.org/10.1063/1.1852708. – DOI 10.1063/1.1852708

[16] Qiu, Y. ; Hu, Y. ; Dong, G. ; Wang, Li. ; Xie, J. ; Ma, Y.: H2O effect on the stability of organic thin-film field-effect transistors. In: *Applied Physics Letters* 83 (2003), Nr. 8, 1644-1646. http://dx.doi.org/10.1063/1.1604193. – DOI 10.1063/1.1604193

[17] Schwoerer, M. ; Wolf, H. C.: *Organic Molecular Solids*. Wiley-VCH, 2007

[18] Katz, H. E. ; Bao, Z. ; Gilat, S. L.: Synthetic Chemistry for Ultrapure, Processable, and High-Mobility Organic Transistor Semiconductors. In: *Accounts of Chemical Research* 34 (2001), Nr. 5, 359-369. http://dx.doi.org/10.1021/ar990114j. – DOI 10.1021/ar990114j

[19] Podzorov, V. ; Menard, E. ; Borissov, A. ; Kiryukhin, V. ; Rogers, J. A. ; Gershenson, M. E.: Intrinsic Charge Transport on the Surface of Organic Semiconductors. In: *Physical Review Letters* 93 (2004), 086602. http://dx.doi.org/10.1103/PhysRevLett.93.086602. – DOI 10.1103/PhysRevLett.93.086602

[20] Reese, C. ; Bao, Z.: High-Resolution Measurement of the Anisotropy of Charge Transport in Single Crystals. In: *Advanced Materials* 19 (2007), Nr. 24, 4535–4538. http://dx.doi.org/10.1002/adma.200701139. – DOI 10.1002/adma.200701139

[21] Bock, C. ; Pham, D. V. ; Kunze, U. ; Kafer, D. ; Witte, G. ; Terfort, A.: Influence of anthracene-2-thiol treatment on the device parameters of pentacene bottom-contact transistors. In: *Applied Physics Letters* 91 (2007), Nr. 5, 052110. http://dx.doi.org/10.1063/1.2767235. – DOI 10.1063/1.2767235

[22] Boudinet, D. ; Benwadih, M. ; Qi, Y. ; Altazin, S. ; Verilhac, J.-M. ; Kroger, M. ; Serbutoviez, C. ; Gwoziecki, R. ; Coppard, R. ; Blevennec, G. L. ; Kahn, A. ; Horowitz, G.: Modification of gold source and drain electrodes by self-assembled monolayer in staggered n- and p-channel organic thin film transistors. In: *Organic Electronics* 11 (2010), Nr. 2, 227 - 237. http://dx.doi.org/http://dx.doi.org/10.1016/j.orgel.2009.10.021. – DOI http://dx.doi.org/10.1016/j.orgel.2009.10.021

[23] Di, C. ; Yu, G. ; Liu, Y. ; Xu, X. ; Wei, D. ; Song, Y. ; Sun, Y. ; Wang, Y. ; Zhu, D. ; Liu, J. ; Liu, X. ; Wu, D.: High-Performance Low-Cost Organic Field-Effect Transistors with Chemically Modified Bottom Electrodes. In: *Journal of the American Chemical Society* 128 (2006), Nr. 51, 16418-16419. http://dx.doi.org/10.1021/ja066092v. – DOI 10.1021/ja066092v

[24] Schroeder, R. ; Majewski, L. A. ; Grell, M.: Improving organic transistor performance with Schottky contacts. In: *Applied Physics Letters* 84 (2004), Nr. 6, 1004-1006. http://dx.doi.org/10.1063/1.1645993. – DOI 10.1063/1.1645993

[25] Günes, S. ; Neugebauer, H. ; Sariciftci, N. S.: Conjugated Polymer-Based Organic Solar Cells. In: *Chemical Reviews* 107 (2007), Nr. 4, 1324-1338. http://dx.doi.org/10.1021/cr050149z. – DOI 10.1021/cr050149z

[26] Halls, J. J. M. ; Walsh, C. A. ; Greenham, N. ; Marseglia, E. A. ; Friend, R. ; Moratti, S. C. ; Holmes, A.: Efficient photodiodes from interpenetrating polymer networks. In: *Nature* 376 (1995), Nr. 6540, 498–500. http://dx.doi.org/10.1038/376498a0. – DOI 10.1038/376498a0

[27] Yu, G. ; Gao, J. ; Hummelen, J. C. ; Wudl, F. ; Heeger, A. J.: Polymer Photovoltaic Cells: Enhanced Efficiencies via a Network of Internal Donor-Acceptor Heterojunctions. In: *Science* 270 (1995), Nr. 5243, 1789-1791. http://dx.doi.org/10.1126/science.270.5243.1789. – DOI 10.1126/science.270.5243.1789

[28] Klauk, H. ; Halik, M. ; Zschieschang, U. ; Schmid, G. ; Radlik, W. ; Weber, W.: High-mobility polymer gate dielectric pentacene thin film transistors. In: *Journal of Applied Physics* 92 (2002), Nr. 9, 5259-5263. http://dx.doi.org/10.1063/1.1511826. – DOI 10.1063/1.1511826

[29] Breuer, T. ; Witte, G.: Epitaxial growth of perfluoropentacene films with predefined molecular orientation: A route for single-crystal optical studies. In: *Physical Review B* 83 (2011), 155428. http://dx.doi.org/10.1103/PhysRevB.83.155428. – DOI 10.1103/PhysRevB.83.155428

[30] Haas, B. ; Beyer, A. ; Witte, W. ; Breuer, T. ; Witte, G. ; Volz, K.: Application of transmission electron microscopy for microstructural characterization of perfluoropentacene thin films. In: *Journal of Applied Physics* 110 (2011), Nr. 7, 073514. http://dx.doi.org/10.1063/1.3646549. – DOI 10.1063/1.3646549

[31] Breuer, T. ; Salzmann, I. ; Götzen, J. ; Oehzelt, M. ; Morherr, A. ; Koch, N. ; Witte, G.: Interrelation between Substrate Roughness and Thin-Film Structure of Functionalized Acenes on Graphite. In: *Crystal Growth & Design* 11 (2011), Nr. 11, 4996-5001. http://dx.doi.org/10.1021/cg200894y. – DOI 10.1021/cg200894y

[32] Marks, M. ; Schmidt, C. ; Schwalb, C. H. ; Breuer, T. ; Witte, G. ; Höfer, U.: Temperature Dependent Structural Phase Transition at the Perfluoropen-

tacene/Ag(111) Interface. In: *The Journal of Physical Chemistry C* 116 (2012), Nr. 2, 1904-1911. http://dx.doi.org/10.1021/jp2094577. – DOI 10.1021/jp2094577

[33] Breuer, T. ; Celik, M. A. ; Jakob, P. ; Tonner, R. ; Witte, G.: Vibrational Davydov Splittings and Collective Mode Polarizations in Oriented Organic Semiconductor Crystals. In: *The Journal of Physical Chemistry C* 116 (2012), Nr. 27, 14491-14503. http://dx.doi.org/10.1021/jp304080g. – DOI 10.1021/jp304080g

[34] Schmidt, C. ; Breuer, T. ; Wippermann, S. ; Schmidt, W. G. ; Witte, G.: Substrate Induced Thermal Decomposition of Perfluoro-Pentacene Thin Films on the Coinage Metals. In: *The Journal of Physical Chemistry C* 116 (2012), Nr. 45, 24098-24106. http://dx.doi.org/10.1021/jp307316r. – DOI 10.1021/jp307316r

[35] Salzmann, I. ; Moser, A. ; Oehzelt, M. ; Breuer, T. ; Feng, X. ; Juang, Z.-Y. ; Nabok, D. ; Della Valle, R. G. ; Duhm, S. ; Heimel, G. ; Brillante, A. ; Venuti, E. ; Bilotti, I. ; Christodoulou, C. ; Frisch, J. ; Puschnig, P. ; Draxl, C. ; Witte, G. ; Müllen, K. ; Koch, N.: Epitaxial Growth of Pi-Stacked Perfluoropentacene on Graphene-Coated Quartz. In: *ACS Nano* 6 (2012), Nr. 12, 10874-10883. http://dx.doi.org/10.1021/nn3042607. – DOI 10.1021/nn3042607

[36] Breuer, T. ; Witte, G.: Thermally activated intermixture in pentacene-perfluoropentacene heterostructures. In: *The Journal of Chemical Physics* 138 (2013), Nr. 11, 114901. http://dx.doi.org/10.1063/1.4795004. – DOI 10.1063/1.4795004

[37] Schwaben, J. ; Münster, N. ; Breuer, T. ; Klues, M. ; Harms, K. ; Witte, G. ; Koert, U.: Synthesis and Solid-State Structures of 6,13-Bis(trifluoromethyl)- and 6,13-Dialkoxypentacene. In: *European Journal of Organic Chemistry* 2013 (2013), Nr. 9, 1639-1643. http://dx.doi.org/10.1002/ejoc.201201714. – DOI 10.1002/ejoc.201201714

[38] Kelley, T. W. ; Muyres, D. V. ; Baude, P. F. ; Smith, T. P. ; Jones, T. D.: High Performance Organic Thin Film Transistors. In: *MRS Proceedings* 771 (2003), 0. http://dx.doi.org/10.1557/PROC-771-L6.5. – DOI 10.1557/PROC–771–L6.5

[39] Witte, G. ; Wöll, C.: Growth of aromatic molecules on solid substrates for applications in organic electronics. In: *Journal of Materials Research* 19 (2004), 6, 1889–1916. http://dx.doi.org/10.1557/JMR.2004.0251. – DOI 10.1557/JMR.2004.0251

[40] Bouchoms, I.P.M. ; Schoonveld, W.A. ; Vrijmoeth, J. ; Klapwijk, T.M.: Morphology identification of the thin film phases of vacuum evaporated pentacene on SiO2 substrates. In: *Synthetic Metals* 104 (1999), Nr. 3, 175 - 178. http://dx.doi.org/10.1016/S0379-6779(99)00050-8. – DOI 10.1016/S0379–6779(99)00050–8

[41] Akimichi, H. ; Inoshita, T. ; Hotta, S. ; Noge, H. ; Sakaki, H.: Structure of pentacene/tetracene superlattices deposited on glass substrate. In: *Applied Physics*

Letters 63 (1993), Nr. 23, 3158-3160. http://dx.doi.org/10.1063/1.110234. – DOI 10.1063/1.110234

[42] Kiyomura, T. ; Nemoto, T. ; Yoshida, K. ; Minari, T. ; Kurata, H. ; Isoda, S.: Epitaxial growth of pentacene thin-film phase on alkali halides. In: *Thin Solid Films* 515 (2006), Nr. 2, 810 - 813. http://dx.doi.org/10.1016/j.tsf.2005.12.228. – DOI 10.1016/j.tsf.2005.12.228

[43] Kakudate, T. ; Yoshimoto, N. ; Kawamura, K. ; Saito, Y.: Observation of epitaxial growth of pentacene thin films on KCl substrate by X-ray diffractometry. In: *Journal of Crystal Growth* 306 (2007), Nr. 1, 27 - 32. http://dx.doi.org/10.1016/j.jcrysgro.2007.02.044. – DOI 10.1016/j.jcrysgro.2007.02.044

[44] Götzen, J. ; Käfer, D. ; Wöll, C. ; Witte, G.: Growth and structure of pentacene films on graphite: Weak adhesion as a key for epitaxial film growth. In: *Physical Review B* 81 (2010), 085440. http://dx.doi.org/10.1103/PhysRevB.81.085440. – DOI 10.1103/PhysRevB.81.085440

[45] Käfer, D. ; Ruppel, L. ; Witte, G.: Growth of pentacene on clean and modified gold surfaces. In: *Physical Review B* 75 (2007), 085309. http://dx.doi.org/10.1103/PhysRevB.75.085309. – DOI 10.1103/PhysRevB.75.085309

[46] Käfer, D. ; Witte, G.: Evolution of pentacene films on Ag(111): Growth beyond the first monolayer. In: *Chemical Physics Letters* 442 (2007), Nr. 4–6, 376 - 383. http://dx.doi.org/10.1016/j.cplett.2007.06.006. – DOI 10.1016/j.cplett.2007.06.006

[47] Helou, M. E. ; Lietke, E. ; Helzel, J. ; Heimbrodt, W. ; Witte, G.: Structural and optical properties of pentacene films grown on differently oriented ZnO surfaces. In: *Journal of Physics: Condensed Matter* 24 (2012), Nr. 44, 445012. http://dx.doi.org/10.1088/0953-8984/24/44/445012. – DOI 10.1088/0953–8984/24/44/445012

[48] Lanzilotto, V. ; Sanchez-Sanchez, C. ; Bavdek, G. ; Cvetko, D. ; Lopez, M. F. ; Martin-Gago, J. A. ; Floreano, L.: Planar Growth of Pentacene on the Dielectric TiO_2(110) Surface. In: *The Journal of Physical Chemistry C* 115 (2011), Nr. 11, 4664-4672. http://dx.doi.org/10.1021/jp111011z. – DOI 10.1021/jp111011z

[49] Campbell, R. B. ; Robertson, J. M. ; Trotter, J.: The crystal structure of hexacene, and a revision of the crystallographic data for tetracene. In: *Acta Crystallographica* 15 (1962), Nr. 3, 289–290. http://dx.doi.org/10.1107/S0365110X62000699. – DOI 10.1107/S0365110X62000699

[50] Siegrist, T. ; Kloc, C. ; Schön, J. H. ; Batlogg, B. ; Haddon, R. C. ; Berg, S. ; Thomas, G. A.: Enhanced Physical Properties in a Pentacene Polymorph. In: *Angewandte Chemie International Edition* 40 (2001), Nr. 9, 1732–1736. http://dx.doi.org/10.1002/1521-3773. – DOI 10.1002/1521–3773

[51] Schiefer, S. ; Huth, M. ; Dobrinevski, A. ; Nickel, B.: Determination of the Crystal Structure of Substrate-Induced Pentacene Polymorphs in Fiber Structured Thin Films. In: *Journal of the American Chemical Society* 129 (2007), Nr. 34, 10316-10317. http://dx.doi.org/10.1021/ja0730516. – DOI 10.1021/ja0730516

[52] Afzali, A. ; Dimitrakopoulos, C. D. ; Breen, T. L.: High-Performance, Solution-Processed Organic Thin Film Transistors from a Novel Pentacene Precursor. In: *Journal of the American Chemical Society* 124 (2002), Nr. 30, 8812-8813. http://dx.doi.org/10.1021/ja0266621. – DOI 10.1021/ja0266621

[53] Käbisch, S. ; Pingel, P. ; Rabe, J. P. ; Koch, N.: Substrate- and oxidation-induced roughness of individual terraces of pentacene thin films. In: *Thin Solid Films* 519 (2011), Nr. 6, 1857 - 1860. http://dx.doi.org/10.1016/j.tsf.2010.10.032. – DOI 10.1016/j.tsf.2010.10.032

[54] Schmidt, C.: *Eigenschaften fluorierter Aromaten an Metall/Organik-Grenzflächen*, Philipps-Universität Marburg, Diss., 2012

[55] Sakamoto, Y. ; Suzuki, T. ; Kobayashi, M. ; Gao, Y. ; Fukai, Y. ; Inoue, Y. ; Sato, F. ; Tokito, S.: Perfluoropentacene: High-Performance p-n Junctions and Complementary Circuits with Pentacene. In: *Journal of the American Chemical Society* 126 (2004), Nr. 26, 8138-8140. http://dx.doi.org/10.1021/ja0476258. – DOI 10.1021/ja0476258

[56] Delgado, M. C. R. ; Pigg, K. R. ; Silva Filho, D. A. ; Gruhn, N. E. ; Sakamoto, Y. ; Suzuki, T. ; Osuna, R. M. ; Casado, J. ; Hernandez, V. ; Navarrete, J. T. L. ; Martinelli, N. G. ; Cornil, J. ; Sanchez-Carrera, R. S. ; Coropceanu, V. ; Bredas, J.-L.: Impact of Perfluorination on the Charge-Transport Parameters of Oligoacene Crystals. In: *Journal of the American Chemical Society* 131 (2009), Nr. 4, 1502-1512. http://dx.doi.org/10.1021/ja807528w. – DOI 10.1021/ja807528w

[57] Inoue, Y. ; Sakamoto, Y. ; Suzuki, T. ; Kobayashi, M. ; Gao, Y. ; Tokito, S.: Organic Thin-Film Transistors with High Electron Mobility Based on Perfluoropentacene. In: *Japanese Journal of Applied Physics* 44 (2005), Nr. 6A, 3663-3668. http://dx.doi.org/10.1143/JJAP.44.3663. – DOI 10.1143/JJAP.44.3663

[58] Salzmann, I. ; Duhm, S. ; Heimel, G. ; Rabe, J. P. ; Koch, N. ; Oehzelt, M. ; Sakamoto, Y. ; Suzuki, T.: Structural Order in Perfluoropentacene Thin Films and Heterostructures with Pentacene. In: *Langmuir* 24 (2008), Nr. 14, 7294-7298. http://dx.doi.org/10.1021/la800606h. – DOI 10.1021/la800606h

[59] Hinderhofer, A. ; Frank, C. ; Hosokai, T. ; Resta, A. ; Gerlach, A. ; Schreiber, F.: Structure and morphology of co-evaporated pentacene-perfluoropentacene thin films. In: *The Journal of Chemical Physics* 134 (2011), 104702. http://dx.doi.org/10.1063/1.3557476. – DOI 10.1063/1.3557476

[60] Broch, K. ; Heinemeyer, U. ; Hinderhofer, A. ; Anger, F. ; Scholz, R. ; Gerlach, A. ; Schreiber, F.: Optical evidence for intermolecular coupling in mixed films of pentacene and perfluoropentacene. In: *Physical Review. B* 83 (2011), 245307. http://dx.doi.org/10.1103/PhysRevB.83.245307. – DOI 10.1103/PhysRevB.83.245307

[61] Anger, F. ; Ossó, J. O. ; Heinemeyer, U. ; Broch, K. ; Scholz, R. ; Gerlach, A. ; Schreiber, F.: Photoluminescence spectroscopy of pure pentacene, perfluoropentacene and mixed thin films. In: *The Journal of Chemical Physics* 136 (2012), 054701. http://dx.doi.org/doi:10.1063/1.3677839

[62] http://www3.physik.uni-greifswald.de/method/afm/AFM_laser.gif. 10.05.2013

[63] http://www.schaefer-tec.com/en/germany/products/scanning-probe-microscopy/mikromasch.html. 10.05.2013

[64] http://www.doitpoms.ac.uk/tlplib/afm/tip_surface_interaction.php. 10.05.2013

[65] Gross, L. ; Mohn, F. ; Moll, N. ; Liljeroth, P. ; Meyer, G.: The Chemical Structure of a Molecule Resolved by Atomic Force Microscopy. In: *Science* 325 (2009), Nr. 5944, 1110-1114. http://dx.doi.org/10.1126/science.1176210. – DOI 10.1126/science.1176210

[66] http://www.doitpoms.ac.uk/tlplib/afm/tip_related.php. 20.06.2013

[67] Eleftheriou, E. ; Antonakopoulos, E. T. ; Binnig, G. K. ; Cherubini, G. ; Despont, M. ; Dholakia, A. ; Dürig, U. ; Lantz, M. A. ; Pozidis, H. ; Rothuizen, H. E. ; Vettiger, P.: Millipede - A MEMS-Based Scanning-Probe Data-Storage System. In: *IEEE Transactions on Magnetics* 39 (2003), 938-945. http://dx.doi.org/10.1109/TMAG.2003.808953. – DOI 10.1109/TMAG.2003.808953

[68] https://upload.wikimedia.org/wikipedia/commons/c/ca/Bragg.svg. 10.06.2013

[69] Reichelt, K. ; Lutz, H.O.: Hetero-epitaxial growth of vacuum evaporated silver and gold. In: *Journal of Crystal Growth* 10 (1971), Nr. 1, 103 - 107. http://dx.doi.org/10.1016/0022-0248(71)90052-2. – DOI 10.1016/0022–0248(71)90052–2

[70] DeRose, J.A. ; Thundat, T. ; Nagahara, L.A. ; Lindsay, S.M.: Gold grown epitaxially on mica: conditions for large area flat faces. In: *Surface Science* 256 (1991), Nr. 1–2, 102 - 108. http://dx.doi.org/10.1016/0039-6028(91)91204-B. – DOI 10.1016/0039–6028(91)91204–B

[71] Birkholz, M. ; Fewster, P. F. ; Genzel, C. ; Birkholz, M. (Hrsg.): *Thin Film Analysis by X-Ray Scattering*. Wiley VCH, 2006

[72] Hinderhofer, A. ; Heinemeyer, U. ; Gerlach, A. ; Kowarik, S. ; Jacobs, R. M. J. ; Sakamoto, Y. ; Suzuki, T. ; Schreiber, F.: Optical properties of pentacene

and perfluoropentacene thin films. In: *The Journal of Chemical Physics* 127 (2007), Nr. 19, 194705. http://dx.doi.org/10.1063/1.2786992. – DOI 10.1063/1.2786992

[73] Kronik, L. ; Stein, T. ; Refaely-Abramson, S. ; Baer, R.: Excitation Gaps of Finite-Sized Systems from Optimally Tuned Range-Separated Hybrid Functionals. In: *Journal of Chemical Theory and Computation* 8 (2012), Nr. 5, 1515-1531. http://dx.doi.org/10.1021/ct2009363. – DOI 10.1021/ct2009363

[74] Davydov, A. S.: The theory of molecular excitons. In: *Soviet Physics Uspekhi* 7 (1964), 145. http://dx.doi.org/10.1070/PU1964v007n02ABEH003659. – DOI 10.1070/PU1964v007n02ABEH003659

[75] Kasha, M. ; Rawls, H. R. ; El-Bayoumi, M. A.: The exciton model in molecular spectroscopy. In: *Pure and Applied Chemistry* 11 (1965), 371-392. http://dx.doi.org/10.1351/pac196511030371. – DOI 10.1351/pac196511030371

[76] Hafner, J.: Ab-initio simulations of materials using VASP: Density-functional theory and beyond. In: *Journal of Computational Chemistry* 29 (2008), Nr. 13, 2044–2078. http://dx.doi.org/10.1002/jcc.21057. – DOI 10.1002/jcc.21057

[77] Kresse, G. ; Furthmüller, J.: Efficient iterative schemes for *ab initio* total-energy calculations using a plane-wave basis set. In: *Physical Review B* 54 (1996), 11169–11186. http://dx.doi.org/10.1103/PhysRevB.54.11169. – DOI 10.1103/PhysRevB.54.11169

[78] Gazdzicki, P.: *Adsorption and Thermally Induced Reactions of Methanol on Bimetallic X/Ru(0001) Layers (X = Cu, Pt)*, Philipps-Universität Marburg, Diss., 2011

[79] Gazdzicki, P. ; Jakob, P.: Formation of Methoxy on Cu/Ru(0001) Layers. In: *The Journal of Physical Chemistry C* 115 (2011), Nr. 5, 1961-1968. http://dx.doi.org/10.1021/jp107981x. – DOI 10.1021/jp107981x

[80] Bougeard, D. ; Buback, M. ; Cao, A. ; Gerwert, K. ; Heise, H. M. ; Hoffmann, G. G. ; Jordanov, B. ; Kiefer, W. ; Korte, E.-H. ; Kuzmany, H. ; Leipertz, A. ; Lentz, E. ; Liquier, J. ; Röseler, A. ; Schnöckel, H. ; Schrader, B. ; Schrötter, H. W. ; Spiekermann, M. ; Taillandier, E. ; Willner, H. ; Schrader, B. (Hrsg.): *Infrared and Raman Spectroscopy: Methods and Applications*. VCH: Weinheim, 1995

[81] Roggo, Y. ; Chalus, P. ; Maurer, L. ; Lema-Martinez, C. ; Edmond, A. ; Jent, N.: A review of near infrared spectroscopy and chemometrics in pharmaceutical technologies. In: *Journal of Pharmaceutical and Biomedical Analysis* 44 (2007), Nr. 3, 683 - 700. http://dx.doi.org/10.1016/j.jpba.2007.03.023. – DOI 10.1016/j.jpba.2007.03.023

[82] Wartewig, S. ; Neubert, R. H.: Pharmaceutical applications of Mid-IR and Raman spectroscopy. In: *Advanced Drug Delivery Reviews* 57 (2005), Nr. 8, 1144 - 1170. http://dx.doi.org/10.1016/j.addr.2005.01.022. – DOI 10.1016/j.addr.2005.01.022

[83] Larkin, P.: *Infrared and Raman Spectroscopy; Principles and Spectral Interpretation.* Elsevier: Amsterdam, 2011

[84] Arnold, R.: *Struktur und Ordnung selbstordnender Monolagen aliphatischer und aromatischer Thiole auf Goldoberflaechen*, Lehrstuhl für Physikalische Chemie I - Ruhr-Universität Bochum, Diss., 2001

[85] Gottfried, J. M.: *CO Oxidation over Gold*, FU Berlin, Diss., 2003

[86] Feulner, P. ; Menzel, D.: Simple ways to improve "flash desorption" measurements from single crystal surfaces. In: *Journal of Vacuum Science and Technology* 17 (1980), Nr. 2, 662-663. http://dx.doi.org/10.1116/1.570537. – DOI 10.1116/1.570537

[87] Käfer, D.: *Characterization and Optimization of Growth and Electronic Structure of Organic Thin Films for Applications in Organic Electronics*, Ruhr-University Bochum, Diss., 2008

[88] Lüth, H. ; Lüth, H. (Hrsg.): *Solid Surfaces, Interfaces and Thin Films.* Springer, 2001

[89] Alagia, M. ; Baldacchini, C. ; Betti, M. G. ; Bussolotti, F. ; Carravetta, V. ; Ekstrom, U. ; Mariani, C. ; Stranges, S.: Core-shell photoabsorption and photoelectron spectra of gas-phase pentacene: Experiment and theory. In: *The Journal of Chemical Physics* 122 (2005), Nr. 12, 124305. http://dx.doi.org/10.1063/1.1864852. – DOI 10.1063/1.1864852

[90] Frey, S. ; Stadler, V. ; Heister, K. ; Eck, W. ; Zharnikov, M. ; Grunze, M. ; Zeysing, B. ; Terfort, A.: Structure of Thioaromatic Self-Assembled Monolayers on Gold and Silver. In: *Langmuir* 17 (2001), Nr. 8, 2408-2415. http://dx.doi.org/10.1021/la001540c. – DOI 10.1021/la001540c

[91] Stöhr, J. ; Gomer, R. (Hrsg.): *NEXAFS Spectroscopy.* Springer, 1992

[92] Reiss, S.: *Spektroskopische Untersuchungen verschiedener molekularer Adsorbate auf der Titandioxid(110)-Oberfläche*, Ruhr-Universität Bochum, Diss., 2001

[93] Yuan, Y. ; Randall Lee, T. ; Lytken, O. ; Drescher, H.-J. ; Kose, R. ; Gottfried, J. M. ; Allara, D. ; Stapleton, J. ; Canepa, M. ; Richter, L. J. ; Sakata, O. ; Nakamura, M. ; Gibaud, A. ; Chebil, M.S. ; Beuvier, T. ; Verdini, A. ; Krüger, P. ; Floreano, L. ; Zegenhagen, J. ; Nefedov, A. ; Wöll, C. ; Ott, F. ; Holst, B. ; Bracco, G. ; Jardine, A. ; Farias, D. ; Minniti, M. ; Miranda, R. ; Esaulov, V. A. ; Maas, D. J. ; Gastel, R. van ; Vattuone, L. ; Savio, L. ; Rocca, M. ; Figuera, J. de l. ; McCarty, K. F. ;

Della Pia, A. ; Costanini, G. ; Lyles, V. D. ; Serem, W. K. ; Yu, J.-J. ; Garno, J. C. ; Krok, F. ; Such, B. ; Kolodziej, J. J. ; Szymonski, M. ; Bracco, G. (Hrsg.) ; Holst, B. (Hrsg.): *Surface Science Techniques*. Springer, 2013

[94] Mikami, T. ; Yanagi, H.: Epitaxial structuring of blue light-emitting p-phenylene oligomers. In: *Applied Physics Letters* 73 (1998), Nr. 5, 563-565. http://dx.doi.org/10.1063/1.121856. – DOI 10.1063/1.121856

[95] Resel, R.: Crystallographic studies on hexaphenyl thin films — a review. In: *Thin Solid Films* 433 (2003), Nr. 1–2, 1 - 11. http://dx.doi.org/10.1016/S0040-6090(03)00312-2. – DOI 10.1016/S0040–6090(03)00312–2

[96] Smilgies, D.-M. ; Kintzel, E. J.: Epitaxial orientations of *para* -sexiphenyl platelets grown on alkali halide (001) surfaces. In: *Physical Review B* 79 (2009), 235413. http://dx.doi.org/10.1103/PhysRevB.79.235413. – DOI 10.1103/PhysRevB.79.235413

[97] Ashida, M.: The Orientation Overgrowth of Metal-phthalocyanines on the Surface of Single Crystals. II. Vacuum-condensed Films of Copper-phthalocyanine on Alkali Halides. In: *Bulletin of the Chemical Society of Japan* 39 (1966), Nr. 12, 2632-2638. http://dx.doi.org/10.1246/bcsj.39.2632. – DOI 10.1246/bcsj.39.2632

[98] Yanagi, H. ; Kouzeki, T. ; Ashida, M. ; Noguchi, T. ; Manivannan, A. ; Hashimoto, K. ; Fujishima, A.: Molecular orientation of vacuum-deposited thin films of zincnaphthalocyanine. In: *Journal of Applied Physics* 71 (1992), Nr. 10, 5146-5153. http://dx.doi.org/10.1063/1.350569. – DOI 10.1063/1.350569

[99] Chaudhari, P. ; Scott, B. A. ; Laibowitz, R. B. ; Tomkiewicz, Y. ; Torrance, J. B.: Characterization of epitaxially grown films of (TTF) (TCNQ). In: *Applied Physics Letters* 24 (1974), Nr. 9, 439-442. http://dx.doi.org/10.1063/1.1655252. – DOI 10.1063/1.1655252

[100] Simonyi, E.E. ; Scott, B.A. ; White, E.A.D.: Growth of epitaxial films of the organic conductor (TTF)(TCNQ). In: *Materials Research Bulletin* 11 (1976), Nr. 3, 347 - 353. http://dx.doi.org/10.1016/0025-5408(76)90201-4. – DOI 10.1016/0025–5408(76)90201–4

[101] Mainka, C. ; Bagus, P. S. ; Schertel, A. ; Strunskus, T. ; Grunze, M. ; Wöll, C.: Linear dichroism in X-ray absorption spectroscopy of strongly chemisorbed planar molecules: role of adsorption induced rehybridisations. In: *Surface Science* 341 (1995), Nr. 3, L1055 - L1060. http://dx.doi.org/10.1016/0039-6028(95)00795-4. – DOI 10.1016/0039–6028(95)00795–4

[102] Lorente, N. ; Hedouin, M. F. G. ; Palmer, R. E. ; Persson, M.: Chemisorption of benzene and STM dehydrogenation products on Cu(100). In: *Physical Review B* 68 (2003), 155401. http://dx.doi.org/10.1103/PhysRevB.68.155401. – DOI 10.1103/PhysRevB.68.155401

[103] Lukas, Simon ; Söhnchen, Sandra ; Witte, Gregor ; Wöll, Christof: Epitaxial Growth of Pentacene Films on Metal Surfaces. In: *ChemPhysChem* 5 (2004), Nr. 2, 266–270. http://dx.doi.org/10.1002/cphc.200300892. – DOI 10.1002/cphc.200300892

[104] Zou, Y. ; Kilian, L. ; Schöll, A. ; Schmidt, T. ; Fink, R. ; Umbach, E.: Chemical bonding of PTCDA on Ag surfaces and the formation of interface states. In: *Surface Science* 600 (2006), Nr. 6, 1240 - 1251. http://dx.doi.org/10.1016/j.susc.2005.12.050. – DOI 10.1016/j.susc.2005.12.050

[105] Duhm, S. ; Hosoumi, S. ; Salzmann, I. ; Gerlach, A. ; Oehzelt, M. ; Wedl, B. ; Lee, T.-L. ; Schreiber, F. ; Koch, N. ; Ueno, N. ; Kera, S.: Influence of intramolecular polar bonds on interface energetics in perfluoro-pentacene on Ag(111). In: *Physical Review B* 81 (2010), 045418. http://dx.doi.org/10.1103/PhysRevB.81.045418. – DOI 10.1103/PhysRevB.81.045418

[106] Götzen, J. ; Schwalb, C. H. ; Schmidt, C. ; Mette, G. ; Marks, M. ; Höfer, U. ; Witte, G.: Structural Evolution of Perfluoro-Pentacene Films on Ag(111): Transition from 2D to 3D Growth. In: *Langmuir* 27 (2011), Nr. 3, 993-999. http://dx.doi.org/10.1021/la1022664. – DOI 10.1021/la1022664

[107] Kitaigorodsky, A. I.: *Mixed Crystals*. Springer-Verlag, Berlin (Springer Series in Solid-State Sciences). http://dx.doi.org/10.1002/bbpc.19850890521

[108] Hinderhofer, A. ; Schreiber, F.: Organic-Organic Heterostructures: Concepts and Applications. In: *ChemPhysChem* 13 (2012), Nr. 3, 628–643. http://dx.doi.org/10.1002/cphc.201100737. – DOI 10.1002/cphc.201100737

[109] Hinderhofer, A. ; Gerlach, A. ; Kowarik, S. ; Zontone, F. ; Krug, J. ; Schreiber, F.: Smoothing and coherent structure formation in organic-organic heterostructure growth. In: *Europhysics Letters* 91 (2010), Nr. 5, 56002. http://dx.doi.org/10.1209/0295-5075/91/56002. – DOI 10.1209/0295–5075/91/56002

[110] Cantrell, R. ; Clancy, P.: A computational study of surface diffusion of {C60} on pentacene. In: *Surface Science* 602 (2008), Nr. 22, 3499 - 3505. http://dx.doi.org/10.1016/j.susc.2008.09.027. – DOI 10.1016/j.susc.2008.09.027

[111] Cantrell, R. A. ; James, C. ; Clancy, P.: Computationally Derived Rules for Persistence of C60 Nanowires on Recumbent Pentacene Bilayers. In: *Langmuir* 27 (2011), Nr. 16, 9944-9954. http://dx.doi.org/10.1021/la201576z. – DOI 10.1021/la201576z

[112] Muccioli, L. ; D'Avino, G. ; Zannoni, C.: Simulation of Vapor-Phase Deposition and Growth of a Pentacene Thin Film on C60 (001). In: *Advanced Materials* 23 (2011), Nr. 39, 4532–4536. http://dx.doi.org/10.1002/adma.201101652. – DOI 10.1002/adma.201101652

[113] Fu, Y.-T. ; Risko, C. ; Bredas, J.-L.: Intermixing at the Pentacene-Fullerene Bilayer Interface: A Molecular Dynamics Study. In: *Advanced Materials* 25 (2013), Nr. 6, 878–882. http://dx.doi.org/10.1002/adma.201203412. – DOI 10.1002/adma.201203412

[114] Yi, Y. ; Coropceanu, V. ; Bredas, J.-L.: Exciton-Dissociation and Charge-Recombination Processes in Pentacene/C60 Solar Cells: Theoretical Insight into the Impact of Interface Geometry. In: *Journal of the American Chemical Society* 131 (2009), Nr. 43, 15777-15783. http://dx.doi.org/10.1021/ja905975w. – DOI 10.1021/ja905975w

[115] Verlaak, S. ; Beljonne, D. ; Cheyns, D. ; Rolin, C. ; Linares, M. ; Castet, F. ; Cornil, J. ; Heremans, P.: Electronic Structure and Geminate Pair Energetics at Organic–Organic Interfaces: The Case of Pentacene/C60 Heterojunctions. In: *Advanced Functional Materials* 19 (2009), Nr. 23, 3809–3814. http://dx.doi.org/10.1002/adfm.200901233. – DOI 10.1002/adfm.200901233

[116] Salzmann, I. ; Duhm, S. ; Opitz, R. ; Johnson, R. L. ; Rabe, J. P. ; Koch, N.: Structural and electronic properties of pentacene-fullerene heterojunctions. In: *Journal of Applied Physics* 104 (2008), Nr. 11, 114518. http://dx.doi.org/10.1063/1.3040003. – DOI 10.1063/1.3040003

[117] Zheng, Y. ; Pregler, S. K. ; Myers, J. D. ; Ouyang, J. ; Sinnott, S. B. ; Xue, J.: Computational and experimental studies of phase separation in pentacene:C[sub 60] mixtures. In: *Journal of Vacuum Science & Technology B: Microelectronics and Nanometer Structures* 27 (2009), Nr. 1, 169-179. http://dx.doi.org/10.1116/1.3072516. – DOI 10.1116/1.3072516

[118] Jin, W. ; Dougherty, D. B. ; Cullen, W. G. ; Robey, S. ; Reutt-Robey, J. E.: C60-Pentacene Network Formation by 2-D Co-Crystallization. In: *Langmuir* 25 (2009), Nr. 17, 9857-9862. http://dx.doi.org/10.1021/la900968d. – DOI 10.1021/la900968d

[119] Smerdon, J. A. ; Rankin, R. B. ; Greeley, J. P. ; Guisinger, N. P. ; Guest, J. R.: Chiral "Pinwheel" Heterojunctions Self-Assembled from C60 and Pentacene. In: *ACS Nano* 7 (2013), Nr. 4, 3086-3094. http://dx.doi.org/10.1021/nn304992c. – DOI 10.1021/nn304992c

[120] Conrad, B. R. ; Tosado, J. ; Dutton, G. ; Dougherty, D. B. ; Jin, W. ; Bonnen, T. ; Schuldenfrei, A. ; Cullen, W. G. ; Williams, E. D. ; Reutt-Robey, J. E. ; Robey, S. W.: C60 cluster formation at interfaces with pentacene thin-film phases. In: *Applied Physics Letters* 95 (2009), Nr. 21, 213302. http://dx.doi.org/10.1063/1.3266857. – DOI 10.1063/1.3266857

[121] Yoo, S. ; Domercq, B. ; Kippelen, B.: Efficient thin-film organic solar cells based on pentacene/C60 heterojunctions. In: *Applied Physics Letters* 85 (2004), Nr. 22, 5427-5429. http://dx.doi.org/10.1063/1.1829777. – DOI 10.1063/1.1829777

[122] Cheyns, D. ; Gommans, H. ; Odijk, M. ; Poortmans, J. ; Heremans, P.: Stacked organic solar cells based on pentacene and. In: *Solar Energy Materials and Solar Cells* 91 (2007), Nr. 5, 399 - 404. http://dx.doi.org/10.1016/j.solmat.2006.11.002. – DOI 10.1016/j.solmat.2006.11.002

[123] Noever, S. J. ; Fischer, S. ; Nickel, B.: Dual Channel Operation Upon n-Channel Percolation in a Pentacene-C60 Ambipolar Organic Thin Film Transistor. In: *Advanced Materials* 25 (2013), Nr. 15, 2147–2151. http://dx.doi.org/10.1002/adma.201203964. – DOI 10.1002/adma.201203964

[124] Breuer, T.: *Wachstum und Struktur von Perfluoropentacen auf Alkalihalogeniden*, Philipps-Universität Marburg, Diplomarbeit, 2010

List of Figures

List of Tables

Appendix I: NEXAFS-Dichroism Plots for different Substrate Symmetry

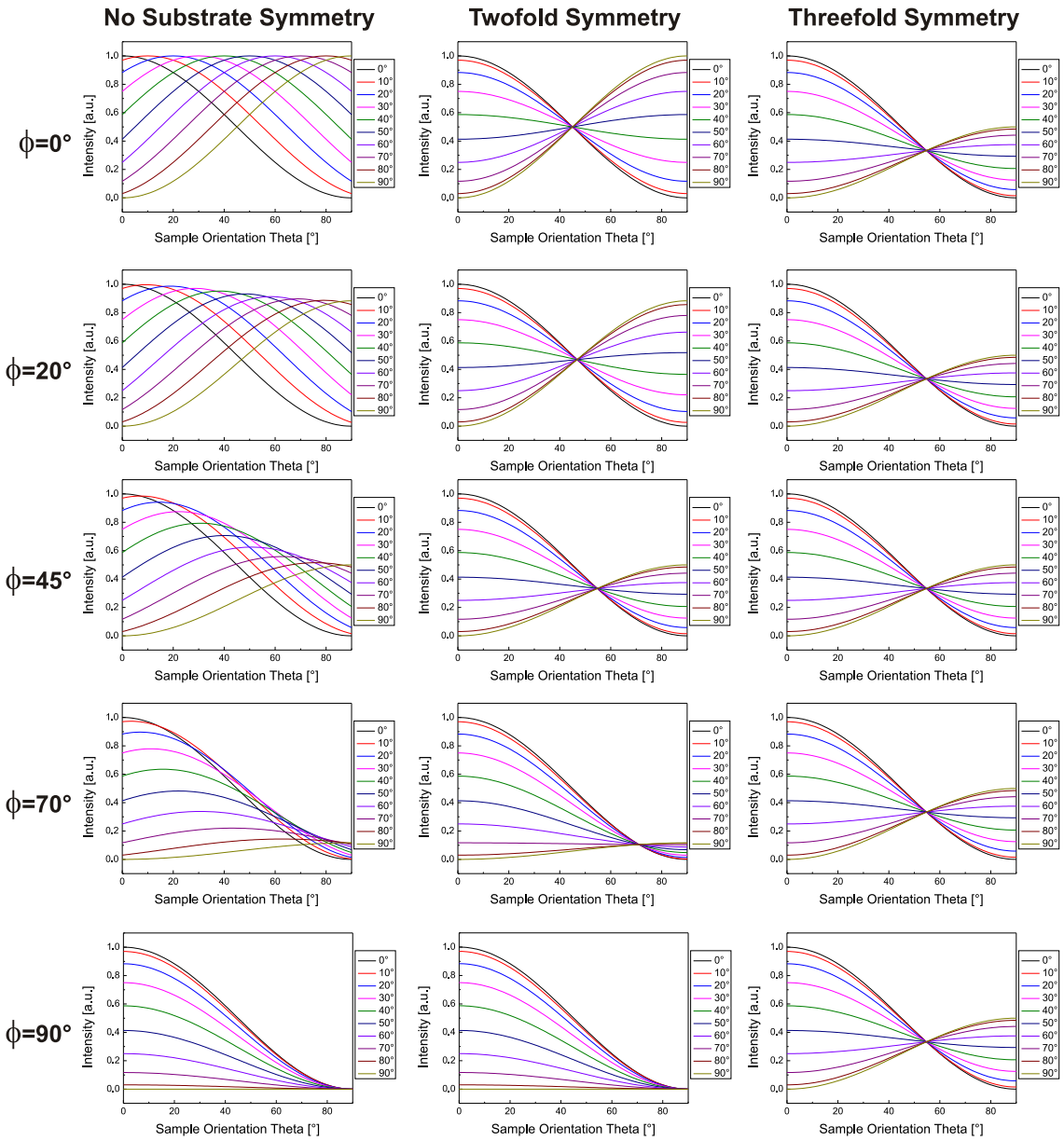

All cases are plotted for ideally linear-polarized light (P=1). As discussed in the main text, for non-ideal polarizations, both the spectra and the magic angles are different.

Abstract

This thesis summarizes a number of studies regarding the preparation and spectroscopic characterizations of thin films of the organic semiconductor perfluoropentacene (PFP) and pentacene-tetrone (P-TET), as well as heterostructures of PFP and pentacene (PEN) and of PEN and Buckminster-Fullerene (C_{60}).

By combining various techniques, the morphology and structure of the thin films was analyzed and it was examined, how modifications of the preparation procedure such as the variation of the diffusion lengths of the molecules by tuning the substrate temperature influence the film formation. By specific choice of substrates with diverse geometrical and chemical properties, molecular films in different, highly ordered conformations have been prepared. This enabled detailed polarization-resolved spectroscopic characterizations, and thus allowed to determine the anisotropic electronic and vibrational characteristics of crystalline organic semiconductors. Furthermore, the influence of the nanoscopic quality of the substrate on the resulting thin films has been investigated for the combination of highly oriented pyrolitic graphite as substrate and PFP as well as P-TET as adsorbates. It was shown that the weak, but efficient interaction between substrate and adsorbate, results in planar adsorption conformation and large crystal sizes. This is especially interesting as it allows spectroscopic access to thin films with recumbent molecular orientation in the absence of chemical modification of the molecules by the substrate as often found in the case of metal substrates. Moreover, it was found that this template effect is suppressed even by microscopic substrate defects. In the case of deposition of PFP on HOPG a new crystalline structure (polymorph) has been identified and resolved, in which the PFP-molecules stack in parallel sequence relative to one another instead of adopting the common herringbone-motif. As this parallelism leads to effective overlap of the molecular π-orbitals, it was found that the charge carrier mobility is enhanced by a factor greater than 10 compared to the bulk structure to a value which is even higher than the one found for pentacene.

Furthermore, the PFP-metal-interfaces in case of the metals gold, silver and copper were studied. Because these interfaces are of great significance for the efficiency of actual devices, the comprehension and the stability of them is very important for the advancement of organic electronic devices. We found that the stability against catalytic processes, which had been ascribed to PFP, actually is not as high as projected. Instead, at reactive silver and copper surfaces, upon supply of thermal energy significant changes of the structural

and electronic properties occur, which lead to complete dissociation of the molecule at high temperatures.

Finally, studies have been conducted which are supposed to gain insights into structure formation and interaction of organic molecules with one another in so-called organic heterostructures. Organic heterostructures are of great importance, because a high number of prototypical electronic devices as organic solar cells and ambipolar organic field-effect transistors, are made of more than one compound. The efficiency of such devices in turn critically depends on the electronic interaction, the intermixture and the relative conformation. This leads to the necessity of conducting studies which investigate these correspondences with the aid of appropriate model systems. Such studies have been performed in this thesis, choosing heterostructures of PFP and PEN as well as PEN and C_{60} as model systems. Due to their high structural and electronic compatibility, crystalline molecular intermixture of PFP and PEN is found. It was furthermore shown that the proposed efficient quadrupolar of both compounds indeed results in electronic interaction and enhanced thermal stability of the heterostructure compared to the single compound. Moreover, different preparation methods of this heterostructure were compared and detailed insight was gained into the influence of the intermixture on the electronic properties. Although in turn heterostructures of PEN and C_{60} exhibit molecular separation, they nevertheless influence each other regarding their nanostructure. It was shown that by tuning the effective diffusion length of the fullerenes, C_{60} nanostructures of different dimensionality can be prepared, which furthermore renders possibilities to fabricate buried molecular nanostructures of low dimensionality.

Zusammenfassung (Abstract in German)

Diese Arbeit ist eine Zusammenfassung der Studien zur Präparation und spektroskopischen Charakterisierung von Dünnfilmen des organischen Halbleitermoleküls Perfluoropentacen (PFP) und Pentacenetetrone (P-TET), sowie von Heterostrukturen von PFP und Pentacen (PEN) und von PEN und Buckminster-Fulleren (C_{60}).

Durch die Kombination verschiedener Messtechniken wurden die Morphologie und Struktur der Dünnfilme analysiert und der Effekt von Veränderungen des Präparationsprozesses wie zum Beispiel der Variation der Diffusionslängen der Moleküle durch Einstellung der Substrattemperatur auf die Dünnfilme untersucht. Durch die gezielte Auswahl von Substraten verschiedener geometrischer und chemischer Eigenschaften wurden molekulare Dünnfilme in verschiedener, hochgeordneter Ausrichtung hergestellt. Dies ermöglichte die detaillierte polarisationsaufgelöste spektroskopische Vermessung dieser Dünnfilme, wodurch die anisotropen elektronischen, morphologischen und Vibrationseigenschaften der organischen Halbleitermoleküle in kristalliner Form bestimmt werden konnten. Weiterhin wurde der Einfluss der nanoskopischen Qualität des Trägersubstrates auf die resultierenden Dünnfilm-Eigenschaften für die Kombination von hochorientiertem pyrolitischen Graphit (HOPG) als Substrat und PFP und P-TET als Adsorbate untersucht. Hierbei zeigte sich, dass die schwache, aber effiziente Wechselwirkung zwischen dem Graphit-Substrat und dem Adsorbat in einer planaren Adsorptionsgeometrie und großer Kristallitgröße der Acene auf HOPG resultiert. Dies ist speziell interessant, da es spektroskopischen Zugang zu Dünnfilmen in liegender molekularer Orientierung ermöglicht, ohne dass die Moleküle durch starke Wechselwirkung mit dem Substrat chemisch verändert werden, wie es oft bei Kontakt mit Metalloberflächen der Fall ist. Durch Variation der Substratqualität wurde festgestellt, dass bereits mikroskopische Fehlstellen im Substrat diesen Effekt unterbinden, sodass die Substratqualität als kritischer Parameter für die Strukturbildung in molekularen Dünnfilmen identifiziert wurde. Im Falle der Deposition von PFP auf HOPG wurde eine neuartige Kristallphase (Polymorphismus) von PFP entdeckt, in der die PFP-Moleküle relativ zueinander parallel stapeln statt das typische Herringbone-Muster einzunehmen. Da diese Parallelität zu einer effektiven Überlappung der molekularen π-Orbitale führt, konnte eine um mehr als den Faktor 10 erhöhte Ladungsträgermobilität, die damit sogar höher ist als jene von Pentacen, in diesen Filmen nachgewiesen werden.

Weiterhin wurden die PFP-Metall-Grenzflächen an den Metallen Gold, Silber und Kupfer studiert. Da diese Grenzflächen von entscheidender Bedeutung für die Effizienz realer Bauteile sind, ist ihr Verständnis und die Stabilität dieser Grenzfläche von großer

Bedeutung für die Weiterentwicklung organischer elektronischer Bauteile. Es zeigte sich hierbei, dass die für PFP postulierte Stabilität gegenüber katalytischen Prozessen weitaus schwächer ist als vorhergesagt. Als Konsequenz treten an Grenzflächen mit reaktiven Silber- und Kupferoberflächen bei Zufuhr von thermischer Energie signifikante Veränderungen der strukturellen und elektronischen Eigenschaften auf, die bei hohen Temperaturen zu einer vollständigen Dissoziation des Moleküls führen.

Zudem wurden Studien durchgeführt, die zu einem erweitertem Verständnis in der Strukturbildung und Wechselwirkung organischer Moleküle miteinander beitragen sollen. Solche organische Heterostrukturen sind von großer Bedeutung, da eine Vielzahl prototypialer elektronischer Bauelemente, wie beispielsweise organischer Solarzellen oder ambipolarer organischer Feldeffekttransistoren, auf Kombinationen mehrerer Komponenten zurückgreifen. Da die Effizienz dieser Bauteile wiederum kritisch von der elektronischen Wechselwirkung, der Durchmischung und relativen Anordnung der Komponenten zueinander bestimmt wird, sind die Ergebnisse dieser Arbeit, in der anhand geeigneter Modellsysteme eben solche Zusammenhänge untersucht wurden, von großer Bedeutung. Als Modellsysteme wurden Heterostrukturen von PFP und PEN sowie von PEN und C_{60} untersucht. Aufgrund der hohen strukturellen und elektronischen Kompatibilität tritt kristalline molekulare Durchmischung von PEN und PFP auf. Es wurde in dieser Arbeit nachgewiesen, dass die vorhergesagte effektive Quadruopol-Wechselwirkung beider Komponenten zu elektronischer Wechselwirkung und erhöhter thermischer Stabilität gegenüber den Einzelkomponenten führt. Darauf aufbauend wurden verschiedene Präparationsmethoden zu ihrer Herstellung verglichen. Zudem wurden detaillierte Erkenntnisse über die Auswirkungen der Durchmischung auf die elektronischen Eigenschaften gewonnen. Obwohl Heterostrukturen von PEN und C_{60} dagegen molekularer Entmischung unterliegen, beeinflussen sie sich dennoch in ihrer Nanostruktur. Es wurde gezeigt, dass durch Einstellung der Diffusionslängen der Fullerene C_{60}-Nanostrukturen unterschiedlicher Dimensionalität mit gezielter Anlagerung an PEN-Molekularstufen hergestellt werden können. Dies bietet die Möglichkeit zur Fabrikation vergrabener molekularer Nanostrukturen, die spektroskopisch adressiert werden können.

Acknowledgements

I would like to express my great thanks to a lot of people who helped me to finish this thesis.

First of all I want to thank my supervisor, Gregor Witte. His enormous motivation, interest in the latest experiments and his infinite energy have been constant stimuli. I appreciate the great opportunity he provided, that allowed to do research at up-to-date, challenging topics. I am very aware that the quality of mentoring that he provides is exceptional.

Furthermore I want to express my gratitudes to Sangam Chatterjee for his role als second assessor of this thesis as well as the stimulating discussions concerning our cooperations. The same is true for the further members of the examination board, Peter Jakob and Reinhard Noack.

For their assistance and encouragement upon struggles in experiments and complicated data interpretations, I want to thank all members of the MolFk-group. Especially Christian Schmidt and Michael Klues have been faithful companions, whose helpfulness, creativity and support have been a great help.

Of course I would also like to thank all cooperation partners. Combining different techniques and perspectives to gain insights into complex questions, is indispensable in order to achieve reliable results and has been very beneficial.

Always having a sympathetic ear and being ready to be of assistance in repairing and improving our equipment, Peter Osswald was a steady supporter and enormous help in providing a good working atmosphere.

This gratitude shall also be expressed to all members of the fine mechanics and electronics workshops, who facilitated great instruments and motivation to enable the realization of novel experiments.

Special thanks go to my friends for their great support and their ability to provide some diversion from work-related thoughts.

Finally I want to thank my wife Carina and my little daughter Louisa, as they were always able to put a smile on my face, regardless of the struggles and unexpected problems that may have occured along the day.